The microscopic structure of water under extreme conditions

Dissertation

zur Erlangung des Doktorgrades der Naturwissenschaften
der Fakultät Physik der Technischen Universität Dortmund

vorgelegt von
Mirko Elbers

April 2021

1. Gutachter: Prof. Dr. Metin Tolan
2. Gutachter: Prof. Dr. Max Wilke

Contents

1 Introduction

The appearance of liquid water on this planet was essential for the emergence of life. Consequently, a common attribute of all living beings on Earth is the need for water to survive [1]. Apart from its biological importance in everyday life, water is a key component for numerous industrial processes, e.g. to synthesize chemicals, refine petroleum, produce primary metals, cool thermoelectric power plants or manufacture semiconductors [2, 3]. In addition, water is also an important factor on a planetary scale, occurring in subsurface materials in the Earth's interior. There, it influences the rheology of the surrounding rock and, as a transport agent for heat and mass, alters the viscosity of melts and thus significantly affects igneous processes [4–6]. The latter is assumed to be a necessity for the occurrence of present-day plate tectonics. When both thermodynamic conditions are elevated, as likewise the case for a large proportion of subsurface water, the increased pressure prevents liquid water from undergoing the phase transition to the gaseous state rendering it a hydrothermal fluid. The properties of hydrothermal water differ drastically compared to water at ambient conditions and are, e.g. the reason for its enormous influence on the large-scale geological processes mentioned above. Another more specific instance is the change in polarity of water at high temperatures, making it a nonpolar solvent that is completely miscible with organic materials, which is exploited in many different chemical processes [7]. Thus, the study of water at high temperatures has been a long-standing research topic with numerous studies aiming to elucidate water's properties in this extreme state [8–10]. However, the majority of the studies focusing on the analysis of the structural arrangements of the water molecules at elevated temperatures used theoretical methods such as molecular dynamics simulations, while experimental evidence is scarce due to the considerable difficulties in conducting experiments under these conditions [11–15]. Liquid water is not only exposed to extreme conditions in Earth's interior, but also occurs at elevated, albeit significantly lower, pressures in the deep sea, providing habitat for a variety of marine organisms that have adapted to the pressure conditions with a mechanism that is not yet fully understood but appears to involve a strong interaction with the water structure [16, 17]. Furthermore, there is also evidence that liquid water exists under the icy shell of celestial bodies such as Europa or Enceladus under similar high pressure conditions, possibly even with simulta-

neously elevated temperatures due to suspected hydrothermal vents, which could provide the energy source for the potential evolution of life [18–20]. Controlled pressure changes also provide a promising opportunity to more thoroughly test and investigate various proposed structural models for liquid water [21, 22]. Furthermore, pressurised aqueous liquids are used in various industrial applications, e.g. in the food industry, where high pressures are used to pasteurise liquid foods such as milk [23]. Therefore, the importance of water and the variety of its use cases are by no means limited to its properties at ambient conditions, but numerous astonishing characteristics solely manifest under extreme environments such as high pressure and/or high temperature.

In natural processes, water rarely occurs in pure form but rather with a variety of dissolved salts or other substances. The most abundant salt in seawater and also in the majority of natural hydrothermal fluids is sodium chloride. Dissolved NaCl in the ocean directly influences the density of seawater and thus the circulation of ocean currents from tropical areas at the equator to the poles, which also affects global climate [24, 25]. In the Earth's upper mantle, NaCl is also a major constituent in hydrothermal fluids. Thereby, dissolved salts, play an essential role in the formation of ore deposits as they facilitate the transport of metal by forming metal bearing complexes. For instance, chloride in particular is known to highly increase the solubility of sulfide minerals by acting as a ligand for metal complexation [26, 27].

One of the most fascinating properties of water which is caused by its polar nature is its capability to form hydrogen bonds with the surrounding water molecules. These hydrogen bonds define the dynamic local structure of liquid water, which in turn is related to various unique properties and anomalies such as the famous density maximum at around 4 °C [28]. Moreover, the structure has a profound influence on the response of the water system to external thermodynamic conditions. In the last decades, several scenarios have been proposed to explain the anomalous behaviour exhibited by many thermodynamic parameters of water under the influence of an external parameter such as temperature [29–32]. These scenarios for the phase behaviour of water have different implications for the properties of the liquid, which, however are partly extreme difficult or plainly infeasible yet to experimentally investigate and thus to verify. This is due to the so-called no-man's land, a region in the phase diagram of water between a temperature of 160 K and 232 K, where ice nucleation occurs so quickly that the study of liquid water with conventional experimental techniques is not yet possible [33]. Two famous scenarios, namely the second-critical point scenario and the singularity-free scenario, suggest the existence of two distinct structural arrangements in liquid water with a corresponding liquid-liquid transition further emphasizing the importance of understanding the structure of water at a microscopic level over a wide range of

thermodynamic conditions [30, 32].
Addressing the elaborated immense importance of the water network for water's numerous properties, the main objective of this thesis is to investigate the microscopic structure of water and in particular its changes as induced by a large variety of thermodynamic conditions. In this regard, water and aqueous sodium chloride solutions are studied in highly relevant thermodynamic ranges in terms of temperature and pressure up to maximum values of 600 °C and 8.5 kbar, respectively. The high temperature corresponds to conditions found in geological and industrial hydrothermal fluids [34, 35]. Due to the abundance and crucial role of salts in natural subsurface hydrothermal fluids, aqueous sodium chloride solutions are likewise examined at high temperatures. With respect to the applied high pressures at ambient temperature, 8.5 kbar is close to the phase transition boundary to ice VI at approximately 9 kbar, meaning it renders the system in one of the most extreme states in terms of compressibility, allowing to study the structure of liquid at the edge of its thermodynamic stability regime [36]. The investigated pressure range covers various interesting pressure regions, e.g. the highest pressure in the ocean (Mariana Trench with about 1 kbar) and the range between 2 kbar and 4 kbar in which different structural anomalies were observed in previous studies [37–40].
The structure of liquid water has been investigated in the previous literature by means of various experimental techniques such as X-ray absorption spectroscopy, X-ray and neutron scattering to name but a few, which provide structural information on various length scales and with different advantages and disadvantages in terms of their experimental set-up i.e. exploitable sample environments [41, 42]. In this thesis, inelastic X-ray scattering (IXS) is used for the structural investigation of liquid water at extreme conditions [43]. In particular, the IXS associated experimental technique, X-ray Raman scattering (XRS) spectroscopy, is predominantly exploited, a well-established powerful technique to study absorption edges of elements via the IXS process [10, 44–50]. Here, XRS spectroscopy enabled to measure the oxygen K-edge spectrum of liquid water in extreme challenging sample environments such as diamond anvil cells, which are employed to generate high temperature and pressure conditions. The oxygen K-edge spectrum of water contains valuable information about the averaged local structure surrounding the scattered atoms. The accessible information is further extended by density functional theory calculation of XRS spectra based on structural models and subsequent comparison with the experimental data.
In the following, the structuring of this thesis is outlined. The subsequent chapter is devoted to establish water as a sample system by introducing the most famous scenarios, which aim to explain the thermodynamic and structural properties of liquid water, and by elaborating its structural properties at ambient conditions as a reference point. Furthermore, the most exploited structural parameters in this

thesis as determined from simulated models are explained as well as the correlation of the spectral features of the oxygen K-edge with the local structural environment of the scattered atom. The third chapter establishes the theoretical foundation for the various experimental techniques used in this thesis and provides an overview of density functional theory, which was employed to calculate theoretical spectra based on structural models to complement the experimental data. The theory chapter is followed by the four main studies of this thesis. These are largely self-contained, i.e. in addition to the actual results and discussion section, they each include their own further introduction, which provides a more detailed insight into the respective topic, as well as an experimental section and a summary. In the first study, respectively in the fourth chapter, XRS spectroscopy measurements are combined with spectral calculations based on structures obtained from provided *ab initio* molecular dynamics simulations to investigate the structural changes in aqueous sodium chloride solution with increasing temperature up to 600 °C at a maximum pressure of 1.2 kbar. In addition, the results are further compared with the findings from a previous study that utilized the same approach on hydrothermal pure water [10]. The fifth chapter deals with the pressure behaviour of the water structure at room temperature up to a pressure of 8.5 kbar using a similar combined experimental and theoretical approach as in the previous chapter. Furthermore, the pressure induced spectral changes are compared with the spectral and structural differences between several ice phases to gain more insights into the local arrangement of the water network [51, 52]. In the sixth chapter, the pioneering work of Abbamonte *et al.*, in which they used IXS to study water at sub-angstrom length and femtosecond time scales, is further extended to investigate water and aqueous sodium chloride solutions at temperatures up to 250 °C and 90 °C, respectively, on even smaller time and length scales [53, 54]. This includes the development of a new data treatment scheme to systematically analyse the measured spectra over a much larger scan range which introduces additional requirements on a consistent analysis. Chapter seven contains the results of a side project on the structural characterisation of two molecular and two polymerized ionic liquids by means of X-ray diffraction and X-ray absorption spectroscopy. Ionic liquids are salts with a complex organic cation and an organic or inorganic anion, which causes a significant reduction of the melting point below 100 °C. They are involved in many chemical processes and since numerous ionic liquids are hygroscopic, they incorporate water into their structure when exposed to air [55, 56]. This incorporation of water strongly influences the properties of these liquids and renders a structural understanding at the microscopic level necessary [57]. Thus, the salt structure is first investigated without the addition of water, which paves the way for further analyses of the combined system. In the last chapter, a comprehensive summary of the individual studies is provided as well as an outlook for further research potential.

2 Water as a sample system

This chapter is devoted to introduce water as a sample system by briefly compiling some of its unique properties, describing its intra- and intermolecular structure and finally explaining how the experimental X-ray Raman scattering spectra and the theoretical data were utilized to obtain structural information about the local arrangement of water molecules.
As underlined in the previous chapter, water is one of the most important liquids on the planet for the evolution of life and our modern civilisation. This makes it an extensively studied sample system in various scientific branches [10, 58–64]. The exceptional importance is due to the various anomalies of water. Four instances of the drastic difference water inherits in contrast to a typical liquid are shown in Figure 2.1 taken from the literature [33, 65, 66]. The plot on the far left depicts the density of water as a function of temperature and shows the most striking anomaly of water, namely its density maximum at 4 °C, while the density of a typical liquid increases at lower temperatures. This anomaly causes ice to float on water, which allows fish to survive even at extremely low surface temperatures below a layer of ice. The anomaly is closely linked to the ability of water to form hydrogen bonds [28]. The second is the isothermal compressibility of water, shown in the second diagram from the left. It decreases when the temperature is above 46 °C and is reduced, comparable to a normal liquid, but increases when the temperature is further reduced below 46 °C. Since the isothermal compressibility is related to volume i.e. density fluctuations in the system, this indicates an increase in fluctuations even though the thermal energy in the system decreases. The second plot from the right represents the isobaric heat capacity as a function of temperature, which is related to entropic fluctuations in the system and its temperature-dependent evolution shows a similar deviation from a typical fluid as the isothermal compressibility. Furthermore, Figure 2.1 shows the coefficient of thermal expansion on the far right side as a function of temperature which is a measure of the cross-correlation between density and entropy fluctuations in the systems and deviates from the evolution of a typical liquid as it becomes negative below 4 °C at the maximum density i.e. the entropy decrease with increasing volume [65, 66]. Apart from density, these changes are most pronounced at very low temperatures, yet the anomalous behavior is already observed at ambient conditions and affects the properties of water in

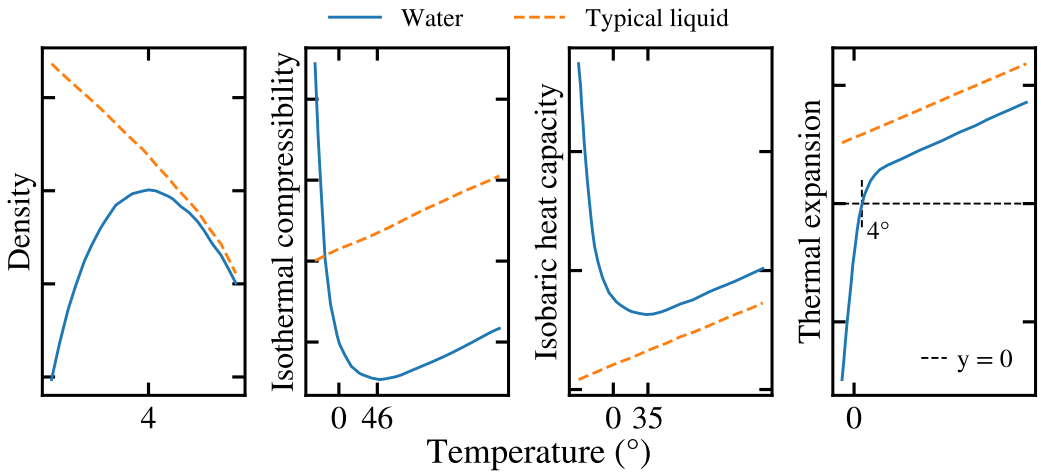

Figure 2.1: Four instances of the anomalous behaviour of water compared to a typical liquid, from left to right: Maximum density of water at 4 °C, isothermal compressibility κ_T with a minimum at 46 °C, isobaric heat capacity C_p with a minimum at 35 °C and the coefficient of thermal expansion α_p which is negative below 4 °C. The data is taken from the literature [33, 65, 66].

this biologically relevant range [66]. Several different scenarios for water were proposed since the beginning of the 80s to explain its unique properties. However, the unambiguous confirmation of a single scenario could not yet be provided, as many important properties lie in the so-called no-man's land between 160 K and 232 K, in which the ice nucleation occurs too rapidly for a conventional experimental technique to probe the liquid water system [33]. An insightful depiction of the differences of the four most prominent and discussed scenarios is given in the phase diagram of Figure 3 in the paper of Gallo *et al.* together with a brief introduction [33]. The first proposed scenario is the so-called Speedy's stability limit conjecture as it was introduced by R. Speedy [29]. In this scenario, the liquid state boundary at high temperatures reverses its temperature dependence where the line of density maxima meets the liquid-vapor spinodal at negative pressure. It then continues to define the low temperature limit of liquid water. As the name suggests, the second-critical point scenario proposes a second critical point at a positive pressure below 0 °C, at which a liquid-liquid transition line ends [30]. The critical-point-free scenario also involves a liquid-liquid transition but with the critical point at negative pressure where it meets the liquid-vapor spinodal and the two become indistinguishable as their characteristic fluctuations merge [31]. The last scenario introduced by Sastry *et al.* is the singularity-free scenario which exhibit a quasi-critical point only at 0 K without a liquid-liquid transition and pronounced maxima

of different response functions e.g. the isothermal compressibility at different temperatures [32]. For a detailed explanation of the different scenarios, it is referred to the listed literature. A new promising approach to study these scenarios despite the experimental challenge of the no-man's land, is to investigate water properties e.g. the line of density maxima at negative pressure [67, 68]. In contrast, one approach of this thesis is to apply high pressures to liquid water in order to tune the structural conversion of the proposed structural forms and to investigate the respective structures [69].
The question that has engaged scientists for over a century is how the unique properties of liquid water are linked to the structure and dynamics of the water network formed by hydrogen bonds. Addressing this question, this thesis focuses on the changes in the structure of liquid water over a wide range of the phase diagram, i.e. under the influence of extreme conditions such as high temperature and pressure. Hence, an overview of the known intra- and intermolecular structural properties of a water molecule at ambient conditions is given in the following to provide the basis for a comprehensive analysis. From the literature known deviations from the introduced water structure due to high temperature or pressure are further explained and discussed in the respective chapters. Moreover, the analysis scheme is elaborated to exploit the obtained experimental and theoretical data in order to extract detailed structural information of the water network.

2.1 Structural properties

Water consists of two hydrogen atoms covalently bonded to an oxygen atom. The distance between the oxygen and the two hydrogen atoms is approximately 0.97 Å, with slightly different results from various theoretical and experimental studies [70–72]. The angle H-O-H between the three atoms is approximately 104.5° which is slightly smaller than the angle 109.5° for a typical tetrahedron due to the stronger interaction of the two lone electron pairs of the oxygen [72, 73]. A schematic depiction of a single water molecule with its structural properties is shown in Figure 2.2. With respect to its charge particles, water consists of ten protons and ten electrons, hence, its net charge is zero. However, the charge is not evenly distributed as the attraction of the shared electrons to the oxygen is larger than to the two hydrogen atoms. Therefore, the two hydrogen atoms have a positive partial charge and the opposing oxygen a partial negative one which makes water a polar molecule. This enables water to form hydrogen bonds with the surrounding water molecules with an average interaction strength of about 23.3 kJ/mol in pure water at room temperature [74]. Compared to the covalent bonds in the water molecule itself which are

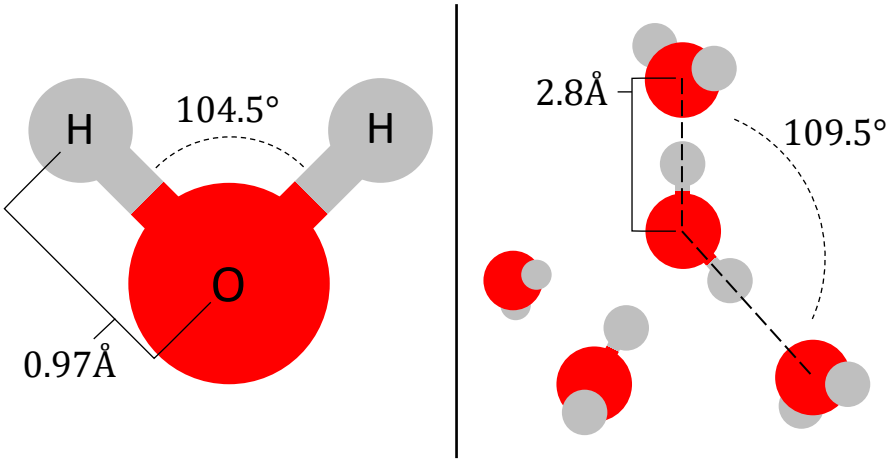

Figure 2.2: (left) Schematic of a single water molecule with its structural properties. (right) Tetrahedral arrangement of a water pentamer.

about a factor 20 larger with approximately 490 kJ/mol [75], hydrogen bonds are a comparably weak attraction, however, they are responsible for various physical properties of water. An example that can be experienced in everyday life is the boiling point of water, which is significantly increased as energy is required to break the hydrogen bonds between molecules. In total, water can form four hydrogen bonds with its nearest neighbours by donating and accepting hydrogen atoms to and from the surrounding molecules, respectively. However, averaged over time, each molecule only forms approximately 3.6 hydrogen bonds at room temperature [10, 73]. The ability of forming hydrogen bonds in combination with the position of the two hydrogen atoms and the two lone pairs of the central oxygen atom, leads to the arrangement of the four neighbouring water molecules in a tetrahedral-like structure. At room temperature, these water molecules are located at a distance of about 2.8 Å from the oxygen of the central water molecule from whose point of view they span O-O(central)-O angles with a peak at about 109.5° in the associated angular distribution [37, 76–78]. These hydrogen bonds and the resulting tetrahedral structural arrangements are temporally volatile, as they break on a time scale of femto- to picoseconds and reform in possibly different orientations. [79, 80]. However, the ability to form hydrogen bonds with up to four water molecules is considered to be the reason for some of waters most astonishing properties and anomalies. Two examples are the decrease in viscosity of water under pressure and the high surface tension of water [28]. Water also exhibits a second hydration shell with about 12 water molecules at an average distance of 4.5 Å [81]. Some of these water molecules are hydrogen bonded to the first shell.
Two of the four scenarios for liquid water mentioned in the previous section sug-

gest the existence of a liquid-liquid transition indicating two forms of water with distinguishable structural properties and different densities [33]. These two forms of water are referred to as low-density water (LDW) and high-density water (HDW) analogous to the two different forms of amorphous ice. Under, e.g. ambient conditions, these two structures continuously transform into each other. The structure of the two phases were indirectly investigated by Soper *et al.* by performing neutron diffraction experiments on liquid water under various pressures [69]. Assuming that the extracted O-O partial structure factor can be described as a linear combination of the structure factors of LDW and HDW with varying ratio depending on the applied pressure, they linearly extrapolated the O-O partial structure factor to the respective end points. The O-O partial structure factor of the two end points were attributed to LDW and HDW, respectively. Soper *et al.* determined the structure corresponding to each O-O partial structure factor and found an increase of density from 0.0295 molecules/$Å^3$ to 0.0402 molecules/$Å^3$ as a result of the transition from LDW to HDW due to an inward movement of the second hydration shell accompanied by the breaking of hydrogen bonds between the first and second shell [69]. As mentioned earlier, such interconversion can be tuned by pressure, which is further studied in this thesis.

Water dissolves salts or other charge carriers due to its polar nature with a dielectric constant of 78.4 at room temperature [82]. In the case of anions, the water molecules orient themselves with the hydrogen side towards the ion and form hydrogen bonds. In contrast, a hydration shell is also formed around the cation, but the oxygen side of the water molecules points in the direction of the cation. In order to investigate the influence of salts on the water structure, the widely studied sodium chloride is used in this work. Aqueous sodium chloride solution is a prototypical model system for fluids both in a geochemical context and for solution chemistry. At ambient conditions sodium chloride is solvable up to a concentration of 360 g/l [83]. The water molecules form hydration shells around the two ions with a coordination number of 4-6 and around 6 for sodium and chloride, respectively, if the solution is not too highly concentrated [64, 84]. The average distance between the water molecules and the sodium ion is approximately 2.5 Å and about 3.1 Å for the chloride ion [64]. The solubility properties of water are strongly connected to its dielectric constant, which changes as a function of temperature. For instance, the amount of ion association is much larger at hydrothermal temperatures than at ambient temperatures [85].

2.2 Analysis of water

The local structure around a water molecule affects the spectral shape of the associated oxygen K-edge, thus the qualitative analysis of oxygen K-edge spectra is a powerful tool to study the microscopic structure of water. Therefore, the correlation between the structural environment of the absorbing atom and the spectral features are introduced in the following. However, beforehand, the structural parameters are explained, which are determined using both, the molecular dynamics (MD) simulation trajectories published by Imoto *et al.* [62] and provided by Prof. Dr. Sandro Jahn, since several of these evaluated parameters are correlated to the spectral features [86]. The terms used in this paper with reference to the water structure, such as water network, refer to the parameters introduced below, unless otherwise stated.

2.2.1 Structural parameter

In order to perform an extensive analysis of the MD simulation, various structural parameter are extracted from the trajectories. The number of hydrogen bonds are evaluated based on the criteria introduced by A. Luzar and D. Chandler [87]. According to these criteria, a hydrogen bond is present between two molecules when the distance between the two oxygen atoms is less than 3.5 Å and the donor(H)-donor(O)-acceptor(O) angle as seen from the donating oxygen, is less than or equal 30°. In addition, the degree of deviation from a perfect tetrahedron is quantified in terms of angle and distance using the criteria from Niskanen *et al.* to analyse the changes of the tetrahedral structure as a function of an external parameter such as temperature or pressure [86]. The parameters are calculated using a central water molecule and the closest four neighbouring water molecules with the vectors $\hat{\boldsymbol{r}}_{i,j}^{\mathrm{loc}} = \boldsymbol{r}_{i,j}^{\mathrm{loc}}/|\boldsymbol{r}_{i,j}^{\mathrm{loc}}|$ pointing from the oxygen of the central water molecule to the oxygen of the different water molecules. Using the equations

$$\Delta_a = \sum_{i=1}^{3} \sum_{j=i+1}^{4} |\mathrm{acos}(\hat{\boldsymbol{r}}_i^{\mathrm{loc}} \cdot \hat{\boldsymbol{r}}_j^{\mathrm{loc}}) - 109.5°| \tag{2.1}$$

$$\Delta_d = \max\{|\boldsymbol{r}_i^{\mathrm{loc}}|\}_i - \min\{|\boldsymbol{r}_i^{\mathrm{loc}}|\}_i, \tag{2.2}$$

the parameters are calculated for each water molecule in the employed trajectory and then all the values obtained are averaged. The first equation 2.1 describes Δ_a, the summed absolute deviation from the tetragonal O-O(central)-O angle of 109.5° by evaluating the absolute angular difference between 109.5° and the angle

spanned between the oxygen of the central water molecule and the oxygen of two of the four neighbouring water molecules. This angle is calculated and summed for all six different unique combinations of the central water molecule and the four neighbouring water molecules. Thus, Δ_a also describes the average deviation from the angle of a perfect tetrahedron after the value is divided by six. The second parameter Δ_d is calculated according to equation 2.2 by determining the distance between the oxygen of the closest and farthest water molecule with respect to the four neighbouring water molecules. Both parameters are zero when the water molecules are arranged in a perfect tetrahedron but increase when the angles or the distances start to deviate from the structure. Although absolute values of the two parameters are difficult to unambiguously interpret, they provide for an extensive analysis of relative changes as a function of an external parameter. If parameters are calculated separately for the first coordination shell of liquid water, the first minima of the determined oxygen-oxygen radial distribution function (RDF) at a value of 3.5 Å is used as cut-off radius.
In addition, certain parameters are also determined with respect to the aqueous salt solutions. A Na^+ or Cl^- ion is considered to be part of an ion pair or a larger ion cluster if its distance to another ion in the system is smaller than the first minimum of the Na-Cl RDF at 3.75 Å. The structural properties of the hydration water surrounding the ions and the bulk water are also separately determined by considering any water molecule outside the first coordination shell of the ions as bulk water. Here, the first coordination shells of the two ions are likewise defined by the first minima of the Na-O and Cl-O RDF with a value of approximately 3.4 Å and 3.9 Å, respectively. The described parameters are used in different chapters of this thesis. Further more chapter-specific parameters are introduced when necessary.

2.2.2 Analysing the oxygen K-edge of liquid water

The majority of the experiments performed in this work are XRS measurements at the oxygen K-edge of pure water or aqueous sodium chloride solution under extreme conditions. Therefore, this section describes the different spectral features and their intensity correlation with various structural arrangements of the water structure. A detailed theoretical description of the fundamental XRS process is provided in the next chapter. The oxygen K-edge of liquid water at ambient conditions is shown in Figure 2.3 and exhibits three distinctive features which are known in literature as pre-edge, main-edge and post-edge at energies around 535 eV, 537 eV and 540 eV, respectively. Numerous studies have focused on deciphering the correlation between the absolute and relative intensity of these spectral features and the surrounding structure of the absorbing/scattering oxygen atom. Although

some details are still debated in the recent literature, especially with respect to the pre-edge feature, a conclusive picture emerges that is suitable for performing an unambiguous qualitative and quantitative analysis of the spectral intensities to investigate the structure of liquid water [52, 66, 86, 88, 89].

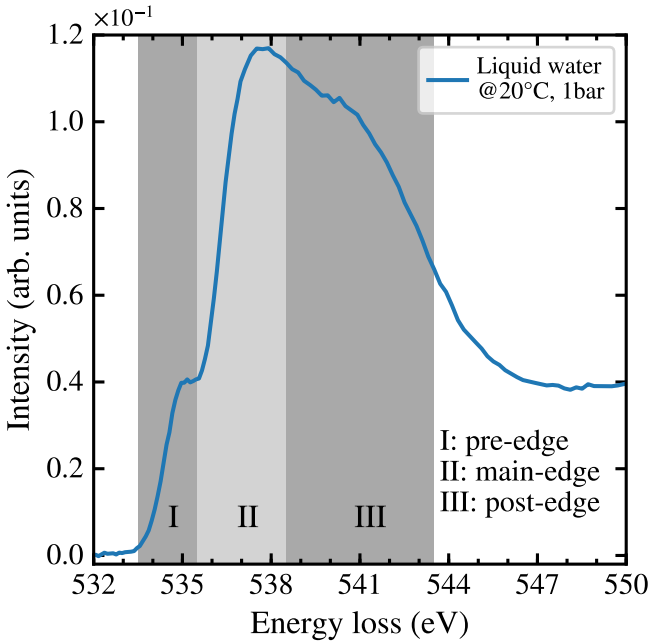

Figure 2.3: Experimentally recorded spectrum of the oxygen K-edge of liquid water at ambient conditions. The position of the three most distinctive feature are labelled and indicated in shades of grey namely, I: pre-edge at 353 eV, II: main-edge at 537 eV and III: post-edge at 541 eV.

The origin of the pre-edge intensity is the excitation into the $4a_1$ lowest unoccupied molecular orbital of water. The intensity of the spectral feature shows a negative correlation with the number of hydrogen bonds formed by the water molecule associated with the absorbing/scattering oxygen with its neighbouring molecules, and a positive correlation with the deviation from a tetrahedral structure with respect to the surrounding water molecules. Therefore, the pre-edge intensity of hydrothermal water is significantly increased compared to room temperature since the tetrahedral order is strongly reduced at high temperatures accompanied by a breaking of the hydrogen bonds up to possibly complete absence [10, 90]. The origin of the main-edge feature is largely attributed to localized excitations [88]. This is consistent with the intensity increase observed when comparing different ice phases as the main-edge becomes more pronounced with increasing density of the ice phases. Since the number of hydrogen bonds are very similar for each

ice phase, this indicates a correlation of main-edge intensity with the number of non-hydrogen bonded water molecules approaching the first shell and causing an increase in density from, e.g. ice III to ice VI [52]. In addition, a disturbance of the water structure, e.g. at high temperatures, also appears to increase the intensity of the main-edge.
The correlation of the post-edge with the number of hydrogen bonds in the system as well as the tetrahedral order is similar but contrary to the pre-edge feature. Thus, the post-edge is more pronounced if there is an increased formation of hydrogen-bonds in the system allowing a larger fraction of water molecules to arrange in a more defined tetrahedral structure. A well-defined tetrahedral structure also allows the formation of a potential well for a shape resonance [89]. In contrast to the main-edge, which can be attributed to a localized excitation, the corresponding excitation process of the post-edge is rather delocalized. Since these excitations have a higher probability of occurrence in crystalline solids than in disordered systems due to the more spatially extended wave functions, the post-edge becomes the dominant spectral region for low-density ice phases such as ice Ih [52, 88]. Hence, the redistribution of the spectral weight from the post- to the main-edge can be interpreted as a change in excitation probability that favours localized over delocalized excitations, due to an increase of structural disorder in the system as observed for amorphous ice phases [88].

3 Theory

In this chapter, the theoretical principles of the different experimental methods used in this thesis are explained, namely inelastic X-ray scattering (IXS), X-ray absorption spectroscopy and elastic X-ray scattering. Since the majority of the conducted experiments is related to IXS, a more detailed description of the underlying scattering process is given in the first part of this chapter. This includes a theoretical description of the measured quantity, the double differential scattering cross section and its basic relation to the excitation of core electrons. The relation leads to X-ray Raman scattering spectroscopy, a powerful tool to study structural and electronic properties of a system. Furthermore, the relationship between the IXS process and the imaging of an X-ray induced electron density disturbance in space and time is explained. The second part briefly covers the X-ray absorption fine structure spectroscopy, a technique used to determine the local structure surrounding an absorbing atom. Subsequently, the principles of elastic X-ray scattering to study structural correlations in liquids are explained. Additionally, a qualitative explanation of the basic concepts of density functional theory (DFT), a computational method to calculate electronic properties of a many-body system, is given.

3.1 Inelastic X-ray scattering

In an IXS process, a photon with the energy $\hbar\omega_1$, the wave vector $\boldsymbol{k_1}$ and the polarization $\boldsymbol{e}_1$ is interacting with the electronic system of a sample and is scattered into a photon with the energy $\hbar\omega_2$, the wave vector $\boldsymbol{k_2}$ and the polarization $\boldsymbol{e}_2$. Prior to the scattering process, the sample system can be characterised by an initial state vector $|i\rangle$ with the energy E_i, which is excited by the scattered photon into the state $|f\rangle$ with the energy E_f. The energy $\hbar\omega = \hbar(\omega_1 - \omega_2)$ and momentum $\hbar\boldsymbol{q} = \hbar(\boldsymbol{k_1} - \boldsymbol{k_2})$ difference between the incoming and outgoing photon is transferred to the sample, whereby due to the conservation of energy $\hbar\omega = E_f - E_i$ applies. For the given case that the transferred energy is small compared to the incident energy, the ab-

solute value of the momentum transfer corresponding to a scattering angle 2θ is approximated by the formula

$$q = 2k_1 \cdot \sin(2\theta/2) \tag{3.1}$$

A schematic drawing of the scattering geometry is depicted in Figure 3.1.

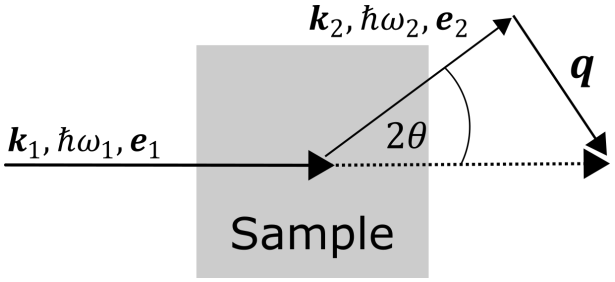

Figure 3.1: A schematic of the inelastic X-ray scattering process. The incident photon with the energy $\hbar\omega_1$, the wave vector $\boldsymbol{k_1}$ and the polarization $\boldsymbol{e}_1$ is scattered at the sample by the angle 2θ. The energy of the outgoing photon is reduced to $\hbar\omega_2$ with the wave vector $\boldsymbol{k_2}$ and the polarization $\boldsymbol{e}_1$. The energy and momentum difference is transferred to the sample in the process.

The measured quantity in an IXS experiment is the double differential scattering cross section (DDSCS) given by the expression,

$$\frac{\mathrm{d}^2\sigma}{\mathrm{d}\Omega_2 \mathrm{d}\hbar\omega_2} = \frac{\begin{array}{c}\text{current of photons scattered into the solid angle element } [\Omega_2, \mathrm{d}\Omega_2] \\ \text{and into the range of energy } [\hbar\omega_2, \mathrm{d}\hbar\omega_2]\end{array}}{\text{current density of the incident photons} \cdot \mathrm{d}\Omega_2 \cdot \mathrm{d}\hbar\omega_2}$$

as a function of the energy $\hbar\omega_2$ of the scattered photons and the solid angle element $\mathrm{d}\Omega_2$ of the detector, which defines the corresponding momentum transfer q. On account for its importance, the DDSCS is derived based on the derivation by W. Schülke [43] and M. Blume [91] from basic principles of photon-electron interactions. Starting point of the derivation is the Hamiltonian for j electrons in a quantized electromagnetic field given by the formula

$$\begin{aligned} H = &\sum_j \frac{1}{2m}[\boldsymbol{p}_j - (e/c)\boldsymbol{A}(\boldsymbol{r}_j)]^2 + \sum_{jj'} V(r_{jj'}) - \frac{e\hbar}{2mc}\sum_j \boldsymbol{\sigma}_j \cdot \nabla \times \boldsymbol{A}(\boldsymbol{r}_j) \\ &- \frac{e\hbar}{4m^2c^2}\sum_j \boldsymbol{\sigma}_j \cdot \boldsymbol{E}(\boldsymbol{r}_j) \times [\boldsymbol{p}_j - (e/c)\boldsymbol{A}(\boldsymbol{r}_j)] + \sum_{\boldsymbol{k}\lambda} \hbar\omega_{\boldsymbol{k}} \left[c^+(\boldsymbol{k}\lambda)c(\boldsymbol{k}\lambda) + \frac{1}{2}\right]. \end{aligned} \tag{3.2}$$

The natural constants appearing in the equation are the electron mass m, the electron charge e, the speed of light c and the Planck constant $\hbar$. Furthermore, the

momentum operator is described with $\boldsymbol{p}$ and the vector potential of the electromagnetic wave at the position $\boldsymbol{r}$ with $\boldsymbol{A}(\boldsymbol{r})$, which can be expressed by the formula

$$\boldsymbol{A}(\boldsymbol{r}) = \sum_{\boldsymbol{k}\lambda} \left(\frac{2\pi\hbar c^2}{V\omega_{\boldsymbol{k}}} \right)^{\frac{1}{2}} \left[\boldsymbol{e}(\boldsymbol{k}\lambda) c(\boldsymbol{k}\lambda) e^{i\boldsymbol{k}\cdot\boldsymbol{r} - i\omega_{\boldsymbol{k}} t} + \boldsymbol{e}^*(\boldsymbol{k}\lambda) c^+(\boldsymbol{k}\lambda) e^{-i\boldsymbol{k}\cdot\boldsymbol{r} + i\omega_{\boldsymbol{k}} t} \right]. \tag{3.3}$$

$\boldsymbol{E}(\boldsymbol{r}_j)$ describes the operator of the electric field at the electron position $\boldsymbol{r}$. The electron system is further defined by the Pauli spin matrices $\boldsymbol{\sigma}$. The sum in equation 3.3 and in the last term of equation 3.2 is over all modes $\boldsymbol{k}\lambda$ of the photon field, with λ counting the two orthogonal polarization states to the corresponding wavevector $\boldsymbol{k}$. The two operators $c^+(\boldsymbol{k}\lambda)$ and $c(\boldsymbol{k}\lambda)$ are the corresponding photon creation and annihilation operators, respectively. The first term of equation 3.2 represents the kinetic energy of the electrons under the influence of the external electromagnetic field. The second term is the potential of the Coulomb interactions between the electrons in the system. The potential energy of the magnetic momentum $(e\hbar/2mc)\boldsymbol{\sigma}$ in the magnetic field $\nabla \times \boldsymbol{A}(\boldsymbol{r})$ of the radiation is described by the third term. Similar to the third term, the fourth term also corresponds to the potential energy of the magnetic momentum in a magnetic field $(1/c)(\boldsymbol{v} \times \boldsymbol{E})$ but induced by the electron moving with the velocity $\boldsymbol{v} = (1/m)[\boldsymbol{p} - (e/c)\boldsymbol{A}]$. The terms with the spin matrix $\boldsymbol{\sigma}$ and the vector potential $\boldsymbol{A}$ highlight the capability of IXS to investigate magnetic properties. However, since the magnetic interactions are minor for the systems studied in this work, these terms are neglected in the following. The last term considers the energy of the photon field.
In order to derive the DDSCS from equation 3.2, the terms which explicitly contain the vector potential and thus describe the interaction of the radiation field with the electron system are separated and then treated within perturbation theory as small perturbation. For this purpose Coulomb gauge $\nabla \boldsymbol{A} = 0$ is used with the scalar Coulomb potential ϕ to substitute the operator of the electric field with

$$\boldsymbol{E} = -\nabla\phi - \frac{1}{c}\dot{\boldsymbol{A}} \tag{3.4}$$

After evaluating the square in the first term, the following parts of the Hamiltonian can be identified as describing the perturbation of the system

$$H_{i1} = \frac{e^2}{2mc^2} \sum_j \boldsymbol{A}^2(\boldsymbol{r}_j) \tag{3.5}$$

$$H_{i2} = -\frac{e}{mc} \sum_j \boldsymbol{A}(\boldsymbol{r}_j) \cdot \boldsymbol{p}_j. \tag{3.6}$$

The unperturbed part of the electron system is expressed by the three remaining parts

$$H_0 = \sum_j \frac{1}{2m} \boldsymbol{p}_j^2 + \sum_{jj'} V(r_{jj'}) + \frac{e\hbar}{4m^2c^2} \sum_j \boldsymbol{\sigma}_j \cdot (\nabla\phi \times \boldsymbol{p}_j) \tag{3.7}$$

with the last one including the spin-orbit coupling term for electrons. The remaining term is the Hamiltonian for the radiation field

$$H_R = \sum_{\boldsymbol{k}\lambda} \hbar\omega_{\boldsymbol{k}} \left[c^+(\boldsymbol{k}\lambda)c(\boldsymbol{k}\lambda) + \frac{1}{2} \right]. \tag{3.8}$$

Since IXS is a two-photon process and considering that the vector potential in equation 3.3 is linear in the creation and annihilation operators, it follows that a second order perturbation theory is necessary to treat the interaction term H_{i2}, which is linear in $\boldsymbol{A}$. In contrast, a first order perturbation theory is needed for the term H_{i1} since it is quadratic in $\boldsymbol{A}$. Using Fermi's golden rule, the transition probability up to the second order perturbation theory is given by

$$w = \frac{2\pi}{\hbar} \left| \langle f|H_{i1}|i\rangle + \sum_n \frac{\langle f|H_{i2}|n\rangle\langle n|H_{i2}|i\rangle}{E_i - E_n} \right|^2 \delta(E_i - E_f). \tag{3.9}$$

The first term describes the direct excitation of the initial state $|i\rangle$ to the final state $|f\rangle$, while the second term considers the excitation via an intermediate state $|n\rangle$. Conservation of energy is ensured with the delta function. All states in equation 3.9 are products of the incident and outgoing photon field states with the initial and final states of the electron system. Therefore the initial and final states in the equation are given by $|i\rangle = |i, \boldsymbol{k_1}, \lambda_1, 0\rangle$ and $|f\rangle = |f, 0, \boldsymbol{k_2}, \lambda_2\rangle$, respectively. Two possible intermediate states of $|n\rangle$ are shown in Figure 3.2. In the first state, the incident photon is annihilated before the electron is excited into the intermediate state, in contrast to the second, where the outgoing photon is created first. The first state can be described by $|n\rangle = |n, 0\rangle$ and the second state by $|n\rangle = |n, \boldsymbol{k_1}, \lambda_1, \boldsymbol{k_2}, \lambda_2\rangle$. Inserting the introduced states in equation 3.9 it becomes apparent that only the intermediate state $|n\rangle = |n, 0\rangle$ leads to a resonant contribution. In order to take the finite lifetime of the intermediate state into account, an imaginary part $i\Gamma_n/2$ is added to the denominator in w. The DDSCS can be derived from equation 3.9 by multiplying the transition probability with the density of states and the volume in $\boldsymbol{k_2}$-space and by further dividing w by the incident flux and the solid angle and

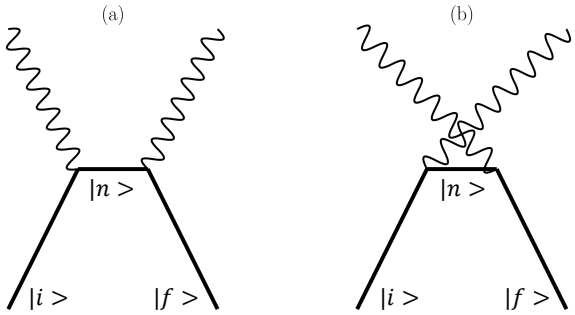

Figure 3.2: Feynman diagrams of the two possible intermediate states: The electron is excited in an intermediate state (a) after the incident photon is annihilated or (b) after the final photon is created.

energy element ($d\Omega_2 d\hbar\omega_2$). The resulting expression of the DDSCS

$$\begin{aligned}\frac{\mathrm{d}^2\sigma}{\mathrm{d}\Omega_2 \mathrm{d}\hbar\omega_2} = &\left(\frac{e^2}{mc^2}\right)^2 \left(\frac{\omega_2}{\omega_1}\right) \Bigg| (\boldsymbol{e}_1 \cdot \boldsymbol{e}_2^*) \langle f| \sum_j \exp(i\boldsymbol{q}\cdot\boldsymbol{r}_j)|i\rangle \\ &+ \frac{\hbar^2}{m} \sum_n \sum_{jj'} \Bigg(\frac{\langle f|\boldsymbol{e}_2^* \cdot \boldsymbol{p}_j/\hbar \cdot \exp(-i\boldsymbol{k}_2\cdot\boldsymbol{r}_j)|n\rangle\langle n|\boldsymbol{e}_1\cdot\boldsymbol{p}_{j'}/\hbar\cdot\exp(i\boldsymbol{k}_1\cdot\boldsymbol{r}_{j'})|i\rangle}{E_i - E_n + \hbar\omega_1 - i\Gamma_n/2} \\ &+ \frac{\langle f|\boldsymbol{e}_1\cdot\boldsymbol{p}_j/\hbar\cdot\exp(i\boldsymbol{k}_1\cdot\boldsymbol{r}_j)|n\rangle\langle n|\boldsymbol{e}_2^*\cdot\boldsymbol{p}_{j'}/\hbar\cdot\exp(-i\boldsymbol{k}_2\cdot\boldsymbol{r}_{j'})|i\rangle}{E_i - E_n - \hbar\omega_2} \Bigg) \Bigg|^2 \\ &\cdot \delta(E_i - E_f + \hbar\omega)\end{aligned} \tag{3.10}$$

is also called the Kramers-Heisenberg formula[92]. The equation includes most of the interaction of X-rays with matter up to order $(\hbar\omega/mc^2)^2$, provided that relativistic effects can be neglected. Non-resonant and resonant inelastic X-ray scattering are taken into account if $|i\rangle \neq |f\rangle$ applies. Provided that the energy transfer during the X-ray scattering process is zero i.e. $|i\rangle = |f\rangle$, the first term of equation 3.10 describes elastic X-ray scattering [91, 93].

3.1.1 Non-resonant inelastic X-ray scattering

The first term in the Kramers-Heisenberg equation 3.10 describes the non-resonant inelastic X-ray scattering (NRIXS). If the scattering process is occurring with incident energies far away from inner atomic shell excitations, the resonant term can further

be neglected [43]. In this case, the DDSCS of the NRIXS process is reduced to the formula

$$\frac{\mathrm{d}^2\sigma}{\mathrm{d}\Omega_2 \mathrm{d}\hbar\omega_2} = \left(\frac{e^2}{mc^2}\right)^2 \left(\frac{\omega_2}{\omega_1}\right) |\boldsymbol{e}_1 \cdot \boldsymbol{e}_2^*|^2 \left| \langle f | \sum_j \exp(i\boldsymbol{q} \cdot \boldsymbol{r}_j) | i \rangle \right|^2 \cdot \delta(E_i - E_f + \hbar\omega). \tag{3.11}$$

This formula can be separated into the Thomson differential scattering cross section with the classical electron radius $r_0 = e^2/(mc^2)$

$$\left(\frac{d\sigma}{d\Omega_2}\right)_{\mathrm{Th}} = r_0^2 \frac{\omega_2}{\omega_1} |\boldsymbol{e}_1 \boldsymbol{e}_2^*|, \tag{3.12}$$

which describes the scattering of photons by free charges, and the so-called dynamic Structure factor $S(q, \omega)$

$$S(\boldsymbol{q}, \omega) = \left| \langle f | \sum_j \exp(i\boldsymbol{q} \cdot \boldsymbol{r}_j) | i \rangle \right|^2 \cdot \delta(E_i - E_f + \hbar\omega). \tag{3.13}$$

The dynamic structure factor $S(\boldsymbol{q}, \omega)$ contains all the information accessible with a NRIXS experiment and is given in equation 3.13 within the excitation picture, which describes the amount of excitations the scattering system is undergoing from the initial state $|i\rangle$ to the final state $|f\rangle$. More precisely, the initial state is defined as $\sum_i \rho_i |i\rangle$ with ρ_i as the occupation probability dictated by the Boltzmann distribution at thermal equilibrium [94]. Another depiction of the dynamic structure is the so-called correlation picture. It was introduced by L. van Hove [95] and describes scattering as being originated from electron density fluctuations of the system, i.e. the correlation of the electron density between two different points in space and time. This depiction can be derived by introducing the electron density fluctuation operator $\rho(\boldsymbol{q}) = \sum_j \exp(-i\boldsymbol{q} \cdot \boldsymbol{r}_j)$ and by replacing the energy conserving delta function with its integral representation. Combining these in equation 3.13 and utilizing the Heisenberg representation of the density operator $\rho(\boldsymbol{q}, t)$ leads to the dynamic structure factor in the correlation picture [43]

$$S(\boldsymbol{q}, t) = \frac{1}{2\pi\hbar} \int_{-\infty}^{\infty} \mathrm{d}t \exp(-i\omega t) \left\langle f | \sum_{i,j} \exp(\boldsymbol{q} \cdot \boldsymbol{r}_i(0)) \exp(i\boldsymbol{q} \cdot \boldsymbol{r}_j(t)) | i \right\rangle. \tag{3.14}$$

This representation of $S(\boldsymbol{q}, t)$ underlines the importance of dynamics in the many-particle electron system, which will be of particular importance in section 3.1.3. Depending on the energy $\hbar\omega$ and the momentum q transferred by the inelastic X-ray scattering process, W. Schülke [43] distinguishes between four different types of experiments that enable the investigation of various properties of the electron system:

(1) Valence electron excitations are examinable by choosing ω close to the plasmon frequency ω_P and a value of $q \cdot r_c \approx 1$ for the momentum transfer with r_c as inter-particle distance.

(2) In the so-called X-ray Raman scattering regime, inner-shell excitations are investigated with $\hbar\omega \approx E_B$ at energy loss values close to the binding energy of inner-shell orbitals E_B and momentum transfer values of $q \cdot a \leq 1$, where a is the corresponding orbital radius. This measurement technique is the most extensively used in this thesis, therefore it is explained in more detail in the following section 3.1.2.

(3) The combination of $\omega = \omega_{\mathrm{Ph}}$ and $\boldsymbol{q} \cdot d \approx 1$, with ω_{Ph} as phonon frequency and d as interionic distance, allows the investigation of collective ion excitations such as phonons.

(4) Within the Compton scattering regime the electron momentum density is studied by choosing energy loss values $\hbar\omega > E_0$ far greater than any characteristic energy E_0 of the system and momentum transfer values according to $\boldsymbol{q} \cdot r_c \gg 1$.

3.1.2 X-ray Raman scattering spectroscopy

X-ray Raman scattering (XRS) spectroscopy is a NRIXS technique, which utilizes hard X-rays as a bulk sensitive probe to investigate absorption edges of low Z-elements even in extreme sample environments such as diamond anvil cells, which are impenetrable by soft X-rays or electrons. This enables the study of systems under extreme thermodynamic conditions. XRS experiments are typically performed at high incident X-ray energies that are not close to electron binding energies. In this case, the resonant term of the equation 3.10 becomes negligible and the measured quantity in an XRS experiment can be expressed by equation 3.11. The most common representation of $S(\boldsymbol{q}, \omega)$ in the field of XRS spectroscopy is the excitations picture given by equation 3.13. As mentioned in the previous section, the momentum transfer values in an XRS experiment are in the order of $q \cdot a \leq 1$, where a is the orbital radius. These small values justify the approximation of the matrix element in equation 3.13 with a Taylor series:

$$\exp(i\boldsymbol{q} \cdot \boldsymbol{r}) = 1 + i\boldsymbol{q} \cdot \boldsymbol{r} + (i\boldsymbol{q} \cdot \boldsymbol{r})^2/2 + ... \tag{3.15}$$

The first term of the Taylor series does not contribute owing to the orthogonality between the initial and final states. At low momentum transfers $\boldsymbol{q}a \ll 1$, the third term becomes likewise negligible and the second term is dominant. In this regime,

the so-called dipole limit applies, as mainly dipole transitions occur. Therefore, the dynamic structure factor becomes directly proportional to that of soft X-ray absorption spectroscopy (XAS) [43]. XAS is a widely used technique to study absorption edges with incident energies close to the corresponding binding energies of core electrons, which is further elaborated in section 3.2. Comparing the cross section σ of the two experimental techniques within the one-electron and dipole approximation,

$$\sigma_{\mathrm{XAS}} \propto |\langle f|\boldsymbol{e}_1\boldsymbol{r}|i\rangle|^2\delta(E_i - E_f + \hbar\omega_1)$$
$$\sigma_{\mathrm{XRS}} \propto |\langle f|\boldsymbol{q}\boldsymbol{r}|i\rangle|^2\delta(E_i - E_f + \hbar\omega),$$

it becomes apparent that the accessible information content is substantially identical when both processes induce the same core electron transition [45]. In this comparison, the role of the polarisation $\boldsymbol{e}_1$ of the incoming photon is equivalent to the transferred momentum $\boldsymbol{q}$ and the energy transferred to the electron $\hbar\omega$ corresponds to the absorbed energy $\hbar\omega_1$. However, the incident energy in an XAS experiment $\hbar\omega_1$ has to be tuned in the vicinity of the energy of the absorption edge under investigation, which leads to the already mentioned limitations in the experimental set-up. These limitations are overcome by XRS and the inherently unrestricted choice of high incident X-ray energies, which reduces the absorption of X-ray photons in the sample environment and also eliminates any saturation effects. Here it is the energy transfer that needs to be varied across the electron's binding energies leaving the choice of the incident photon energy more or less free. A disadvantage of the XRS technique, however, is the much smaller cross section, which is orders of magnitude smaller than that of photoelectric absorption, thereby necessitating the use of highly brilliant beamlines with efficient spectrometers. Typically, the cross section is 4-5 orders of magnitude smaller when using incident energies in the kiloelectronvolt range [96]. Noteworthy, XRS allows it to even study absorption edge at electron binding energies below 100 eV e.g. the $M_{2,3}$-edge of iron [97].
In contrast to XAS, dipole forbidden transitions become accessible with XRS by tuning the momentum transfer to higher values [98]. Based on a real-space multiple-scattering approach, Soininen *et al.* calculated the core-excited states in XRS, which enables a quantitative analysis of the momentum transfer dependence [99]. Following their approach, the dynamic structure factor can be expressed by

$$S(\boldsymbol{q},\omega) = \sum_{LL'} M_L(-\boldsymbol{q},E)\rho_{LL'}(E)M_{L'}(\boldsymbol{q},E) \tag{3.16}$$

where $\rho_{LL'}$ represents the matrix elements of the final-state density matrix and $M_L(\boldsymbol{q},E)$ characterises the atomic transition matrix elements, which describe the

transition from a ground state to a state with Energy $E = E_i + \hbar\omega$ and angular momentum $L = (l, m)$ [99]. The q-dependence of the excitation process is covered in the transition matrix, thus by evaluating $M_L(-\boldsymbol{q}, E)$ for different excitation energies and momentum transfers, different transitions of L become important. As described earlier, at low q-values dipole transitions with $\Delta l = \pm 1$ are dominant, whereas at higher q-values transitions such as quadrupole $\Delta l = \pm 2$ and monopole $\Delta l = 0$ transitions become increasingly probable [99]. Furthermore, the real-space multiple-scattering approach can be used to extract the symmetry-resolved unoccupied local density of states $\rho_l(E)$ by performing momentum transfer-dependent XRS experiments and combining them with the calculations of the transition elements [100]. In addition, a recent study utilized a large momentum transfer to investigate the s to d transition of Nickel to directly map the quadrupolar scattering intensity as a function of the direction of the momentum transfer $\boldsymbol{q}$ with reference to the crystal lattice [101].

3.1.3 Imaging electron density correlations in time and space

The representation of the dynamic structure factor in the correlation picture (see equation 3.14 in section 3.1.1) emphasises the connection of the measured intensity in an IXS experiment with the dynamics of the many-particle electron system. This connection can be utilized to investigate dynamic electron-related phenomena in space and time down to the sub-Angstrom and attosecond scale. A direct Fourier transformation of the dynamic structure in its correlation picture into time and space yields the van Hove space-time correlation function $C(x, t)$, which describes how strongly the electron density at the origin at time $t = 0$ is correlated with a later time at position x [95]. Although $C(x, t)$ contains information about the dynamics of the system, it lacks causal properties, making it unsuitable for the direct study of electron dynamics [54]. However, $S(\boldsymbol{q}, \omega)$ is also linked to the density response function $\chi(\boldsymbol{q}, t)$, which is also referred to as electron density propagator. $\chi(\boldsymbol{q}, t)$ is causal and a direct measure of electron dynamics [54]. The imaginary part of $\chi(\boldsymbol{q}, t)$ can be derived with the quantum mechanical version of the Fluctuation–Dissipation theorem

$$S(\boldsymbol{q}, \omega) = \frac{1}{\pi} \frac{1}{\exp(-\hbar\omega / k_B T) - 1} \operatorname{Im}[\chi(\boldsymbol{q}, \omega)], \tag{3.17}$$

with k_B as Boltzmann constant and T as temperature of the system. The Fluctuation-Dissipation theorem states a general relationship between the dissipation of energy in a many-particle system caused by an external disturbance with fluctuations of characteristic properties of this system in the absence of an external disturbance, i.e.

in its ground state [43, 102]. Without knowledge of the temperature, the imaginary part of the response function can be accessed by symmetrising the obtained data with

$$\mathrm{Im}[\chi(\boldsymbol{q},\omega)] = \pi[S(\boldsymbol{q},\omega) - S(\boldsymbol{q},-\omega)]. \tag{3.18}$$

This way, the measurable quantity of an IXS experiment is directly related to the imaginary part of the density response function. In order to investigate electron dynamics explicitly, the real part is likewise required, which makes the solution of the so-called inverse scattering problem necessary, also often referred to as phase problem. This problem concerns the loss of information when performing an IXS measurement, since only the imaginary part is probed. Hence, it is important to know which information has been lost with the real part of χ. An inherent characteristic of any propagator is its causality, the choice of which is arbitrary. For instance, the retarded and the advanced propagator represent the dynamics of a system on different time scales, namely for t larger and smaller than 0, respectively. Thus the former shows an increase and the latter a decrease in entropy. However, transformed into momentum transfer and energy space, all propagators exhibit the same imaginary part, with the differences in the respective causality convention being embedded in their real part. Therefore, the causality itself is lost in the IXS experiment [54]. Abbamonte *et al.* introduced a method to solve the phase problem by reconstructing the real part of χ and to properly transform the density response function into space and time [53, 54, 103]. First, it is utilized that $\chi(\boldsymbol{q},\omega)$ satisfies the condition for the Kramers-Kronig relations to calculate the missing real part

$$\mathrm{Re}[\chi(\boldsymbol{q},\omega)] = \frac{2}{\pi} P \int_0^\infty d\omega' \frac{\mathrm{Im}[\chi(\boldsymbol{q},\omega)]}{\omega' - \omega}, \tag{3.19}$$

where P is the Cauchy principal value. The calculated real part retrieves the missing causality of the retarded propagator by ensuring $\chi = 0$ for $t < 0$. In order to utilize the Kramers-Kronig relation, $\mathrm{Im}[\chi(\boldsymbol{q},\omega)]$ needs to be integrated along an infinity and continuous frequency axis. This is achieved numerically by extrapolation of $\mathrm{Im}[\chi(\boldsymbol{q},\omega)]$ with a suitable fitting function and subsequent linear interpolation of the resulting curve to an equidistant energy transfer grid with a sufficiently small increment $\Delta\omega$. Then $\chi(\boldsymbol{q},\omega)$ can be transformed into the time domain using a discrete Fourier transformation

$$\chi(\boldsymbol{q},t) = \pi^{-1} \int_0^\infty (\sin(\omega t)\,\mathrm{Im}[\chi(\boldsymbol{q},\omega)] + \cos(\omega t)\,\mathrm{Re}[\chi(\boldsymbol{q},\omega)]) d\omega. \tag{3.20}$$

The linear interpolation beforehand ensures that the repetition period $T = 2\pi/\Delta\omega$, of the $\chi(\boldsymbol{q},t)$ dynamics resulting from the use of the discrete Fourier transform, is

large enough to satisfy the condition $\chi(\boldsymbol{q}, t) = 0$ for $t < 0$ and to study phenomena occurring on larger time scales [53]. With a final spherical Fourier transform the spatial inversion from $\boldsymbol{q}$ to $\boldsymbol{r}$ is performed and using the appropriate determinant $\boldsymbol{r}$ can be replaced by its scalar value r. This leads to the following representation of the density response function in time and space,

$$\chi(r, t) = -\frac{i}{\hbar}\langle[\hat{n}(r, t), \hat{n}(0, 0)]\rangle\theta(t). \tag{3.21}$$

Equation 3.21 contains the commutator [,], the electron density operator $\hat{n}(x, t)$ and a Heaviside step function $\theta(t)$. The propagator $\chi(r, t)$ describes the probability that an initial electron disturbance $\hat{n}(0, 0)$ caused at the time, space coordinates $x, t = 0, 0$ will propagate to the position x at a later time t. Furthermore, causality is ensured by the Heaviside step function $\theta(t)$, since the system response at time t only occurs after the causal cause at time $t = 0$ [43, 54]. In this way, the electron density propagator becomes a powerful tool for studying ultrafast electron dynamics in the sub-angstrom and attosecond range, enabled by the use of IXS.

3.2 Extended X-ray absorption fine structure spectroscopy

The term X-ray absorption spectroscopy (XAS) covers various spectroscopic methods, the most prominent being EXAFS (Extended X-Ray absorption fine structure) and XANES (X-Ray absorption near edge structure). All X-ray absorption techniques are based on the energy-dependent measurement of the absorption coefficient in the vicinity of an absorption edge, but differ in their theoretical description and experimental procedure [104–106]. Depending on the method used, different information about the spatial and electronic structure of a system can be determined. In this thesis EXAFS was used to investigate changes in the microscopic structure of a sample system as a function of an external parameter. EXAFS is used in a wide variety of research fields, for instance, to determine small changes of less than 0.1 Å in the coordination of germanate glass at high pressure up to 131 GPa or to study the structure of the inner- and outer-sphere of chloroaquo complexes [107, 108]. In the following, a short theoretical derivation of the quantitative description of the absorption process is given.
The derivation of the X-ray absorption cross section is similar to the determination of the DDSCS in section 3.1: The non-negligible electron-photon interaction terms of the Hamiltonian are treated as small perturbation using Fermi's golden rule to calculate the transition probabilities of the system. These transition probabilities

are directly proportional to the X-ray absorption cross-section, which in turn is part of the measured quantity in an EXAFS experiment, namely the absorption coefficient. Since X-ray absorption is a resonant process that can be described as a one-photon process, the dominant Hamiltonian term in evaluating Fermi's golden rule is the term linear in the creation and annihilation operators

$$H_{i2} = -\frac{e}{mc}\sum_j \boldsymbol{A}(\boldsymbol{r}_j)\cdot\boldsymbol{p}_j. \tag{3.22}$$

The definition of the vector potential of the electromagnetic wave is given in equation 3.3. In contrast to XRS, XAS is a one-photon process leading to a contribution of 3.22 in the first order perturbation theory since it is linear in $\boldsymbol{A}$. Assuming that the spatial extend of the incident electromagnetic field is large compared to the dimensions of the core state, the dipole approximation can be applied to treat the overlap of the core state with the incident field as uniform $\exp(i\boldsymbol{K}\cdot\boldsymbol{r}) \approx 1$. Applying further the one-electron approximation, the evaluated transition probability is given by

$$\sigma \propto w = \frac{2\pi}{\hbar}\left|\langle f|\frac{e}{m}\boldsymbol{r}\cdot\boldsymbol{e}_1|i\rangle\right|^2 \delta(E_i - E_f + \hbar\omega_1), \tag{3.23}$$

where beforehand the commutator representation $\boldsymbol{p} = m/i\hbar[\boldsymbol{r}, H_0]$ of the momentum operator as position operator was used. Similar to the XRS cross section, equation 3.23 contains information about the quantity of excitations occurring in the system. Thus, the absorption coefficient $\mu = \rho\sigma$ is determined by the wave function of the two states and the position $\boldsymbol{r}$ with respect to the polarisation direction $\boldsymbol{e}_1$ of the incident X-ray beam [109, 110].
The excited electron propagates as an electron wave through the surrounding material with the wavelength $2\pi\lambda^{-1} = \sqrt{(2m/\hbar^2)\cdot(\hbar\omega_1 - E_0)}$, which depends on the incident energy $\hbar\omega_1$ and the binding energy of the excited state E_0. Whenever this spherical electron wave reaches the surrounding atoms, it is scattered by them. The relative phase between the outgoing and the backscattered electron wave at the absorber atom determines whether the two waves interfere with each other constructively or destructively. Depending on the interference, this leads to a decrease or increase in the measured absorption coefficient. Since the average distance between the atoms does not change, the phase relationship of the waves depends only on the wavelength of the photoelectron, which in turn depends on the energy $\hbar\omega_1$ of the incident X-ray beam. Thus, an alternating increase and decrease of the absorption coefficient can be observed depending on the energy of the X-ray beam and the local structure of the absorber atom. This oscillation of the absorption coefficient is called EXAFS oscillation or fine structure. To derive a qualitative description of this oscillation, it is important to identify which part of the matrix

element in equation 3.23 is the origin of the EXAFS oscillation. In the initial state $|i\rangle$, the electron is strongly bond to the absorber atom and is therefore localized independently of the surrounding atoms. Since the Hamiltonian H_{i2} is also not influenced by the neighbouring atoms of the absorber atom, the origin of the fine structure lies in the final state of the electron $|f\rangle$. The final state can be divided into two parts, the part of the free atom $|f_0\rangle$ and the part $|\Delta f\rangle$, which contains the influence of the neighbouring atoms on the photoelectron

$$|\langle f_0 + \Delta f|H_{i2}|i\rangle|^2 = |\langle f_0|H_{i2}|i\rangle|^2 \left(1 + \left[\frac{\langle f_0|H_{i2}|i\rangle^* \langle \Delta f|H_{i2}|i\rangle}{|\langle f_0|H_{i2}|i\rangle|^2} + c.c. + \delta(\Delta f^2)\right]\right).$$

where the absorption of an isolated atom is described by the factor in front of the bracket $\mu_0(E) = |\langle f_o|H_{i2}|i\rangle|^2$. Thus, the fine structure $\chi(E)$ is proportional to the disturbance of the final state $\langle f_0|H_{i2}|i\rangle$, which depends on the atomic environment of the absorbing atom. The fine structure can therefore be calculated using the expression

$$\chi(E) = \frac{\mu(E) - \mu_0(E)}{\mu_0(E)}. \tag{3.24}$$

The highly localized initial state can be approximated by a delta function, whereas the modification of the final state is expressed by $\psi_{\text{back.sc}}(r)$ in the following [111]. This leads to the following expression for the fine structure

$$\langle \Delta f|H_{i2}|i\rangle \propto \int \psi_{\text{back.sc}}(r)\delta(r)d\boldsymbol{r} = \psi_{\text{back.sc}}(0). \tag{3.25}$$

using the previously mentioned dipole approximation with $\exp(i\boldsymbol{K}\cdot\boldsymbol{r}) \approx 1$. A qualitative derivation of $\psi_{\text{back.sc}}(0)$ is given in the book from J. Als-Nielsen [111], which results in the following expression

$$k\chi(k) \propto \sum_j N_j \frac{t_j(k)\sin(2kR_j + \delta_j(k))}{R_j^2} \exp(-2k^2\sigma_j^2)\exp(-2R_j/\Lambda(k)). \tag{3.26}$$

The derivation starts with a spherical wave of the form $\exp(ikr)/r$ and the interference with its reflection. It further takes the potential landscape into account in which the electron wave is moving by adding a phase shift $\delta_j(k)$. Furthermore, the displacement of the neighbouring atoms due to thermal motion is considered by the Debye-Waller factor $\exp(-2k^2\sigma^2)$. The finite lifetime of the unoccupied state also influences the EXAFS signal, since an occupation by another electron becomes more likely the further the photoelectron moves through the sample. The inelastic scattering of the photoelectron on a surrounding atom also becomes more probable the longer it moves without recombining. Both processes reduce the resulting

EXAFS signal and are taken into account by the mean-free path length Λ with the factor $\exp(-2R_j/\Lambda)$. In addition, equation 3.26 considers that the signal is composed of the contributions of scattering at N_j neighbouring atoms with an element-specific back scattering amplitude $t_j(k)$ [111]. The equation 3.26 is a notation of the famous EXAFS equation, which was first introduced in the seventies by D.E. Sayers, A. Stern and F.W. Lytle on the assumption that the neighbouring atoms can be described as a system of point scatterers [112]. The equation is often used to determine the structural parameters R_j, N_j and σ_j of the system after the corresponding scattering properties $\delta_j(k)$, $t_j(k)$ and Λ have been calculated based on a model system [113, 114].

3.3 Elastic X-ray scattering at liquids

The elastic scattering of monochromatic X-rays allows to study the structure of matter with high precision. Elastic X-ray scattering covers a wide range of techniques without strict boundaries, which differ mainly in the wave vector transfer q used and thus in the structural dimensions that can be investigated in the experiment and if amorphous, liquid or crystalline matter is studied. The q-domain investigated in this thesis can be assigned to the so-called wide angle X-ray scattering (WAXS) technique. The wave vector transfer is defined as $\boldsymbol{q} = \boldsymbol{k}_1 - \boldsymbol{k}_2$ with the corresponding absolute value $|\boldsymbol{q}| = \frac{4\pi}{\lambda_1}\sin(\frac{2\Theta}{2})$, where 2Θ is the scattering angle and λ_1 the wavelength of the incident X-ray beam. Following a classical description of the scattering process, the radiation field of the incident X-ray beam causes the electrons in the system to oscillate, resulting in the emission of a spherical wave propagating from the atomic positions $\boldsymbol{r}_{nm} = \boldsymbol{r}_m - \boldsymbol{r}_n$ with respect to the reference atom at $\boldsymbol{r}_n$. The scattered intensity I then results from the interference between all emitted waves, which leads to the expression

$$I_{\mathrm{coh}}(\boldsymbol{q}) = f(\boldsymbol{q})^2 \sum_n \sum_m \exp(i\boldsymbol{q} \cdot (\boldsymbol{r}_n - \boldsymbol{r}_m)) \tag{3.27}$$

for monoatomic systems with the atomic form factor $f(\boldsymbol{q})$ [111]. The atomic form factor is defined as the Fourier transform of the electron density distribution of an atom [115]. It is a measure of the scattering amplitude of a wave at a single, isolated atom in dependence of the wave vector transfer $\boldsymbol{q}$. Equation 3.27 can be further evaluated by separating the terms in the double summation $n = m$ and replacing the changed sum with an integral over the volume element dV_m. Since the X-ray scattering is modulated by electron density deviations in the system, an additional

term proportional to the average density ρ_{at} is added and subtracted to finally yield the scattering intensity

$$I(\boldsymbol{q}) = Nf(\boldsymbol{q})^2 + f(\boldsymbol{q})^2 \sum_n \int_V (\rho_n(\boldsymbol{r}_{nm}) - \rho_{\mathrm{at}}) \exp(i\boldsymbol{q} \cdot (\boldsymbol{r}_n - \boldsymbol{r}_m)) dV_m \tag{3.28}$$
$$+ f(\boldsymbol{q})^2 \rho_{\mathrm{at}} \sum_n \int_V \exp(i\boldsymbol{q} \cdot (\boldsymbol{r}_n - \boldsymbol{r}_m)) dV_m,$$

where $\rho_n(\boldsymbol{r}_{nm})$ defines the density in the volume element dV_m at the position $\boldsymbol{r}_m - \boldsymbol{r}_n$ in relation to the reference atom at r_n and N the total number of scattering atoms [111]. The second term tends towards zero after $|r_{nm}|$ becomes larger than a few interatomic distances as $\rho_n(\boldsymbol{r}_{nm})$ converges towards ρ_{at} in this case. Therefore, the second term is only sensitive to short-range order in the system and is of particular interest for this thesis. The third term only contributes for $\boldsymbol{q} \to 0$ and is therefore neglected in the following. However, it is widely used to investigate size and shape of large scale structures such as proteins [116]. Equation 3.29 can be further simplified by averaging $\langle \rho_n(\boldsymbol{r}_{nm}) \rangle \to \rho(\boldsymbol{r})$ over all different choices of origin and subsequently replacing the argument $\rho(\boldsymbol{r})$ with the scalar $\rho(r)$ by referring to the isotropy of a liquid sample without preferred orientation [111]. The volume integral can additionally be performed in spherical coordinates, which leads to the following definition of the structure factor of a mono-particle non-crystalline system

$$S(q) = \frac{I(q)}{Nf(q)^2} = 1 + \frac{4\pi}{q} \int_0^\infty r(\rho(r) - \rho_{\mathrm{at}}) \sin(qr) dr. \tag{3.29}$$

The structure factor is directly related to the radial distribution function (RDF), which is defined as $g(r) = \rho(r)/\rho_{\mathrm{at}}$ and describes the probability of finding an atom at the distance r to the reference atom

$$g(r) = 1 + \frac{1}{2\pi^2 r \rho_{\mathrm{at}}} \int_0^\infty q(S(q) - 1) \sin(qr) dq. \tag{3.30}$$

Thus, it is a measure for density variations in a system as a function of distance. For instance, a crystalline structure exhibits values larger and smaller than one in $g(r)$ on an indefinite length scale due to its long range order, whereas for a liquid or amorphous system the short range order likewise causes maxima and minima for smaller distances but which attenuate and converge towards unity for larger distances [111]. This way, the structure factor is directly related to short range density deviations and local structural correlations. In order to transfer the quantitative description of the scattering process of a purely mono-particle system to a multicomponent system, the concept has to be extended by the introduction of a RDF $g_{ij}(r)$, which describes the correlations between different atomic species i and j. Furthermore, this also leads to the introduction of the corresponding partial structure factor $S_{ij}(q)$ [111].

3.4 Calculation of X-ray Raman scattering spectra

For the analysis of XRS and XANES spectra, there is no general procedure that can be applied to every sample system. Widely used methods are the comparison with reference spectra or the analysis of spectral features with known correlations as a function of an external parameter. For instance, the former can be used in a so-called fingerprint analysis e.g. to determine the composition of a sample [117], whereas the latter is used e.g. in the pressure and temperature-dependent investigation of spin states in samples that occur in Earth's interior [118]. Another analysis procedure is to combine the XRS experiment with the calculation of spectra based on a theoretical structural model. In this approach, the accordance between theory and experiment can be quantified and when sufficient agreement is achieved, detailed information about the structural arrangements in the system can be extracted from the model. Several codes are available to calculate the XANES and/or XRS spectrum based on a given structure using different theoretical approaches. For instance, FEFF9 uses a real space multiple scattering approach [119] and OCEAN calculates spectra with the use of density-functional theory (DFT) and solving the Bethe-Salpeter equation [120]. In this thesis the ERKALE code was used, which performs Hartree-Fock and DFT calculations to obtain i. a. theoretical spectra of XRS, XAS and Compton scattering [121]. Hence a brief overview of the basic concept of DFT based on the book by C. Fiolhais *et al.* is given in the following [122]. The aim of the DFT is to find the ground state density and the corresponding energy of a many-electron system. Starting point of this overview is the many-electron time-independent Schrödinger equation in atomic units

$$H\Psi(\boldsymbol{r}_1, \sigma_1, ..., \boldsymbol{r}_N, \sigma_N) = E\Psi(\boldsymbol{r}_1, \sigma_1, ..., \boldsymbol{r}_N, \sigma_N) \tag{3.31}$$

with the eigenstates Ψ, the particles position r_i and spins σ_i and the Hamiltonian H

$$H = [T + V_{\text{ext}} + V_{\text{ee}}] = \left[-\frac{1}{2}\sum_{i=1}^{N} \nabla_i^2 + \sum_{i=1}^{N} \upsilon(\boldsymbol{r}_i) + \frac{1}{2}\sum_i \sum_{j \neq i} \frac{1}{|\boldsymbol{r}_i - \boldsymbol{r}_j|} \right] \tag{3.32}$$

where T is the kinetic energy, V_{ext} the external potential and V_{ee} the electron-electron repulsion summed over distinct pairs of different electrons. In order to determine the ground state wave function and the corresponding energy, $\langle\Psi|H|\Psi\rangle$ has to be minimized under the orthogonality condition $\langle\Psi|\Psi\rangle = 0$. This can be achieved by setting the first variation equal to zero

$$\delta\left\{\frac{\langle\Psi|H|\Psi\rangle}{\langle\Psi|\Psi\rangle}\right\} = 0 \tag{3.33}$$

and minimizing the term in the curly brackets. The calculation of the many-electron wave function Ψ involves an immense computational effort and is therefore often not feasible for extended systems. Furthermore, the complete information content of the wave function is in most cases not needed to solve a scientific problem. Therefore, Ψ is replaced by the electron density $n(r)$ as variational object. An essential finding of P. Hohenberg and W. Kohn in this regard was that the ground state wave function of an interacting electron system in an external potential is uniquely defined by the ground state density, or in other words, two different ground state wave functions do not yield the same electron density [123]. This finding can also be extended to quantum mechanical observables, since these are also uniquely defined by the ground state density of the system. Hence the minimization problem shifts from finding the wave functions Ψ in the equation 3.33 to finding the density $n(\boldsymbol{r})$ that minimizes the functional

$$E[n] = \min\langle\Psi|H|\Psi\rangle_n$$
$$E[n] = T[n] + V_{ee}[n] + \int d^3\boldsymbol{r}\upsilon(\boldsymbol{r})n(\boldsymbol{r}) = F[n] + \int d^3\boldsymbol{r}\upsilon(\boldsymbol{r})n(\boldsymbol{r}), \tag{3.34}$$

where for the last term the relation $\langle V_{\text{ext}}\rangle = \langle\Psi|\sum_{j=1}^{N}\upsilon(\boldsymbol{r})|\Psi\rangle = \int d^3\boldsymbol{r}\upsilon(\boldsymbol{r})n(\boldsymbol{r})$ with the external potential $\upsilon(\boldsymbol{r})$ was used and the universal functional $F[n]$ was introduced. The external potential is kept fixed during the minimization. The ground state density is then defined by the density that minimises the functional. After introducing a Lagrange multiplier μ to take into account the constraint of a fixed number of electrons N, a variation in terms of density $\delta n(\boldsymbol{r})$ yields the Eeuler equation

$$\frac{\delta F[n]}{\delta n(\boldsymbol{r})} + \upsilon(\boldsymbol{r}) = \mu. \tag{3.35}$$

In order to prevent the direct calculation of the computational intense many-body electron interaction Hamiltonian term, W. Kohn and L.J. Sham introduced an approximation method which instead solves the one-electron Schrödinger equation for a fictitious system with non-interacting electrons, that has the same ground state density as a system of interacting electrons [124]. Following this approach $V_{ee}[n]$ becomes zero for a non-interacting electron system and equation 3.35 can be written as

$$\frac{\delta T_s[n]}{\delta n(\boldsymbol{r})} + \upsilon_s(\boldsymbol{r}) = \mu, \tag{3.36}$$

with the Kohn-Sham potential $\upsilon_s(\boldsymbol{r})$ as a functional of $n(\boldsymbol{r})$. Any differences between the chemical potentials of the interacting and non-interacting system of the same

density are compensated by the Kohn-Sham potential $v_s(\boldsymbol{r})$. The functional for this system of non-interacting electrons is defined with

$$F[n] = T_s[n] + U[n] + E_{\mathrm{XC}}[n]. \tag{3.37}$$

where V_{ee} was separated into two parts: the electrostatic self-repulsion of the electron density $U[n]$ and the exchange-correlation energy $E_{\mathrm{XC}}[n]$. The two Euler equations 3.35 and 3.36 are consistent with each other if

$$v_s(\boldsymbol{r}) = v(\boldsymbol{r}) + \frac{\delta U[n]}{\delta n(\boldsymbol{r})} + \frac{\delta E_{\mathrm{XC}}[n]}{\delta n(\boldsymbol{r})}, \tag{3.38}$$

With the Kohn-Sham method, $T_s[n]$ is calculated exactly, while $E_{\mathrm{XC}}[n]$ is approximate. Several different approaches exist to approximated $E_{\mathrm{XC}}[n]$. For instance, the local density approximation (LDA) was introduced in the paper by W. Kohn and L.J. Sham [124] together with the Kohn-Sham method. Another approximation is the so-called generalised gradient approximation, which is more accurate than LDA for modelling hydrogen bonds [125, 126]. In order to determine the electron ground state density that satisfies equation 3.38, the one-electron Schrödinger equation

$$\left(-\frac{1}{2}\nabla + v(\boldsymbol{r}) + \frac{\delta U[n]}{\delta n(\boldsymbol{r})} + \frac{\delta E_{\mathrm{XC}}[n]}{\delta n(\boldsymbol{r})}\right)\phi_i(\boldsymbol{r}) = \epsilon_i \phi_i(\boldsymbol{r}) \tag{3.39}$$

can be solved, which is also called 'The Kohn-Sham equation' [124]. The density is calculated with the following definition

$$n(\boldsymbol{r}) = \sum_{i=1}^{N} |\phi_i(\boldsymbol{r})|^2. \tag{3.40}$$

Since the term $U[n]$ and $E_{\mathrm{XC}}[n]$ both depend on $n(\boldsymbol{r})$, which depends on $\phi_i(\boldsymbol{r})$, which in turn depends on $v_s(\boldsymbol{r})$, the Kohn-Sham equation is solved self-consistently, i.e. iteratively, with $n(\boldsymbol{r})$ usually being estimated at the beginning. In summary, the Kohn-Sham approach utilizes an auxiliary system of non-interacting electrons located in a fictitious external potential, which takes the many-particle interactions into account. The solution of the Kohn-Sham equation of this system yields the same electron ground state density as the original interacting many-electron system and therefore enables the determination of e.g. the ground state energy. The Kohn-Sham orbitals have no inherent physical meaning but, besides of being a necessity to calculate the ground state density, are often used to construct a Slater determinant as an approximation to the real wave function of the system, which can be used for spectral calculations [127, 128].
In order to take into account the changes in the electronic structure due to the electronic excitations induced by the XRS process, the ERKALE code utilizes the

transition potential approximation (TPA) [129, 130]. Within this approximation, the one-electron initial and final states are only half occupied in the self-consistent calculation, while the other states remain unchanged [130]. The TPA was successfully used to calculate the XAS spectra of liquid water and ice [131]. The XRS spectra can then be calculated using equation 3.13. However, the TPA does not generate a reliable energy scale to compare calculations based on the same amorphous system but different structural inputs. Therefore, for the energy value of the first transition, the energy difference of the ground state and a state with a full core hole and the excited electron occupying the previous lowest unoccupied state is used [121]. For a comparison with experimental spectra, a broadening scheme is further applied to the data to consider finite lifetime effects and instrumental broadening.

4 Aqueous sodium chloride solutions under hydrothermal conditions

4.1 Introduction

Aqueous fluids at elevated temperatures or so-called hydrothermal fluids are of immense importance for various technologies used in a diverse range of industries. Examples include the treatment of hazardous wastes [35, 132], the recycling processes of polymers and more complex composite materials [133, 134], the gasification of biomasses [135] and the fabrication of nanomaterials [136] to name but a few. Furthermore, hydrothermal fluids are of uttermost importance for various geochemical processes in particular for heat and mass transport mechanisms in the Earth's mantle. One important processes is the formation of magma and volcanic arcs in the vicinity of subduction zones as hydrothermal fluids disrupt the bonds in the minerals that make up the mantle thereby significantly lowering the melting point and causing it to melt. This makes hydrothermal fluids an indispensable key component to understand the mechanism of these processes [34, 137]. As hydrothermal water is very efficient in permeating rocks, it often contains a large amount of dissolved salts which can form metal bearing complexes enabling the transport of metals within the fluid and thus the genesis of ore deposits [138, 139]. Therefore, changes in the structural properties of water and aqueous solutions with temperature and their causes have been a long-standing research topic [9, 85, 140]. In this regard, ion pairing in these high temperature liquids is of particular interest due to its large influence on the ion-solvent interaction [141, 142] and, in addition, the temperature and pressure-dependent changes of ion hydration in liquids are an important factor involving i.a. the formation of mineral solubility, metal complexes and the phase equilibria of a liquid system [143, 144].
Involved in many of theses processes are dissolved sodium and chloride (NaCl) ions as it is the most common solute in seawater and most natural hydrothermal fluids [145]. Moreover, the analysis of brine inclusions in natural diamonds shows that NaCl is a major component of hydrous fluids in the Earth's upper mantle [146]. Fluids in the H_2O-NaCl binary system have therefore been extensively studied as a reasonable first estimate for the key properties of natural subsurface fluids and a

typical mock-up system for Cl-rich fluids in many geological environments. One such environment is the fluid involved in the formation of lead-zinc ore deposits, as there is strong evidence that the concentration of salinity in these types of aqueous solutions is as high as 30 wt% NaCl [26]. In addition, numerous theoretical studies have studied the binary H_2O-NaCl system with respect to the temperature induced structural changes [147–149], with the results indicating that larger polyatomic NaCl clusters are forming in the solution due to the decreasing dielectric constant of water at such extreme conditions [27, 143, 144, 150].
Although ions with a high atomic number (Z) have been extensively investigated by means of X-ray absorption spectroscopy (XAS) in liquids under extreme conditions such as high temperature and/or high pressure [114, 151–154], studies on low Z ions or of the hydration water itself are scarce due to the experimental limitations dictated by the sample environment [10, 155]. Thus, most previous X-ray spectroscopy studies of aqueous sodium chloride solutions were performed at low pressure conditions i.e. below the boiling point of water at ambient conditions. Overall, they pointing towards an overall destabilizing effect of the dissolved sodium and chloride ions on the water structure, limited to the first hydration shell, which becomes less pronounced at an elevated temperature of 90 °C [156, 157].
In this thesis, the influence of sodium chloride on the water structure in aqueous solutions at elevated temperatures and pressures of up to 600 °C and 120.6 MPa, respectively, was investigated by means of XRS spectroscopy combined with the analysis of calculated spectra based on structures generated with *ab initio* MD simulations. A net destabilizing effect of the dissolved ions on the water network at room temperature was found, which declines with rising temperature as the increased formation of ion pairs and larger clusters mitigate the ions' influence on the water structure. Hence, with rising temperature, an increasing similarity of the microscopic structure of aqueous sodium chloride solution and pure water was observed both in the spectral fingerprints of the experimental spectra and in the simulated trajectory.
This work was published in the journal *Physical Chemistry Chemical Physics* with the title *Ion association in hydrothermal aqueous NaCl solutions: Implications for the microscopic structure of supercritical water* authored by Mirko Elbers, Christian Schmidt, Christian Sternemann, Christoph J. Sahle, Sandro Jahn, Christian Albers, Robin Sakrowski, Hlynur Gretarsson, Martin Sundermann, Metin Tolan and Max Wilke [158].

4.2 Experiment and modelling

4.2.1 Experimental set-up

In this chapter, XRS spectroscopy was used to study the oxygen K-edge of aqueous sodium chloride solutions at elevated temperatures up to 600 °C by means of a resistively heated diamond anvil cell (DAC). First preliminary XRS experiments were performed at beamline ID20 of ESRF and a second experimental run with an improved set-up with respect to the sample cell was carried out at beamline P01 of PETRA III. The first experiment at beamline ID20 of ESRF exploited the large-solid-angle XRS spectrometer with the Si(660) analyser crystals at a fixed analyser energy of $E_0 = 9.7$ keV [159]. Due to the relatively small opening of the sample cell, only one analyser vessel with 12 analyser crystals in forward scattering geometry at a scattering angle of 30° could be used, which provided an energy resolution of approximately 0.75 eV. The scattering angle together with an incident energy tuned from 10.22 keV to 10.29 keV, leads to a momentum transfer value of (2.7 ± 0.3) Å^{-1} at which dipole excitations are predominant. In order to scan the incident energy and thus acquire spectra of the oxygen K-edge, a combination of a Si(111) high heat-loaded and a Si(311) channel-cut monochromator was used. In order to prevent beam damage due to excessive X-ray photon density, the beam size was set to 70 µm × 50 µm (v x h). The energy was changed with an energy increment of 0.2 eV and 4 eV from E_0+520 eV to E_0+550 eV and from E_0+550 eV to E_0+590 eV, respectively, since the part of the spectrum at higher energies is only needed for fitting a suitable background function and for a proper normalization [89]. The final spectrum is the sum of several single spectra, yielding a total acquisition time of 5 h for each final spectrum. A total of 7 of these final spectra were recorded at various temperature and pressure conditions. A diode was placed behind the sample cell to detect the air scattering of the outgoing beam, which is proportional to the incident beam intensity and thus can be used to normalize the spectra. The experimental set-up at ID20 is shown in the labelled photography of Figure 4.1 (b). The second XRS experiment was performed at beamline P01 of PETRA III using the XRS spectrometer in forward scattering geometry with its 12 spherically bend analyser crystals at a fixed energy of $E_0 = 9.7$ keV exploiting the Si(660) reflection [160]. An overall energy resolution of 0.85 eV was achieved. The incident energy was scanned with a Si(311) monochromator in a range from 10.22 keV to 10.3 keV which resulted in combination with a scattering angle of 27° in a momentum transfer of (2.4 ± 0.3) Å^{-1}. To monitor the intensity of the incident beam, a diode was placed below the beam path in front of the sample to detect the air scattering. At the sample position, the beam was focused to a size of 50 µm × 50 µm (v x h). An

energy increment of 0.2 eV and 0.4 eV was chosen for the range between $E_0 + 520$ eV and $E_0 + 550$ eV and between $E_0 + 550$ eV and $E_0 + 600$ eV, respectively. Similar to the measurements at ID20, one final spectrum consists of the sum of several single scans with an overall acquisition time of about 320 min. This way, a total of 7 spectra were measured at different temperature and pressure conditions. A labelled photography of the experimental set-up is shown in Figure 4.1 (a).
Using the XRStools program package, the oxygen K-edge spectra were extracted from the 2D detector images [161]. The program package allows to fully utilize the imaging properties of the XRS technique to separate the signal of the sample from the background of the sample environment via a pixel-by-pixel analysis of the detector images [162, 163]. In addition, XRStools was used for the further data treatment, i.e., to compare the individual spectra of each analyser crystal for each energy loss scan for consistency before merging, to subtract a suitable background function, and to normalize the final spectra to the area between 525 eV and 575 eV. At least three individual scans were recorded at the same thermodynamic conditions and averaged for a final spectrum.

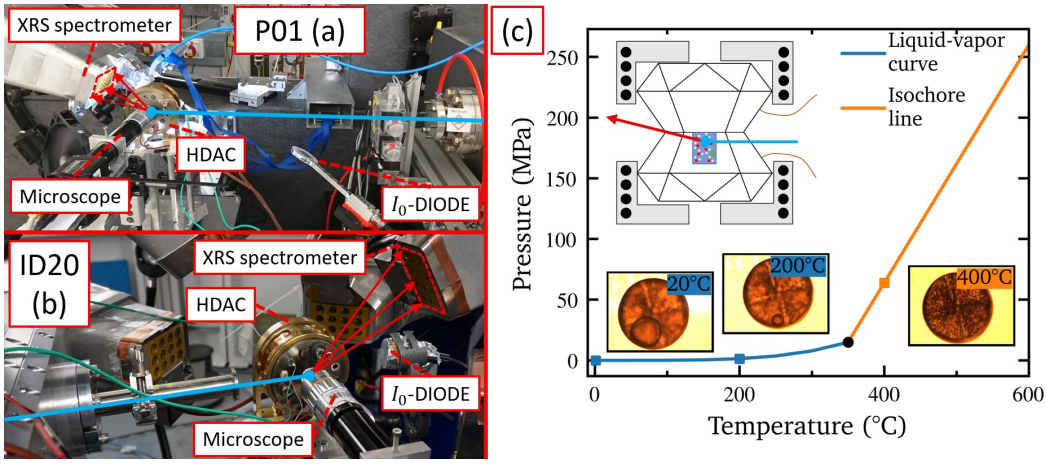

Figure 4.1: A photograph of the experimental set-up at the P01 (a) and ID20 (b) beamline. The beampath of the incident X-rays is shown in light blue and the scattered X-rays are indicated with a red arrow. The following components are labelled: The exploited XRS spectrometer, the hydrothermal diamond anvil cell (HDAC), the microscope for the visual observation of a vapour bubble contained in the sample volume and thus for determining the homogenization temperature, and the normalization diode (I_0-DIODE). The right side (c) shows a typical temperature-pressure path following the course of the experiment (see text for details) with images of the sample volume at various temperature steps. The homogenization temperature is marked with a black dot. A schematic of the HDAC is depicted in the upper left corner.

For the measurements, two aqueous sodium chloride solutions were prepared with a concentration of 1.9 molal and 2.0 molal using water and NaCl (ultrapure, Alfa, >99.0 %). In order to apply high temperature and pressure conditions to the aqueous sodium chloride solutions, a modified Bassett-type hydrothermal diamond anvil cell (HDAC) [164] was used for both experiments, which was designed by C. Schmidt and T.M. Seward [165]. The modifications allow to omit the conventional gasket by drilling a cylindrical recess in one of the diamond culets, which contains the sample volume. The recess was drilled with a diameter of 0.5 mm and a depth of 0.11 mm by using an UV femtosecond pulse laser ablation system. Making the gasket obsolete has a considerable effect on improving the overall data quality by significantly increasing the accessible solid angle and thus the acquired signal. However, to seal the sample volume without a gasket requires the two diamonds to be perfectly aligned, which is facilitated by mounting them on movable seats, where one can be moved translationally and the other rotationally. In order to change and measure the temperature, both seats are wrapped with heating wires and a thermocouple is attached to the surface of each diamond with an overall accuracy of at least ±1 °C [166]. The innermost part of the HDAC, i.e. the two diamonds and their seats, is shown schematically in Figure 4.1 (c) in the top left corner, where the small black dots representing the heating wires and the thin orange lines the two thermocouples. The pressure and density of the samples were determined using appropriate equations of state, necessitating the measurement of the liquid-vapor homogenization temperature via visual observation of the disappearance of a vapour bubble contained in the sample volume [164, 167]. This was achieved by using a microscope with a camera, which was also used to verify that no radiation damage occurred during the measurements. The determination of the homogenization temperature reveals whether the temperature of the sample is changed along the liquid-vapour curve or an isochoric line. The typical temperature-pressure path following the course of the experiment is shown in Figure 4.1 (c) exemplified for a homogenization temperature of 350 °C together with three images of the sample volume at different temperatures. This illustrates an only slight increase in pressure on the liquid-vapor curve as the vapour bubble is getting smaller with increasing temperature, but changes more drastically on the isochoric line when the bubble has completely disappeared. Furthermore, the use of the equation of states requires the exact concentration of the enclosed aqueous NaCl solution, which differs significantly from the stock solution due to the evaporation of water from the small droplet which is placed into the sample chamber but is exposed to air before aligning the two diamonds. Thus, the concentration was determined after preparing the sample via cryoscopy applying the equation for the freezing point depression of aqueous NaCl solutions by R.J. Bodnar [168]. This way, the actual concentration was evaluated with a value of (2.63 ± 0.25) molal. The data measured

at the P01 beamline, which were primarily used for the analysis due to the superior statistical quality, was recorded within two temperature runs. The two runs differ in the size of the initial vapour bubble contained in the sample volume and thus in the homogenisation temperature. In the first run, a maximum temperature of 200 °C was applied without reaching the homogenization, while the temperature was increased up to 600 °C in the second run crossing the homogenization temperature at 470 °C. Hence, at 400 °C a pressure of approximately 26 MPa was generated, while the isochoric temperature change resulted in much higher pressures of 63 MPa and 120.6 MPa at 500 °C and 600 °C, respectively. The experimental conditions for each spectrum, measured at P01 are listed in Table 4.1 with respect to the applied temperature, pressure and density of the sample.

Sample	°C	g/cm^3 (Exp.)	g/cm^3 (Theo.)	MPa (Exp.)
H_2O + NaCl	25	1.09	1.09	0.1
H_2O + NaCl	100	1.05	1.04	0.1
H_2O + NaCl	200	0.96	0.96	1.4
H_2O + NaCl	300	0.86	0.86	7.8
H_2O + NaCl	400	0.72	0.72	25.4
H_2O + NaCl	500	0.60	0.62	62.7
H_2O + NaCl	600	0.60	0.62	120.6
H_2O	20	1	1	0.1
H_2O	200	0.86	0.86	1.6
H_2O	370	0.45	/	21
H_2O	400	0.54	0.54	48
H_2O	600	0.45	0.45	134

Table 4.1: The thermodynamic conditions in terms of temperature, density and pressure for each measured spectrum of the aqueous salt solution as well as the performed AiMD simulations (without pressure). For completeness, the table also includes the experimental conditions of the study from which the spectra of pure water were taken [10]. All density values are rounded to the second decimal place. The relationship between applied temperature and the resulting density is depicted in Figure 4.11(d).

4.2.2 Modelling of XRS spectra

In order to compare the measured spectra with calculated spectra on the basis of a suitable structural model that can be further utilized in the analysis, *ab initio* MD (AiMD) simulations were performed and provided by Prof. Dr. Sandro Jahn from the University of Cologne using the QUICKSTEP module of the CP2K code [169]. The electronic structure calculations were performed using Kohn-Sham density functional theory, employing a mixed Gaussian and plane wave approach [170]. The BLYP method was utilized to treat the exchange-correlation functional [171, 172]. The core electrons, i.e. 1s for oxygen and sodium and 1s, 2s and 2p for chlorine, were included in the pseudo-cores of the Goedecker-Teter-Hutter pseudopotentials [173] and the double-zeta valence plus polarization basis sets were employed [174]. In order to replicate the experimental conditions as accurately as feasible, the simulations were performed using a box containing 100 H_2O molecules and 4 or 5 Na^+ and Cl^- atoms, resulting in concentrations of approximately 2.2 molal and 2.8 molal, respectively. Temperatures and densities were also chosen according to the experimental conditions by adjusting the simulated box sizes and controlling the temperature with the canonical sampling through velocity rescaling thermostat [175]. The initial structures were generated by several AiMD simulations with varying densities and at a temperature of 727 °C, where the original cell contained 100 H_2O and 10 NaCl. To achieve a concentration closely to the experiment, the number of ions were subsequently decreased. These boxes were then equilibrated at 727 °C for a few tens of picoseconds. Afterwards, the temperature and box size were changed to match the experimental conditions and another equilibration run of approximately 10 ps was conducted for each thermodynamic condition. A time step of 0.5 fs was used for the integration of the equations of state. Each simulation was carried out in the canonical NVT ensemble i.e. at a constant number of particles, volume and temperature. In addition, periodic boundary conditions were applied for every simulation. After reaching equilibrium, production runs of 20 ps were executed. Finally, a total of 100 structural snapshots were taken from the generated trajectories at equal time intervals as basis for the calculation of the XRS spectra and for further analysis. The temperature and density condition of each simulated AiMD trajectory is listed in Table 4.1.
In this work, the ERKALE code was used to calculate the oxygen K-edge spectra based on the individual structural snapshots as extracted from the AiMD simulations [121]. Using the ERKALE code, the calculation of the oxygen K-edge spectra was performed applying the transition potential approximation (TPA) within the density functional theory by further employing the Perdew-Burke-Ernzerhof functional [125, 176]. Both density functional theory in general and the TPA are explained in

more detail in the theory chapter 3.4 of this thesis. Two different basis sets were used for the calculations, namely Dunning's augmented correlation consistent polarized valence double zeta basis set for all atoms in the system except the excited oxygen atom, for which the IGLO-III basis set was applied [177, 178]. In addition, once the convergence of the self-consistent field was reached, the basis set of the excited oxygen atom was extended with diffuse function to further refine the description of the virtual orbitals. To obtain a theoretical spectrum for a certain thermodynamic condition, several spectra were calculated on the basis of different oxygen sites in the extracted structures, which are then averaged. This requires the establishment of an absolute energy scale for the calculated individual spectra to prevent errors due to averaging. An uniform energy scale for each spectrum can be introduced by setting the energy value of the first TPA transition to the total energy difference of the first core-excited state and the ground state [121].
At each p/T condition, approximately 600 calculations of oxygen K-edge spectra were performed, at which number convergence was found to be achieved. In order to calculate a single spectrum, an oxygen atom in the structure is randomly chosen as excited oxygen atom and a spherical cluster containing approximately 30 water molecules is cut-out around it for the calculation. The cut-out radius depends on the density to ensure a similar amount of water molecules for each calculation starting from 6.1 Å at room temperature and going up to 7.4 Å at 600 °C. Convergence in terms of cluster size proved to be reached. All calculations were performed at a momentum transfer value of 2.65 $Å^{-1}$, close to the value of the experiment. The final oxygen K-edge spectrum at each p/T condition is then obtained by merging the calculated individual spectra based on a statistical average of the structural snapshots. Furthermore, infinite lifetime effects and instrumental broadening were considered by applying a Gaussian broadening scheme with a full width at half-maximum that increase linearly from 0.4 eV to 10 eV between 535 eV and 545 eV [52, 179]. Finally, in order to allow a comparison of the different spectral features of the experimentally recorded and calculated spectra, the theoretical spectra were shifted to match the pre-edge onset of the respective experimental spectra owing to the difficulty of core electron calculation to provide an correct energy scale with respect to the experiment. In addition, the MD trajectories published by Sahle *et al.* as part of their study on hydrothermal pure water, were employed to calculate spectra using the same computational procedure as described here to consistently compare the calculated spectra of the aqueous NaCl solutions with those of pure water [10, 155].

4.3 Analysis and results

The spectra of the aqueous sodium chloride solution (H_2O + NaCl) recorded at P01 and ID20 at different temperatures are shown in comparison in Figure 4.2, together with the integrated spectral intensities of the pre- and post-edge, which are explained in more detail in the further analysis. The measured spectra at P01 exhibit

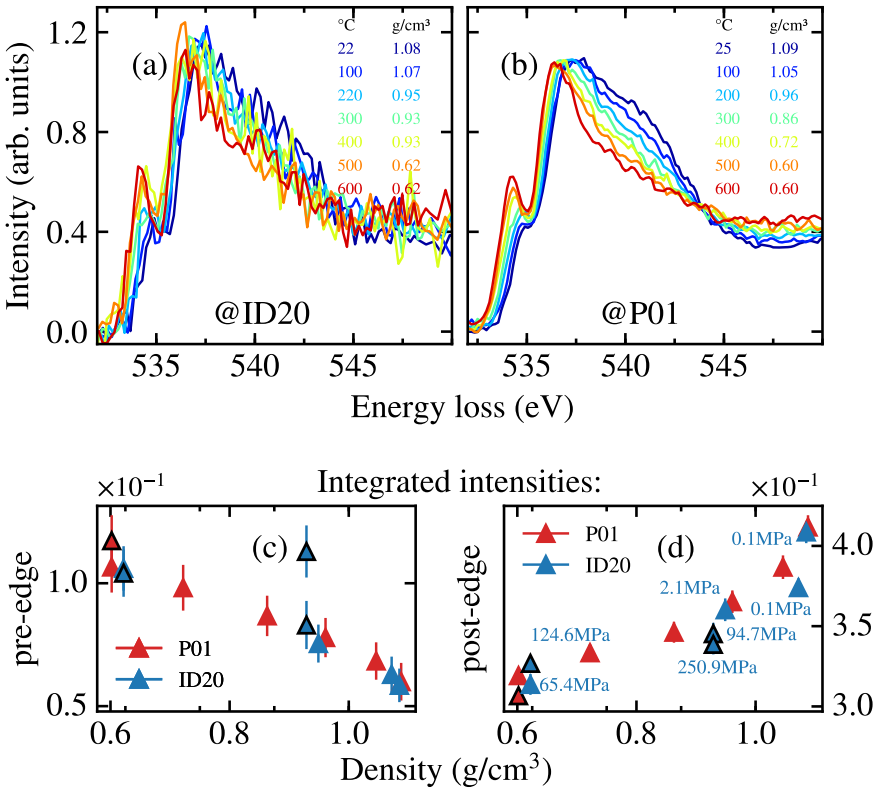

Figure 4.2: The oxygen K-edge spectra at various temperatures measured at the P01 beamline of DESY (a) and ID20 of ESRF (b). Improvements to the set-up by reducing the used cement to attach the diamonds to their seats resulted in significantly better data quality for the spectra measured at P01. The integrated intensities of the pre-edge (c) and post-edge (d) for both experiments as a function of density. Isochoric temperature changes of data points are indicated by a black marker edge color, i.e. they are obtained at significantly higher pressures.

a significant improvement in spectral quality compared to the preliminary measurements at ID20, which is achieved by using less cement to attach the diamonds to their seats, as this considerably reduces the absorption of the X-ray signal in the sample environment. Hence, the further analysis is performed with the spectra

obtained at P01, but the additional data from ID20 nevertheless nicely confirms the present results.
The oxygen K-edge spectra of liquid water or an aqueous solution exhibits three dominant spectral features namely, the pre-, main- and post-edge which are explained in detail in chapter 2.2.2. In the case of the aqueous sodium chloride solution, the pre-edge gains more spectral weight with increasing temperature and shifts to lower energy loss-values. A similar shift is also observed for the main-edge but without the drastic changes in terms of intensity, which is hardly affected by the temperature. The temperature dependence of the post-edge is contrary to the pre-edge as the feature is dominant at ambient conditions but looses intensity when the temperature is increased. In order to investigate the effect on the water struc-

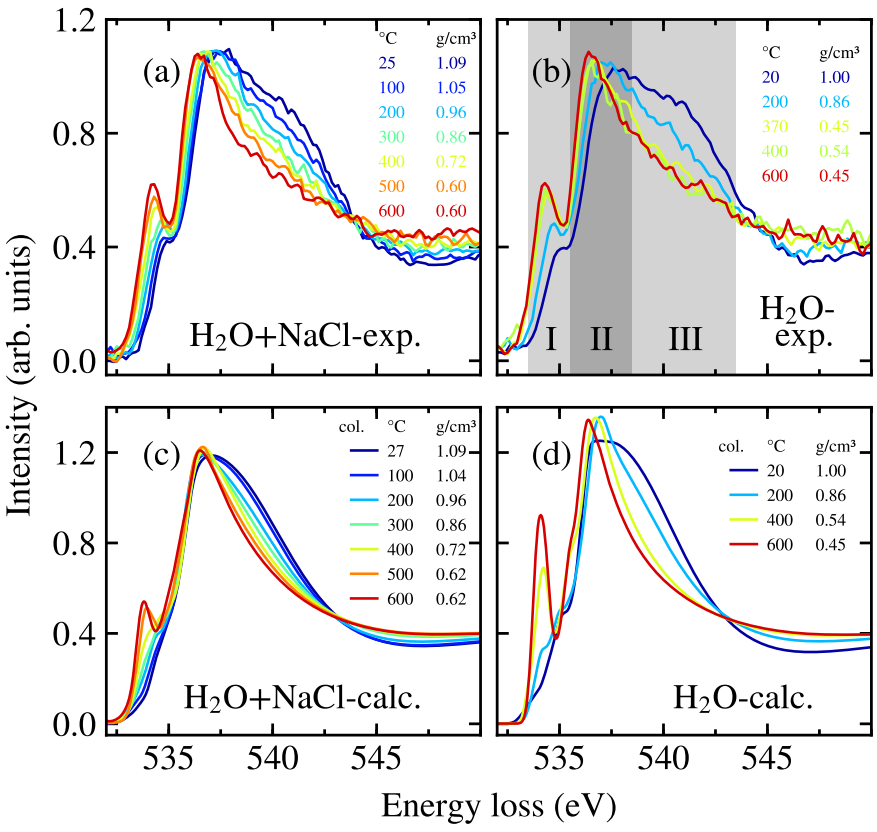

Figure 4.3: The experimental and calculated XRS spectra of the aqueous sodium chloride solution (H_2O + NaCl) (a and c) and pure water (b and d) at various temperatures between 25 °C to 600 °C. The most prominent spectral features are emphasised by grey shapes in (b) namely, I (pre-edge), II (main-edge) and III (post-edge).

ture at ambient and high temperature conditions due to the addition of salts, the recorded spectra are further compared with the spectra of pure water at various temperatures between 25 °C and 600 °C taken from a study of Sahle *et al.* [10, 155]. The experimental conditions of each pure water spectrum are also listed in Table 4.1. A qualitative analysis of the XRS spectra of pure water in Figure 4.3 (b) reveals a similar temperature dependence of the spectral features as for the XRS spectra of the aqueous NaCl solution in Figure 4.3 (a). The effect of the increased pressure on the spectral shape, as observed in the literature or in the following chapter (see chapter 5.3), is negligible compared to the major changes caused by the applied temperatures [180].
In accordance with the correlation between the spectral weight of the different features in the oxygen K-edge spectrum and the local structural environment of the excited oxygen as elucidated in chapter 2.2.2, the spectral changes of the aqueous NaCl solutions and pure water indicate a reduced number of hydrogen bonded molecules at lower densities in conjunction with a greater deviation from a tetrahedral structure in terms of angle and distance in both systems.
The various XRS spectra calculated on the basis of the two AiMD simulations are plotted in Figure 4.3 for the aqueous NaCl solution (c) and pure water (d). Overall, the calculated spectra are in good agreement with the experimental data, in particular with respect to the relative changes as a function of increasing temperature and decreasing density, respectively. Three snapshots at different temperatures as extracted from the AiMD trajectories for the calculation of the spectra are exemplary shown in Figure 4.4.

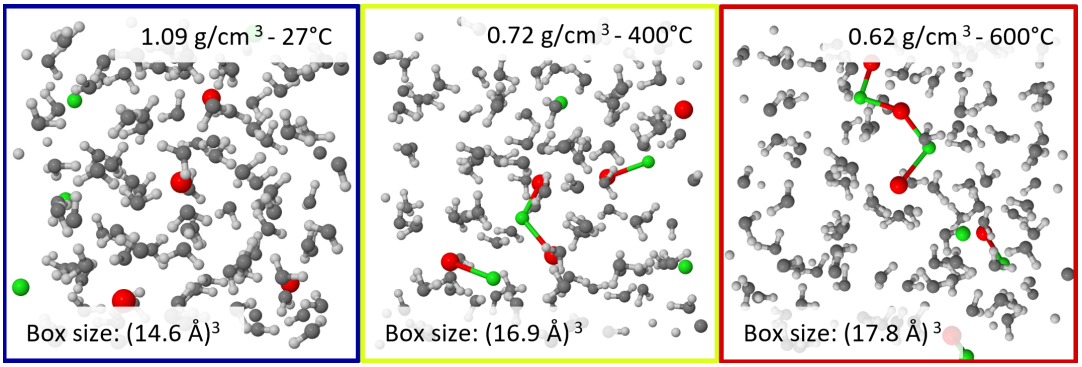

Figure 4.4: Three different snapshots from the AiMD trajectory at 20 °C, 400 °C and 600 °C. The water molecules are depicted in light grey to highlight the increased ion association of the sodium (red) and chlorine (green) which is indicated by a schematic connection between the ions.

In order to quantify the spectral changes of the two systems as a function of density and to verify the accordance of the experimentally recorded and calculated spectra,

a well established scheme for analysing XRS spectra consists of utilizing the peak or integrated intensity of spectral features [10, 52, 89, 155, 181, 182]. In this thesis, the spectral intensities of the two features with the most pronounced temperature-dependent changes, i.e. the pre- and post-edge, were integrated using the composite trapezoidal rule in a range from 532.5 eV to 535.5 eV and from 538.5 eV to 543.5 eV, respectively. The resulting integrated values of the experimentally recorded and with ERKALE calculated spectra are shown in Figure 4.5 as a function of density for the aqueous sodium chloride solution and pure water. Since an error propagation

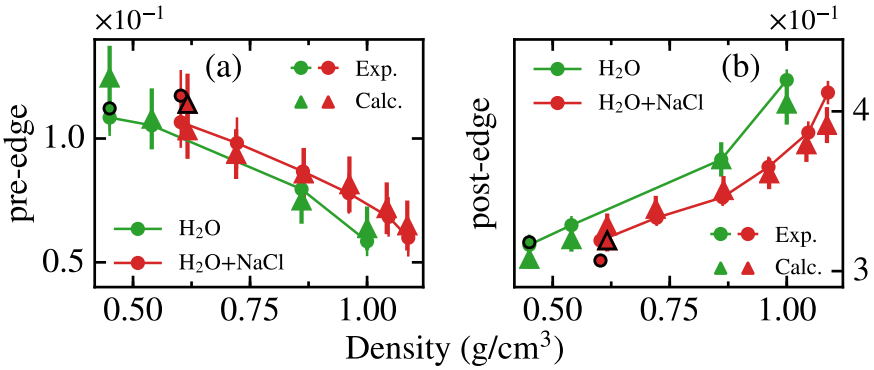

Figure 4.5: The integrated spectral intensities of the of the pre-edge (a) and post-edge (b) are plotted as a function of density for the two systems as small dots with lines and triangle symbols for the measured and calculated spectra, respectively.

of the statistical uncertainties of each measured data point in the integration range resulted in a negligible error of the integrated values, the errors in Figure 4.5 were obtained by calculating several integrals after shifting the integration limits by ±0.2 eV and using the standard deviation of the mean value. Furthermore, the discrepancies between the calculated and experimentally recorded spectra in terms of absolute intensities were compensated by scaling the integrated values of the theoretically obtained spectra by a constant factor. The scaling factors are rather small as the integrated values for the pre- and post-edge of pure water were scaled by 1.015 and 1.066, respectively, and for the aqueous sodium chloride solution by 0.965 and 1.068, respectively. The necessity of these factors underline the difficulty of core-level calculations to reproduce single experimental features on an absolute intensity scale [155]. However, applying such a scaling factors allows a thorough comparison and verification of the relative spectral changes as a function of density. The integrated values of the aqueous sodium chloride solution approach those of the pure water system for densities below 0.75 g/cm^3. Overall, the quantitative comparison of the calculated and measured XRS spectra with respect to the pre-edge and post-edge intensities reveals an excellent agreement for both systems. The largest exceptions

are observed for pure water, as there is a slight overestimation of the calculated pre-edge intensities at the lowest density. Although the quantitative comparison of experiment and theory shows an overall good agreement, the question has yet to be verified how uniquely the models (AiMD structure + ERKALE calculation) of water and the salt solution represent the respective measured system or, in other words, are the experimental data of pure water and the aqueous sodium chloride solution described equally well by both models, which would significantly weaken any conclusive analysis. In order to address this question, a χ^2 test was conducted by performing a fit of the integrated pre- and post-edge intensities of the calculated spectra to the respective values of the experimental data using the aforementioned scaling factor as fit parameter. Specifically, the density-dependent course of the integrated intensities of the pre- and post-edge for each model (H_2O and H_2O + NaCl) was scaled to the course of the integrated experimental intensities of each sample to determine the minimum χ^2 value for each combination of calculated model and experimentally measured sample. Thereby, in particular, the agreement of the relative density-dependent changes between the experimental and theoretical data is examined. Since neither the measurements nor the simulations could feasibly be conducted at the same densities, the integrated pre-edge and post-edge intensities of each model, as well as the experimental data, were interpolated to the same equidistant density grid before the χ^2 test was performed. Hence, only the overlapping density range of the measured densities of pure water and the aqueous NaCl solution were considered for the fit. The achieved best fit of each combination of theoretical model and experimental data set is shown in Figure 4.6 (left (a, c): pre-edge, right(b, d): post-edge) and reveal in conjunction with the corresponding χ^2 values (e: pre-edge, f: post-edge), that the models are not interchangeable and describe best the respective experimental system. It should be noted that this procedure requires obtaining XRS spectra for a large number of different experimental conditions, e.g. pressure or temperature, otherwise a precise fit of the theoretical to the experimental data is not achievable and thus their agreement cannot be adequately verified.

The results of the χ^2 test together with the good agreement of the calculated and experimentally obtained XRS spectra as shown in Figure 4.3 and Figure 4.5 makes it appropriate to exploit the underlying structural model to obtain detailed information on the local structural environment of the water molecules. Therefore, several parameters are calculated based on the employed structures, which were previously introduced in chapter 2.2.1 together with a detailed explanation of their calculation. In summary, the number of hydrogen bonds in the system per molecule, the fraction of ions in an ion pair bond or a larger ion cluster and two parameters to evaluate the deviation of the local water structure from a perfect tetrahedra in terms of distance Δ_d and angle Δ_a are determined. The determined parameters are depicted in Figure

4.7 as a function of density and reveal that both investigated systems exhibit the same trends with decreasing density but in the case of the aqueous NaCl solution,

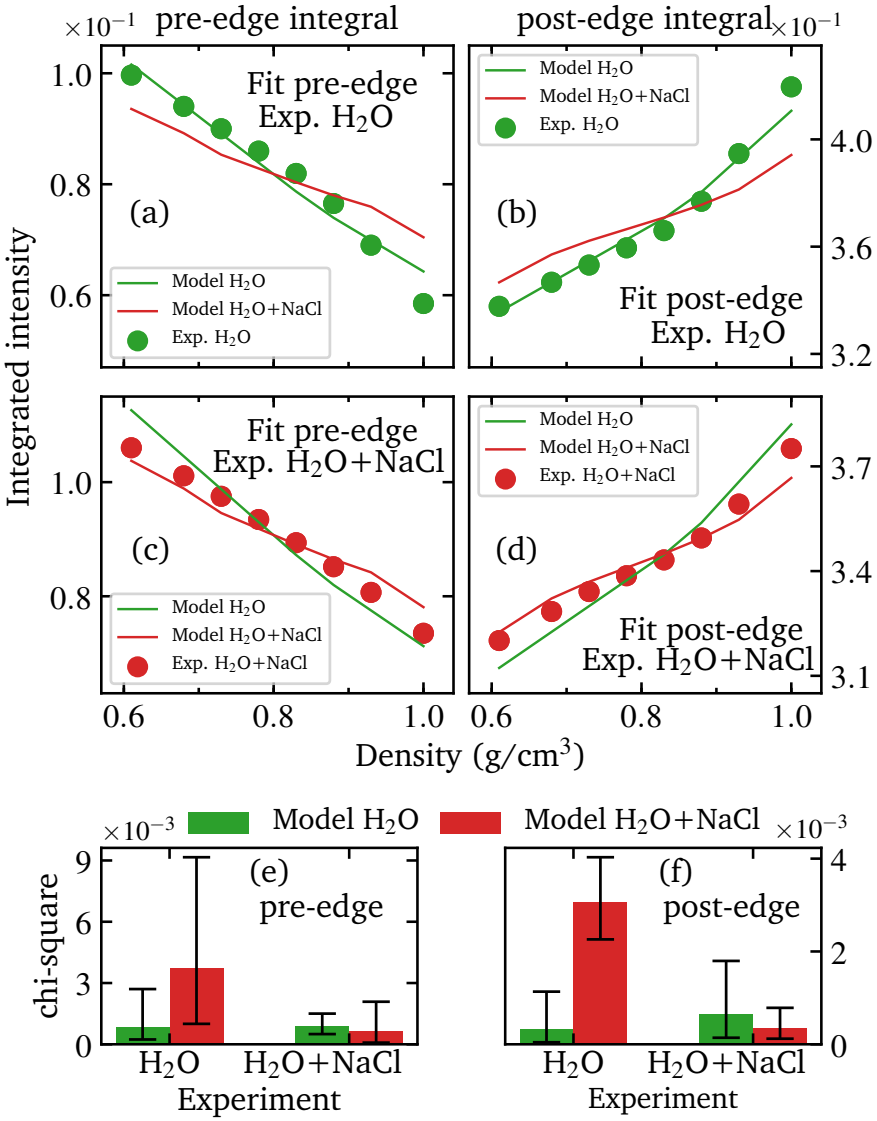

Figure 4.6: The left side shows the best first results of the pre-edge for all combination of models and experimental data (a, c) together with the corresponding χ^2 values (e). These same results are shown for the post-edge on the right side. Prior to the fit, the integrated values were interpolated on an equidistant density grid in the overlapping density range of water H_2O and the aqueous NaCl solution H_2O+NaCl. To estimate the error, χ^2 is calculated for the upper and lower error limits of the integrated values, and the smallest and largest χ^2 values are summed.

an overall lower number of hydrogen bonded molecules is observed together with a less ordered tetrahedral structure. These results are in agreement with the integrated pre-edge and post-edge intensities as shown in Figure 4.5, which are higher and lower, respectively, for the aqueous sodium chloride solution with respect to pure water.
However, as the density decreases, the calculated parameters of the aqueous sodium chloride solution approach the respective values of pure water at similar densities. The analysis of the simulated structures reveals a decrease in the number of hydrogen bonds per molecule from 3.13 at ambient conditions in the aqueous NaCl solution to 0.87 at the lowest density of 0.62 g/cm^3 (600 °C). Pure water on the other hand, exhibits a larger number of hydrogen bonds per molecule at ambient conditions with a value of 3.56 but only an average of 0.67 hydrogen bonds persists

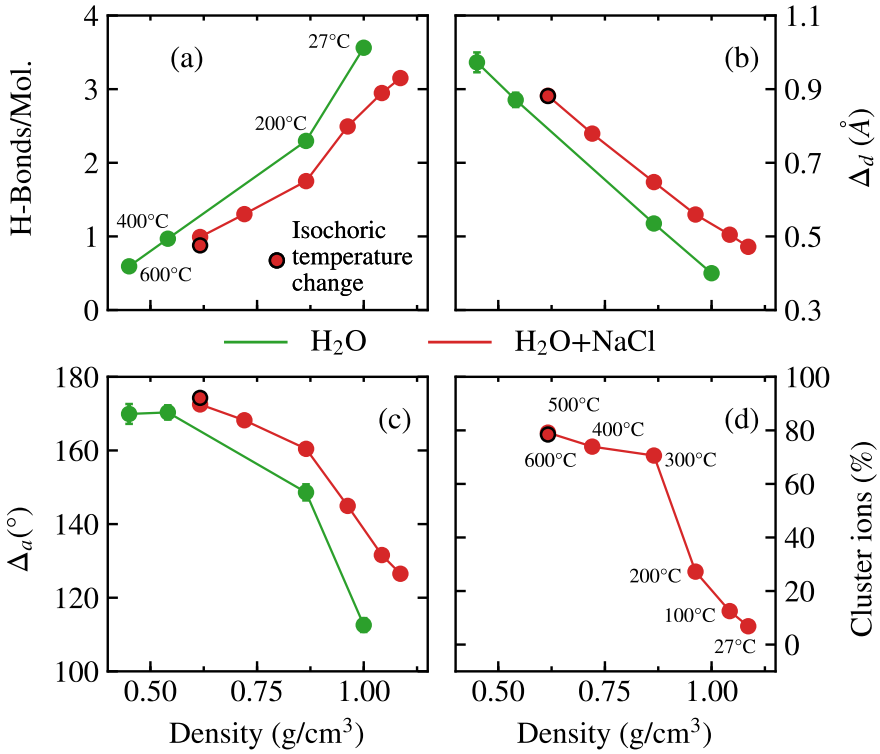

Figure 4.7: The determined structural parameters for pure water (green) and the aqueous NaCl solution (red) based on the structure obtained from the AiMD trajectories. Plotted as a function of density are, the determined number of H-bonds per molecule (a), the deviation from a tetrahedral structure in terms of distance Δ_d (b) and angle Δ_a (c), and the percentage of ions that are part of an ion cluster (d). An isochoric temperature change of a data point is indicated with a black edge color.

at an elevated temperature of 600 °C due to the much lower density of 0.45 g/cm^3. From the parameter Δ_a in Figure 4.7 (c), the mean angular deviation from a tetrahedral structure can be derived by dividing its value by 6, which corresponds to the number of unique combinations between the central water molecule and two of the four closest neighbouring molecules, resulting in a value of 21.08° and 29.05° for the aqueous sodium chloride solution and of 18.76° and 28.32° for pure water at the highest and lowest densities, respectively. The temperature dependence of the extracted parameters for the two systems is depicted on the right side of Figure 4.8, where an indistinct intersection of the two curves between 200 °C and 300 °C is observable for the number of hydrogen bonded molecules and the Δ_d parameter. On the left side of Figure 4.8, the parameters for pure water are shown as a function of density and the corresponding parameters for the aqueous NaCl solution are plotted as a function of bulk density, further illustrating the similarities between the two systems at smaller densities.
In addition, the fraction of ions in a contact pair bond or larger ion cluster was determined as defined in chapter 2.2.1, which introduces two ions as pairing if they are closer than the first minimum of the Na-Cl RDF at 3.75 Å. As shown in Figure 4.7, the percentage of associated ions in the system is 7 % at ambient conditions, but rapidly ramps up to 70 % at a density of 0.86 g/cm^3 (300 °C), at which point the slope decreases significantly as the percentage of cluster ions increase to only 78 % at 0.62 g/cm^3 (600 °C). The exact distribution of the different cluster sizes at each simulated density or temperature is shown in Figure 4.9 and reveals that the most ion pairs occur at 300 °C and that at higher temperatures predominantly large clusters are formed consisting of up to 8 ions at 600 °C.

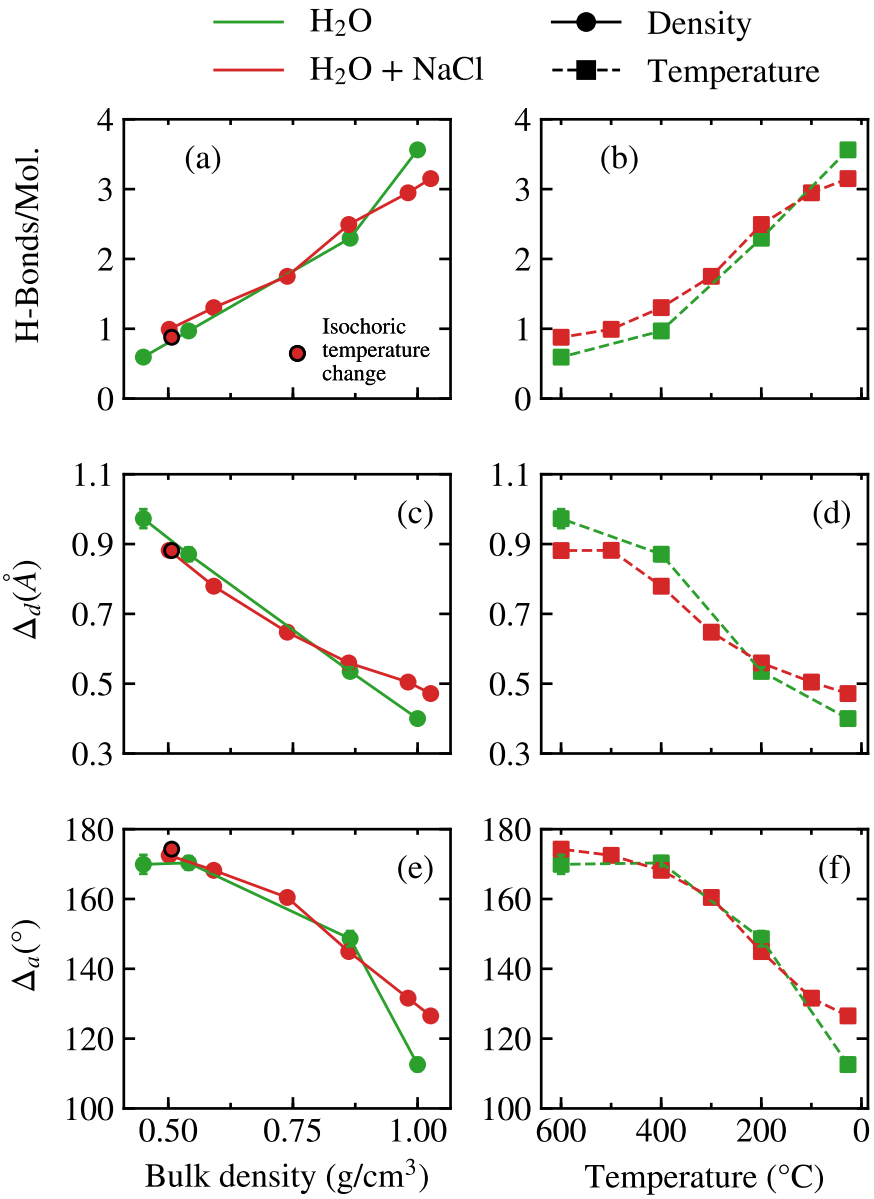

Figure 4.8: The extracted parameter from the AiMD trajectories of pure water (green) aqueous NaCl solution (red) regarding the water structure as a function of bulk density (left) and temperature (right) namely, the number of hydrogen bonds per molecule (a, b) and the deviation from a tetrahedral structure in terms of distance (c, d) and angle (e, f). The temperature axis on the right side is reversed for a better comparison with the density. Ioschoric temperature changes of the parameters are indicated by a black edge color.

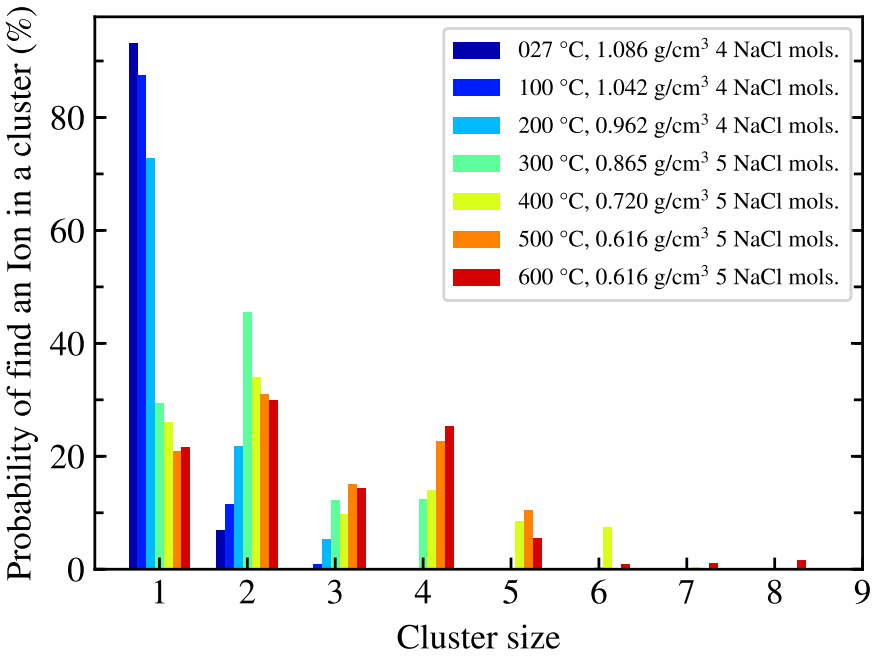

Figure 4.9: A bar chart of the distribution of ionic cluster sizes in the aqueous NaCl solution at each simulated temperature and density, respectively. For completeness, the ions that are not in an ion-pair bond at a cluster size of one are also listed although this is not actually a cluster.

4.3.1 The role of ion pairing in hydrothermal solutions

The identified changes in the measured and calculated XRS spectra caused by the addition of NaCl reveal a destabilizing effect of the dissolved ions on the microscopic water structure at ambient conditions, which is clearly supported by the determined structural parameters based on the AiMD trajectory. This finding confirms previous work on aqueous NaCl solutions that used optical Raman and X-ray absorption spectroscopy [157, 183–186]. Following the objective of this work to study the structural changes in the water network with increasing temperature up to the hydrothermal state, the conducted analysis shows that this destabilizing effect of the ions on the water structure at room temperature does not persist to the same extent over the entire density range investigated. Thus, the integrated spectral intensities together with the calculated structural parameters indicate a weakening of this effect since both approach the corresponding values of pure water with rising temperature. By comparing this increasing structural similarity of water and aqueous NaCl solution with the enhanced association of ions in the system, it becomes evident that there is a direct relationship between these two phenomena.

The observed increased ion association at higher temperatures is consistent with previous experimental and theoretical studies on aqueous sodium chloride solutions and other salt solutions [8, 152, 187–190]. This increased occurrence of ion pairs and clusters in hydrothermal fluids is caused by the negative correlation of the dielectric constant of water with the increasing temperature, resulting in a stronger ion-ion than ion-water interaction at these conditions, thereby reducing the influence of ions on the surrounding water structure [142, 191]. An example is provided by the results of a high-temperature neutron diffraction study on nickel sulphate dissolved in heavy water, where a significant weakening of the hydration structure of Ni^{2+} ions induced by the high temperatures is observed, which could be explained by the increased formation of nickel-sulphate ion pairs [192]. The association of ions in hydrothermal fluids is also preferential from an entropic point of view in terms of the entropic loss, which is lower for ion pairs or clusters than for free ions due to the electrostriction by water molecules [85]. Although the fraction of associated ions observed in this work around 200 °C and 300 °C is consistent with previous MD simulations, the amount of ion pairing is significant higher than deduced from conductivity measurements on dilute NaCl solutions up to 0.1 molal [150, 193, 194]. The reason for this, according to Sherman *et al.*, is the determination of ion pairs by structural criteria, ignoring the lifetime of these structural configurations and thus also counting transient ion pairs, which are undetectable in conductivity experiments due to their short lifetime [188]. In contrast to conductivity experiments, the structural average of a system is probed by the XRS process on an attosecond time scale reflecting the sensitivity to structural changes with very short life times and thus leading to an influence of transient ion pairs on the measured XRS spectrum. In the following, the previously mentioned relationship between the increased ion association in aqueous NaCl solution and the concomitant increase in structural similarity to pure water is further investigated. This is accomplished by calculating the difference between the two systems in terms of the integrated experimental intensities as a function of density by determining the absolute differences between the respective values of water and the salt solution. This approach allows to directly compare the evolution of a theoretically determined parameter, here the number of cluster ions in the system, as a function of density with solely experimental quantities which directly correlate with the microscopic water structure. Before calculating the absolute differences, the integrated values of both systems were interpolated in the overlapping density range onto the same density grid. The resulting absolute differences of the integrated experimental intensities are shown in Figure 4.10 for the pre-edge and post-edge, with a flipped y-axis for a better comparison with the variation of the percentage of associated ions in the system, which is also plotted on the right y-axis. This reveals a significant correlation between the decreasing differences between the two systems in terms of spectral intensi-

ties of the pre- and post-edge, and the increasing formation of ion clusters in the aqueous NaCl solution. Thus, it can be inferred that the association of ions in the salt solution is the driving force for the measured spectral convergence of the two systems and is therefore probably responsible for the increasing structural similarity of the water network in the salt solution to pure water, which is consistent with the analysis of the parameters extracted from the MD trajectories. It should be emphasized that the structural differences between the two systems as a function of density were not deciphered in this analysis solely on the basis of theoretical parameters by correlating the number of ion pairs in the solution with another structural parameter from the same modelled system, but rather by exploiting an entirely experimentally measured quantity that could be related to a simulated parameter, making the derived results substantially more conclusive with this approach.

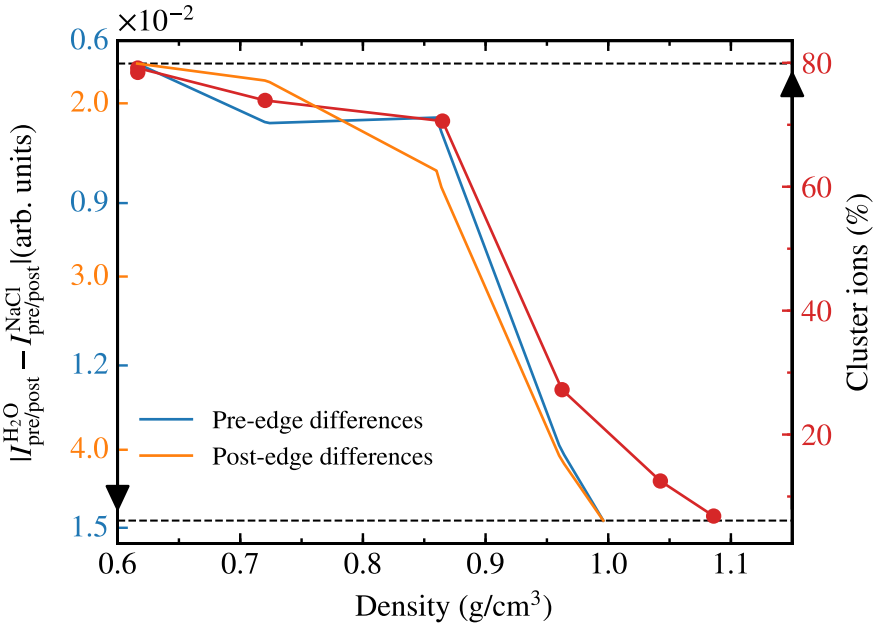

Figure 4.10: This Figure elucidates the correlation of the increasing spectral similarity between pure water and the aqueous NaCl solution with the enhanced association of ions in the system: On the left y-axis, the absolute differences of the integrated experimental intensities (see Figure 4.5) between the aqueous NaCl solution and pure water for the pre-edge (blue) and post-edge (orange) are shown as a function of density in the overlapping density range. On the right y-axis, the percentages of associated ions (red) in the system are plotted as a function of density. The left y-axis of the absolute differences of the integrated intensities is upside down for a better comparison with the percentage of cluster ions in the system.

The release of water from the hydration shells of the associated ions results in a larger fraction of bulk water being probed with XRS. Since the two systems become more similar with decreasing density in terms of spectral features and theoretical structural parameters, it can be concluded that the perturbation of the water structure by the dissolved ions is greatly reduced beyond the first coordination shell of Na^+ and Cl^-, respectively [27, 183, 188, 195]. This can be investigated in more detail by exploiting the generated MD trajectories to determine the previously utilized structural parameters but separately for the first hydration shell of the dissolved salts and the bulk water. The results as a function of density are shown in Figure 4.11 (a-c), in which the values for the total system H_2O-NaCl and pure water from Figure 4.7 (a-c) are also plotted as reference. The separate analysis of the determined parameters shows that the structure of the water molecules within the first coordination shell of Na^+ and Cl^- is strongly interfered by the presence of the ions, while the structural resemblance to pure water is significantly higher for the bulk water.
Despite the fact that the ion association is enhanced with increasing temperature and thus the influence of the dissolved salts on the water structure decreases, the ions still occupy volume in the system leaving less vacant space for the bulk water which is therefore more confined, resulting in a higher density relative to pure water at an identical temperature. This is illustrated in Figure 4.11 (d), where the density of pure water and the aqueous sodium chloride solution is plotted against the applied temperature along with the determined bulk density of the salt solution. The effect of the increased density on the water structure due to the additional presence of the ion clusters becomes evident when the parameters determined from the MD trajectories are plotted as a function of bulk density and temperature, as displayed in the left and right columns of Figure 4.8, respectively. A comparison of the density-dependent evolution of the parameters between pure water and the aqueous sodium chloride solution as a function of bulk density reveals that the two systems are structurally almost indistinguishable in terms of the extracted parameters below a density of about $0.87\,g/cm^3$, which corresponds to the density at which the formation of ion pairs and larger clusters is strongly increased. Furthermore, since the bulk density at a certain applied temperature of the aqueous sodium chloride solution is higher than the density of pure water at the same temperature, some parameters of the salt solution at higher temperatures exhibit an apparently more stable structure due to the addition of ions when compared directly to pure water as a function of temperature, as shown on the right side of Figure 4.8. Thus, the number of hydrogen bonded molecules is slightly increased in the salt solution compared to water and likewise the tetrahedral order in terms of distance is enhanced. In addition, this explains the aforementioned intersection point between the two systems with respect to the evolution of these two parameters.

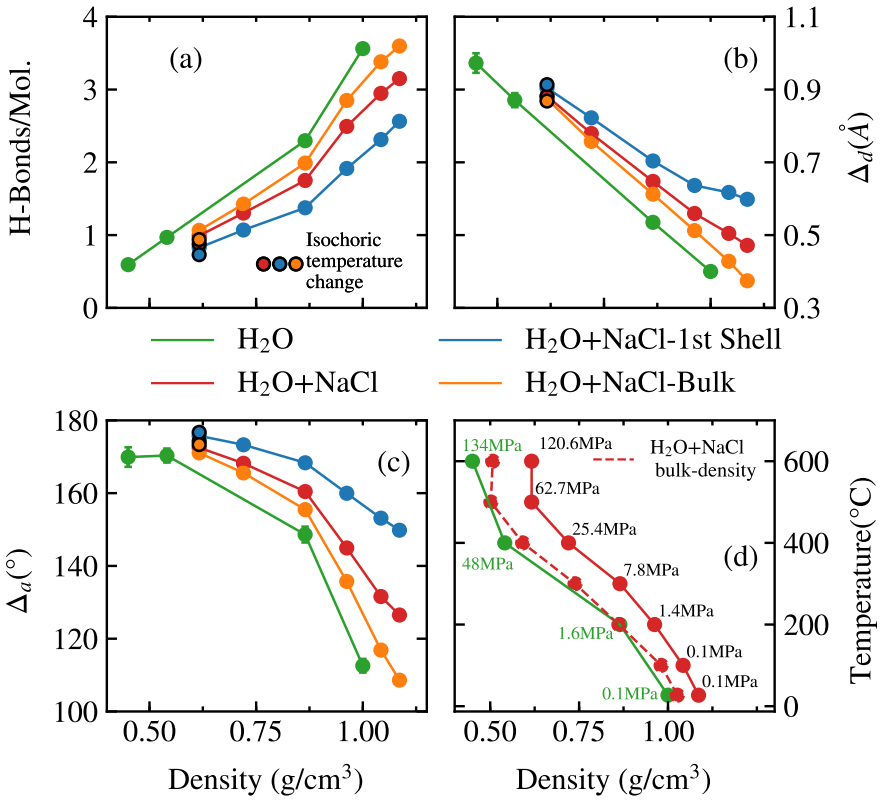

Figure 4.11: The extracted parameters from the AiMD trajectories separately determined for pure water (green) the whole aqueous NaCl solution (red), the water molecules inside the hydration shell of Na^+ and Cl^- (blue) and the water molecules in the bulk (orange). Plotted as a function of density are, the determined number of H-bonds per molecule (a), the deviation from tetrahedral shape in terms of distance Δ_d (b) and angle Δ_a (c). An isochoric temperature change of a data point is indicated with a black border color. The experimental conditions, i.e. the applied temperature and the resulting density of the sample, for each measured spectra of the aqueous sodium chloride solution (red - solid: density, dashed: bulk density) are shown in (d) together with the values for pure water (green). The generated pressures are written next to the respective data point.

4.3.2 Comparison with previous work on aqueous salt solutions

A recent study by Sahle *et al.* investigated salt solutions at hydrothermal conditions also by means of a combined XRS and AiMD simulations approach [155]. In this study, highly concentrated aqueous sodium hydroxide and hydrochloric acid with a concentration of up to 13 molal and 4.4 molal, respectively, were measured in a temperature range from 20 °C to 600 °C. The XRS calculation were performed within the Bethe–Salpeter equation formalism as implemented in the OCEAN code using structures obtained by AiMD calculations [120]. At ambient conditions, a net destabilizing effect of the ions on the water structure was observed in the two solutions, changing to a slight stabilizing effect at higher temperatures, similar to the effects observed for aqueous sodium chloride solution as a function of temperature. Therefore, interestingly, this effect is observed for all salt solutions investigated in this work and the study of Sahle *et al.*, regardless of concentration, pH, or how the respective salt ions integrate into the water structure. For instance, the additional dissolved hydrogen in the HCl solution leads to an enhanced formation of Eigen and Zundel cations. Thus, this might imply a general tendency of dissolved salts to exert an overall stabilizing effect on the water structure at elevated temperatures. Examining the structural parameters in the NaOH solution from the study which are determined the same manner as in this work, it is evident that there is a stronger stabilizing effect at higher temperatures than in the NaCl solution as indicated by a larger number of hydrogen bonded molecules and less deviation from a tetrahedral structure. This might be connected to the strong hydration shells formed not only around the Na^+ cation but also around the OH^- anion, as can be concluded from the spectral differences between the calculated XRS spectra of the water molecules associated with the bulk and hydration shells of Na^+ and OH^-, whereas the stabilizing effect due to the hydration of the Cl^- anion turns out to be weaker [155]. This result is supported by a neutron diffraction study of concentrated NaOH solutions, which shows strong hydrogen bonding of the OH^- anion to its neighbouring water molecules, even determining the orientation of the surrounding water molecules it shares with the cation by outperforming the Coulomb interaction of the Na^+ with the shared water molecules [196]. Moreover, a recent high-pressure XRD study reports an extremely stable hydration shell surrounding the Na^+, withstanding even pressures up to 1700 MPa, while the hydration shell of the Cl^- is severely altered due to the high pressures [64]. The results of these previous studies suggest a stronger stabilization of the water structure due to the influence of the OH^- ions at higher temperatures in comparison to the stabilization effects of the Cl^- ions as observed in this work. However, the differences in the concentrations of the aqueous salt solutions studied in this work and the previous study by Sahle *et al.*

might need to be considered for a direct comparison.
An X-ray study from Waluyo *et al.* exploited X-ray absorption spectroscopy to investigate the oxygen K-edge in aqueous NaCl solution with a concentration of 4 molal and pure water at 4 °C and 90 °C [157]. By analysing difference spectra with respect to the two samples and the applied temperature, they revealed a net destabilizing effect of the added salt ions on the water structure in agreement with the results of this work. These structural changes were related to the enhanced transformation from a low-density water (LDW) to a high density-water (HDW) induced by the increased temperature and the addition of ions [197]. The observed differences between water and the aqueous salt solution at 90 °C were interpreted in terms of the Na^+ and Cl^- ions exerting less influence on the water structure at elevated temperature, since a larger fraction of the water molecules are already present as HDW. Therefore, fewer possible water molecules are available in the LDW structure for the ions to disrupt and thus convert to HDW. However, the effect of ion pairing on the water structure was neglected in the study. According to the result of this work of 2.63 molal NaCl aqueous solution, ion pairing formation at 90 °C has presumably a significant contribution to the reported decrease in perturbation at elevated temperatures, since the percentage of associated ions is almost twice as high at 90 °C compared to room temperature. This effect is arguably even more distinct at a higher concentration and thus probably provides an adequate explanation for the spectral differences observed in the study.

4.4 Summary and conclusion

In this chapter, the microscopic structure of aqueous sodium chloride solution was investigated using a combined approach which exploits XRS spectroscopy measurements at the oxygen K-edge together with AiMD simulations of the system in a wide temperature range from 25 °C to 600 °C. Furthermore, the results were compared with the XRS spectra of pure water at elevated temperatures taken from a study of Sahle *et al.* together with the utilized trajectories [10]. In summary, an overall destabilizing effect of the dissolved salt ions on the water structure was observed at room temperature, however, this effect decreases with rising temperature, as the association of the ions to pairs and larger clusters is significantly enhanced at higher temperatures, thus weakening the influence of the ions on the water structure. Therefore, with decreasing density, an increasing similarity between the aqueous NaCl solution and pure water can be identified in terms of the microscopic

water structure in the two systems, as revealed by spectral fingerprints in the measured data and the structural analysis of the generated trajectory. The numerous structures generated by the AiMD simulations of the aqueous sodium chloride solution and pure water at different temperature and pressure conditions were used to calculate the XRS spectra, whose temperature-dependent spectral changes fully reproduce the relative temperature-induced changes in the experimental data. In addition, a χ^2 was performed indicating that the two theoretical models are not interchangeable and best describe the respective experimental system which further confirms the overall good agreement between experiment and theory. Justified by this thorough verification of the consistency of the theoretical data, the underlying model was exploited to extract detailed structural information of the water network. The detailed analysis of the microscopic structure in pure water and the aqueous sodium chloride solution based on the AiMD simulations, showed that the destabilizing influence of the ions at room temperature leads to a reduced number of hydrogen bonded molecules accompanied by a decrease of the tetrahedral order in the system. In agreement with these results is the qualitative and quantitative analysis of the experimental pre-edge and post-edge features, as they increase and decrease in intensity, respectively, due to the addition of salts.
The association of ions could be identified as the main driving force controlling the structure of aqueous solutions at elevated temperatures. For various geochemical processes this experimental evidence of the formation of ion pairs and larger polyatomic ion clusters is of great importance, since according to theoretical studies these clusters may form metal bearing complexes which might significantly contribute to the transport of such metals in hydrothermal fluids and thus enabling the formation of ore deposits [143].
A slight stabilizing effect of the dissolved ions on the water structure could be observed at higher temperatures when analysing the determined parameters as a function of temperature, which was attributed to the higher bulk density of the water in the salt solution compared to pure water at the same elevated temperature, caused by the occupied volume of the ions in the solution. This minor increase in density thus results in a slightly more ordered water structure. In addition, a comparison of the extent of this effect with a previous study on aqueous sodium hydroxide solutions under hydrothermal conditions revealed that this stabilizing influence at high temperatures is even more pronounced for NaOH probably due to the rigid hydration shells that forms around the OH^- anions, which are much stronger than the hydration of the chloride ions [155].
While Waluyo *et al.* account for the observed spectral difference between water and an aqueous salt solution at 4 °C and 90 °C by a change in the ratio of LDW to HDW due to the addition of salts, in this work an alternative explanation for the spectral changes was proposed based on the influence of ion pairing on the water structure.

To gain further insight into how electrolytes affect the water structure and interact with each other at hydrothermal conditions, measurements with a variety of concentrations and different ion combinations are further necessary. In order to improve the understanding of geochemical mechanism involved in the formation of ore deposits, experimental XRS data obtained not only at the right temperature but also the natural pressure conditions during this highly relevant transportation and formation process would help by providing crucial information on the local water structure.

5 The structure of water under high pressure

5.1 Introduction

Although the microscopic structure of water has been thoroughly investigated in numerous studies, many of the reported results are still highly debated and a conclusive picture that applies over a wide range of thermodynamic conditions has yet to be obtained [28, 33, 198]. While the last chapter focused on the changes of the water structure under the influence of high temperatures and the addition of ions, this chapter deals with the effect of high pressure on the water structure. The pressure-induced changes in liquid water are highly relevant to a variety of scientific fields [62–64].
The evolution of water characteristics with pressure may help to understand and benchmark various proposed water models. Several different water scenarios suggest the existence of two structurally distinct forms of water with different densities, referred to as low-density water (LDW) and high-density water (HDW) [30, 32]. It is assumed that by changing the pressure in the system, the ratio of the two structural forms can be actively altered. This potential pressure induced conversion of LDW to HDW was used by a neutron diffraction study to investigate the structure of LDW and HDW, by extrapolating the experimental data to their low and high pressure limit, respectively and determining the spatial density function of each structural form [69]. The transition between LDW and HDW was associated in the study with a breaking of hydrogen bonds between the first and second coordination shells and was therefore referred to as the collapse of the latter. Numerous subsequent pressure-dependent studies aimed to further proof this proposed model and to investigate the transition between the LDW and HDW phase, e.g. [21, 22, 199, 200].
In the field of chemistry and biology, the pressure evolution of the water structure is particularly interesting for a deeper understanding of the survival mechanism of marine animals which live at great depth. For instance, the abilities of deep-sea fish to live under extreme pressure conditions are assumed to involve the incorporation of trimethylamine-N-oxide into the fish tissue, which stabilizes the proteins presumably via a direct influence on the water structure [201, 202]. In addition, a

high-pressure small angle X-ray scattering study on aqueous protein solutions found a non-monotonous pressure evolution of the attractive part of the protein-protein interaction with a distinct minimum at 2 kbar [39]. This behaviour was related to changes in the microscopic structure of liquid water induced by high pressure.
XRS spectroscopy provides a unique insight into the local water structure due to the high sensitivity of the oxygen K-edge spectrum to the hydrogen bonds of the nearest water molecules and their tetrahedral arrangement. Furthermore, the oxygen K-edge can be utilized to study more distant non-hydrogen bonded molecules and their approach to the first shell [52]. This makes XRS a suitable tool to investigate and characterise potential structural transition and an accompanying collapse.
In this chapter, XRS was utilized with two different experimental set-ups to obtain XRS spectra of pressurised liquid water up to 8.5 kbar. The experimental data were extensively analysed with regard to investigate the collapse of the second hydration shell and to characterise the pressure evolution of the water structure. The trajectory of a recent AiMD study [62] was further utilized to calculated XRS spectra with ERKALE and to extract detailed structure information after a comparison of the experimental and theoretical XRS spectra yielded a good agreement. The experimental spectra were further compared with measured and calculated spectra of ice Ih, III and VI to draw conclusions about the spectral and structural differences as well as similarities between water and ice Ih, III and VI. Moreover, first XRS test experiments on 1 M aqueous trimethylamine-N-oxide solution were performed to study its effect on the water structure as a function of pressure.

5.2 Experiment and modelling

5.2.1 Experimental set-up

Preliminary XRS measurements on water under high pressure up to 5.25 kbar were performed at beamline P01 of PETRA III with a custom-made hydrostatic pressure cell. Further experiments were carried out at the beamline ID20 of the ESRF with an improved set-up and a membrane diamond anvil cell at a maximum pressure of 8.5 kbar. High purity water ($R > 18\,\mathrm{M\Omega}$) was measured in both experiments, whereas in the first experiment a 1 M aqueous trimethylamine-N-oxide (TMAO) solution prepared with Trimethylamine N-oxide dihydrate ($(CH_3)_3NO{\cdot}2H_2O$, CAS : 62637-93-8) powder of 99.0% $\geq$ purity purchased from Sigma Aldrich was additionally investigated.
The set-up of the first experiment at beamline P01 is shown in Figure 5.1 together with a schematic drawing of the used hydrostatic pressure cell, which was initially

developed for small angle X-ray scattering experiments [203] and was successfully employed in further experimental studies [39, 114, 204]. The cell is constructed of high strength steel and maintains its pressure stability up to a maximum pressure of 5.3 kbar. The pressure is adjusted with a spindle press, resulting in an accuracy of 20 bar over the entire pressure range. To determine the pressure, a pressure gauge is attached to both the cell and the pressure pump. The temperature can be adjusted with a chiller connected to the cooling/heating ducts inside the cell, which ensure that the temperature is evenly distributed. The sample is loaded into a small inner cell with a thickness of 1.8 mm, which is sealed with flexible Kapton to ensure good pressure transfer. The surrounding pressurised volume is sealed with two diamonds, each 1 mm thick. At an incident X-ray energy of 10 keV, about 80 % of the incident X-ray intensity is absorbed by the two diamonds. Nano-polycrystalline diamond (NPD) discs were used instead of standard diamonds to avoid contamination of the spectra by interference due to Bragg reflections when scanning the incident X-ray energy [114, 205]. The XRS spectra were measured with the XRS spectrometer of P01, which contains 12 spherically bent Si analyser crystals, 7 of which were used owing to the restricted cell geometry [160]. In order to measure the spectra as a function of energy loss, the incident energy was scanned with the Si(311) monochromator in a range from 10.2 keV to 10.235 keV exploiting the Si(660) reflection of the spherically bent analzyer crystals at a fixed energy of 9.675 keV. This way, an overall energy resolution of about 0.8 eV to 0.9 eV was achieved. The spectrometer was set to a scattering angle of 26° resulting in a momentum transfer of $(2.25 \pm 0.40)\,\text{Å}^{-1}$. To prevent beam damage due to excessive X-ray photon density, the beam was defocused to $150\,\mu\text{m} \times 150\,\mu\text{m}$ (v x h). The incident energy was monitored with a PIN diode, which measured the air scattering in front of the sample cell. With an acquisition time of 6 hours for each spectrum, a total of 12 spectra at different pressures for pure water and 3 spectra of a TMAO solution at various pressure steps were recorded.

The experimental set-up and the sample cell of the second conducted experiment at the ID20 beamline of ESRF is shown in Figure 5.2 [159]. Instead of a hydrostatic pressure cell, a diamond anvil cell (DAC) was used which works with both membrane and conventional screws to generate high pressures [206]. In order to precisely adjust the pressure, the metal membrane of the DAC was pressurised with gas to force the diamonds against each other and thereby increase the pressure of the sample with the accuracy of a few hundred bars. The diamonds used had a culet size of 0.8 mm and were combined with beryllium gaskets, which had an inner cut-out with a diameter of 0.4 mm for the sample. Beryllium gaskets are much more permeable to X-rays compared to metal gaskets and therefore lead to a better overall statistics of the measured spectra and makes a larger solid angle accessible. The

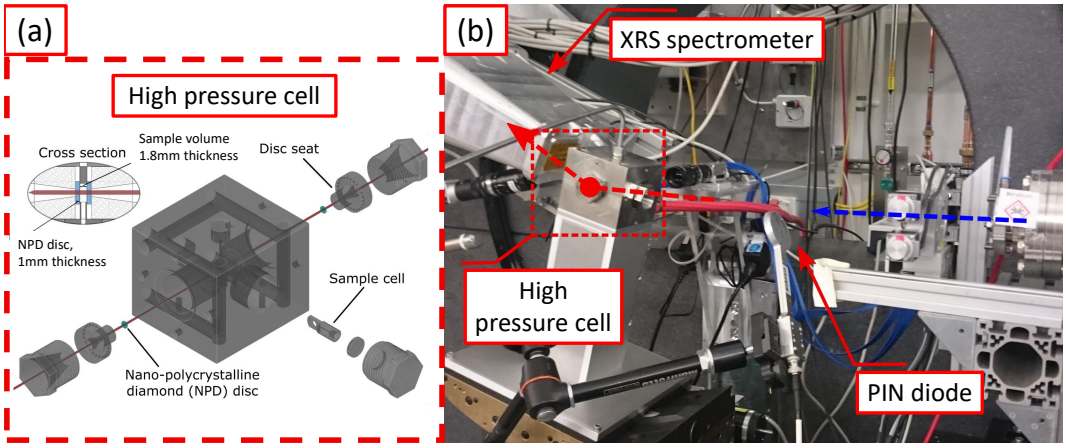

Figure 5.1: (a) Schematic drawing of the beam path going through the used hydrostatic pressure cell, divided into its various components: The different screws, disc seats, NPD discs and the inner sample cell. The top left image shows an enlarged cross section view of the sample cell section. The image is taken and modified from [114] with the permission of Taylor & Francis. (b) Labeled photography of the experimental set-up at beamline P01 of PETRA III. The beam path of the incident and scattered beam is shown in blue and red, respectively.

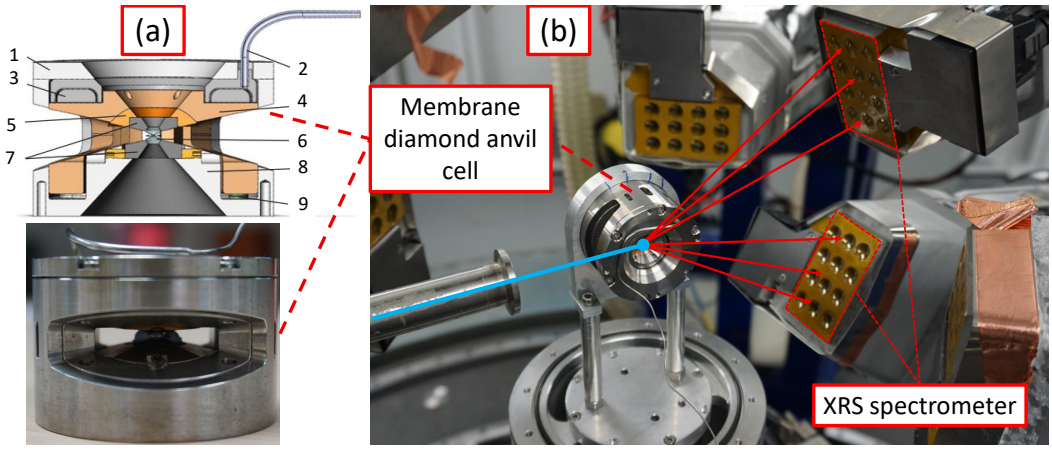

Figure 5.2: (a, top) Lateral cross-sectional view of the used membrane DAC. The image is reprinted from [206], with the permission of AIP Publishing. In the study, the numbers are described accordingly: (1) membrane ring holder, (2) gas membrane, (3) membrane spacer, (4) the piston, (5) rocker seat, (6) conical diamonds, (7) flat tungsten carbide seat, (8) cylinder, (9) pressurizing screws. (a, bottom) photography of the cell. (b) Labeled photography of the experimental set-up at beamline ID20 of ESRF. The beam path of the incident and scattered beam is shown in blue and red, respectively.

pressure was determined by measuring the optical Raman spectrum of a quartz crystal contained in the sample volume. As exemplified in Figure 5.3, the ν_{206} and ν_{464} lines of the spectrum are sensitive to the applied pressure as they shift to higher frequencies with increasing pressure. Therefore, by determining one of the two positions with an Gaussian fit, the pressure inside the cell can be calculated according to reference [207]. Since the ν_{206} line is at the limits of the measurable range, the ν_{464} line was used in this work to determine the pressure. A corresponding error was estimated by comparing the pressure inside the cell before and after recording the spectrum. Beamline ID20 is equipped with one of the most advanced XRS spec-

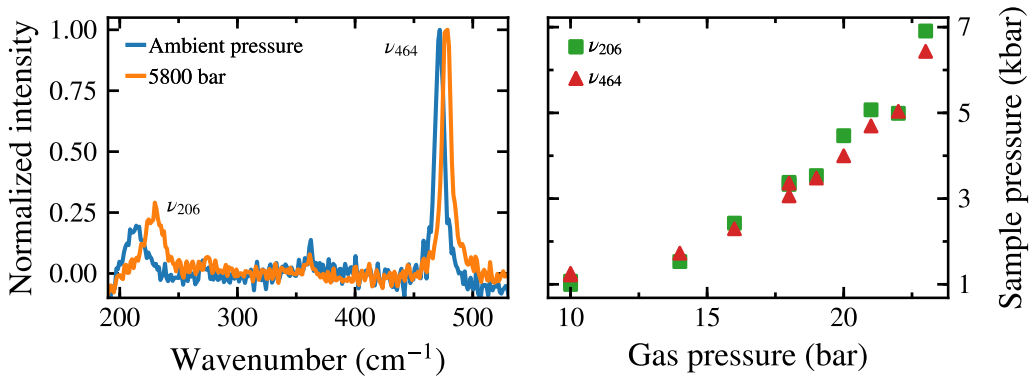

Figure 5.3: (left) Optical Raman spectrum of quartz at ambient pressure and at 5.8 kbar, the labeled ν_{206} and ν_{464} lines shift to higher wavenumbers with increasing pressure (right) The applied gas pressure is plotted against the pressure inside the DAC determined with the shift of the ν_{206}-line and ν_{464}-line according to the reference [207].

trometers in the world [159]. A total of 72 spherically curved analyser crystals are evenly distributed over 6 analyser chambers, 3 of which are in the horizontal plane and 3 in the vertical plane. For this experiment, two of the vertical analyser vessels were set to an angle of $-27°$ and 27°, taking advantage of the large panoramic side opening of the DAC with an opening angle of 110°. The Si(311) monochromator was used to change the incident energy from 10.207 keV to 10.287 keV, while using the Si(660) reflection of the analyser crystals to fix the analyser energy to 9.687 keV with an overall energy resolution of 0.8 eV. The incident energy combined with the scattering angle results in a momentum transfer of $(2.35 \pm 0.40)\,\text{Å}^{-1}$. The energy increment of the scan range was varied according to the observable spectral features. The smallest step size with a value of 0.1 eV was chosen for the oxygen K-edge from 530 eV to 550 eV. The scan range before 530 eV starts at 520 eV and that after 550 eV expands to 600 eV, both measured with a coarser grid of 2 eV and 4 eV respectively, as they are only important for the normalization and data treatment procedure. On

average, the acquisition time for each final spectrum was about 5 hours, resulting in 8 XRS spectra at various pressure steps between ambient conditions and a pressure of 8.5 kbar. For both experiments, the oxygen K-edge spectra were extracted from the 2D detector images using the XRStools [161] program package, analysing the detector images pixel by pixel to optimally separate the signal from the background. XRStools was also utilized for further data treatment, i.e. consistency checking of the individual spectra of each analyser crystal and each scan before merging, background reduction, and normalization of the final spectra. The spectra taken at ID20 and P01 were normalized to the area between 522 eV and 595 eV and between 527 eV and 550 eV, respectively, due to the smaller scan range utilized in the experiments at P01. However, in each figure below comparing spectra from both data sets, the spectra measured at ID20 are renormalized using the same range as the spectra recorded at P01 for better comparison.

5.2.2 Modelling of XRS spectra

The oxygen K-edge spectra were calculated using the ERKALE code [121] based on structures obtained from molecular dynamics (MD) simulations. The used trajectories were taken from the work of Imoto *et al.* [62]. In this study, *ab initio* MD (AiMD) simulations were carried out with 128 water molecules in a canonical ensemble. The referenced paper contains detailed information about the performed simulations, therefore only some of them are briefly presented in the following. The simulations were carried out with the QUICKSTEP module of the CP2k software package based on the Born-Oppenheimer propagation [169]. The RPBE functional was exploited in combination with the triple-zeta TZV2P basis set [174, 176]. The 128 water molecules were simulated within a cubic box with a constant volume and a box length between 14.572 Å and 15.662 Å depending on the pressure and density of the system. A Nosé-Hoover thermostat was set to 300 K in order to control the temperature of the system. Furthermore, periodic boundary conditions were used. Based on structural snapshots generated from the trajectories of the AiMD simulation, the oxygen K-edge spectra were calculated using the ERKALE code within the transition potential approximation[1]. The parameters used for the ERKALE calculation are identical to the calculation of the XRS spectra in the last chapter, therefore it is referred to section 4.2.2 for informations on e.g. the utilized functional and used basis sets. Furthermore, the procedure for cutting out suitable clusters for the spectral calculations is likewise identical and can therefore also be found in the previous chapter. In contrast to the high temperature study of aqueous salt solutions,

[1]The transition potential approximation is elucidated in section 3.4

about 750 spectra (25 % more) were simulated for this system to obtain a converging structural average, as the pressure-induced changes are less pronounced compared to the strong redistribution of spectral weight with increasing temperature observed in the last chapter. All simulations were performed at a momentum transfer value of 2.65 $Å^{-1}$ close to the experimental values. After merging all spectra at a certain pressure, a Gaussian broadening scheme with a linearly increasing full width at half maximum from 0.6 eV to 8 eV between 536 eV and 545 eV was applied to account for finite lifetime effects and the experimental broadening of the apparatus [52, 179]. Furthermore, the final spectra were shifted on the energy loss scale with respect to the experimental K-edge onset as the ERKALE calculation fails to reproduce the absolute energy scale of the experiment.

5.3 Analysis and results

The measured spectra at various pressure steps are shown in Figure 5.4 for the first conducted experiment at beamline P01 on the right side and for the experiment at beamline ID20 on the left side. The improvement of the experimental set-up and the use of three times as many analyser crystals significantly increases the spectral quality. However, the spectral changes are observable in both experiments.

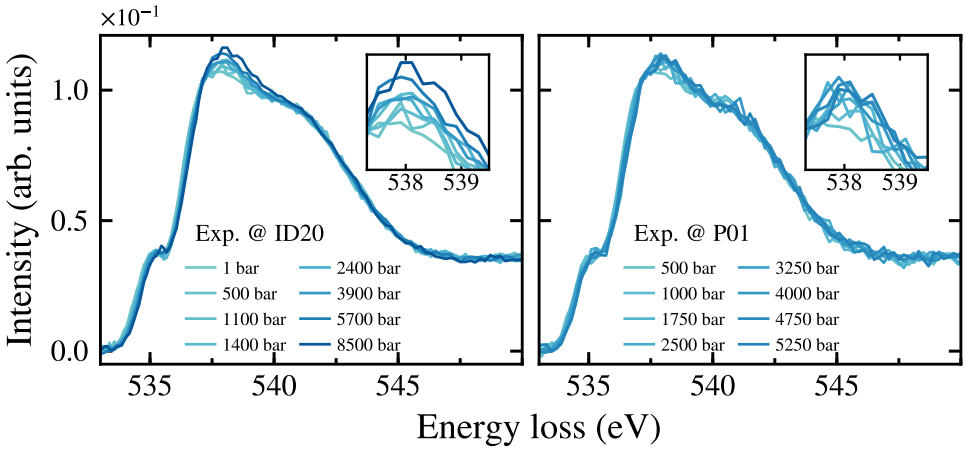

Figure 5.4: Experimental spectra of water under pressure recorded at beamline ID20 (left) and beamline P01 (right). The inset plots show an enlargement of the main-edge region, which exhibit an increased intensity with increasing pressure. The error of the determined pressure is given in Figure 5.7, where the integrated main-edge intensities are shown as a function of pressure with a respective errorbar.

The spectra shift to higher energy loss values with increasing pressure and the main-edge feature gains more spectral weight. In contrast, the pre-edge and the post-edge hardly change with pressure. According to the interpretation scheme of these spectral features introduced in chapter 2.2.2, the absence of spectral changes in the pre-edge and post-edge regions indicates that no major structural changes occur with increasing pressure in terms of the number of hydrogen bonded water molecules or the tetrahedral order of the water structure. The interpretation of the main-edge feature is more ambiguous. Spectral changes in this region could be attributed to a change in density of the sample but also to an increasing disorder of the water structure, e.g. due to a rise of temperature [52, 197]. However, the latter contradicts the lack of observed spectral changes in the pre- and post-edge and can therefore probably be ruled out. As pointed out by Pylkkänen *et al.*, an increased density accompanied by an unchanged structure of the first coordination shell reflects the approach of distant, non-hydrogen bonded water molecules [52]. The term non-hydrogen bonding water molecules refers here and in the following to the fact that these molecules do not form hydrogen bonds with the respective central atom or, in the case of XRS, the absorbing/scattered atom, which does not exclude that these molecules form hydrogen bonds with other water molecules in the system.
The resulting calculated XRS spectra based on the structures obtained from the AiMD simulations are shown in Figure 5.5 together with the experimentally recorded spectra of ID20. The calculated spectra exhibit similar spectral changes, as the main-

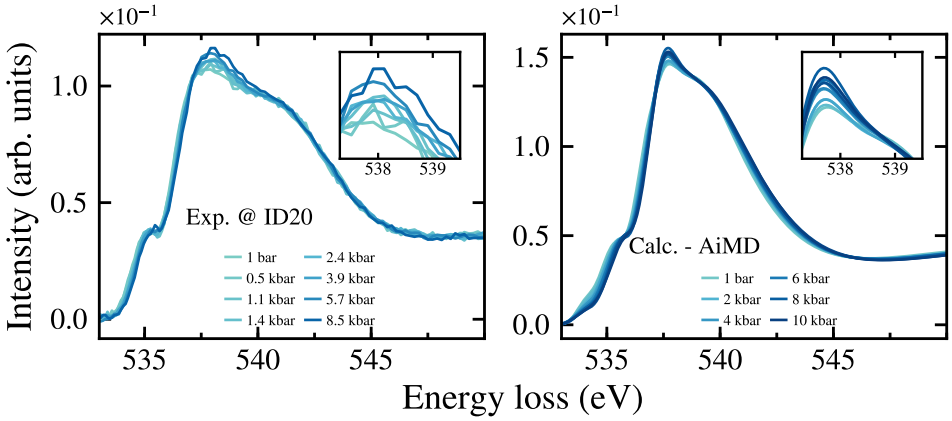

Figure 5.5: The measured spectra of water at different pressure steps as recorded at beamline ID20 (left) compared to the calculated spectra based on structures obtained from the AiMD simulations (right). The legend in the right plot only includes every second pressure step, as the pressure increment is constant at 1 kbar, for clarity. The inset plots show an enlargement of the main-edge region.

edge gains more spectral weight with increasing pressure. Furthermore, the other two prominent features are in agreement with the measured spectra, as they hardly show any pressure-dependent changes. The most pronounced difference between the experimental and calculated spectra is a subtle shift in the post-edge region, which only occurs in the theoretical spectra approximately between 540 eV and 545 eV. In addition, the calculated spectra exhibit a narrower post-edge region compared to the experimental spectra. Both of these differences might be an artefact of the applied linear broadening scheme causing an error in accounting for lifetime broadening at higher energies, or result from difficulties of the ERKALE calculation to completely reproduce the shape of the spectra at higher energies. The latter explanation is supported by similar observation in several studies employing DFT calculations, which were explained by the use of an energy-independent exchange-correlation potential that treats all excited states equally [208–210].
In order to further analyse the evolution of the spectral changes with increasing pressure and compare them with the performed calculations, the difference spectra with respect to the measured and calculated spectrum at 1 bar, respectively, are shown in Figure 5.6. The determined differences of the measured spectra exhibit

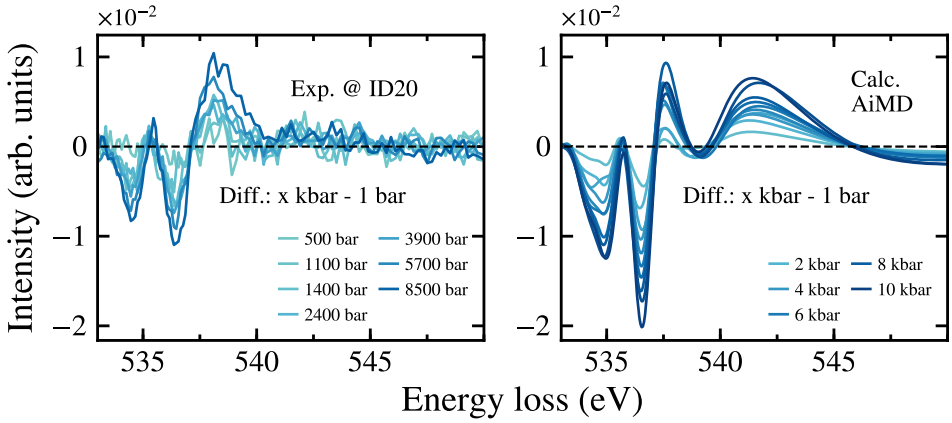

Figure 5.6: The experimental and calculated spectra after subtracting the respective spectrum at 1 bar. Difference spectra are calculated for the measured spectra at beamline ID20 (left) and the spectra calculated based on the AiMD trajectory (right). The legend in the right plot only includes every second pressure step, as the pressure increment is constant at 1 kbar.

three features that gradually become more pronounced with increasing pressure. The first two features occur due to the increasing blue shift of the edge onset region to higher energy loss values. The last pronounced peak emphasises the continuous pressure-dependent changes of the main-edge region. For higher energy loss values, e.g. in the post-edge region, hardly any spectral differences are observed

between the spectrum measured at 1 bar and the subsequently recorded spectra at higher pressures. The first three features of the differences of the calculated spectra are similar to the ones obtained for the experimental spectra. While the first two strongly depend on the shift of the calculated spectra, the third feature reflects the spectral differences due to pressure-related changes in the employed trajectory. A comparison of the main-edge differences of the experimental spectra with the calculated ones reveals a good agreement of the pressure-dependent intensity increase in this region. However, there is a noticeable difference regarding the width of the feature, which might be related to the mentioned difficulties of the DFT calculation to correctly reproduce the spectral width at higher energies, although this is most pronounced for the post-edge region. In addition, the main-edge region of the calculated spectra exhibits an intensity decrease for pressures at 9 kbar and above, which exceeds the maximum pressure generated in the experiment.
For a quantitative analysis of the main-edge changes with increasing pressure, the integrated intensities as a function of pressure are shown in Figure 5.7, with the integrated values of the experimental spectra on the left side and the values of the theoretical spectra on the right side. The experimental spectra were integrated in a range from 537 eV to 540 eV corresponding to the isobestic points, whereas for the theoretical spectra a smaller range from 537.2 eV to 538.8 eV was chosen due to the narrower feature. The error was estimated by calculating the integrals two more times after shifting the integral intervals by ±0.4 eV and then evaluating the standard deviation of the mean value. This gives a better (and larger) error estimation than an error propagation of the uncertainties of the recorded values. The integrated values for the respective experiments at P01 and ID20, have an offset

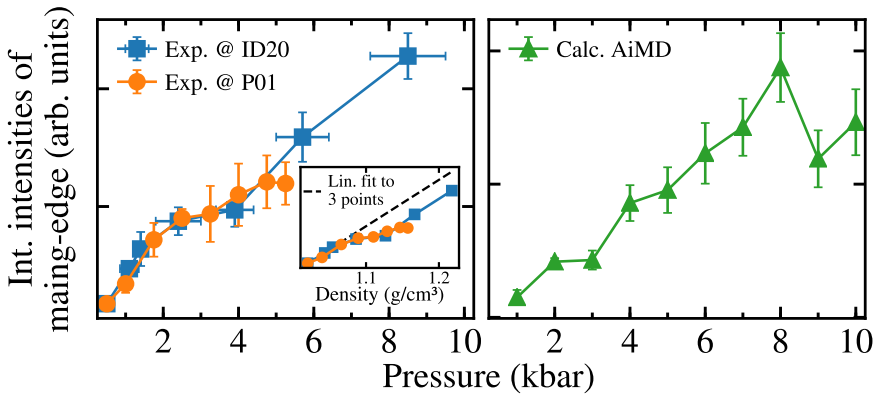

Figure 5.7: The integrated intensities of the main-edge region of the measured (left) and calculated (right) spectra as a function of pressure. The inset plot on the left side shows the integrated values as a function of density.

to each other, presumably due to the normalization in conjunction with a slightly different background subtraction. Therefore, the integrated value at 500 bar was subtracted from the other values of the measurement series to ensure comparability of the pressure dependence. The offset between both measurements at 500 bar is a mere 0.4 % which is about 7.5 % of the total change between the integrated main-edge intensities at 500 bar and 8.5 kbar. Within the error bars, the integrated values corresponding to the first performed experiment are fully reproduced by the second measurements at beamline ID20 with the membrane DAC. The integrated intensities of the main-edge for both experiments show a steeper increase within the first 2 kbar to 3 kbar, which then decrease significantly. To verify whether the pressure dependence of the main-edge region is strongly correlated with the density changes of the sample, the inset plot in Figure 5.7 (left) displays the calculated values as a function of density. The NIST database was used to determine the density for each pressure step [211]. An exclusively linear increase of the main-edge intensity with increasing density would indicate a strong or complete correlation. The inset plot reveals a linear increase of the integrated values up to 1.08 g/cm^3 followed by a deviation of this linear increase. Hence, a strong or complete correlation over the entire density range can be excluded. The pressure response of the integrated intensities of the calculated spectra is shown in Figure 5.7 (right) and exhibits an overall good agreement with that of the experimentally obtained values. However, at 9 kbar, which is outside the studied pressure range of the experiment, the values show a significant decrease. Since the following analysis of the parameters extracted from the MD simulations does not reveal a similar abrupt change at 9 kbar, this rapid decline might be related to problems of the ERKALE calculation to reproduce the XRS spectra at such high densities.
This good agreement between the calculated and experimentally recorded spectra, in particular shown by the integrated main-edge intensities, justifies using the generated trajectory to extract detailed structural information about the water structure described by the model. As introduced in chapter 2.2.1, the number of hydrogen bonds in the system were determined according to Luzar *et al.* and two parameters were calculated that characterise the tetrahedral structure of the water molecules in terms of distance and angle [86, 87]. In addition, the number of water molecules in the first coordination shell was evaluated using the first minimum of the oxygen-oxygen radial distribution function as cut-off radius with a value of 3.5 Å. Although the minimum position is shifting with increasing pressure, it was kept constant for the evaluation to investigate how the distant molecules approach the first coordination shell. The extracted parameters as a function of pressure and density are shown in Figure 5.8 and 5.9, respectively. Over the entire pressure range, the number of hydrogen bonds slightly increases by about 3 % from approximately 3.4 to 3.5 hydrogen bonds per molecule. The two parameters characterising the tetrahedral

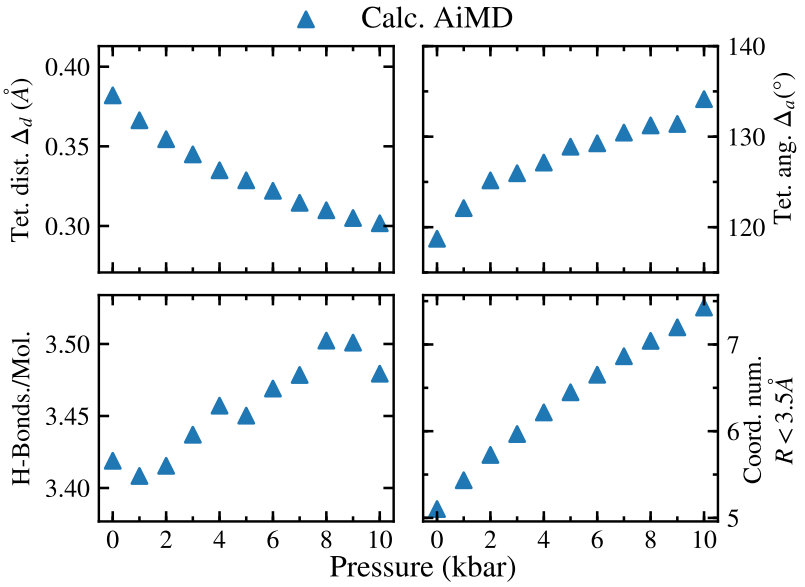

Figure 5.8: The parameters extracted from the trajectory of the AiMD simulations as function of pressure: The deviation from a tetrahedral structure in terms of distance (upper left) and angle (upper right), the number of hydrogen bonds per water molecule (lower left) and the coordination number (lower right).

order of the water structure show an contrary behaviour as the distance parameter Δ_d is decreasing with increasing pressure indicating a more tetrahedra like structure, whereas in terms of angle deviation the parameter Δ_a is increasing pointing towards a decrease of tetrahedral order. However, the interpretation of the decrease of Δ_d as an increase in tetrahedral order is ambiguous in this case, since the decrease in the parameter can also be explained by the shrinking distances in the system due to the increasing density, which is supported by the linear correlation between Δ_d and the density as shown in Figure 5.9. In addition, the pressure-induced changes for both parameters are minor compared e.g. to the drastic changes observed with increasing temperature (see chapter 4.3) Interestingly, Δ_a shows a similar pressure dependence as the integrated experimental main-edge intensities, since a larger increase is observed up to 2 kbar or 3 kbar, which is damped significantly for higher pressures. As expected from an increase of density due to the compression of the sample, the coordination number also increases over the entire pressure range. By analysing the parameters as a function of density instead of pressure as shown in Figure 5.9, it is noticeable that Δ_d, the number of hydrogen bonds in the system and the coordination number all exhibit a strong correlation with the increasing density, as all increase linearly. The tetrahedral angular deviation parameter Δ_a

likewise shares similarities with the integrated main-edge values in terms of its density dependence, since it increase linearly up to 1.08 g/cm^3, at which value it changes its slope.

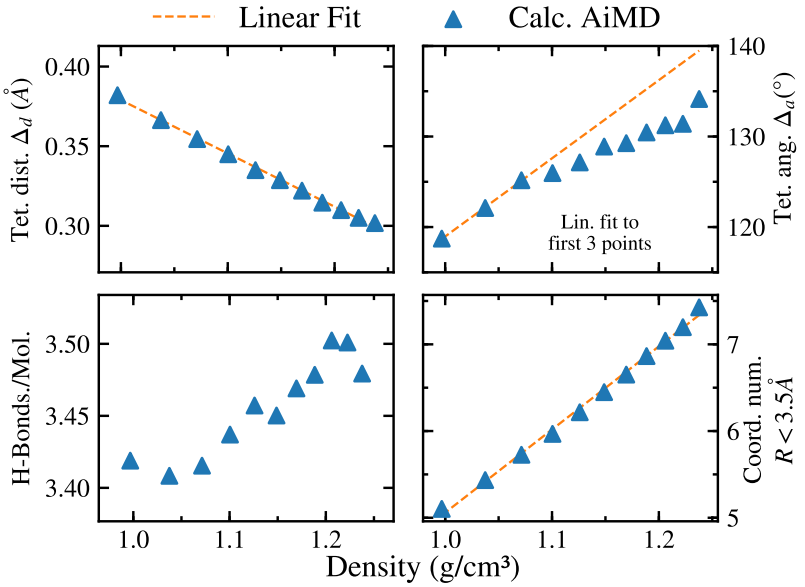

Figure 5.9: The parameters extracted from the trajectory of the AiMD simulations as function of density: The deviation from a tetrahedral structure in terms of distance (upper left) and angle (upper right), the number of hydrogen bonds per water molecule (lower left) and the coordination number (lower right). The results of some linear fits are shown in orange to emphasize the (in parts) linear relationship of the parameters with increasing density.

5.3.1 Collapse of the second coordination shell

One of the goals of this chapter is to further study and characterise the so-called collapse of the second hydration shell which was first introduced by Soper *et al.* [69]. In their study, they extrapolated a series of neutron diffraction patterns recorded at different pressure points to an upper and lower bound, respectively. They further proceeded from the assumption of previous studies that the structure of water can be represented as a linear combination of these endpoints, to which the structures of high-density water (HDW) and low-density water (LDW) were attributed [212]. Analysing those two structures, they claimed that a collapse of the second shell is taking place accompanied by a breaking of hydrogen bonds between the first and

second shell which leads to a density increase.
According to the aforementioned results of the XRS analysis, significant structural changes with increasing pressure can also be confirmed by the experiments. However, in conjunction with both the experimental changes in the pre- and post-edge and the theoretical analysis, the number of hydrogen bonds are hardly altered by the increasing pressure and, in particular, do not decrease. Since the most significant changes occur in the main-edge feature, it can be concluded that non-hydrogen bonded molecules approaching the interstitial sites of the first shell are responsible for the structural difference of LDW and HDW. It should be noted that an XRS study of pressurised liquid water up to 6 kbar reports no significant increase of main-edge intensity with increasing pressure but observes a non-linear change in intensity of the pre-edge feature [180]. However, the results are difficult to evaluate as no analysis of the main-edge intensity is reported and no error bar is given for the Gaussian fit method used to determine the pre-edge intensity. The significantly better data quality of the recorded spectra in this thesis might also explain the differences to the previous study as the achieved data quality enables a more accurate analysis of the spectral changes. In addition, the results of this thesis are consistent with a classical MD study of water up to 10 kbar that reveals through an extensive analysis that the hydrogen bonds in the system remain largely intact and that the interstitial, non-hydrogen bonded water molecules of the second shell, approach the first shell and are thus responsible for most of the observed changes [81]. Furthermore, various experimental studies confirm the persistence of the hydrogen bonds in the system with increasing pressure or likewise attribute the changes to the approach of non-hydrogen bonded water molecules to the first shell [22, 213–215]. For instance, a femtosecond mid-infrared pump-probe spectroscopy study of liquid water mixed with D_2O at a temperature of 25 °C and pressures up to 10 kbar found by comparing their spectroscopic data with MD simulations, how the dynamical configuration of water changes at higher pressure with an increase of non-bonded molecules at short distances but without altering the local hydrogen bonded tetrahedral configuration [22]. This is also confirmed by an X-ray diffraction study examining the structure of liquid water with a high q-range to determine the pair distribution function, which indicates that most of the changes occur at higher distances in the probably non-hydrogen bonded interstitial neighbouring molecules [215]. An optical Raman study by Kawamoto *et al.* even suggests an increase in hydrogen bond strength with increasing pressure, which possibly explains the slight increase in the number of hydrogen bonds at higher pressure observed in this thesis, as determined from the analysis of the AiMD trajectory in Figure 5.8 [199].
In accordance with the changes in the hydrogen bond network, only minor changes in the tetrahedral order are observed in terms of both spectral changes and extracted parameters from the AiMD simulation. This is plausible since the tetrahedral order

of the water network is closely related to the number of hydrogen bonds. Therefore, changes in the latter are often linked to a corresponding alteration of the tetrahedral order, as observed, for example, with increasing temperature [10]. The increase of the Δ_a parameter might be caused by a slight sideways movement of the four nearest water molecules due to the influence of the approaching interstitial molecules.
The question arises regarding the pressure dependence of the observed approach of the non-hydrogen bonded molecules and whether there is a signature of the proposed phase transition from LDW to HDW. From an experimental point of view, the integrated main-edge intensity is a suitable quantity to investigate these changes as it is directly correlated to the number of non-hydrogen bonded molecules. Furthermore, the AiMD simulation was utilized to extract the ratio of hydrogen bonded to non-hydrogen bonded molecules in the first coordination shell[2] to study the pressure evolution in more detail. The ratio is shown in Figure 5.10 in the plot on the left together with the corresponding derivative in the right plot. At ambient conditions, there are twice as many hydrogen bonded as non-hydrogen bonded water molecules in the first shell. This ratio decreases with increasing pressure, falling below a ratio of 1:1 at 8 kbar. This determined ratio as well as the integrated

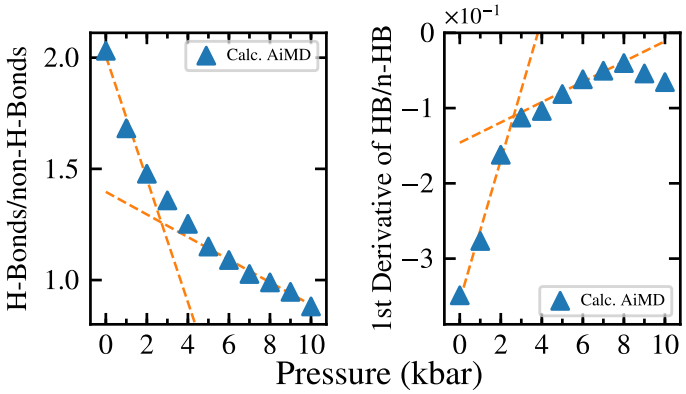

Figure 5.10: (left) The ratio of hydrogen bonded to non-hydrogen bonded water molecules in the first shell of a water molecule together with its (right) derivative. To emphasis the change of slope of the determined parameters, two straight (dashed blue lines) were fitted to the data of the two plots using the first three data points and data points between 5 kbar and 8 kbar, respectively.

experimentally recorded main-edge intensities are changing continuously over the entire pressure range, a sudden collapse accompanied by an abrupt change is not observed. However, the slope of the integrated values exhibit a significant change as

[2]For this calculation, the first coordination shell comprises all water molecules within a range of 3.5 Å around a central water molecule.

it decreases at approximately 3 kbar. A change of slope can be likewise observed for the determined ratio around the same pressure. This becomes especially apparent in the right plot of Figure 5.10, where the derivative of the ratio is depicted.
Several other high pressure studies on liquid water observe likewise an anomaly somewhere between 2 kbar and 4 kbar in their respective measured quantity [22, 40, 199, 216–218]. For instance, an X-ray diffraction study from the mid 90's reveals a non-linear pressure dependence of the oxygen-oxygen distances with a minimum at around 2 kbar [37]. In addition, an IXS study by Krisch *et al.* reports an anomaly around 3 kbar in the measured infinite-frequency limit of the sound velocity, a quantity that correlates with the microscopic dynamic and structural properties of liquid water. In the previously mentioned optical Raman study by Kawamoto *et al.*, a change in the slope of the measured Raman shift at approximately (4 ± 1) kbar was observed and interpreted as a change in the compression behaviour which might indicate a structural transition [199]. Furthermore, a more recent optical Raman study on liquid water under pressures up to 12 kbar exploiting a more sophisticated analysis scheme, concluded that a structural transition might occur around 4 kbar based on the measured non-linear pressure evolution of two Raman peaks [40]. Moreover, a Brillouin scattering study utilized the determined sound velocity to calculate the elastic constant of water as a function of pressure, which often changes when a phase transition occurs for example at the transition from ice VI to ice X [21, 219]. The logarithm of the elastic constant shows a change of slope when plotted against the logarithm of the density at a pressure value of approximately 2.9 kbar which was interpreted as an evidence for the liquid-liquid phase transition and is pointing towards a more compact second shell of HDW which is harder to compress in comparison to LDW [21]. To name but a few related studies. The result from the last mentioned study is especially interesting as a decrease of compressibility at around 3 kbar could also explain the observed decrease of the slope of the integrated main-edge intensities and the determined ratio of hydrogen bonded to non-hydrogen bonded molecules.
From the conducted analysis the congruent picture emerges in accordance with the literature that the hydrogen bonds in the system stay mostly intact in the studied pressure range accompanied by a largely unchanged tetrahedral structure. In contrast, the non-hydrogen bonded water molecules undergo major continuous changes as they approach the first shell and fill the interstitial void between the first and second shell. At lower pressures, the approach of the water molecules to the first shell is fully correlated with the increasing density of the sample, as revealed by the integrated main-edge intensities and the theoretically determined parameters. However, the approach with increasing pressure weakens at a pressure of about (3 ± 1) kbar, which is consistent with the pressure at which several other studies found an anomaly in the pressure-dependent evolution of their measured

quantities. Hence, in conjunction with the literature, this change in slope could indicate a transition from LDW to HDW, with the HDW structure having a lower compressibility. It should be noted, that the transition from LDW to HDW is no phase transition in the conventional thermodynamic sense, as both structural motifs continuously convert into each other.
The results are in line with the theoretical study of Saitta *et al.* in which they performed an extensive analysis of their MD trajectory using the TIP4P model to simulated water up to a pressure of 10 kbar [81]. In short, they also found that the number of hydrogen bonds are largely unaffected by the increased pressure and that interstitial molecules are approaching the first shell. The good agreement between the experimental and calculated spectra enables to verify the changes determined by Saitta *et al.* by performing the same advanced analysis on the MD trajectory used in this thesis [81]. Applying the analysis scheme as described in Saitta *et al.*, three different distributions were calculated and are shown in Figure 5.11, namely a neighbour distribution, an oxygen orientational distribution and a hydrogen orientational distribution [81]. The obtained distributions reproduce nicely the main features from the previous work and are further explained in the following. The distribution in the upper plot lists the amount of water molecules of the 1st-16th neighbours as a function of distance to the central molecule. The first shell is plotted in blue and contains the 1st–4th neighbours and the second shell, shown in red, includes the 5th–16th neighbours. The first peak hardly changes with increasing pressure and only slightly narrows. However, the second shell undergoes significant changes as a peak splitting of the broad peak with its maxima at about 4.6 Å into two peaks with their maxima at 3.2 Å and 4.4 Å is observed. Following the interpretation of Saitta *et al.*, this suggests that mainly the 5th–8th are involved in the structural rearrangement of the second shell. In the lower left plot, the oxygen orientation distribution ($\measuredangle \mathrm{O}^{I} - \mathrm{O} - \mathrm{O}^{II}$) is shown. The distribution is determined by calculating the angle that spans between a central oxygen atom and the various combinations of an oxygen atom of the first shell and an oxygen of the 5th to 8th neighbours of the second shell. Compared to the previous study, some differences above 120° appear which might be related to the smaller box size employed in this thesis but the main features between 30° and 100° are in good agreement. According to Saitta *et al.*, the two peaks at ambient conditions at about 45° and 75° correspond to second shell molecules which are hydrogen bonded either directly to the other water molecule whose oxygen is used to calculate the angle or one of the other three water molecules in the first shell. Those two peaks merge together with increasing pressure into a single peak at approximately 65° which can be attributed to interstitial molecules. However, further analysis of Saitta *et al.* reveals that the changes are not caused by the breaking of hydrogen bonds between the first and second shell and an approach of the respective water molecules but that

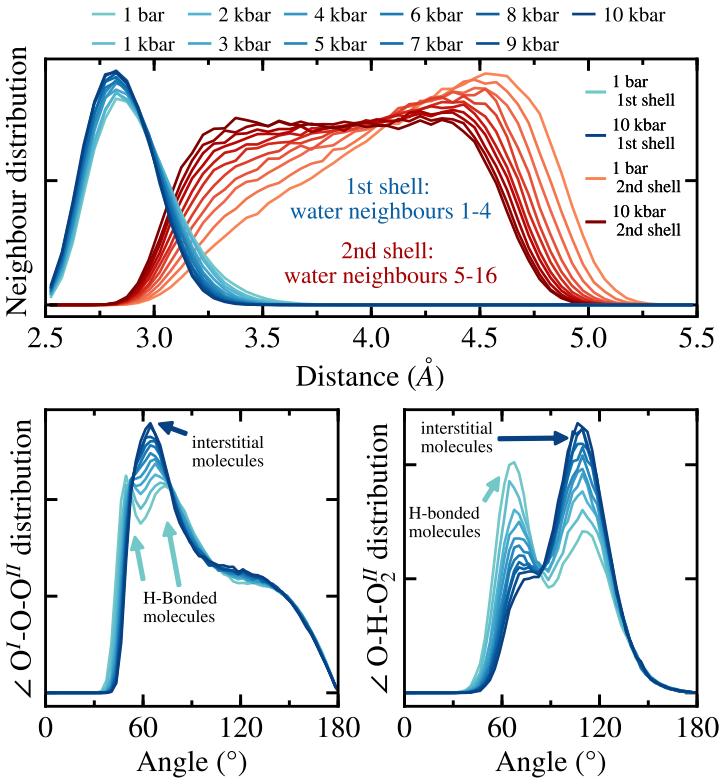

Figure 5.11: Several distributions in terms of distance (upper plot) and angles (lower plots) determined according to Saitta *et al.*, see text for details [81].

the 5th to 8th closest neighbours change. As aforementioned those neighbours are mostly occupied at ambient conditions by water molecules hydrogen bonded to the first shell but are replaced with increasing pressure as more non-hydrogen bonded molecules move closer to the first shell from the view of the center molecule, thus leading to the increase of the peak at 65°. The angular distribution in the lower right plot of Figure 5.11 is obtained by evaluating the angle as seen from the hydrogen atom of the central water molecule between the covalent bonded oxygen and the oxygen of the water molecule belonging to the closest non-hydrogen bonded water molecule with reference to the initial hydrogen. This distribution exhibits two peaks at 65° and 110° with the first one appearing due to a water molecule which is non-hydrogen bonded to the central water molecule but to a different molecule in the first shell, while the second peak can be explained by water molecules that are not hydrogen bonded to either of these molecules. With increasing pressure significant changes are observed as the first peak decreases and the second peak gains more intensity surpassing the first one as global maxima, whereas the peak

position is unchanged for both features. Saitta *et al.* concluded that the distribution indicates that the non-hydrogen bonded water molecules can only approach the central water molecule from a defined range of directions with respect to the structural orientation of the first coordination shell. The good agreement of the spectral changes between the experimentally recorded spectra and the spectra calculated on the basis of the analysed trajectory suggests that the underlying model largely reflects the structural changes in pressurised water. Further confirming the previous study of Saitta *et al.* as the same pressure-dependent evolution of the theoretical parameter is observed in this thesis. Moreover, the conclusions derived from the AiMD simulation are also consistent with a purely qualitative analysis of the experimental spectra.

5.3.2 Structural comparison of pressurised water with ice Ih, III and VI

In previous studies, the oxygen K-edge has not only been investigated to analyse the local structure of liquid water but also to probe a variety of ice phases with X-ray spectroscopy techniques [51, 52, 76, 88, 220, 221]. Since the spectrum of the oxygen K-edge is composed of the average contributions of all structural arrangements occurring in the sample system, information on structural similarities and differences can be derived by comparing spectra of different ice phases with those of liquid water. The spectral comparison between water and ice phases is particularly interesting when the water structure changes as a function of an external parameter such as pressure. Depending on the changes, it is possible to investigate whether the occurrence of spectral similarities increases or decreases between the two systems and how these changes correlate with the pressure at phase boundaries of different ice phases. The spectral differences and similarities can further be related to the structure of the two systems. The shared phase boundary between liquid water and the various crystalline ices raises the question whether the local structure of the high-density crystalline ice may persist into the liquid when comparing ice and liquid water at similar pressure. Previous XRS experiments on ice III and ice VI allow to compare the recorded spectra of pressurised water with those of the two ice phases, both of which share a phase boundary with liquid water over large parts of the investigated pressure range. The spectra of the two ice phases are taken from two different studies, namely Cai *et al.* (ice III) and Pylkkänen *et al.* (ice VI) [51, 52]. In addition, the spectra of ice Ih is used from the Pylkkänen *et al.* study as prominent reference for a low-density ice phase.
In the following, a brief overview over the structural properties of the three ice

phases is given. For a more comprehensive insight, it is referred to the literature [222–227]. The water molecules within ice Ih are located on a hexagonal lattice (space group $P6_3/mmc$) with each oxygen, hydrogen bonded to its four nearest neighbouring water molecules at a distance of about 2.75 Å forming a regular tetrahedron with an O-O-O angle close to 109.5° [225, 228]. The resulting density is 0.926 g/cm^3 at ambient pressure [227]. Water and ice Ih share a phase boundary from 0 bar at −201 °C to 2099 bar at −21.99 °C. Ice III has a tetragonal crystalline structure (space group $P4_12_12$) containing a tetrahedrally connected hydrogen bonded framework with a bond length between 2.76 Å and 2.8 Å [223]. Compared to ice Ih, ice III exhibits a higher density of 1.16 g/cm^3 which is achieved by a distortion of the ideal tetrahedral framework that allows two or three non-bonded water molecules to approach the first shell to a distance of about 3.6 Å much closer than the corresponding distance in ice Ih of 4.5 Å [52, 223]. This approach results in a convoluted formation of hydrogen bonded molecules as five-membered rings with a comparatively large variation in bond angles resulting in a root-mean-square deviation of 16.4° with an expected average value around 109.5° [223, 225]. It shares a phase boundary with liquid water in a temperature and pressure range of 2099 bar at −21.99 °C to 3501 bar at −16.99 °C [225]. Ice VI forms a tetragonal crystalline structure (space group $P4_2/nmc$) which consists of two interpenetrating separate networks of hydrogen bonded molecules with no connecting hydrogen bonds between the two networks [222]. In comparison to ice III, these interpenetrating but independent networks allow for a higher density of 1.31 g/cm^3 with a similar average inter-site distance of the tetrahedral framework at 2.77 Å, but with eight nearest neighbour water molecules that are not hydrogen bonded and are at a closer average distance that varies in the literature between 3.41 Å and 3.51 Å [222, 224, 225]. Furthermore, the angles between the hydrogen bonded water molecules (O-O-O) exhibit a large variation between 77° to 128° resulting in a complex structural arrangement which is nicely depicted in the schematic drawings in the original XRD study of B. Kamb, to which reference is made here [222, 227]. The shared phase boundary of ice VI with liquid water ranges from 6324 bar at 0.16 °C to 22160 bar at 81.85 °C [227]. Ice Ih, III, and VI are all hydrogen-disordered ice phases.

The spectra of ice Ih, III and VI are shown in Figure 5.12 (right) next to the recorded spectra of pressurised liquid water (left). The spectra taken from reference [52] of ice Ih and ice VI were each recorded with an incident energy of 9.68 keV at a scattering angle of 49° yielding a momentum transfer value of $(4.2 \pm 1.2)\,\text{Å}^{-1}$. This is similar to the experimental set-up of the ice III spectrum from reference [51], which was recorded with an incident energy of 9.88 keV at a scattering angle of 35° resulting in a momentum transfer value of $3\,\text{Å}^{-1}$. Although the use of a large momentum transfer value (e.g. $9.4\,\text{Å}^{-1}$) significantly affects the measured intensity

of the pre-edge, the other two spectral features are hardly effected as revealed by the study of Pylkkänen *et al.* [52]. Furthermore, the used momentum transfer in this thesis with a value of $(2.25 \pm 0.40)\,\text{Å}^{-1}$ differs only slightly from the previous studies. Since the previous measurements employed a more limited energy scan range, all spectra in Figure 5.12 are normalized to the area between 533.3 eV and 547.7 eV.

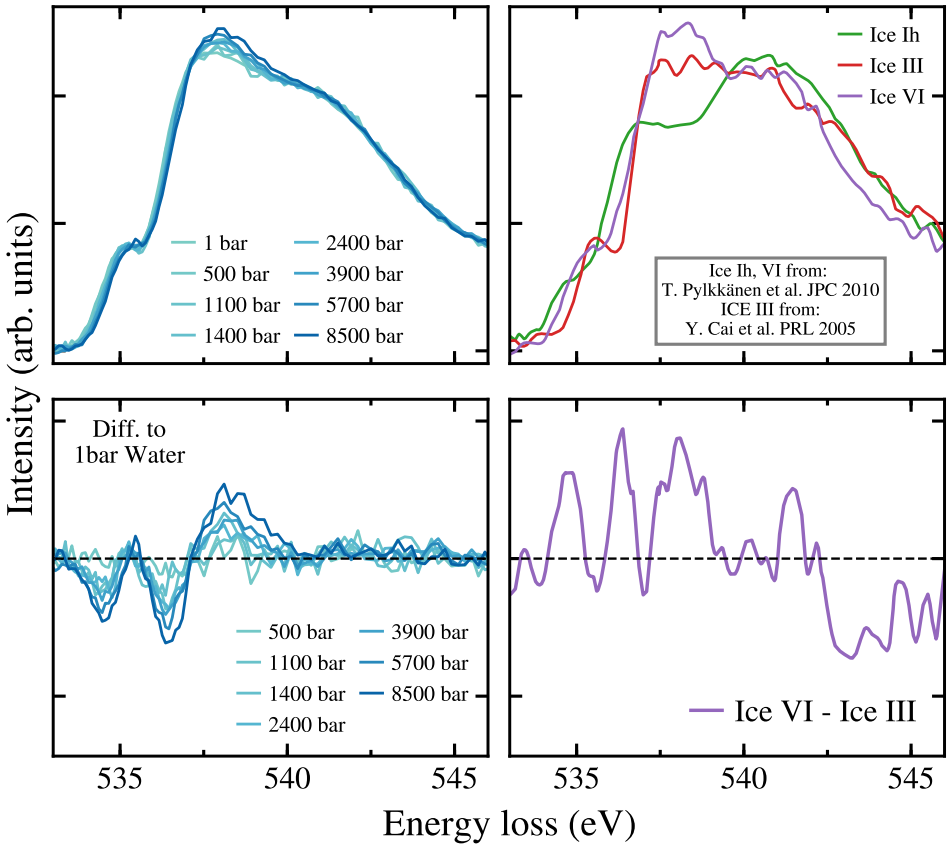

Figure 5.12: (Upper, left) The XRS spectra of pressurised water in a pressure range from 1 bar to 8.5 kbar together with (upper, right) the experimentally recorded spectra of ice Ih, ice III ice VI as taken from Reference [52] (ice Ih, ice VI) and [51].(Bottom, left) the corresponding difference spectra of pressurised liquid water with respect to the measured spectrum of liquid water at 1 bar and (bottom, right) the difference spectrum between the spectra of ice VI and ice III.

The structural differences between the ice phases have a direct impact on the shape of the XRS spectra. The ice Ih spectra show a pronounced post-edge feature, which exceeds the intensity of the main-edge. In contrast, the most pronounced spectral feature of ice III and ice VI is the main-edge, whereas the post-edge is weakened

in comparison to ice Ih which is even more distinct for ice VI. However, the differences of post-edge intensity between the ice phases are exceeded by the more drastic changes of the main-edge. In their study, Pylkkänen *et al.* found a linear correlation between the main-to-post-edge ratio and the distance of the second coordination shell of each system which is in line with the previously described structural differences of the various ice phases. Hence, the increase in main-edge intensity reflects the approach of outer, non-hydrogen bonded water molecules to the first shell since the first shell only changes minorly between the different ice phases.
An absolute comparison of the spectra of the different ice phases with the spectra of liquid water at different pressures is prone to error because the usable normalization range is relatively limited, which can lead to an underestimation or overestimation of the spectral features of a certain spectrum [89]. Furthermore, when comparing XRS spectra from different studies, inconsistencies may occur due to differences in the energy scale. Considering these two factors, a relative comparison of the spectral differences of the three different ice phases with the pressure-induced changes of liquid water is performed, with special emphasis on the main edge, as this feature also exhibits the most pressure-dependent changes in liquid water. This comparison reveals that the spectral evolution of water at 1 bar to 8.5 kbar shares the most similarities with the difference of the spectrum of ice III and ice VI especially with respect to changes in the main-edge. This becomes further apparent when directly comparing the difference spectra of liquid water with respect to the spectrum at ambient conditions with the difference spectra of the ice phases calculated by subtracting ice III from ice VI, as shown in the two lower plots in Figure 5.12. With respect to the differences in the main-edge region, the difference spectrum of ice VI - ice III is similar to the difference spectrum between liquid water at 8.5 kbar and 1 bar as the difference in main-edge intensity is only slightly more pronounced and narrower for ice VI - ice III than for liquid water. This indicates that changes in the structure of water with increasing pressure are similar to changes induced by the structural variation from ice III to ice VI. It should be noted, however, that this reflects only the local structure surrounding the water molecule, since water, unlike ice, has no long-range order.
Although a coordination of non-hydrogen bonded molecules is already observed for ice III, the number of these next-nearest neighbouring non-hydrogen bonded molecules is significantly smaller and the distance larger compared to ice VI. Thus, one of the most notable changes between ice III and ice VI is the increased significance of non-hydrogen-bonded molecules near the first coordination shell. These changes are similar to those of pressurised liquid water as revealed in the analysis of the previous section, since an increase in non-hydrogen bonded molecules approaching the first coordination shell was observed with increasing pressure.

Hence, the analysis of the difference spectra is in line with the previous analysis and further indicates that the resulting local structure in terms of the approach of non-hydrogen bonded molecules in pressurised liquid water is comparable with the local structural arrangement in ice VI. From the results, a definite statement of the extent to which the structures of ice VI and pressurised water are similar is difficult to derive. However, the results may suggest that the observed approach of non-hydrogen bonded molecules to the first shell in pressurised liquid water is realized via the interpenetration of two, independent local water networks as in ice VI. It should be noted again that the term water network does not refer to a large-scale structural arrangement of water molecules in pressurised water, but to highly localized structural heterogeneities which are temporally volatile. Such an interpenetrating water network probably consists of the local arrangement of two pentamers of water molecules, which structurally intertwine without forming hydrogen bonds with each other. The results of an theoretical study investigating the interaction of rigid pentamers corroborate this hypothesis [229]. In the MD study, rigid pentamer structures composed of five water molecules forming a tetrahedron with a central water molecule and four water molecules at each corner with a fixed O-O-O angle of 109.47° and a fixed distance of 2.8 Å to the central molecule were investigated. By minimizing the potential energy between two pentamers, they determined four local minima and the corresponding structure which are characterised by different amount of hydrogen bonds between the two pentamers ranging from zero to three. The pentamer structures with two and three bonds were found to be similar to the local structure of ice Ih while the structure with zero bonds between the pentamers are not unlike the structure of ice VI. A MD simulation of liquid water at different pressures, additionally performed in the study, yielded an oxygen-oxygen radial distribution function at 6 kbar whose characteristics are best reproduced by the double-pentamer structure, which has no hydrogen bonds between the two pentamers [229]. Hence, pointing towards a similar intertwined local structure in pressurised liquid water as in ice VI.
In terms of post-edge intensity, the pronounced difference between ice Ih and the two other ice phases might be explained by the results of an XRS study on normal and heavy liquid water, high/low-density amorphous ice (HDA/LDA), ice Ih and the cubic ice phase Ic [88]. Regarding the post-edge intensity, the investigated samples could be divided into two groups. The first group consisting of ice Ic, LDA and Ih, which exhibit a more pronounced post-edge feature than the second group of HDA, H_2O and D_2O. The enhanced post-edge feature of the first group was attributed to the delocalized nature of the corresponding excitation, which occurs with a higher probability in crystalline solids than in disordered solids as the wave functions for higher excited states are spatially more extended for an ordered crystalline structure [88]. This explains the differences in post-edge intensity for the ice phases shown

in this work as well as liquid water. Compared to ice Ih, the structure of ice III is distorted such that non-hydrogen bonded molecules can approach the first shell leading to a decrease in the intensity of the post-edge feature. Furthermore, the tetrahedral framework of ice VI is even more distorted, as can be inferred from a wider distribution of the corresponding O-O-O angles, leading to a further reduction of the post-edge intensity. Naturally, liquid water is lacking a long-range structure and is highly disordered compared to the ice phases, thus exhibiting the least pronounced post-edge feature of the spectra shown in Figure 5.12.
In order to further verify the similarities between the experimentally obtained spectra of liquid water and those of ice III and ice VI, respectively, XRS spectra of the three ice phases were calculated with ERKALE based on structures generated using GenIce, which is an efficient tool for generating hydrogen disordered structures of different ice phases [230]. In addition, the structure of ice V was generated and the spectrum was calculated, since ice V is the intermediate ice phase between ice III and ice VI in the phase diagram. Ice V has a density of 1.24 g/cm^3 and exhibits one of the most complicated structures of all the ice phases as it contains rings which have between four and eight members and groups of seven molecules at four distinct lattice sites, each with a different structural environment [225, 227]. This way, the calculated spectra of pressurised water shown in the previous section can be compared with the calculated spectrum of ice Ih, ice III, ice V and ice VI. The ERKALE calculation of the spectra of the three ice phases have been performed using the same parameters as for pressurised water. The resulting spectra are shown in Figure 5.13 (top, right) together with the spectra of liquid water at various pressures (top, left). The overall trends are nicely reproduced by the calculated spectra, in particular the order of the different ice phases in terms of main- and post-edge intensity. However, as for the calculated spectra of liquid water, the post-edge is overestimated in all calculated spectra. This can be seen in the difference spectra in the lower two plots of Figure 5.13. In contrast to the experimental spectra, all difference spectra here are evaluated with respect to the calculated spectrum of liquid water at 1 bar. This is reasonable since all spectra are calculated with the same procedure, which allows for a better comparison of the spectral differences of pressurised liquid water with the various ice phases. In addition to the overestimated post-edge intensity, the difference spectra show a slightly underestimated main edge intensity for ice III. Besides, the difference spectra reveal a remarkable agreement of the calculated spectra between liquid water at 8 kbar and ice VI in terms of shape and intensity of the main-edge. This good agreement further emphasizes the excellent quality of the simulated AiMD trajectories of pressurised liquid water and the performed ERKALE calculations. Furthermore, as expected from its intermediate position in the phase diagram, the main-edge intensity of the (difference) spectra of ice V is between ice III and ice V. This might indicate that structural changes in pressurised

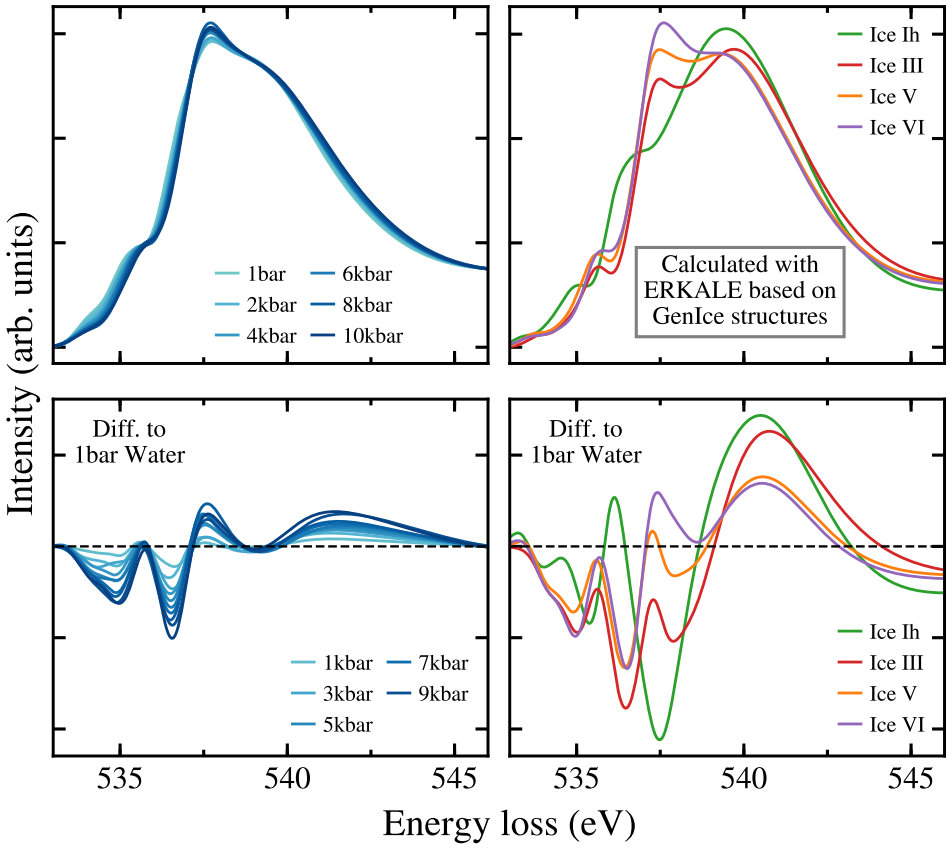

Figure 5.13: (Top, left) XRS spectra calculated with ERKALE in a pressure range from 1 bar to 10 kbar based on the generated trajectory of the AiMD simulation together with XRS spectra (top, right) of ice Ih, ice III, ice V and ice VI calculated with ERKALE based on structure generated with GenIce [230]. (Bottom, left) The corresponding difference spectra of pressurised liquid water and (bottom, right) the three ice phases with respect to the calculated spectrum of liquid water at 1 bar.

liquid water are similar to structural differences induced by the phase transition from ice III to ice V and ice V to ice VI, respectively.
Overall, the calculated spectra show very similar spectral trends and differences between the three ice phases and the pressurised liquid water as the experimentally recorded spectra, further confirming the results derived from the measured spectra. This confirmation of experimental trends by calculating spectra with ERKALE is particularly interesting because the theoretical spectra are all determined with the same procedure, unlike the experimental data, which, including this work, were obtained from three different studies.

5.3.3 Influence of TMAO on the pressure response of the water Structure

In the following, the results of first XRS test experiments on a 1 M aqueous trimethylamine N-oxide (TMAO) solution are presented and discussed. TMAO is a zwitterionic molecule which consists of three hydrophobic methyl (CH_3) groups with a hydrophilic N-O unit on the opposite site. It is found in the bodies of deep-sea fish, where it is assumed to stabilize proteins against the high hydrostatic pressures at great depths [201]. For instance, a correlation is found between TMAO concentrations in the bodies of deep-sea fish and the pressure conditions in their natural habitat [231, 232]. Although its protein-stabilizing effect against perturbation by high pressure conditions is well studied, the underlying mechanism is not fully understood [16, 233]. As a zwitterionic molecule, TMAO interacts strongly with the surrounding water molecules, which is thought to be an important factor in its protein-stabilizing capabilities [202]. Hence, the test experiments performed focus on how the addition of TMAO to water affects the response of the water structure to an increase in pressure up to 5.3 kbar.
The XRS spectrum of the aqueous 1 M TMAO solution at 500 bar is shown in the left plot of Figure 5.14, in comparison with the spectrum of pure water at the same pressure. Due to the shorter acquisition time, the data quality is significantly lower compared to pure water. The spectrum of the aqueous TMAO solution exhibits a more pronounced pre-edge feature than the spectrum of pure water, whereas the intensity of the main-edge seems to be slightly reduced. A previous XRS study on aqueous TMAO solutions up to a concentration of 4 M TMAO revealed overall similar spectral changes due to the addition of TMAO but with less pronounced changes in the pre-edge at similar concentrations [234]. This might be related to statistical uncertainties in the spectrum shown in Figure 5.14, as the earlier study achieved a significantly better signal to noise ratio. This is partly due to the sample system, as a flow cell was used instead of a high pressure cell with a highly absorbing sample environment as in this thesis. The effect of increasing pressure is shown in the middle plot of Figure 5.14 in comparison with pure water at 500 bar and 5250 bar. The pre-edge looses intensity when the pressure is increased, whereas the main-edge slightly gains spectral weight. Although the intensity of the main-edge feature at 5300 bar between 537.5 eV and 540 eV is less pronounced compared to water at a similar pressure, it is slightly increased in the range from 540 eV to 541.5 eV. It is worth noting that another XRS study at ambient pressure reported an increase in the spectral range between 540 eV and 541.5 eV with respect to pure water, but at a higher TMAO concentration of 2 M [235].
Since TMAO contains an oxygen atom, the spectral shape is changed not only by

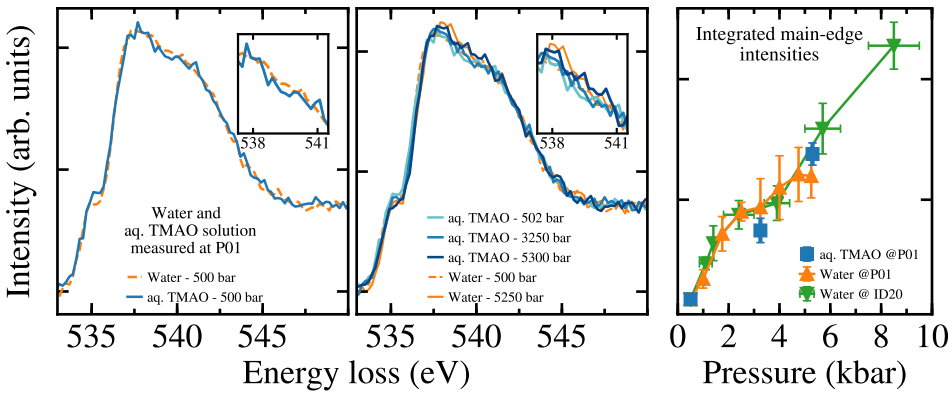

Figure 5.14: (left) The spectrum of a 1 M aqueous TMAO solution (blue) and pure water (orange, dashed), both at 500 bar. (Middle) XRS spectra of a 1 M aqueous TMAO solution (blue) at 502 bar, 3250 bar and 5300 bar in comparison with pure water (orange) at 500 bar and 5250 bar. (Right) The integrated main-edge intensities of the spectra of 1 M aqueous TMAO solution (blue) and pure water measured at beamline P01 (orange) and ID20 (green, see section 5.3.1) as a function of pressure. The integrated values for the TMAO solution are shifted along the y-axis by a constant to allow a relative comparison of the pressure evolution (see text for details).

the influence of TMAO on the water structure, but also due to the contribution of the intramolecular oxygen. Therefore, a straight-forward interpretation of the spectral differences to water according to section 2.2.2 is not feasible. However, a concentration dependent XRS study of aqueous TMAO solutions has been able to decompose the oxygen K-edge spectrum of TMAO into three contributions by performing a non-negative matrix factorization [234]. One component is the spectra of pure water and the other is the spectrum of the unsolved solute i.e. TMAO powder. The third component is interpreted as a representative of the spectral changes due to the influence of the TMAO molecules on the water structure.
The oxygen K-edge onset of the spectrum of TMAO powder is shifted to smaller energy loss values and exhibits a large intensity in the pre-edge region, whereas the intensity is reduced in the main- and post-edge region. The pre-edge intensity of the free component spectrum is comparable with pure water, whereas the main-edge intensity is decreased in comparison but with a slight increase in the 540 eV to 541.5 eV range. Comparing these components with the pressure-evolution of the measured spectral intensities might indicate that the contribution from the pure TMAO component is decreasing with pressure as the pre-edge intensity is reduced. Furthermore, the spectral changes could indicate that the contribution of the free component spectrum, i.e. the changes due to the TMAO-water interaction,

becomes larger as the increase of main-edge intensity is damped at higher pressures compared to pure water, while the spectral region between 540 eV to 541.5 eV is more pronounced. This might indicate that at higher pressures a larger fraction of the water molecules is affected by the TMAO molecules, which is likely associated with larger structural deviations in the water network of the solution.
In order to quantify the pressure-dependent changes, the intensity of the main-edge was integrated as in the previous section and the resulting values are plotted as a function of pressure in the right plot of Figure 5.14 together with the respective values for pure water measured at P01 and ID20. For a comparison of the relative changes with pure water, the integrated values of the aqueous TMAO solution are shifted along the y-axis to match the integrated values of pure water. This shift is necessary because the contribution of the oxygen of the TMAO reduces the intensity of the main-edge. Without the shift, the value of the TMAO solution at 500 bar is around 2.2 % smaller than the respective value for pure water (ID20) with the largest value at 8500 bar as reference being about 5.3 % larger than the value of pure water at 500 bar. It is difficult to draw an unambiguous conclusion from the three data points obtained for the aqueous TMAO solution with merely one point in the critical region between 2 kbar and 4 kbar, where a change in the slope in the pressure evolution of the main edge in liquid water was previously determined. The integrated value at the highest pressure exhibits a good agreement with pure water, while a slight deviation between water and the aqueous TMAO solution is observed for the value at 3250 bar. This deviation might be an indication of the influence of the TMAO on the pressure-dependent changes of the water structure, although it should be noted that the integrated value is still within the error bar of the value determined from the spectra recorded at beamline P01.

5.4 Summary and conclusion

This chapter focused on the evolution of the microscopic structure of water with increasing pressure. Two experiments were performed on pressurised liquid water with two different pressure set-ups at beamline P01 and beamline ID20 reaching pressures of 5.25 kbar and 8.5 kbar, respectively. For the first experiment at beamline P01, a hydrostatic high pressure cell was employed, allowing for high precision pressure adjustment, while for the second experiment at beamline ID20, a membrane diamond anvil cell with a large panoramic opening was used, taking advantage of the large XRS spectrometer. The XRS spectra recorded with both experimental set-ups show a remarkable qualitative and quantitative agreement, which underlines the good reproducibility.

The measured XRS spectra showed hardly any changes in the pre- and post-edge region with increasing pressure but a pronounced increase in main-edge intensity. A qualitative analysis of these spectral changes revealed that the tetrahedral structure as well as the number of hydrogen bonds in the system are rather unchanged with increasing pressure but that non-hydrogen bonded water molecules approach the first shell. Furthermore, XRS spectra calculated with ERKALE based on structures taken from the trajectory of a recent AiMD study exhibit a good agreement with the experimental data, justifying to extract and analyse detailed structural information from the trajectory. This way, the number of hydrogen bonded and non-hydrogen bonded molecules in the first shell were evaluated as well as two parameters to determine the deviation from tetrahedrality in terms of angle and distance according to section 2.2.1. The determined parameters confirmed the qualitative analysis of the spectral features. A quantitative analysis of the spectral changes by integrating the main-edge intensity, together with the theoretically determined ratio of hydrogen to non-hydrogen bonded molecules in the first shell revealed a continuous pressure evolution, thus excluding a sudden collapse of the second shell or a breaking of hydrogen bonds as assumed in an earlier study [69]. However, in accordance with the measured quantity of earlier studies, the integrated main-edge intensities as well as the extracted hydrogen bond ratio exhibit a change of slope at around 3 kbar which might indicate a continuous transition from LDW to HDW. Although the theory completely confirms the experimental findings and provides further detailed information, it is noteworthy that the three main conclusions can be derived solely from the experimental data. These conclusions are that the hydrogen bonds in liquid water are stable, even at high pressure with a simultaneous approach of the non-hydrogen bonded molecules to the first shell, as well as a non-linear evolution of the main-edge integral with increasing density and pressure, respectively.
In addition, the analysis scheme from Saitta *et al.*'s classical MD simulation study on pressurised water up to 10 kbar was applied to the AiMD trajectory. Justified by the good agreement between the experimental and theoretical spectra, the results based on the AiMD trajectory confirm not only the experimental findings but also the conclusions of the previous MD study. Moreover, the analysis gave further insight into how the non-hydrogen bonded molecules approach the first shell.
The experimental and theoretical spectra were further compared with measured and calculated spectra of three different ice phases to investigate structural differences and similarities and to approach the question of whether the local structure of a crystalline ice phase persists to some extent into the liquid phase. For the comparison with experimental spectra, the spectra of the ice phases Ih, VI and III were taken from previous studies. The theoretical spectra of pressurised water, were compared with spectra of the three ice phases and ice V as calculated with ERKALE based on structures generated with GenIce. It was found that the spectral differences

between liquid water at ambient conditions and at 8.5 kbar is best described by the difference of the spectra of ice VI and ice III, indicating that the structural changes in water due to increased pressure are similar to structural differences between ice III and ice VI. The increasing similarity between pressurised water and ice VI was interpreted as an indication that a local interpenetrating water network might form in liquid water at high pressure, comparable to the structure of ice VI, but lacking a long-range order, unlike the ice phase. The calculated spectra of pressurised water and the ice phases exhibited the same similarities as the experimental ones at ambient and high pressure, thus further confirming the results. Extending the theoretical analysis with the additional calculated spectrum of ice V, which lies between ice III and ice VI in terms of its main edge intensity, suggests that a comparison of the experimental spectra of further ice phases such as ice V, measured over a wide energy loss range for an optimal normalization, would provide further insight into the structural similarities and differences of pressurised liquid water and the various ice phases [89].
Furthermore, first XRS test experiments on a 1 M aqueous TMAO solutions at three different pressure conditions up to 5.3 kbar were performed which might indicate that the spectral contribution from the fingerprint of the TMAO-water interaction increases with rising pressure. Hence, pointing towards an increasing influence of TMAO on the water structure at higher pressures. However, spectra with higher data quality measured at several pressure points are necessary for a conclusive analysis. In addition, varying the TMAO concentrations could be helpful to tune the fraction of water molecules affected by TMAO and further dissect the effect on water structure.

6 Time and space evolution of electron density disturbances in water

6.1 Introduction

Water is one of the key components of life on this planet. Its unique properties and anomalies make it highly relevant for many processes in physics, biology and chemistry. Studying the structure and dynamics of water at the molecular level is crucial to a fundamental understanding of many of these processes [33, 41, 66, 236, 237]. Thus, many studies exploited experimental techniques such as X-ray absorption spectroscopy, X-ray/neutron scattering, vibrational echo correlation spectroscopy and terahertz spectroscopy, to name but a few, aiming to enhance the knowledge of the structure or dynamics of liquid water [41, 42, 238, 239]. Most of these techniques are focused to probe either the structural or dynamic properties of water. This impressive catalogue of experimental methods was extended in 2004 as Abbamonte *et al.* introduced a technique which utilizes inelastic X-ray scattering to image the dynamics of an electron density disturbance in liquid water simultaneously in both time and space [53, 54]. In their pioneering study, they measured the dynamic structure factor $S(q, \omega)$ of water in an energy loss and momentum transfer range up to 100 eV and 4.95 Å^{-1}, respectively. Afterwards, the full density response function was reconstructed from $S(q, \omega)$ to study electron density disturbance as induced by the X-ray photons in time and space with a resolution of 41.3 as and 1.27 Å. This technique was further utilized by several studies, which focused on recording IXS spectra in the milli-electronvolt range with high energy resolution, thus enabling to study the dynamics of water in the femto- to picosecond range [240–243]. In addition to water, the technique has also been successfully used to study, for example, the time-dependent structure of excitons in lithium fluoride crystals [244].
Although groundbreaking work was carried out in Abbamonte's study, the data treatment scheme still had some deficiencies, such as the necessary extensive use of data extrapolation due to an insufficient energy loss and momentum transfer range. Hence, this chapter focusses not only on investigating electron dynamics in water on an attosecond time scale with atomic spatial resolution but also aims to establish

a data treatment procedure for future studies which is consistently applicable over a large energy loss and momentum transfer range using the data from Abbamonte *et al.* as benchmark. In addition, hydrothermal fluids at 165 °C and 250 °C have been studied due to their critical importance in numerous chemical technologies (e.g., recycling [133, 134] and fabrication of materials [136]) and geochemical processes related to heat and mass transport in the Earth's crust and mantle [34, 137], which have been discussed in more detail in chapter 4. With respect to geochemical processes of ore formation, e.g. of lead-zinc deposits, sodium chloride is a highly relevant component of hydrothermal ore-forming fluids, with an estimated concentration of up to 30 wt% [26].
In this thesis, IXS was used to investigate the electron dynamics in water and 2 M aqueous sodium chloride solution at various temperature conditions between 20 °C and 250 °C, utilizing a scan range of up to 3 keV and 18.7 $Å^{-1}$ reaching a temporal and spatial resolution below 0.7 as and 0.35 Å, respectively.

6.2 Experimental set-up

The experiments were performed at the Taiwan inelastic X-ray scatting beamline BL12XU at SPring-8 (**S**uper **P**hoton **ring-8** GeV) with a ring current of 100 mA [245–247]. A schematic layout of the beamline is depicted in Figure 6.1. An undulator source (third harmonics) was used to generate the X-ray photons, which were monochromated with a double crystal Si(111) monochromator (DCM) with a listed energy resolution of $\Delta E \approx 3$ eV at 19.5 keV, which is close to the energy resolution of approximately 3 eV achieved during the experiments. The channel-cut high-resolution Si(220) monochromator, which is shown in Figure 6.1 (a) after the DCM, is capable of improving the energy resolution to $\Delta E \approx 0.8$ eV, but at the cost of one-fifth of the photon flux. Since the X-ray intensity is more significant for the performed experiments than the energy resolution, only the DCM was used. A diamond phase retardation plate (PRP) was inserted behind the monochromator at scattering angles above 62° to significantly increase the measured intensity. This is necessary because the X-rays are linearly polarised in the same horizontal plane in which the detector measures the scattered photons, thus reducing the measured intensity by a factor of $\cos^2\phi$ according to the Thomson differential scattering cross-section [111]. Afterwards, the X-ray photons were focused with a platinum-coated toroidal focusing mirror (FM) to a size of 80 µm × 120 µm (v x h), resulting in a flux of about $5 \cdot 10^{12} \cdot \text{photons} \cdot \text{s}^{-1}$ [247]. A Kirkpatrick–Baez (KB) mirror in front of the sample was used to further focus the X-ray beam onto the sample with a final spot size of 30 µm × 30 µm. The background scatter of the KB mirror was reduced by

using a pinhole mounted at the exit. Between the KB mirror and the sample, a PIN diode was used to measure the air scattering in order to obtain a decent normalization signal proportional to the intensity of the incident X-ray beam. The inelastically scattered X-ray photons were measured using a Si(660) cylindrically bent analyser crystal in combination with a scintillator detector consisting of a 3mm-thick NaI(Tl) crystal. As mentioned above, the analyser crystal and the detector were mounted in the horizontal plane on a rotatable arm at a distance of 1.1 m from the sample, with the Rowland circle vertically oriented [248]. The set-up, shown in Figure 6.1(b), makes it possible to measure the scattered X-ray photons as a function of energy.
In this thesis, two separate experiments were carried out on BL12XU with improvements being made to the custom-made sample cell used, which was designed by Dr. Nozomu Hiraoka. A schematic depiction of the sample cell is shown in Figure 6.2 (a). The cell consists of a hollow aluminium cylinder with a thinner and a thicker end. The cylinder has an inner radius of 10 mm, which therefore corresponds to the thickness of the loaded sample. In order to minimize the absorption in the sample environment, the X-ray beam penetrates the sample at the thinner end, which has a

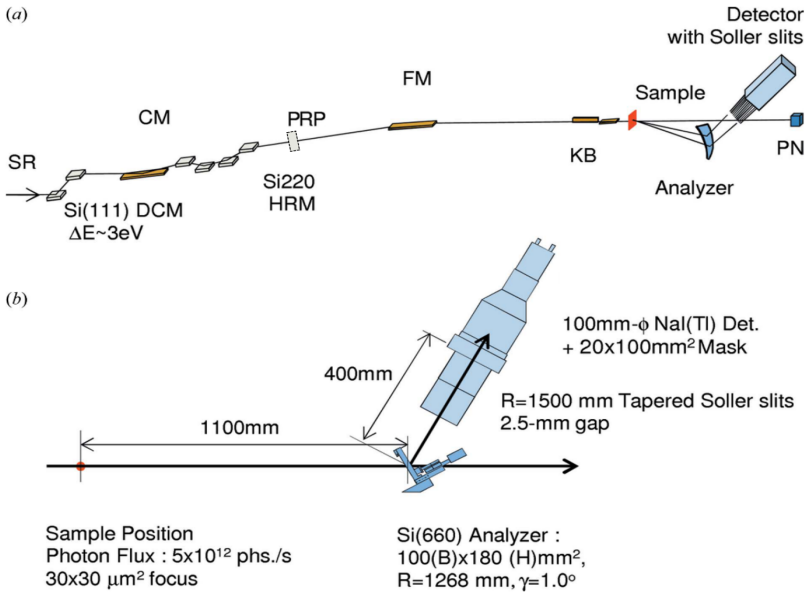

Figure 6.1: (a) A schematic depiction of the beamline BL12XU layout with the following X-ray optics: DCM (double-crystal monochromator), CM (collimating mirror), HRM (channel-cut high-resolution monochromator), FM (focusing mirror), KB (Kirkpatrick– Baez mirror), PN (PIN diode), PRP (phase retardation plate). SR at the beginning stands for synchrotron radiation. (b) Sketch of the used spectrometer consisting of a cylindrically bent Si(660) analyser crystal and a scintillator detector. The image is taken and modified from reference [247]

thickness of 400 µm. The thicker end is used to attach the sample cell to an external tube connected to a pressure pump to adjust the pressure during the experiment. The temperature in the cell is adjusted with a heating wire wrapped around the sample cell. A thread in the bottom of the sample cell (not shown here) allows to attach a thermocouple close to the sample to determine the temperature during the measurements. For the second experiment, an additional collimator and beam stop made of molybdenum was constructed by Dr. Nozomu Hiraoka and inserted into the sample cell. The modification significantly reduced indirect scattering in the vicinity of the sample environment and, in particular, the additional molybdenum beam stop inside the cell prevented the scattering of the incident X-ray beam by the rear aluminium cell wall, one of the main contributions of the measured background. A comparison of the background signal of the empty aluminium sample cell with and without inserted collimator and beamstop is shown in the next section (see Figure 6.5). The sample cell is enclosed in a second aluminium cylinder which is attached to a vacuum pump. This set-up is shown in Figure 6.2 (b) and additionally reduces the detected air scattering.
In the first conducted experiment, ultra pure water ($R > 18\,\mathrm{M\Omega}$) was measured at room temperature and at 165 °C with an incident X-ray energy of 19.42 keV. For the second experiment, an energy of 19.98 keV was used to investigate water of the same purity at an elevated temperature of 250 °C and a 2 M aqueous sodium chloride solution at a temperature of 20 °C and 90 °C. For the investigation of pure

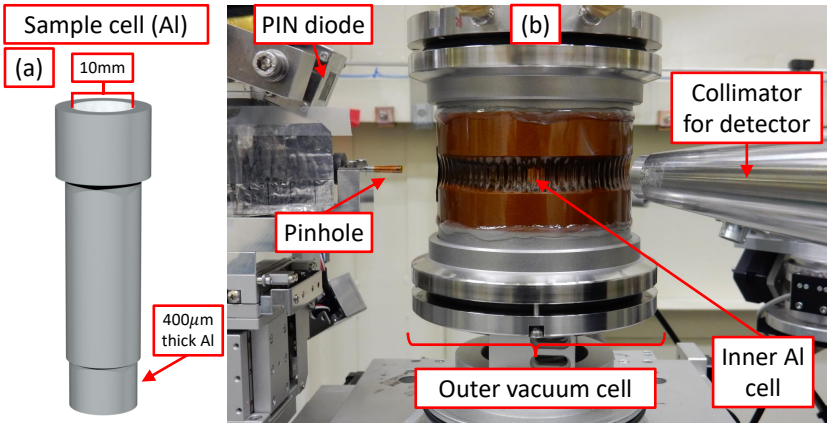

Figure 6.2: (a) 3D-model of the used aluminium sample cell, the lower end is thinner to reduce the amount of X-rays absorbed by the sample cell. (b) Photography of the used experimental set-up with the outer vacuum cell, the PIN diode used to monitor the X-ray intensity, the pinhole at the exit of the KB-mirror and the collimator tube 1.1 m in front of the detector to further reduce the background scattering.

water at elevated temperatures, the pressure was first increased to prevent the transition to the gas phase, whereas the pressure was readjusted to ensure that it did not exceed 75 bar after reaching the final temperature. Since the pressure pump could not be contaminated with aqueous salt solutions and an elevated pressure was not needed to measure the aqueous NaCl solution 20 °C and 90 °C, the salt solutions were filled into capillaries with a diameter of 5 mm, which were sealed and subsequently heated with a simple custom-made cylindrical copper cell (not shown here). In order to heat the salt solution, the sample cell was attached to a heat plate at the bottom and filled with oil for optimal heat transfer without vaporization. The experimental conditions for each set of recorded IXS spectra are listed in Table 6.1.

Sample	°C	g/cm^3	bar	Sample	°C	g/cm^3
H_2O	20	0.99	1	H_2O + NaCl	20	1.075
H_2O	165	0.90	40	H_2O + NaCl	90	-
H_2O	250	0.80	64			

Table 6.1: The experimental conditions of pure water and the 2 M aqueous sodium chloride solution (H_2O + NaCl) for each set of recorded IXS spectra. The densities are rounded to the second decimal place. The density of the salt solution at 90 °C wast not determined and is therefore not listed.

A q-range sufficient for the following analysis was obtained by recording spectra at up to 60 different scattering angles in a range from 2° to 145°. Since the relationship between the scattering angle and the corresponding momentum transfer is not linear but is expressed by $\sin(2\theta/2)$, the step size between two angles was increased at higher angles. This procedure resulted in a final q-range from $(0.34 \pm 0.03)\,\text{Å}^{-1}$ to $(18.77 \pm 0.03)\,\text{Å}^{-1}$ with a maximal increment of $(0.38 \pm 0.03)\,\text{Å}^{-1}$. For the measurements of the aqueous sodium chloride solution, the maximum q-value was reduced to $(15.2 \pm 0.3)\,\text{Å}^{-1}$ due to time constraints, with a maximum step size of $(0.41 \pm 0.03)\,\text{Å}^{-1}$. In terms of energy, the scan range was chosen according to the energy position of the observable spectral features covering the valence and core electron excitations from the plasmon regime to Compton scattering. For smaller scattering angles up to 30°, the spectra were recorded starting from an energy loss value of 10 eV up to 1010 eV. Between 30° and 122° the scan range was increased to 2010 eV and for even higher scattering angles, the scan range was further increased to 2810 eV. Furthermore, the elastic line was measured from an energy loss value of −20 eV to 20 eV after each scan to verify any energy shift and to subtract its tail from the measured spectra in the following data treatment procedure. In order to subtract the background signal caused by the aluminium sample holder, the

same measurement procedure was performed for the empty sample cell. Since the background signal of the empty capillary was almost indistinguishable from the noise of the dark measurement, it is not required in the further data treatment and was therefore not measured.

6.3 Data treatment

This section gives a detailed outline of the data treatment procedure of the recorded inelastic X-ray scattering spectra exemplified by the room temperature measurements. Recent literatures on IXS experiments, which utilize the dynamic structure factor to obtain information on space and time dynamics, are focused on rather small momentum transfer and/or low energy loss values [53, 240, 243, 244, 249]. Therefore, one aim of this thesis is to establish a consistent data treatment procedure that is suitable for a large momentum transfer range and for energy loss values up to several kilo-electronvolt. This enables the investigation of electron density disturbance on the attosecond and sub-Ångstrom time and space scale, respectively. Some of the general key concepts are taken from Abbamonte *et al.*'s [53] first introduction of this experimental technique and are further elaborated to be suitable for a wider scan range in terms of energy and momentum transfer. In summary, the goal of this data treatment procedure is to subtract as much background contribution as accurate from the measured signal and to extrapolate the resulting $S(q, \omega)$ for the calculation of the response function as well as the following Fourier transform, as explained in section 3.1.3. In this context, any contribution that is not part of the dynamic structure factor (DSF) of the sample is considered as background. Since a large part of the measured signal can be assigned to the Compton scattering regime, several data treatment steps are performed accordingly [250].
In a first step, the recorded spectra are normalized with respect to the intensity of the incident X-ray beam and several correction terms are applied. One of the correction terms is the energy dependent reflectivity curve of the used analyser crystal, which is provided by the beamline scientist Dr. Nozomu Hiraoka. In order to subtract the empty cell background from each sample and compare the different samples on a suitable intensity scale, a correction term is applied that takes into account the different absorption of each sample. The correction term is calculated according to Beer-Lambert's law. Since the absorption process is energy-dependent, the absorption from the sample environment as well as the air in the beam path are also taken into account. The last term considers relativistic cross section correction. The importance of such correction for the Compton scattering regime has been

extensively investigated [251–253]. According to P. Holm [254], the relativistic cross section correction is calculated by

$$C_{\gamma-corr} = \frac{R_1}{R_2} + \frac{R_2}{R_1} - 2\sin^2(2\theta)\cos^2(\beta) \tag{6.1}$$

with β as the angle between the scattering plane and the polarization vector of the incident beam, which is zero for the experiments performed in this thesis. The two factors are described by the formulas

$$R_1 = \hbar\omega_1 \left(m_e c^2 - (\omega_1 - \omega_2 \cos(2\theta)) \frac{p_z}{\hbar q} \right) \tag{6.2}$$

$$R_2 = R_1 - \hbar^2 \omega_1 \omega_2 (1 - \cos(2\theta)). \tag{6.3}$$

As described in the theory section, 2θ denotes the scattering angle, while $\hbar\omega_1$ and $\hbar\omega_2$ are the energy of the incident and scattered X-ray beam, respectively. By choosing $\boldsymbol{q}$ to point in the direction of z, p_z is defined with

$$p_z = \frac{m_e \omega}{q} - \frac{\hbar q}{2} \approx m_e c \left(\frac{\omega_1 - \omega_2 - (\hbar\omega_1\omega_2/m_e)(1 - \cos(\theta)))}{\sqrt{\omega_1^2 + \omega_2^2 - 2\omega_1\omega_2\cos(\theta)}} \right), \tag{6.4}$$

which is used several times in the following data treatment procedure. The three correction terms are plotted in Figure 6.3 as a function of the scanned energy and normalized to their value at the lowest energy to better compare their relative influence. The final effect of the combined correction terms on the spectra is depicted in Figure 6.4, where two spectra are shown measured at three different q values each before and after applying the correction terms. It should be noted,

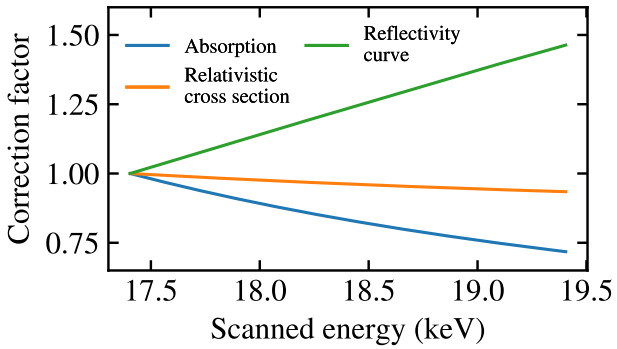

Figure 6.3: The three different applied correction terms plotted as a function of the scanned energy. The correction terms are normalized to their value at the lowest energy to compare their relative impact on the spectra.

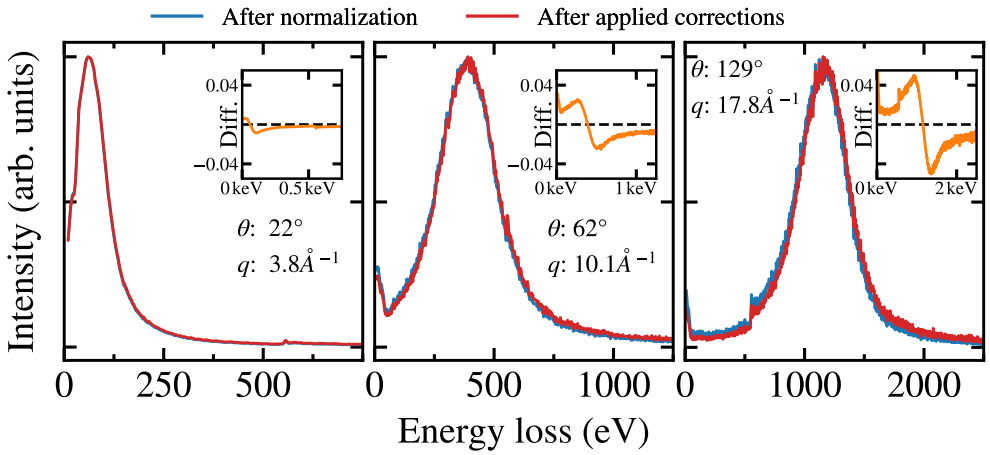

Figure 6.4: The spectrum before and after applying the correction terms at three different q values (see text for details). For a better comparison, both spectra at each q-value are divided by their maximum value. The increase in intensity at low energy loss values is signal from the elastic line, which is subtracted in a later data processing step. The inset plot shows the difference of both spectra and emphasises the change of the intensity ratio between low and high energy values.

that in the following elaboration of the data treatment procedure, the spectra are plotted with arbitrary units and therefore a y-axis is omitted. By normalizing the spectra to their maximum, it becomes apparent that the relative changes are most pronounced at higher energy loss values and that the correction terms change the intensity ratio between low and high energy values.
In a second step, the background from the empty cell as well as the contribution from the elastic line are subtracted. However, before describing this procedure in more detail, a comparison of the background measured with and without the previously described collimator is given in Figure 6.5, as the following subtraction is shown only for the room temperature measurements. This comparison underlines how the background contribution can be drastically reduced by this experimental improvement.
In addition to the signal of the sample cell, the tail of the elastic line contributes significantly to the undesired background, especially in the low-energy part of the measured spectrum. Since it is not possible to distinguish between the overlapping signal of the elastic line and the low-energy spectral contributions, its tail measured for negative energy loss values is mirrored to the positive side. This tail is then fitted and extrapolated with a suitable fit function, which is eventually subtracted from the measured data. For most elastic lines, a Lorentzian function is fitted, which is set to zero for energy values larger than 180 eV to prevent any unphysical

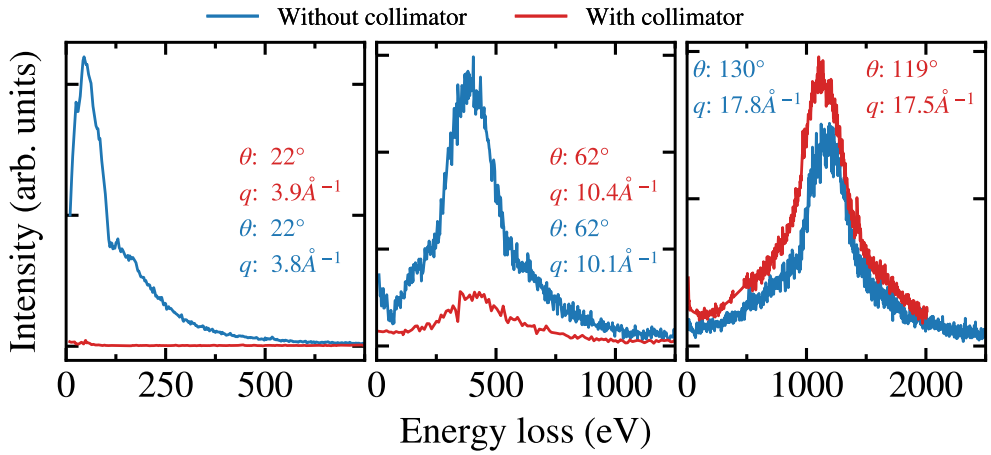

Figure 6.5: The background of the empty aluminium cell measured with (blue) and without (red) the collimator described in section 6.2. All spectra are shown after applying the absorption correction, resulting in a larger background of the aluminium cell with collimator in the right diagram, since the cell used here is 25 % thicker.

offset. If the use of a Lorentzian function does not yield a suitable fitting result, a combination of three or six Gaussian functions is used, not to adequately describe the elastic line but to obtain a decent approximation of its outgoing tail. However, this is necessary for less then 10 % of the recorded spectra and, moreover, the choice of the function hardly affects the results. A comparison of the spectra before and after the background subtraction is shown in Figure 6.6 together with the signal of the empty sample holder, the mirrored elastic line and the corresponding fit result. Another undesired component in the recorded spectra originates from multiple scattering processes, which can account for up to 30 % of the recorded intensity with more typical values around 10 % [250]. Although the proportion of multiple scattering was even lower in the data recorded for this thesis, it is nevertheless not negligible. One way to reduce the relative amount of multiple scattering is to use thinner samples, an approach not suitable for this kind of experiments. Another established method is to simulate the contribution of multiple scattering with Monte Carlo methods [255], which can subsequently be subtracted from the obtained spectra [256–259]. In this thesis, the Monte Carlo calculation is performed with the algorithm presented and elaborated in the paper of Fajardo *et al.* [259], which considers three types of interaction, namely Rayleigh and Compton scattering as well as photoelectric absorption. The tabled cross-sections of these interactions are used to calculate the probability of each process, while the scattering direction is sampled with the angular probability distribution derived from the differential

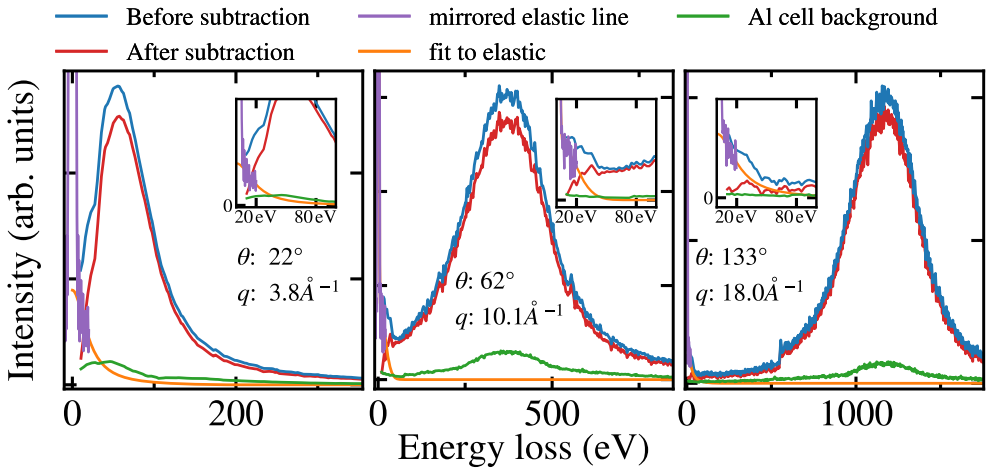

Figure 6.6: The spectra at three different q-values before (blue) and after (red) the background subtraction. The mirrored elastic line (purple) is depicted together with the corresponding fit (orange) and the background of the empty aluminium cell (green).

cross sections. Furthermore, the energy of the scattered X-ray photons is sampled by means of the double differential cross-section, which is proportional to the corresponding Compton profile $J(p_Z)$. By default, the algorithm employs tabulated free atom Compton profiles [260], but optionally a user provided Compton profile can be used. This can greatly improve the calculation of the multiple scattering, since the valence contribution in the tabulated Compton profiles of the free atoms is not well reproduced as it is too narrow. Hence, in this thesis, a Compton profile was calculated for each scattering angle, which was employed by the algorithm. In order to calculate suitable Compton profiles, the valence contribution at the highest angle was extracted by subtracting the scaled tabulated Compton profile of the core electrons from reference [260]. The subtraction of the core profile and the extracted valence contribution is shown in Figure 6.7 for the 20 °C and the 250 °C sample. The extracted profile at 250 °C exhibits a higher symmetry as can be seen in the inset plot. This is probably related to the additional collimator used inside the aluminium sample cell. However, even the extracted profile at 250 °C still exhibits some small degree of asymmetry as expected from previous studies [261]. After extraction, the valence contribution is convolved with a Gaussian function to improve the data quality for the multiple scattering calculation and is finally added to the accordingly scaled tabulated core contribution for each scattering angle. Since the Compton profile at the highest energy and momentum transfer, respectively, best satisfies the impulse approximation and thus exhibits the least

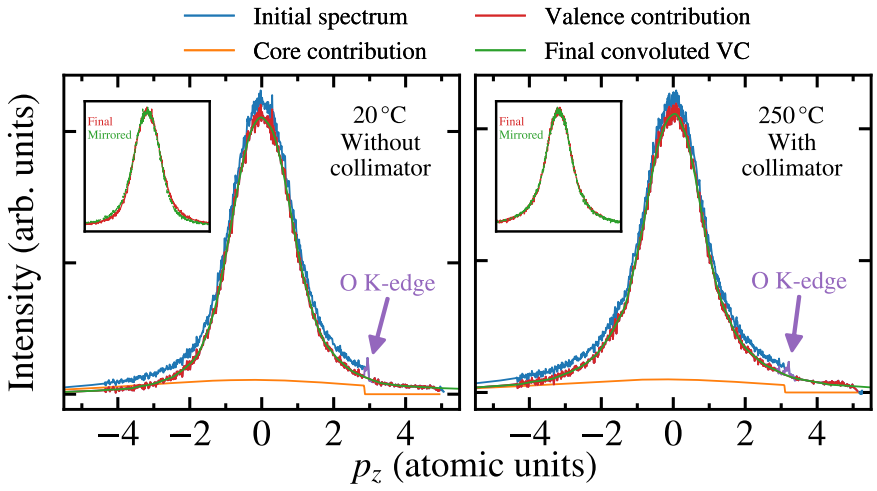

Figure 6.7: Depiction of the extraction of the Compton profile valence contribution by subtracting the scaled tabulated Compton profile of the core electrons from reference [260]. To emphasis the symmetry of the extracted profile, it is mirrored and compared in the inset plot.

asymmetry, calculating the Compton profile for each measured spectrum based on the extracted valence profile leads to a much better final result than using the measured spectra directly or the tabulated Compton profiles as input. The effect of the multiple scattering contribution on the spectra is shown in Figure 6.8, where

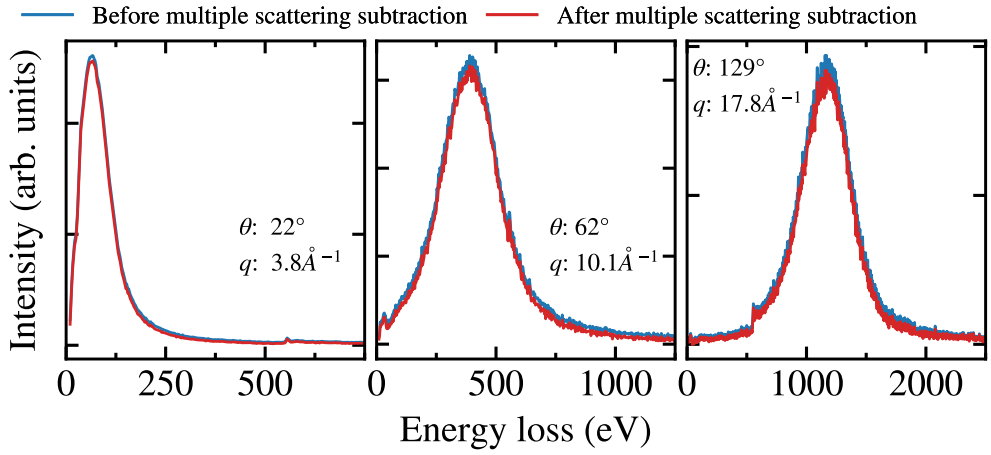

Figure 6.8: The spectrum before and after the subraction of the calculated multiple scattering contribution at three different q values.

the spectra before and after its subtraction are plotted. To calculate the multiple scattering contribution, a total of 10^9 X-ray interaction processes were sampled. In order to obtain the response function $\chi(q,\omega)$ using the Kramers-Kronig relation, the spectra are extrapolated to satisfy the integration limits according to the formula 3.19. Furthermore, a large energy loss range is required to apply the f-Sum rule as defined by

$$\int_0^\infty \omega \cdot S(q,\omega) d\omega = \frac{hq^2}{2m_e}, \tag{6.5}$$

to establish an absolute intensity scale [262]. Therefore, the extrapolation to higher energy loss values is a crucial part of the data treatment with high demands for consistency over the whole investigated momentum transfer range. Instead of fitting a function to the tail of each spectrum, a much higher degree of consistency is achieved by performing the extrapolation on the p_z-scale and using a spectrum measured over a wide p_z-range with a flat tapered tail at high negative p_z-values for the extrapolation of the other spectra. To be suitable for spectra with an even higher p_z-range at smaller q-values, only this so-called reference spectrum is extrapolated by using a scaled tabulated Compton profile. This way, all spectra are extrapolated in the p_z space without the use of an additional scaling factor, which further improves the consistency. To ensure a smooth transition between the high energy loss edge and the high energy loss tail of the reference spectrum a Pearson VII function is

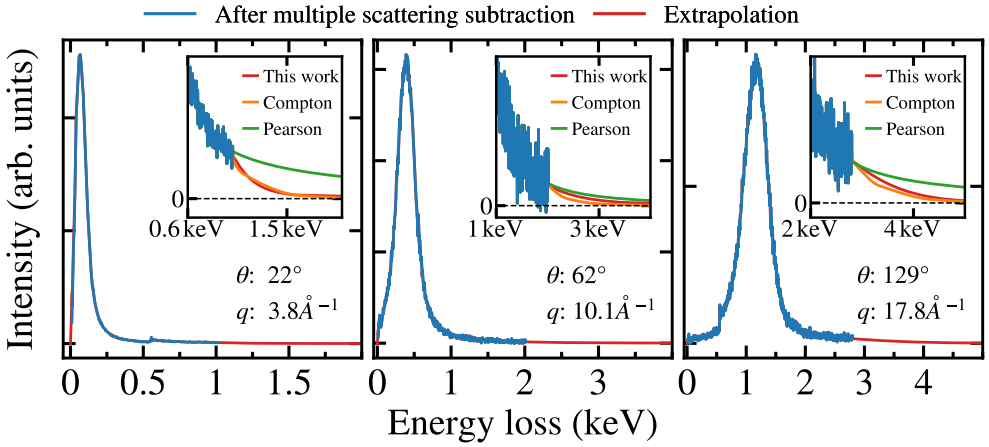

Figure 6.9: The extrapolation of three spectra at different q values. The inset plot shows a close-up comparison of different extrapolation schemes: 'This Work' is the method described in the main text, 'Compton' refers to the extrapolation with the use of scaled tabulated Compton profiles and 'Pearson' with a Pearson VII fit of the tail region of the spectrum.

fitted over a small overlapping p_z-range of approximately 3 Å^{-1} and then inserted. Besides the extrapolation at high energy values, a reasonable extension of the data to an energy loss value of 0 is also crucial. For the extrapolation at low energy loss values, the spectrum is point-symmetrically mirrored and fitted with a power function of third degree together over both, the positive and the new obtained negative site in a range from −50 eV to 50 eV. The obtained values of the power function between −20 eV and 20 eV are then inserted into the spectrum. The fit is additionally constrained to converge to zero for small energy loss values, according to the definition of an IXS spectrum. The extrapolated spectra are shown in Figure 6.9 for three different q-values, together with a close up of the tail of each spectrum showing a comparison of different extrapolating schemes. In order to emphasise the importance of a consistent extrapolation over the entire q range, Figure 6.10 shows the maximum value of each spectrum plotted against the respective scattering angle for the measurements at 20 °C and 165 °C after the spectrum has been extrapolated and the f-sum rule applied. In this figure, 'This work' refers to the previously

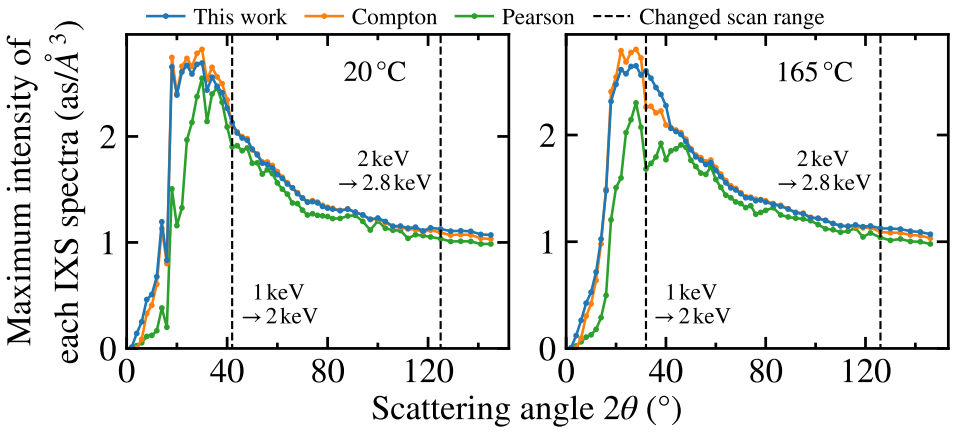

Figure 6.10: The maximum of each spectra after extrapolation with one of three different methods (see main text) plotted against the respective scattering angle for the measurements at 20 °C (left) and 165 °C (right).

described method, while 'Compton' uses scaled tabulated Compton profiles for the extrapolation and 'Pearson' a fit with a Pearson VII function to the tail of each spectrum. Both latter methods depend to some extent heavily on the recorded energy loss range as can be seen by the abrupt changes at the dashed lines and fail to produce a consistent envelope of the measured data with the same quality as the method finally used. Although the use of scaled Compton profiles still leads to acceptable results at 20 °C, this method is unable to adequately extrapolate the individual spectra over the entire q range for the measurements at 165 °C and

250 °C (the latter not shown here), with the deficiencies might be overcome by an overall extend of the scan range. This behaviour is also observed when using other functions to fit the tail of each spectrum, such as a Lorentzian or a Gaussian Function.
After extrapolating the spectra and applying the f-Sum rule, the imaginary part of the density response function is obtained with equation 3.18, while the Kramers-Kronig relation (equation 3.19) is used to calculate the missing real part. Both parts are plotted in Figure 6.11 exemplary at three different momentum transfer values. To calculate the integral in the Kramers-Kronig relation and the subsequent Fourier transformation, an equidistant energy and momentum transfer grid is required to deploy the numerical integration algorithm. Since an equidistant q-lattice is not readily accessible experimentally, one is achieved by linear interpolation of the obtained spectra at each energy value along q.
The density response function shown in Figure 6.11 was calculated using the spectra with core electron contribution. In order to investigate the influence of the core contribution to the density response function, $\chi(r,t)$ is additionally calculated after subtracting a scaled tabulated core Compton profile from each final spectra. This subtraction is performed analogously to the extraction of the valence Compton profile described previously and depicted in Figure 6.7.

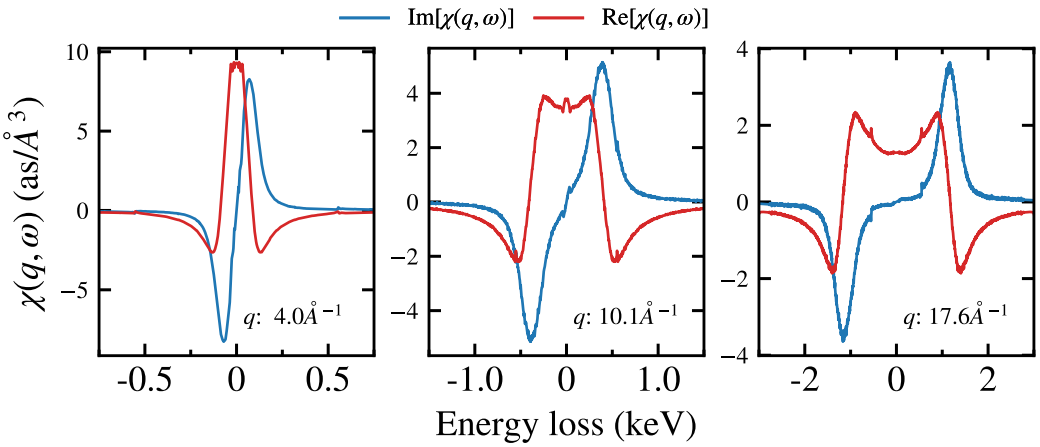

Figure 6.11: The real and imaginary part of the electron density response function at three different q-values. The imaginary part is calculated from equation 3.18 and the Kramers-Kronig relation in equation 3.19 is used to obtain the real part. The shown spectra are the result of the linear interpolation of the spectra along the q-axis to obtain an equidistant q-grid.

6.4 Analysis of the density response function

6.4.1 Qualitative analysis and comparison with previous work

One goal of this thesis is to expand on the work of Abbamonte *et al.* [53]. Therefore, the results of the qualitative analysis of the density response function are presented in the following and compared with the previous study. The imaginary part of the derived density response function $\mathrm{Im}[\chi(q,\omega)]$ over the whole measured q and energy loss range is shown in Figure 6.12 in a 3D colour plot for the water measurements at three different temperatures. Independent of the applied temperature, all measurement series exhibit a broad maximum at around 4.5 Å^{-1} and approximately 90 eV. With increasing momentum transfer value, the maximum gets broader and shifts to higher energy loss values. Furthermore, the increased temperature does not lead to a significant redistribution of spectral intensity. This becomes particularly evident in the inset plots of Figure 6.12, which show all measured spectra of the respective measurement series as a function of energy. In summary, the overall shape of the spectra is hardly affected by the increased temperatures as expected with the statistical accuracy achieved [263].
The resulting $\mathrm{Im}[\chi(q,\omega)]$ of the measurements on aqueous sodium chloride solutions at ambient and elevated temperature are depicted in the 3D colour plots in Figure 6.13 in comparison with the spectra of pure water at 20 °C. In order to com-

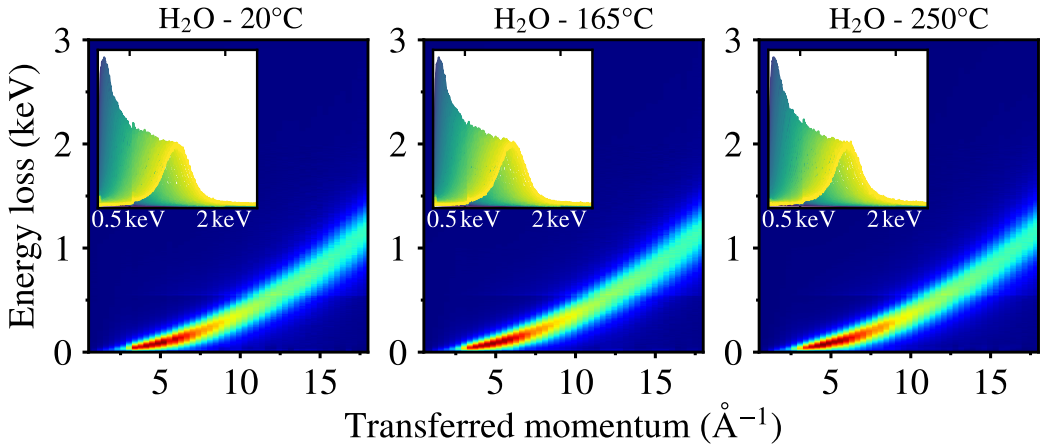

Figure 6.12: 3D colour plot of $\mathrm{Im}[\chi(q,\omega)]$ for pure water at 20 °C (left), 165 °C (middle) and 250 °C (right) as a function of transferred momentum (x-axis) and energy loss (y-axis). The inset plots show the corresponding spectra as a function of energy loss.

pare the spectra of pure water with those of the aqueous sodium chloride solutions, the spectra of pure water are interpolated onto the same q-grid that was used for the measurements of the salt solution. The qualitative comparison reveals hardly any spectral changes due to the addition of salts or the increase in temperature.

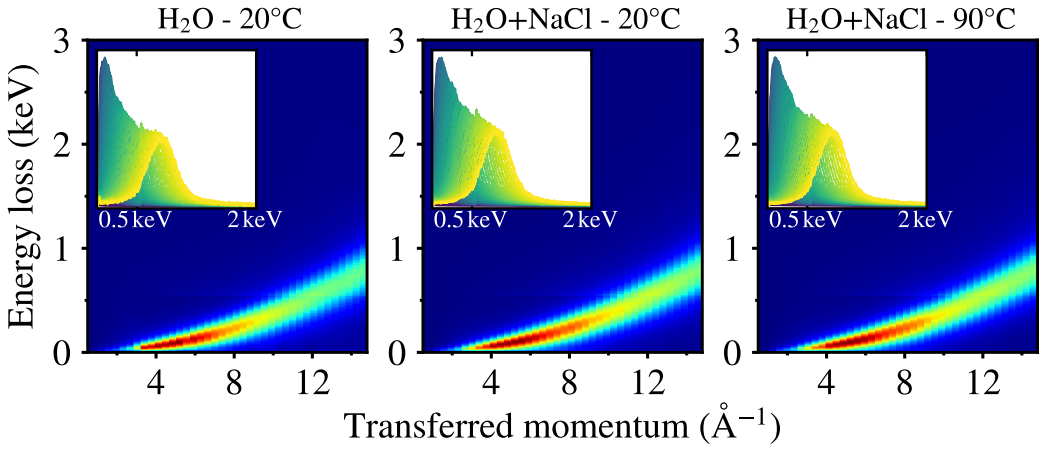

Figure 6.13: 3D colour plot of $\mathrm{Im}[\chi(q,\omega)]$ for pure water at 20 °C (left) and aqueous sodium chloride solution (H_2O+NaCl) at 20 °C (middle) and 90 °C (right) as a function of transferred momentum (x-axis) and energy loss (y-axis). The spectra of pure water were interpolated to match the q-grid of the NaCl solution. The inset plots show the corresponding spectra as a function of energy.

In the pioneering study of Abbamonte *et al.*, they measured $S(q,\omega)$ up to energy loss values of 100 eV and a momentum transfer of 4.95 Å^{-1} to extract $\mathrm{Im}[\chi(q,\omega)]$, therefore the comparison with the data in this paper is conducted on the same parameter range. The $\mathrm{Im}[\chi(q,\omega)]$ obtained in this work is shown on the left side of Figure 6.14 together with the $\mathrm{Im}[\chi(q,\omega)]$ from the Abbamonte *et al.* study [53] in the middle. There are noticeable differences between the density response function derived in this and the previous work, despite reproducing the same overall spectral shape for both investigated samples in Figure 6.13 and especially regardless of the sample cell used. The data from reference [53] exhibit a maximum around 2 Å^{-1}, which decreases rapidly with increasing energy loss and q values along the diagonal of the plot. The reasons for these discrepancies are difficult to discern, as they may be due to differences in the experimental set-ups or, more likely, to an additional data treatment step that was not mentioned in the paper. However, it is striking that the reported maximum of $\mathrm{Im}[\chi(q,\omega)]$ is congruent with the maximum of the static structure factor obtained by XRD measurements with respect to the q-value [264]. In order to verify whether an additional data treatment step using the static structure factor might be an explanation for the differences, the obtained data were multiplied

by the maximum of the respective elastic line at each q-step. The elastic line is described by $S(q,0)$ and is therefore proportional to the static structure factor. The resulting Im$[\chi(q,\omega)]$ is shown on the right side of Figure 6.14 and closer resembles the data from the previous work as a maximum around 2 Å^{-1} is observable which similarly decreases with increasing energy loss and momentum transfer values. The

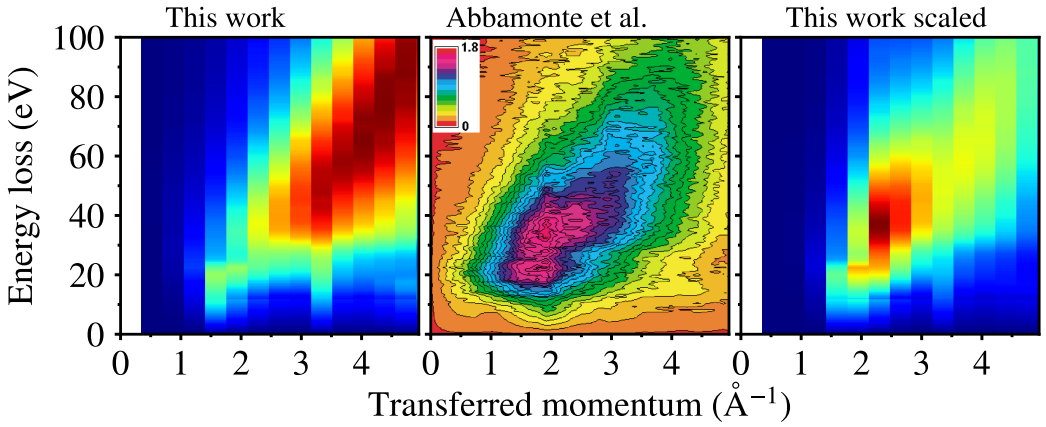

Figure 6.14: Comparison of the imaginary part of the derived density response function Im$[\chi(q,\omega)]$ with the data from Abbamonte *et al.* [53] on the respective momentum transfer and energy loss scale. Im$[\chi(q,\omega)]$ obtained in this work (left), next to the results of the work from Abbamonte *et al.* (middle) and the data of this work after scaling it with the measured static structure factor (right, see text for details).

improved overall agreement due to this procedure, might indicate that a similar scaling was performed in the previous work. However, as a different approach or explanation cannot be excluded and the physical reason for performing such scaling is not obvious, the further analysis is performed with the unscaled data. It should be mentioned that a similar scaling was also applied in a later study measuring phonons in liquid water by means of inelastic X-ray scattering [243]. Nevertheless, according to a recent study that has extensively verified its normalization scheme, the f-sum rule should be used for valence electrons [249].
After qualitatively analysing the density response function as a function of energy and momentum transfer, a Fourier transformation is now used to map the density response function in time and space and thus investigating the dynamics of the electron density disturbances directly at the atomic level. First, the real part of the density response function has to be retrieved with a Kramers-Kronig relation as described in the theory section of this thesis (see chapter 3.1.3). The real part is exemplary shown in in the previous section in Figure 6.11. The resulting time

and space increment is given by the reciprocal of the respective scan range with $\Delta t = 2\pi\hbar/3\,\mathrm{keV} \approx 0.69\,\mathrm{as}$[1] and $\Delta r = 2\pi/18.34\,\mathrm{Å}^{-1} \approx 0.34\,\mathrm{Å}$ applying for the water sample, while the space increment of the NaCl samples $\Delta r = 2\pi/14.4\,\mathrm{Å}^{-1} \approx 0.43\,\mathrm{Å}$ is coarser due to the smaller scan range. The resulting Fourier transform for the water sample at 20 °C, 165 °C and 250 °C is shown in Figure 6.15 to 6.17 at different time steps, i.e. in different time domains. The first Figure 6.15 depicts the evolution of the electron density disturbance right after the interaction with the X-ray beam in a time range from 0.7 as to 11 as, in which the most drastic changes occur. As shown

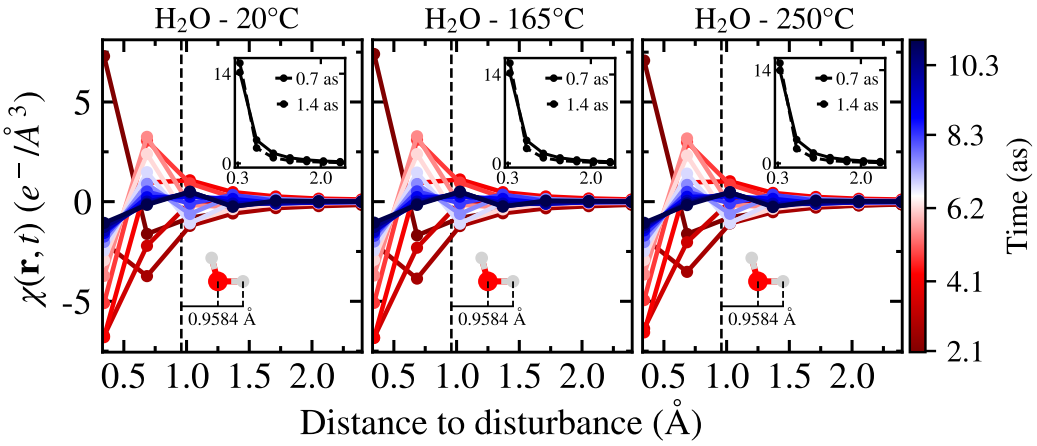

Figure 6.15: The density response function $\chi(r,t)$ as a function of the distance to the initial disturbance for the water sample at 20 °C (left), 165 °C (middle) and 250 °C (right). The evolution of the electron density disturbance is plotted at several different time steps for the first 11 as. The inset plot shows $\chi(r,t)$ in the first two time steps after the perturbation. The dashed black line marks the typical oxygen-hydrogen distance in a water molecule, shown here as size comparison [265].

in the inset plots of Figure 6.15, $\chi(r,t)$ exhibit a strong maximum right after the perturbation of the system, while affecting only a small area around the interaction point. Noteworthy, a positive perturbation was predicted in the previous study but only its negative recoil could be observed due to the small investigated energy range resulting in a time increment of only $\Delta t \approx 16\,\mathrm{as}$. The maximum starts to decline immediately and around 3 as the negative recoil is observable. The closest resolvable distance to the initial disturbance pulse remains negative much longer than it was positive before, since it becomes positive again between 30 as and 40 as as shown in

[1] Even tough the data was extrapolated to 5 keV, 3 keV were used for the time increment to avoid the use of even shorter time domains, which then might depend largely on the extrapolation procedure.

Figure 6.16. Interestingly, the second closest point at approximately 0.7 Å reaches negative values faster and also changes sign with a shorter period. At about 1 Å the periodic change in sign is similar to 0.7 Å but with less intensity. The majority of the intensity of $\chi(r,t)$ is distributed over the first 1.3 Å with respect to the distance to the initial disturbances. This implies that the effect on the electron density is highly local and hardly exceeds the size of a single water molecule in terms of its oxygen-hydrogen distance [265] (shown in Figure 6.15 to 6.17 as size comparison). In accordance with this observation is the temperature-dependent behaviour of

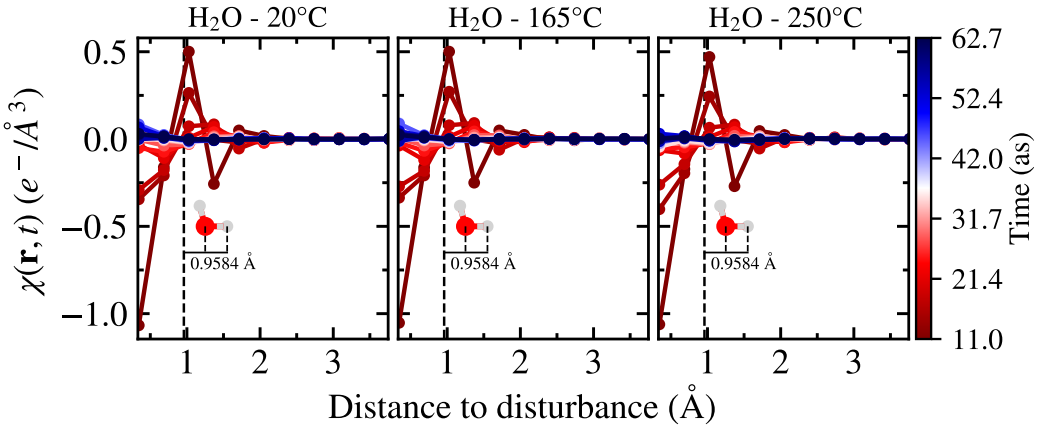

Figure 6.16: The density response function $\chi(r,t)$ as a function of the distance to the initial disturbance for the water sample at 20 °C (left), 165 °C (middle) and 250 °C (right). The evolution of the electron density disturbance is plotted at several different time steps between approximately 11 as and 63 as. The dashed black line marks the typical oxygen-hydrogen distance in a water molecule, shown here as size comparison [265].

$\chi(r,t)$ in this time domain, as no significant changes occur at any time step due to an increased temperature. Since the increase of temperature and decrease in density mainly causes alteration of the microscopic inter molecular structure of water [10, 90, 266], the electron density response of a sole water molecule is hardly affected by it. Hence, $\chi(r,t)$ is largely indistinguishable when compared at different temperatures. Moreover, this is in line with the previous qualitative investigation of the spectral changes of $\chi(q,\omega)$ in the beginning of this section, which revealed no significant redistribution of spectral intensity even at the highest temperature. The remaining intensity in the second time domain between 11 as and 63 as, as shown in Figure 6.16, is less than 4 % of the observed initial intensity. The reported observations in the first time domain regarding the temperature behaviour and the distances where the majority of the intensity of $\chi(r,t)$ is located are also valid for

this time domain. Thus, there is just minor intensity beyond 1.3 Å and no significant changes due to the increased temperatures. However, since the smallest time step in the Abbamonte *et al.* paper is 16.45 as, the Figure 6.16 facilitates an intriguing comparison with the previous study. In their first time step they describe the presence of a negative recoil at the source point which is surrounded by a positive build up at a distances of 1.3 Å [53]. This description is likewise applicable to the derived $\chi(r,t)$ in Figure 6.16 at the respective time step[2] with the exception that the position of the build up is shifted to a slightly lower value of 1.05 Å. However, this is probably related to the finer distance grid achieved in this work, enabling to map $\chi(r,t)$ on a finer space grid. Overall, this comparison underlines the reproducibility of this experimental technique, even if conducted with different experimental set-ups. The third investigated time domain is shown in Figure 6.17, which spans a time range from 63 as to 322 as. In this time range, the intensity has decreased to a

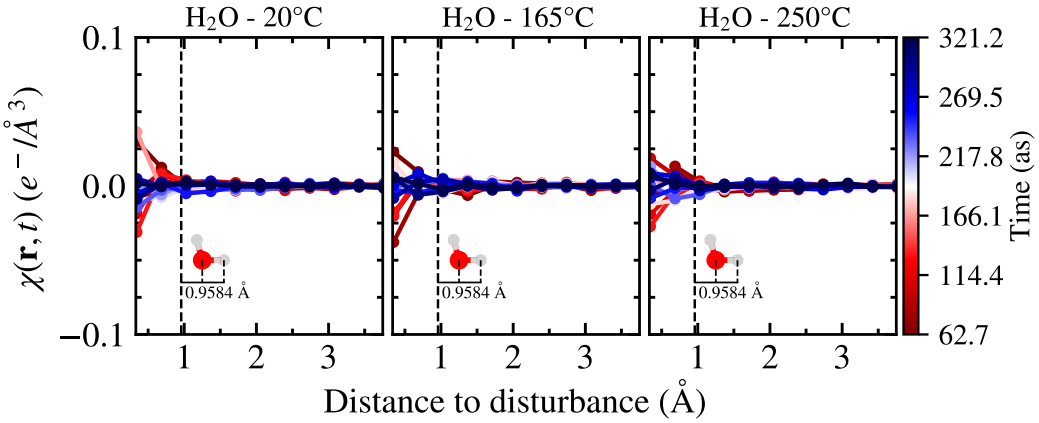

Figure 6.17: The density response function $\chi(r,t)$ as a function of the distance to the initial disturbance for the water sample at 20 °C (left), 165 °C (middle) and 250 °C (right). The evolution of the electron density disturbance is plotted at several different time steps between approximately 63 as and 322 as. The dashed black line marks the typical oxygen-hydrogen distance in a water molecule, shown here as size comparison [265].

minor fraction of its starting value and after 200 as, the effect of the disturbance on the electron density is no longer distinguishable from the background noise with the resolution achieved in this thesis, thus it is considered as completely decayed. Typical time scales related to the dynamics of water, such as solvation dynamics due to the addition of salts or reorientation dynamics of water molecules, are in the range of at least tens to hundreds of femtoseconds [267–271]. Therefore, the water

[2]Between the second 14.47 Å and third 17.92 Å drawn curve when counting from red to blue.

molecules can be assumed to be quasi stationary within the investigatable time range, since, for example, even the fastest solvation process takes at least a factor of 250 longer than the observable time frame. Additionally, this further explains why the temporal propagation of the electron density disturbance is largely irrespective of the applied temperature, as known temperature-dependent changes in the dynamics of water, such as the drastic reduction of the hydrogen bond lifetime, still occur on time scales of a few hundred femtoseconds [79, 80, 90].
The agreement of the density response function from this thesis and the paper of Abbamonte *et al.* has previously been demonstrated for a snapshot at 16.45 as. However, in order to conduct a more comprehensive comparison, Figure 6.18 depicts the derived $\chi(r,t)$ from both works at a time step of about 33 as. Since the

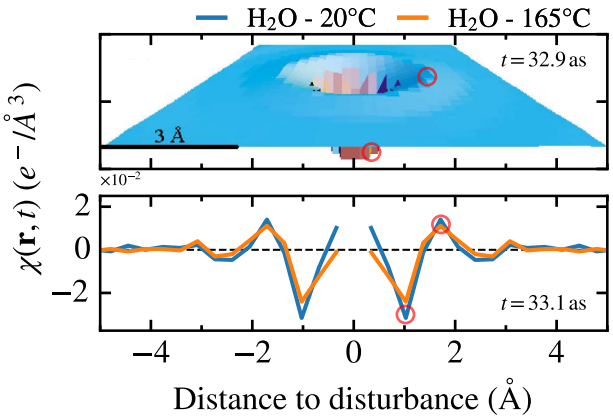

Figure 6.18: A comparison of the derived density response function at 33 as with the work of Abbamonte *et al.* [53]. (upper plot) A 3D rendered image of $\chi(r,t)$ from reference [53] together with (lower plot) $\chi(r,t)$ derived in this work at 20 °C and 165 °C, mirrored to negative values. For better visibility, the two comparable features in each plot are marked with a transparent red circle (see text for details).

the initial intensity is substantially reduced at this time by more than 97 % a comparison between the two data sets is even more conclusive. The influence of the background is emphasized by plotting $\chi(r,t)$ in Figure 6.18 at two different temperatures. However, a direct comparison with the previous work is difficult because the presented data consist of 3D renderers that provide an oblique side view which shrinks the x-axis when moving further 'into' the image. The Abbamonte *et al.* data exhibit two distinct features, which are marked with a small red circle. The first one is a minimum close to the origin of the disturbance and the second is a small positive peak at a slightly larger distance. Determining the exact position of these two peaks is difficult due to the mentioned issues but the first one is probably

located between 0.5 Å and 1.5 Å and the second one further away between 1.5 Å and 2.5 Å. The determined $\chi(r,t)$ in this work shows three features at 33 as. The first one is located at 0.34 Å and corresponds to an intensity close to zero (165 °C) or slightly above (20 °C), the second one is a larger minimum at 1.00 Å while the third one is a small peak at about 1.9 Å. The second and third extrema correspond well with the two identifiable features of the previous work, in terms of position and height. However, the first observable peak cannot be assigned to any feature in the previous work. This can presumably be explained by the much better spatial resolution achieved in this work, enabling features to be investigated much closer to the origin of the disturbance. Hence, an overall good agreement of the derived $\chi(r,t)$ with the previous work can be concluded even at higher time steps [53].
In the following, the contribution of the core electron is further investigated since the analysis of the time evolution of the electron density disturbance so far took the scattering contributions of all electrons in the system into account. However, many effects are only mediated via valence electrons, e.g. plasmonic excitations, therefore it is interesting to investigate the influence of the core electron contribution. It is particularly crucial to determine whether the core contribution leads to a significant unwanted background that could prevent the investigation of dynamic valence electron phenomena. This background is assumed to have a rather local influence in the case of core electron scattering. In order to verify how significant this contribution is, the Fourier transform of $\chi(q,\omega)$ was calculated after subtracting the contribution of the Compton scattering by core electrons and properly removing the residue of the oxygen K-edge as described in section 6.3. The resulting $\chi(r,t)$ at three different distances with and without the core electron contributions are shown in in the upper plots in Figure 6.19 up to 330 as, together with a smaller time frame up to 15 as given in the inset plots. The latter reveal a minor effect of the core electrons on the evolution on very short time scales. This also seems to apply to further distances, since $\chi(r,t)$ changes only slightly due to the subtraction of the core contributions at 1.37 Å and 2.4 Å as shown in the plot in the middle and upper right panel of Figure 6.19, respectively. However, at smaller distances and when about 12 as have passed since the initial disturbance, the effect is clearly visible in the upper left plot on Figure 6.19. This results in a significantly reduced amplitude of the high-frequency oscillation, which lies on an unaffected low-frequency second oscillation. The high-frequency component does not completely disappear due to the normal limitation of the data treatment method to fully subtract the core contribution. By determining the frequency of this fast oscillation, its origin can be identified. The rapid oscillation occurs with a frequency between 7 as and 8 as, which corresponds to the time scale of the oxygen K-edge excitation process at $T = 2\pi\hbar/\omega_{O-Kedge} \approx 7.66$ as with $\omega_{O-Kedge} \approx 530$ eV. The largest contribution of the core electrons can therefore be attributed to their excitation process. This is

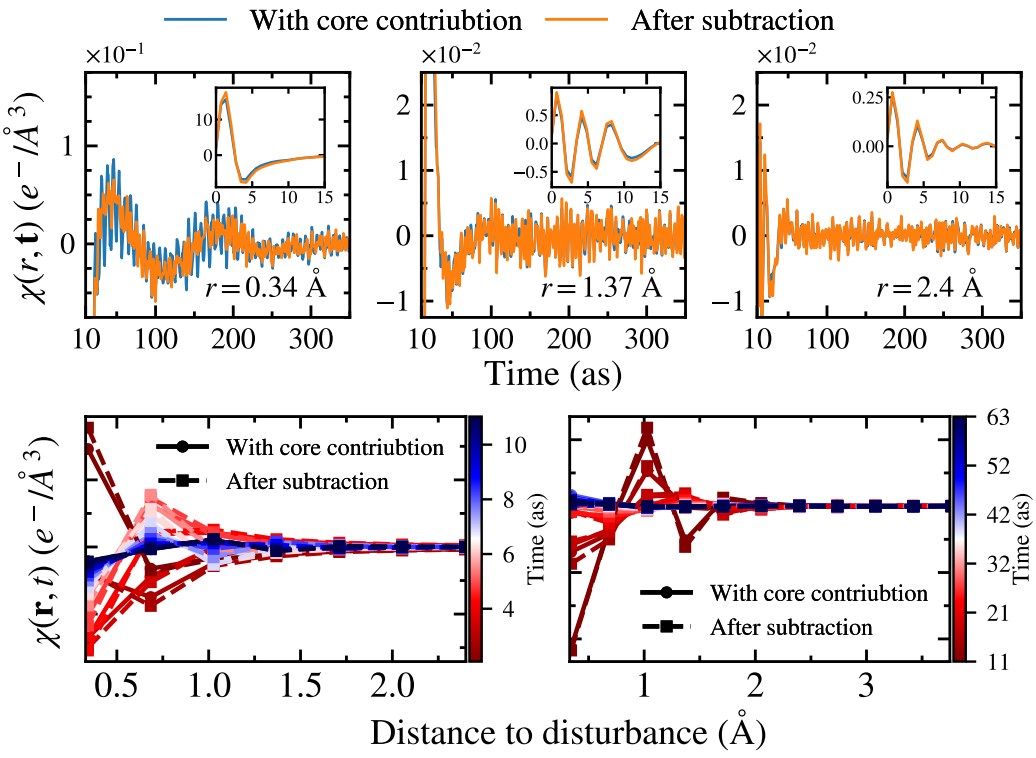

Figure 6.19: (Top) The time evolution of the density response function at three different distances to the origin of the disturbance plotted before (blue) and after (orange) the subtraction of the core electron contribution. The inserted plots display the first 15 as. (Bottom) The density response function as a function of density before (solid line with dots) and after (dashed line with squares) the subtraction of the core electron contribution at various time steps.

further confirmed by comparing the changes to the density response function due to the subtraction of the core contribution as a function of distance at different time steps shown in Figure 6.19 in the lower two plots, as the subtraction exhibits only a minor influence. Thus, the subtraction of the core electron contributions is highly important if low intensity dynamical processes are studied that occur on a similar time scale as the K-edge excitation process of any atomic species in the sample. However, the subtraction of the core electron contribution has only minor impact on longer time scales. Besides, it has a possible influence on the normalization as the f-sum rule has to be reapplied, and with this on absolute values of $\chi(q,\omega)$ and $\chi(r,t)$ [249].
The analysis performed on liquid water at elevated temperatures to calculate the density response function in time and space from the imaginary part of the den-

sity response function Im[$\chi(q,\omega)$] as shown in Figure 6.15 and 6.16, was likewise performed for the determined Im[$\chi(q,\omega)$] (see Figure 6.13) of the aqueous sodium chloride solution. Thus, the Fourier transformed density response functions of the 2 M aqueous sodium chloride solution at 20 °C and 90 °C are depicted in Figure 6.20 for comparison along with the results of the pure water sample at 20 °C, which is analysed on the same limited q-grid. At first glance, the obtained $\chi(r,t)$ for the

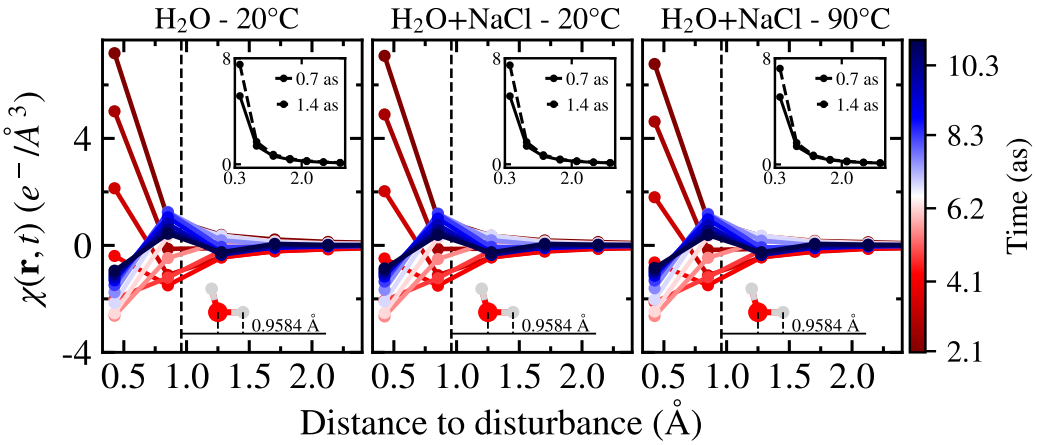

Figure 6.20: The density response function $\chi(r,t)$ as a function of the distance to the initial disturbance for the water sample at 20 °C (left, shown as comparison) and for the aqueous sodium chloride solution 20 °C (middle) and 90 °C (right). The evolution of the electron density disturbance is plotted at several different time steps for the first 11 as. The inset plot shows $\chi(r,t)$ in the first two time steps after the perturbation. The dashed black line marks the typical oxygen-hydrogen distance in a water molecule, shown here as size comparison [265].

NaCl samples appear vastly different compared to the previously shown results of the water sample in Figure 6.15. However, a comparison with the water sample analysed on the same shorter q-grid shows that this limitation is responsible for the differences, since the evolution of the disturbance is largely independent of the addition of salt or a further increase of the temperature to 90 °C. The contribution of the salt itself to the measured signal might be too low at the concentration studied to induce a significant difference in the density response function. Since the ratio of salt ions to water molecules at a concentration of 2 M is rather low at about 4:55, this explanation cannot be ruled out and the measurement of a higher concentrated solution is necessary to study the exact contribution of the salt ions [27, 272]. Despite the differences in $\chi(r,t)$ due to the different q-range and grid, the overall time evolution is similar to Figure 6.15: At the smallest distance a negative recoil is observed after about 5 as, which remains negative for at least 30 as and in addition

the sign of the second closest position oscillates with a shorter period. In contrast to the clear differences in $\chi(r,t)$ between Figure 6.15 and 6.20, the evolution of $\chi(r,t)$ for the aqueous sodium chloride solution in the second time range between 11 as and 63 as in Figure 6.21 significantly coincides with that of water (Figure 6.16), regardless of the poorer spatial resolution. This might indicate that the achieved resolution is suitable enough to properly investigate the evolution of electron density disturbances in this second time domain. However, the comparatively strong dependence of $\chi(r,t)$ on the r lattice in the first attoseconds, although only changed by 0.09 Å, indicates that a probably even finer spatial resolution is necessary to fully spatially map the evolution of the electron density perturbation on the smallest time scales. Furthermore, this emphasises the importance of conducting the experiment with a larger q range, in particular when investigating phenomena below 10 as.

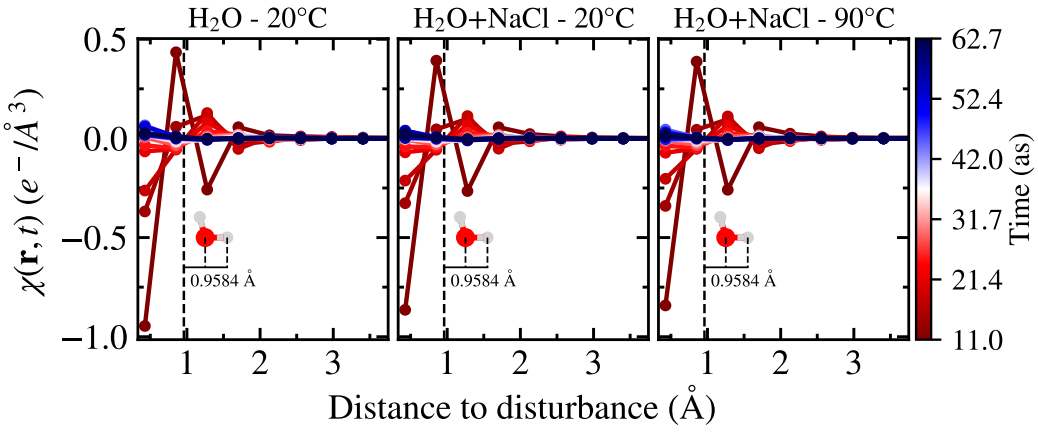

Figure 6.21: The density response function $\chi(r,t)$ as a function of the distance to the initial disturbance for the water sample at 20 °C (left, shown as comparison) and for the 2 M aqueous sodium chloride solution at 20 °C (middle) and 90 °C (right). The evolution of the electron density disturbance is plotted at several different time steps between approximately 11 as and 63 as. The dashed black line marks the typical oxygen-hydrogen distance in a water molecule, shown here as size comparison [265].

6.4.2 Propagation and decay of an electron density disturbance

In the following section, the propagation of the initial disturbance through time and space is investigated. The initial disturbance generates a 'wave'-like motion, which travels through the sample while quickly decaying. This propagation can be studied and quantified by plotting the time evolution of the density response function $\chi(r,t)$ and determining the successive maxima at different distances from the interaction point. In order to obtain the position and height of the maximum, it was fitted with an exponentially modified Gaussian function, which is defined via

$$f(x) = \frac{a_0}{2a_3}\exp\left[\frac{a_2^2}{2a_3^2} + \frac{a_1 - x}{a_3}\right]\left[\mathrm{erf}\left(\frac{x - a_1}{2^{0.5}a_2} - \frac{a_2}{2^{0.5}a_3}\right) + 1\right] \tag{6.6}$$

with a_0,a_1,a_2 and a_3 as fitting parameter and erf as the errorfunction [273]. Two examples of a performed fit of the asymmetric peaks at different positions using the modified Gaussian function are shown in Figure 6.22 for liquid water at 20 °C. This

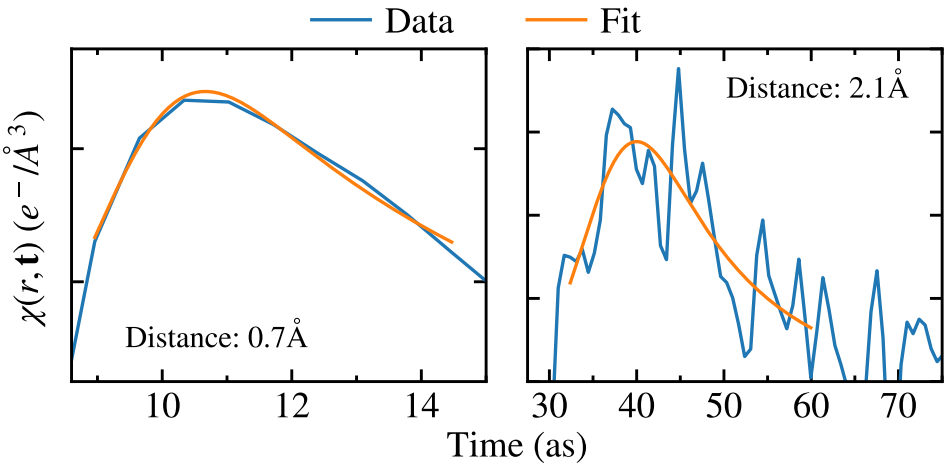

Figure 6.22: The density response function of liquid water at 20 °C as a function of time at two different position together with the corresponding asymmetric fit of the respective peak.

more complex function was necessary since the use of a simple Gaussian function proved insufficient to accurately determine the positions of the maxima due to the asymmetry of the different peaks. The temporal evolution at different positions up to 2.4 Å is shown in Figure 6.23, together with the determined positions and

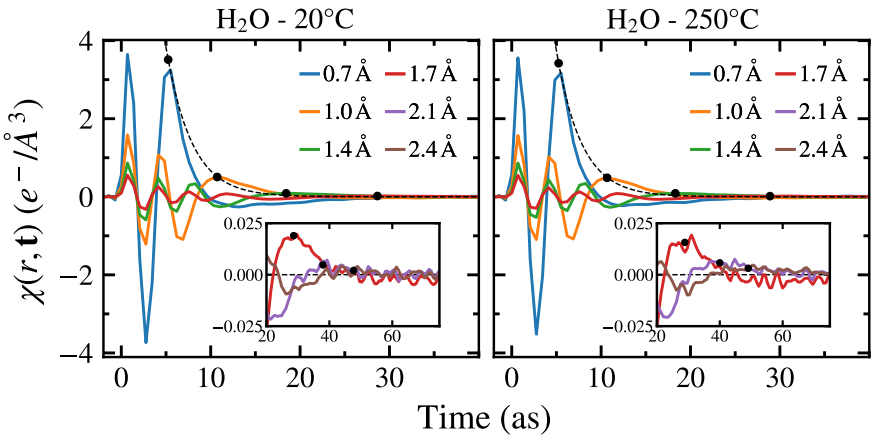

Figure 6.23: The density response function as a function of time at different positions up to 2.4 Å for 20 °C (left) and 250 °C (right). The black dots mark the determined position and height of the propagating initial electron density disturbance, while the dashed black line illustrates the results of the corresponding exponential fit. The inset shows a zoomed-in view of the density response function at larger distances.

heights of the mentioned maxima, which are marked with a black dot. Using those positions and heights, the temporal damping can be investigated and quantified via an exponential decay,

$$N(t) = N_0 \exp(-t/\tau) \tag{6.7}$$

where τ is the exponential time constant i.e. the lifetime. The resulting fit is shown in Figure 6.23 as dashed black line, exemplified for pure water at 20 °C and 250 °C. The lifetimes of this initial propagating electron density disturbances are estimated to (2.85 ± 0.10) as, (2.86 ± 0.10) as and (2.80 ± 0.10) as for the pure water sample at 20 °C, 165 °C and 250 °C. Within the error, the determined values are the same for the different temperatures, which confirms the result of the qualitative analysis that the temporal evolution of the disturbance is indistinguishable between the different thermodynamic conditions. However, using the same exponential fit to determine the life time for the aqueous sodium chloride solution, a dependence of the fit parameters on the smallest accessible distance value was found. This was also confirmed by performing the same analysis again for the pure water sample at 20 °C but interpolated on the same q-grid as used for the data of the aqueous sodium chloride solutions. Therefore, the listed error of the life time values is underestimated but nevertheless representative for a relative comparison of the different samples. In order to determine the life time for the aqueous sodium chloride solution compa-

rable with pure water, the mean fit parameter N_0 determined for the water sample[3] was taken and kept fixed during the fit. The life times thus determined for the aqueous NaCl solution are (2.74 ± 0.10) as at 20 °C and (2.71 ± 0.10) as at 90 °C and (2.78 ± 0.10) as for water at 20 °C analysed on the same grid as the aqueous sodium chloride solution. The minor differences in the lifetimes are probably still related to the coarser space grid of the aqueous NaCl solution. However, within the error, the lifetime is constant, further confirming the results of the qualitative analysis. As described in the previous section, the temperature independence of this initial propagation is reasonable because the well-known time scales of water dynamics in aqueous solutions are on the order of tens of femtoseconds [267, 271]. These time scales are approximately a factor of a thousand slower and thus render the water molecules in the system as quasi-static compared to the propagating disturbance. The propagation of this initial disturbance can be further studied by plotting and fitting the height of the maximum against the respective position instead of time as shown in Figure 6.24. This way, the propagation in space can be studied in more detail and a spatial damping constant can be obtained by an exponential fit,

[3]The deviation of N_0 between the different temperatures was a mere 0.5 %.

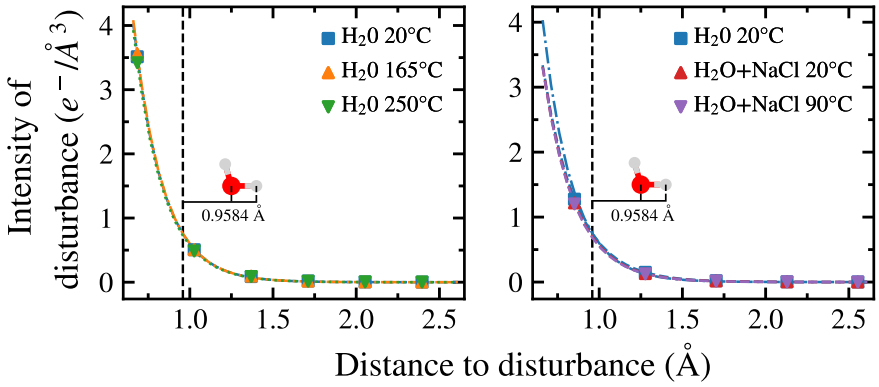

Figure 6.24: The intensity of the propagating electron density disturbance as a function of the respective position plotted together with the resulting curve of an exponential fit for pure water (left) and the aqueous sodium chloride solution (right) at ambient and elevated temperatures. The dashed black line marks the typical oxygen-hydrogen distance in a water molecule, which is only slightly exceeded by the propagating disturbance [265]. The determined positions of the water sample at 20 °C (right) are shown for comparison, the data were interpolated to the q-grid of the NaCl solution before analysis. The resulting exponential fit for water at 20 °C from the left image is also plotted in the right image as dash-dotted line to compare the results from the different grids.

which is equivalent to the life time parameter but for the spatial decay. The determined height of the maximum plotted against the corresponding position is shown in Figure 6.24 for pure water and the aqueous sodium chloride solution. Using the same exponential fit procedure, the values (0.177 ± 0.003) Å, (0.176 ± 0.003) Å and (0.176 ± 0.003) Å for the spatial damping constant are obtained for the pure water at 20 °C, 165 °C and 250 °C degrees and the values (0.173 ± 0.003) Å and (0.173 ± 0.003) Å for the salt solution at 20 °C and 90 °C. In addition, for water at 20 °C but on the same grid as the sodium chloride solutions, a value of (0.174 ± 0.003) Å is determined. The obtained values suffer from the mentioned dependence of the fit on the smallest accessible distance value, therefore an interpretation of the absolute values is difficult. However, the values indicate a rather small value of the spatial damping constant and a relative comparison of the values is nevertheless possible. The resulting curves are shown in Figure 6.24 and exhibit a good agreement with the experimental data, which, in conjunction with the determined spatial damping constant, reaffirm that the propagation of $\chi(r,t)$ is independent of the temperature and the dissolved salts. Furthermore, the analysis reveals that even the influence of this strong first electronic density disturbance mostly affects a small spatial region, only slightly exceeding the size of a single water molecule in terms of its oxygen-hydrogen distance of approximately 0.95 Å. The limited spatial propagation is presumably the reason that $\chi(r,t)$ is identical for all investigated thermodynamic conditions and samples, since the temperature-induced changes in the system are dominant on the intermolecular length scale as previously described in the qualitative analysis [10, 266].
The velocity of the propagating electron density disturbance over the investigated time period can be calculated using the determined position and respective time steps of the maximum. This is plotted in Figure 6.25 for pure water and the aqueous sodium chloride solution. The resulting velocities for pure water at 20 °C, 165 °C and 250 °C are (0.040 ± 0.005) Å/as, (0.041 ± 0.005) Å/as and (0.039 ± 0.005) Å/as, respectively. For the aqueous sodium chloride solution, the velocity was determined with a value of (0.040 ± 0.005) Å/as and (0.041 ± 0.005) Å/as for the sample at 20 °C and 90 °C, respectively. On average, this corresponds to about 0.013 % of the speed of light. Furthermore, the two plots in Figure 6.25 reveal that the velocity is not constant over the whole time range but that the propagations are slightly decelerating over time. However, as could already be deduced from the results of the previous analysis, the determined velocity is neither sensitive to the applied temperature for the pure water nor for the aqueous sodium chloride solution.

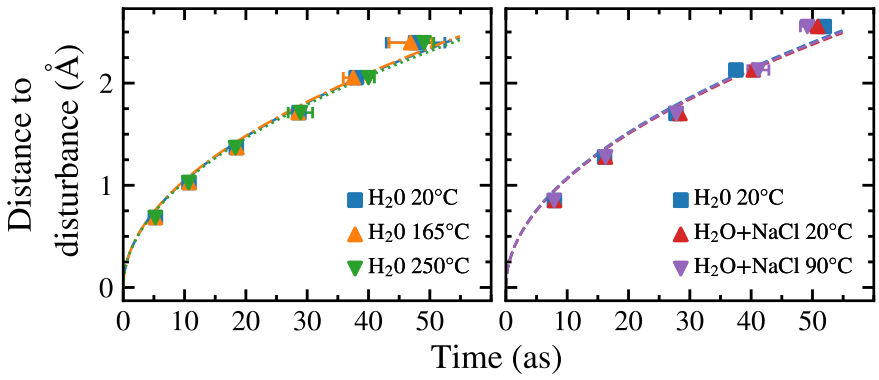

Figure 6.25: The determined positions of the propagating initial electron density disturbance as a function of the respective time step for the pure water sample (left) and the aqueous sodium chloride solution (right) together with a guide to the eye line.

6.4.3 Static density response function

Following linear response theory, the static screening electron density

$$\Delta n(\boldsymbol{q}) = V_{\text{ext}}(\boldsymbol{q}) \cdot \chi(\boldsymbol{q}, \omega = 0) \tag{6.8}$$

as induced by the external potential $V_{\text{ext}}(\boldsymbol{q})$ is related to the static density response function $\chi(\boldsymbol{q}, \omega = 0)$ [274, 275]. Hence, this relationship can be used to calculate the electron screening density for differently shaped external potentials. For instance, previous work has utilized Abbamonte's approach with extremely high energy resolution on the meV scale to study molecular interactions on the femtosecond time scale and to investigate the screening electron density in liquid water surrounding a point charge and a point charge distributed to a Gaussian charge [240]. Furthermore, they considered the influence of the excluded volume of the external charge density on the screening electron density in their study as this is an important factor to adequately investigate hydration processes [240]. However, since this work is primarily focused on relative changes of the water structure induced by a change of temperature or the addition of salts, excluded volume effects were neglected and the external potential was described by a positive point charge focused on sub-femtosecond dynamics. In order to obtain the screening electron density as a function of distance r to the point charge, the formula

$$\Delta n(\boldsymbol{r}) = \int \exp(i\boldsymbol{q}r)\chi(q, \omega = 0) \cdot V_{\text{ext}}(\boldsymbol{q}) \frac{d^3q}{(2\pi)^3} \tag{6.9}$$

was used, which can be further simplified by applying spherical coordinates to

$$\Delta n(r) = \frac{1}{2\pi^2} \int_0^\infty dq \left(\frac{q \sin qr}{r} \right) \chi(q,0) \frac{4\pi e(-e)}{q^2} \tag{6.10}$$

which represents a 3D-Fourier transformation of equation 6.8 after replacing $V_{\text{ext}}(\boldsymbol{q})$ with a positive point charge [249, 276]. Furthermore, since this relationship applies to the valence electrons, the contribution of the core electron was subtracted prior to the analysis, as described in the previous section [249] and the resulting $\chi(q, \omega = 0)$ is shown in Figure 6.26 as an example for pure water at ambient and elevated temperatures.

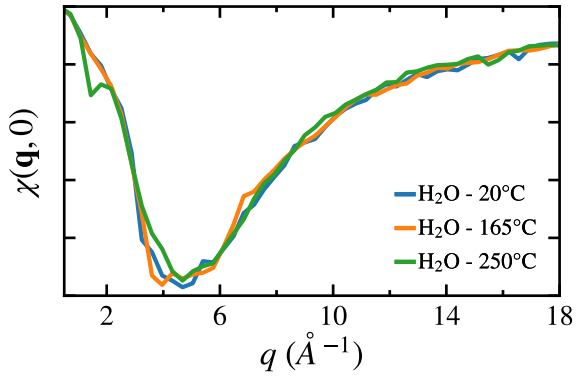

Figure 6.26: The $\chi(q, \omega = 0)$ employed to calculate the static electron screening density using equation 6.10. $\chi(q, \omega = 0)$ is shown exemplary for water at 20 °C, 165 °C and 250 °C.

The resulting screening electron densities are shown in Figure 6.27 for the pure water sample at ambient and elevated temperatures. The strong attraction of the positive charge at $r = 0$ leads to a screening electron density which extends up to approximately 1 Å where it is reduced to 1 % of its maximum height. Within the first Ångstrom, the screening electron density is almost indistinguishable for the different temperatures. Additionally, a long-range oscillation of the electron density is observable at lower intensities. This oscillation is identical at 20 °C and 165 °C, but differs compared to the screening electron density at 250 °C in particular between 1 Å and 4 Å. The differences between 20 °C and 250 °C are indicating that the reduced density of the sample alters the reorientation of the water molecules with respect to the positive charge. However, it is conspicuous that the long-range oscillation of the screening electron density is unaffected by a reduction of density from approximately 1 g/cm^3 (20 °C) to 0.9 g/cm^3 (165 °C) but changes significantly with a further reduction to 0.8 g/cm^3 (250 °C). This points either to an error in

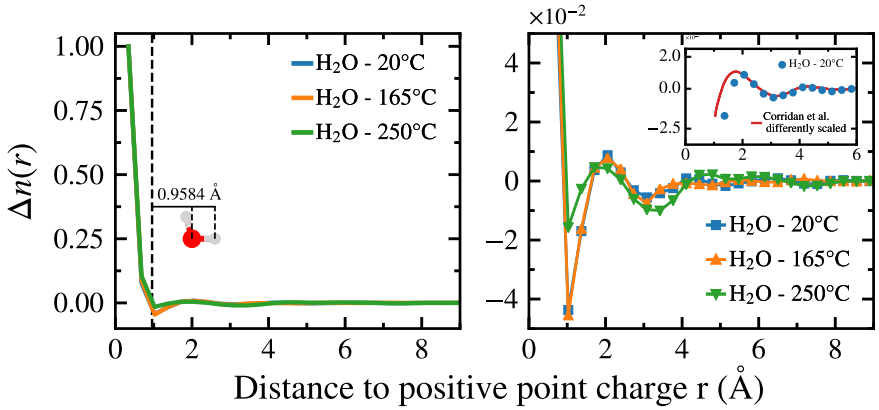

Figure 6.27: (left) The screening electron density $\Delta n(r)$ normalized to its maximum value for pure water at 20 °C, 165 °C and 250 °C. (right) Enlargement of $\Delta n(r)$ shows a long-range oscillation at about 1 % of its maximum intensity. (right, inset plot) Comparison of $\Delta n(r)$ between this thesis (20 °C) and the study from Reference [240], which is scaled in amplitude to match $\Delta n(r)$ in this work since the former study showed $\Delta n(r)$ in arbitrary units.

the accurate determination of $\Delta n(r)$ at low values or to an abrasive change in the screening electron density as a function of temperature. Furthermore, it should be noted that in the study of Hagiya *et al.* the oscillating part of $\Delta n(r)$ considerably depended on the performed data treatment procedure as can be seen in Figure 6 of their work [249]. Both of these factors indicate that the observed temperature differences are ambiguous. The inset plot on the right side of Figure 6.27 shows the long-range oscillation of the screening electron density determined within this thesis at 20 °C in comparison with $\Delta n(r)$ from the work of Coridan *et al.* [240]. Although the two screening electron densities differ at small distances, the overall agreement is remarkably good especially above 2 Å. The differences are probably related to the mentioned dependence of $\Delta n(r)$ on the data treatment procedure and the use of an unspecified interpolation scheme. Another factor to consider in the comparison is the difference in the used q-grid because the previous study utilized a coarser grid with a maximum of only 7.2 Å^{-1}. At these q-values, $\chi(q, \omega = 0)$ exhibits still significant intensity, thus relying more on a suitable extrapolation procedure before applying the Fourier transformation [240]. Nevertheless, considering these factors, the agreement with the previous study is good and indicates a general reproducibility.

The screening electron density for the sodium chloride solution at ambient and elevated temperature is shown in Figure 6.28 in comparison with pure water at 20 °C, which was analysed on the same q-grid as the NaCl sample. The resulting $\Delta n(r)$

exhibits the same build up around the positive charge with a screening radius of about 1 Å regardless of the temperature or the presence of dissolved ions. However, the subtle long-range oscillation on the right side of Figure 6.28 is less pronounced for the NaCl solution compared to pure water, since, for example, $\Delta n(r)$ lacks the pronounced negative peak at about 1.4 Å and is damped at larger distance. This might indicate a reduced mobility of the water molecules accompanied by a lower degree of freedom due to the dissolved ions in the system, which prevent the water molecules to arrange themselves as in pure water, as they are partially trapped in hydration shells. Moreover, the reason for the differences might originate from the contribution of the chloride ions, which are possibly directly involved in the screening process resulting in less pronounced features of $\Delta n(r)$ due to the chloride's vastly different charge distribution compared to the dipolar water molecule. It is also possible that the ions interact with the water molecules or the point charge in some other non-verifiable way. However, as previously mentioned in the comparison of the pure water system at different temperatures, the dependence of the oscillating part of the screening electron density on the performed data treatment procedure makes the validation of these conclusions ambiguous. Nevertheless, since the oscillation of the screening electron density extends over several molecules and is thus structure-dependent, a dependence on the addition of salts or the increased temperature is not implausible.

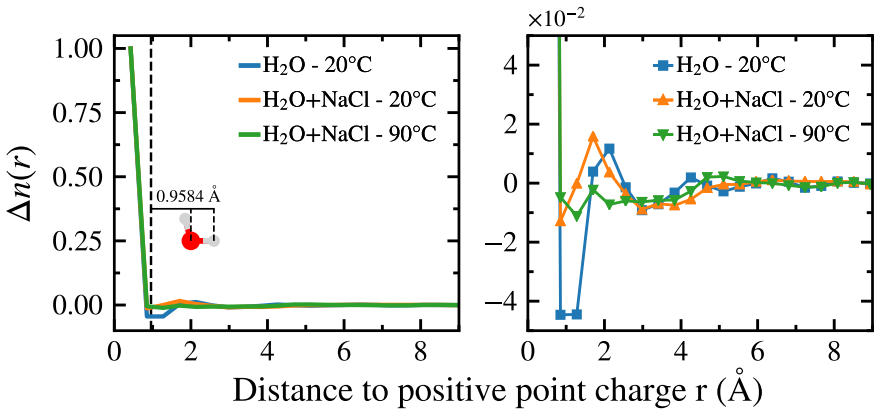

Figure 6.28: (left) The screening electron density $\Delta n(r)$ normalized to its maximum value for pure water at 20 °C and aqueous sodium chloride solution at 20 °C and 90 °C. (right) The enlargement shows a long-range variation of $\Delta n(r)$ with about 1 % of its maximum intensity, which can be interpreted as an oscillation for pure water, whereas it is ambiguous for the aqueous NaCl solution.

6.5 Summary and conclusion

Inelastic X-ray scattering was used to measure the dynamic structure factor $S(q,\omega)$ of pure water and aqueous sodium chloride solution at ambient and elevated temperatures over a large energy loss and momentum transfer range up to 3000 eV and 18.7 Å^{-1} (14.76 Å^{-1} for aqueous NaCl solution), respectively. Using $S(q,\omega)$, the microscopic structure and dynamics of these two systems were studied as a function of applied temperature on atomic length and attosecond time scales. This was achieved by establishing a new data treatment scheme, which is reliable over the large utilized energy loss and momentum transfer range. Following this procedure, the density response function $\chi(q,\omega)$ was determined from the experimentally measured dynamic structure factor $S(q,\omega)$. $\chi(q,\omega)$ was then Fourier transformed and utilized to study the temporal and spatial evolution of an electron density disturbance induced by the incident X-ray beam in pure water at 20 °C, 165 °C and 250 °C as well as in a 2 M aqueous sodium chloride solution at 20 °C and 90 °C. A comparison of the obtained $\chi(r,t)$ with the pioneering study of Abbamonte *et al.* at different time steps revealed an overall good agreement, which indicates a reliable reproducibility using this experimental technique [53]. In addition, the significantly larger scan range in both energy and momentum transfer revealed new insights into the temporal evolution of the electron density disturbance on sub-Ångstrom length scales within the first attoseconds. Within the achieved observable time frame of 200 as, the induced disturbance primarily affects a small region that hardly exceeds the size of a single water molecule. Therefore, $\chi(r,t)$ is drastically reduced at larger distances and mostly indistinguishable from noise. In terms of temperature, the recorded spectra exhibit no spectral redistribution due to the heating of the system, which is a consistent trend that is equally valid for the qualitative analysis of $\chi(r,t)$ as well as all parameters directly derived from it. The reason for this was attributed to the particularly small region affected by the electron density disturbance in combination with the quasi-static water structure in the investigated time period. Furthermore, the system was found to be largely unaffected by the addition of dissolved ions.

The density response function was further used to investigate the propagation and decay of the initial density disturbance through the material by determining the respective height of the maximum of the propagation and the corresponding position in time and space with the fit of a modified asymmetric Gaussian function. Using an exponential fit function revealed a lifetime and a spatial damping constant of about 2.8 as and 0.175 Å, respectively, for all systems and temperatures investigated. These small values again underline the localized character of the disturbance in time and space. Furthermore, the velocity of the propagation was calculated with

an approximated value of 0.04 Å/as or 0.013 % of the speed of light.
The relationship within linear response theory between the density response function $\chi(q, \omega = 0)$, an external potential and the static screening electron density was exploited to calculate the latter one for all systems. The electrons were found to accumulate in a radius of approximately 1 Å around the positive charge. Furthermore, a subtle long-range oscillation was observed, which was less pronounced in the aqueous sodium chloride solution. This oscillation for water at 20 °C proved to largely reproduce the results from a previous study [240], except for some minor deviations probably due to differences in the data treatment scheme. Although the screening electron density is nearly identical for 20 °C and 165 °C, it alters when the temperature is increased to 250 °C, although the cause of the changes could not be determined unambiguously. In addition, the differences of the subtle long-range oscillation between pure water and aqueous sodium chloride solution might indicate that the different charge distribution of the ions compared to the water molecules influences the screening electron density.
In summary, a good reproducibility of the experimental technique can be concluded from the comparison with previous studies. Furthermore, a reliable data treatment procedure suitable for the inherent challenges of an larger scanning range in both energy loss and momentum transfer has been introduced. This opens new and exciting venues for the understanding of ultra-fast dynamics resolved in the sub-Ångstrom range for a variety of interesting sample systems [277–279]. In particular, this type of data acquisition and analysis is applicable to valence electron excitations with emphasis on the discussion of inhomogeneous electron gas. Moreover, as the data treatment procedure provides an absolute intensity scale, the comparison with various theoretical models beyond a relative comparison becomes accessible. With regard to the investigated pure water and the aqueous sodium chloride solution, the overall picture emerges that within the investigated timespan, the observed effect of the electron density disturbance is highly localized, rendering its influence and propagation largely unaffected by the applied temperature or the salt in the system.

7 Temperature response and microscopic structure of polymerized ionic liquids

7.1 Introduction

The key to any high-performance design of electrochemical materials with large energy storage and transport capabilities is an understanding of the structural fundamentals that govern the charge transport in such materials. Therefore, amorphous conductors such as ionic liquids and polymer electrolytes have been extensively studied [280, 281]. In this regard, despite the considerable interest in various scientific fields, information on the rapidly emerging class of materials formed by polymerized ionic liquids is sparse, due to the difficulty in obtaining these materials commercially [282]. Polymerized ionic liquids are synthesized by direct covalent bonding of functional monomers containing ionic liquid fragments [283]. This combines the advantages of ionic liquid in terms of high charge density with those of polymers in terms of mechanical stability. Furthermore, polymerized ionic liquids are not only interesting from a technical viewpoint since, given the substantial difference between the mobilities of their anions and cations, they are considered as a model system in which only one type of ion governs the conductivity. In a previous study by Gainaru *et al.*, the ionic diffusivity of several polymerized ionic liquids has been studied by means of dynamical methods i.e. dielectric spectroscopy combined with nuclear magnet resonance and differential scanning calorimetry [284]. They proposed a new approach using directly the conductivity spectra to estimate the ion diffusivity without the need of any adjustable parameter. In this model, the elementary diffusion step of the ions, is linked to structural details such as the distances between the ions in the system and the local charge coordination number. Motivated by this new approach and the inherent importance of the structure of ionic liquids, this chapter is devoted to extensively investigate the detailed structural properties of various polymerized ionic liquids and their molecular counterparts. Furthermore, as the conductivity strongly depends on the ionic mobility in the system, which is strongly modified by changes in thermodynamic conditions such as temperature, the ionic liquids were studied over a wide range of temperatures [284]. A combined XRD and EXAFS approach is exploited in this chapter to study

the structure of molecular and polymerized ionic liquids and structural changes as a function of temperature in a range from 160 K to 400 K. Combining these two experimental techniques allows to investigate the structure of the ionic liquids over a wide range of distances. The building units of the ionic liquid system, polar and apolar groups can be resolved by means of XRD while EXAFS is highly sensitive to the local structure arrangement of an absorbing atom which is in this case the bromine anion.

7.2 Samples

According to their definition, ionic liquids are salts with a melting point below 100 °C, thus they are in the liquid sate at room temperature conditions. They consist of organic cations, such as imidazolium, and organic or inorganic anions, such as acetate or mesylate in the first case and, for example, simple bromide or more complex bistriflimide in the second case [285, 286]. A comparison of the melting points of one of the most abundant salts on Earth, sodium chloride, which melts at 803 °C, with that of the ionic liquid 1-propyl-3-methylimidazolium chloride, which becomes liquid at a temperature of 60 °C, reveals that the reason for the low melting point of ionic liquids is primarily the replacement of the small inorganic ion, in this case sodium, by large, asymmetric and organic components [287]. In addition to their low melting point, ionic liquids have a number of intriguing properties, including their low vapour pressure, high conductivity and good solubility. The specification of these and other properties can be tuned by the choice of the cation and the anion, thus ionic liquids are often referred to as 'designer solvents' [288]. By polymerizing the cationic component, these properties can be further adjusted, opening up new and versatile areas of applications [289].
In this work, a total of four different samples were investigated, two monomer ionic liquids and their polymerized counterpart. All samples were provided by the workgroup of Prof. Alexei P. Sokolov from the University of Tennessee. A detailed description of the exact synthesis process of the different polymer samples is given in their recent publications [283, 290]. Since the term *monomer ionic liquid* is not widely used, it should be mentioned that it refers here to the standard ionic liquid and is used to distinguish it from the polymerized ionic liquid, which is also named *polymer ionic liquid* in this work. All samples are shown in Figure 7.1 as stick and ball schematics and have two major similarities: The anion in each sample is a bromine atom and the cationic group contains an imidazole ring. However, apart from these shared characteristics, the samples feature a range of structural differences. For instance, the side-chain of the two monomers differ not

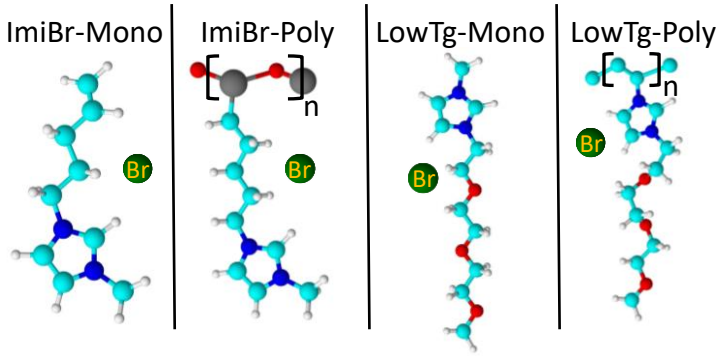

Figure 7.1: Ball and stick schematic of the four investigated samples, named as follows (f.l.t.r.): ImiBr-Mono, ImiBr-Poly, LowTg-Mono and LowTg-Poly. The colored balls represent different atoms, namely: white: hydrogen, blue: nitrogen, cyan: carbon, red: oxygen, brown: silicon, green: bromine.

only in length but one monomer has also oxygen incorporated in their side-chain making it a polar diether chain instead of an alkyl chain. The monomer and its polymerized counterpart with the alkyl side-chain consisting of five carbon atoms are further referred to as ImiBr, while the other monomer and its polymerized species with the diether side-chain containing three oxygen and seven carbon atoms are coined as LowTg. The name LowTg is chosen in reference to a previous study which used the same name for an ionic liquid with the same cation due to its low glass transition temperature (T_g) [284]. An accurate chemical name for the monomer ImiBr is 1-pentyl-3-methyl-imidazolium-bromid and 1-(2-[2-(2-methoxyethoxy)ethoxy]ethyl)-3-methylimidazolium for the monomer LowTg. In addition to the differing monomer group, the polymers exhibit further structural differences. While the polymer backbone in ImiBr consists of silicon and oxygen, the backbone in LowTg is composed of carbon. Another major difference is the position at which the polymer backbone is connected to the cation, as it is attached to the head in the case of LowTg, but to the tail in ImiBr i.e. a very different orientation of the imidazole ring with respect to the backbone. The bromine atom in each sample allows to perform EXAFS experiments on the bromine K-edge and to study the local structural environment of the anion.

7.3 Experimental details

The XRD experiments were conducted at beamline BL2 of DELTA synchrotron radiation source using a multilayer monochromator with an energy bandpass of 1.5 % to obtain an incident energy of 10.876 keV. The beamsize was adjusted with slits to 0.6 x 0.6 mm^2 (H x V). A MAR345 image plate detector with a distance of 351 mm to the sample was used to detect X-rays scattered from the samples, which, considering the usable detector area in combination with the incident energy, resulted in an accessible momentum transfer range (q) from 0.2 $Å^{-1}$ to 2.3 $Å^{-1}$. The XRD analysis tool DIOPTAS v.0.4.1 [291] was utilized to azimuthally integrate the 2D detector images and convert the 2θ-scale to the q scale after applying the measured diffraction pattern of lanthanum hexaboride as calibration. After conversion to the q scale, each scan was normalized to the average beam current during the measurement. In addition, to compare samples measured in different sample environments, the background signal was subtracted from the data by using the signal from an empty sample holder after accounting for sample absorbance. Lead tape was attached to the sample holder to minimize the amount of air scattering detected. In order to perform the background subtraction consistent for all measured diffraction patterns, some scans required an additional scaling of the background signal by up to 5 % due to slight fluctuations in the experimental set-up such as minor beam position movements. After subtracting the scaled background scan, the resulting data were further normalized to the area between 0.25 $Å^{-1}$ and 2.3 $Å^{-1}$.
The EXAFS experiments were performed at the beamline P64 [292] of PETRAIII. The incident energy was scanned across the Br K-edge at 13.474 keV from 13.274 keV to 14.474 keV using a Si(111) double crystal monochromator. In order to determine the absorption coefficient of the sample as a function of the incident energy, the X-ray intensity was detected with an ionization chamber in front of and behind the sample, respectively, each filled with nitrogen gas at ambient pressure. The used experimental set-up is shown in the labelled photo in Figure 7.2. The measurements were conducted running the monochromator in continuous mode with an acquisition time between 40 s and 60 s for a single spectrum. To obtain a sufficient statistics, the final spectrum at each temperature step was averaged over several single spectra resulting in a total acquisition time of about 20 minutes. Since the continuous mode set-up provides the recorded data with an unnecessary fine energy increment, resulting in a poor fit of the background function to the data and thus an unrealistic estimate of the contribution of the isolated absorption atom, the final raw data were binned on a more suitable energy grid. The final energy increment is 10 eV for smaller energies than $E_0 - 30$ eV and 0.5 eV between $E_0 - 30$ eV and $E_0 + 50$ eV, where E_0 is the determined edge energy at 13.474 keV. Furthermore,

the contribution from double electron excitations at approximately 90 eV ($KN_{4,5}$) and 210 eV ($KM_{2,3}$) above the Br K-edge were subtracted from the data according to the study of Burattini *et al.* [293]. The resulting spectrum of each sample is shown in Figure 7.3 as an example for a temperature close to ambient. In order to extract

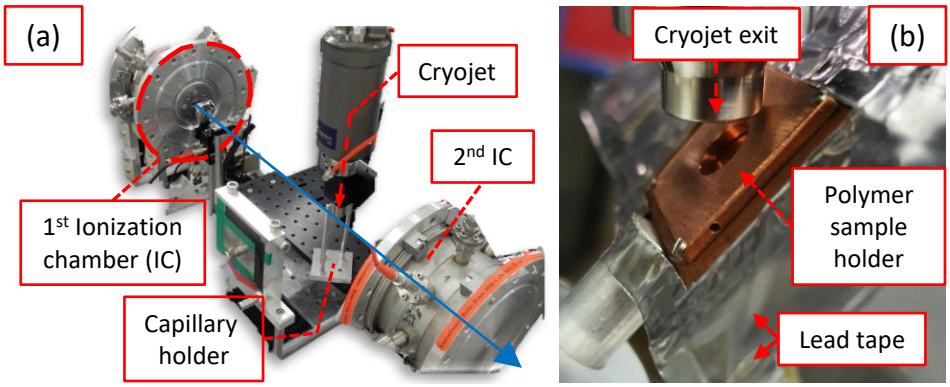

Figure 7.2: (Left) A photograph of the experimental set-up used for the EXAFS experiments at P64. The beam path is shown schematically as a blue arrow and the various components are labelled: The two ionization chambers positioned respectively in front of and behind the sample, the capillary holder and the Cryostream used to cool and heat the sample. (Right) Close-up of the custom-made sample holder for the polymerized ionic liquids. The lead tape used for the XRD experiments to reduce the detected air scattering is also shown together with the exit nozzle of the cryostream.

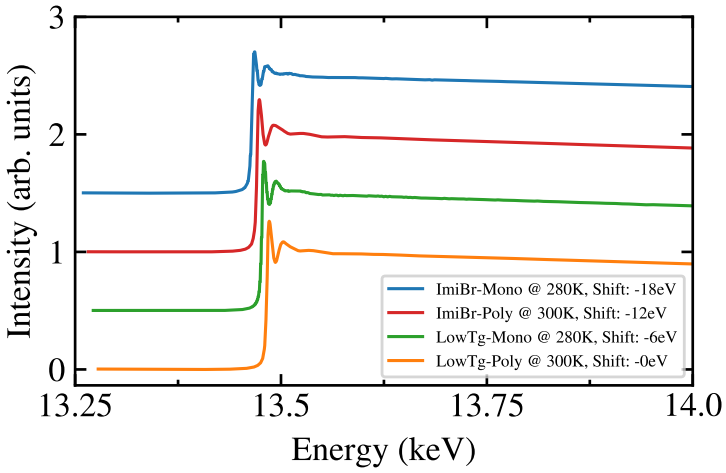

Figure 7.3: The measured absorption coefficient of the four measured ionic liquids at temperatures close to ambient. For reasons of clarity, the spectra are shifted on both, the x-axis and the y-axis.

the EXAFS oscillation and calculate the pseudo radial distribution function (pRDF) from it, standard EXAFS analysis procedures were performed [114, 294–296] within the Larch toolkit v.0.9.42. [297]. This includes determining the energy position of the Br K-edge by evaluating the maximum of the second derivative and the subsequent normalization of each spectrum to the edge jump which was determined by calculating the difference between two linear fits at the edge position. One linear fit was performed before the edge position and one at higher energies where the EXAFS oscillation has a only a minor contribution. Finally, a well-established background function was fitted to the data and subtracted to account for the contribution of an isolated absorbing atoms and the energy values were converted to k, the wave vector of the electron wave [294].
The same sample holders were used for both experiments. The monomer ionic liquids were filled into commercially available borosilicate glass capillaries with a diameter of 0.7 mm which were sealed tight by burning the opening shut. A custom-made sample holder was utilized for the polymer ionic liquids due to their much higher viscosity. This sample holder is shown in Figure 7.2 and consists of a metal plate with a small hole in the middle with a diameter of 3 mm for the sample, which was sealed on both sides with Kapton tape. The thickness of the metal plate i.e. the sample, was chosen depending on the performed experiment with 0.5 mm and 1 mm for the EXAFS and XRD experiments, respectively. In order to control the temperature over a wide range from 160 K to 400 K, a Cryostream set-up was used with the Oxford Cryosystems CryoStream 800 cooler, whose exit nozzle was placed a few millimeter above the sample. It should be mentioned that recent temperature calibration measurements performed by a member of the E1a workgroup at TU Dortmund revealed that a large temperature error of up to 20 K can occur at low and high temperatures.

7.4 Analysis and results

The recorded XRD patterns of the two monomer and polymer ionic liquids are shown in Figure 7.4 at various temperature steps in the two top and two lower plots, respectively. A common feature of all measured samples regardless of their polymerization is the pronounced peak between 1.5 $Å^{-1}$ and 1.75 $Å^{-1}$. In addition, all samples exhibit a peak at low q values between 0.25 $Å^{-1}$ and 0.5 $Å^{-1}$ but with significant differences between the monomer and polymer ionic liquids as the peak is less distinct and broader for the monomers. Comparing the two polymer samples, the low q peak is much more pronounced in LowTg, as it even exceeds the high q peak in terms of intensity at higher temperatures. Another difference between

the two polymer ionic liquids is the intermediate peak which is only present for the ImiBr sample at around 0.85 Å^{-1}. In terms of temperature, the most drastic

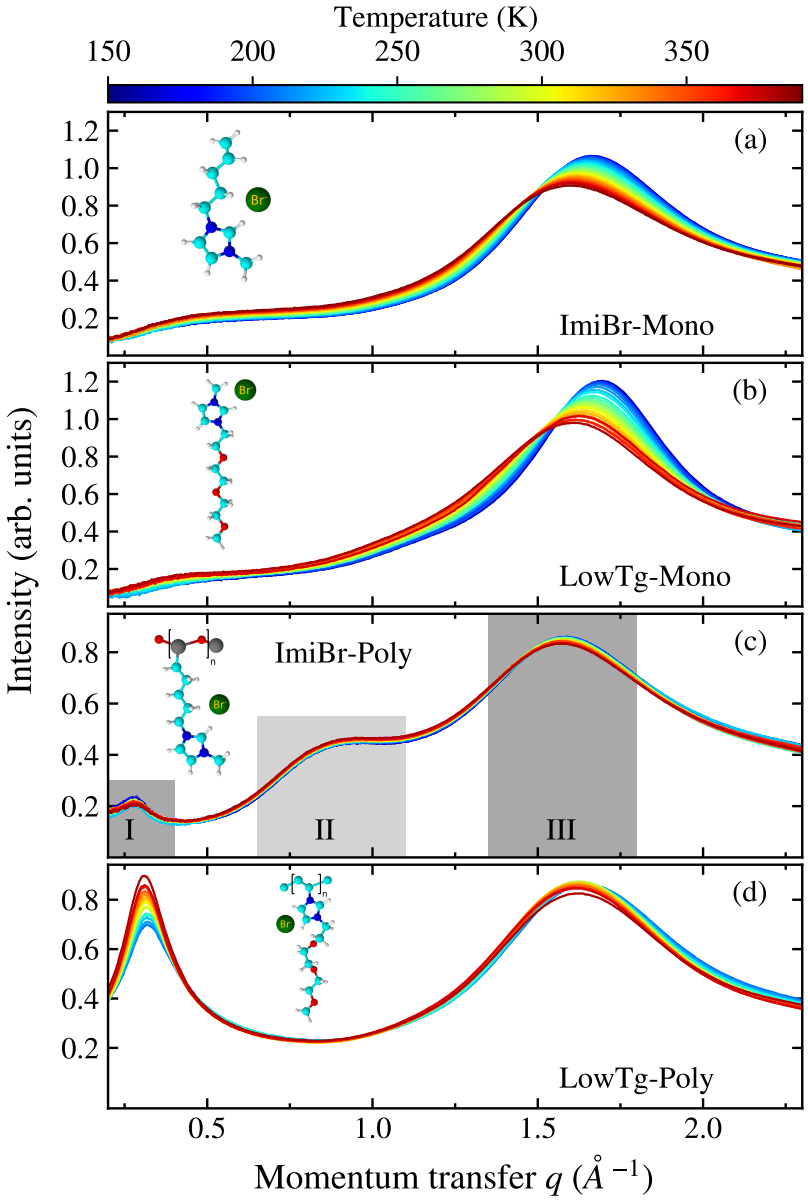

Figure 7.4: The obtained diffraction patterns at various temperatures in a range from 160 K to 400 K for ImiBr-Mono (a), LowTg-Mono (b), ImiBr-Poly (c) and LowTg-Poly (d). The stick and ball model of the corresponding ionic liquid with an arbitrary anion position is shown in each plot. The positions of the three different peaks are indicated in (c) by I: polar-apolar peak, II: charge peak and III: adjacent peak.

changes in the XRD patterns of the two monomer ionic liquids occur in the high q peak as it loses intensity with increasing temperature and shifts to lower q values. The low q peak of the two monomers likewise shifts to lower q values but to a lesser extent and without showing the same intensity decrease as the high q peak. In the case of the two polymers, a less pronounced temperature response is observable, as the high q peak intensity decrease only slightly and hardly moves to lower q values. The low q peak of the polymerized ImiBr reveals no clear temperature dependence. Interestingly, the LowTg polymer shows a significantly different temperature dependence, as the low q peak even increases with rising temperature.
The observed peaks and their temperature-dependent changes are analysed following the interpretation of an extensive XRD study by Araque *et al.* which aimed to further elucidate the general understanding of the structure of ionic liquids and the relationship with the different peaks in the XRD pattern [298]. According to Araque *et al.*, the low q peak is referred to as the apolar-polar peak, the intermediate peak of the polymerized ImiBr as charge peak and the high q peak as adjacent peak. The notations are motivated by the structural correlations associated with the different peaks. Following the interpretation of Araque *et al.*, the origin of the adjacent peak is due to intra- and intermolecular correlations between closely located atoms, which are not unique to ionic liquids but also occur in conventional liquids. The reason for a distinct apolar-polar peak is an alternation of polar and apolar components in the ionic liquid, hence an absence of the peak is an indication, but not a necessity [299, 300], for a small apolar component and the concomitant absence of apolar-polar alternation [298–301]. The origins of the intermediate charge peak are charge alternations in the ionic liquid. However, a missing charge peak does not inherently imply that this characteristic of molten salts is absent, since charge alternation in ionic liquids are always present at room temperature conditions. Rather, the cause of a missing peak is related to cancellation effects of subgroups of atom-atom correlation functions and corresponding structure factors. In the case of the charge peak, the correlations between two positive charges or two negative charges are same-type correlations, but the correlations between positive and negative charges are different-type correlations, which partially or completely cancel out via contributions from peaks and anti-peaks of the corresponding atom-atom structure factors [298]. This is an explanation for the occurrence of the charge peak in the polymerized ImiBr, while the peak is absent for the other ionic liquids. The backbone-chain in polymerized ionic liquids either accumulates the apolar domain of the molecular ionic liquids if the side-chain is attached to the polymerized chain or the polar domain if the connection is realized via the cationic head part. Thus, the resulting apolar-polar peak correlates heavily with the backbone to backbone distance which depends significantly on the extent of the apolar domain of the molecular ionic liquid, i.e. on the length of the side-chain [286, 302–305].

Following the interpretation of Araque *et al.*, a qualitative analysis of the differences in the XRD patterns between the various samples is pointing towards a more pronounced apolar component due to the polymerization of the ionic liquid as the apolar-polar peak at low q values is significantly more distinct.
The resulting k-weighted EXAFS oscillation after performing the aforementioned data treatment procedure is shown in Figure 7.5. Depending on whether the monomer or polymer ionic liquids are probed, the oscillation shows distinguishable frequency contributions. In comparison to the XRD patterns, the difference between ImiBr and LowTG are minor for the monomer and polymer ionic liquids. The increasing temperature leads to a decrease in the intensity of the amplitude without

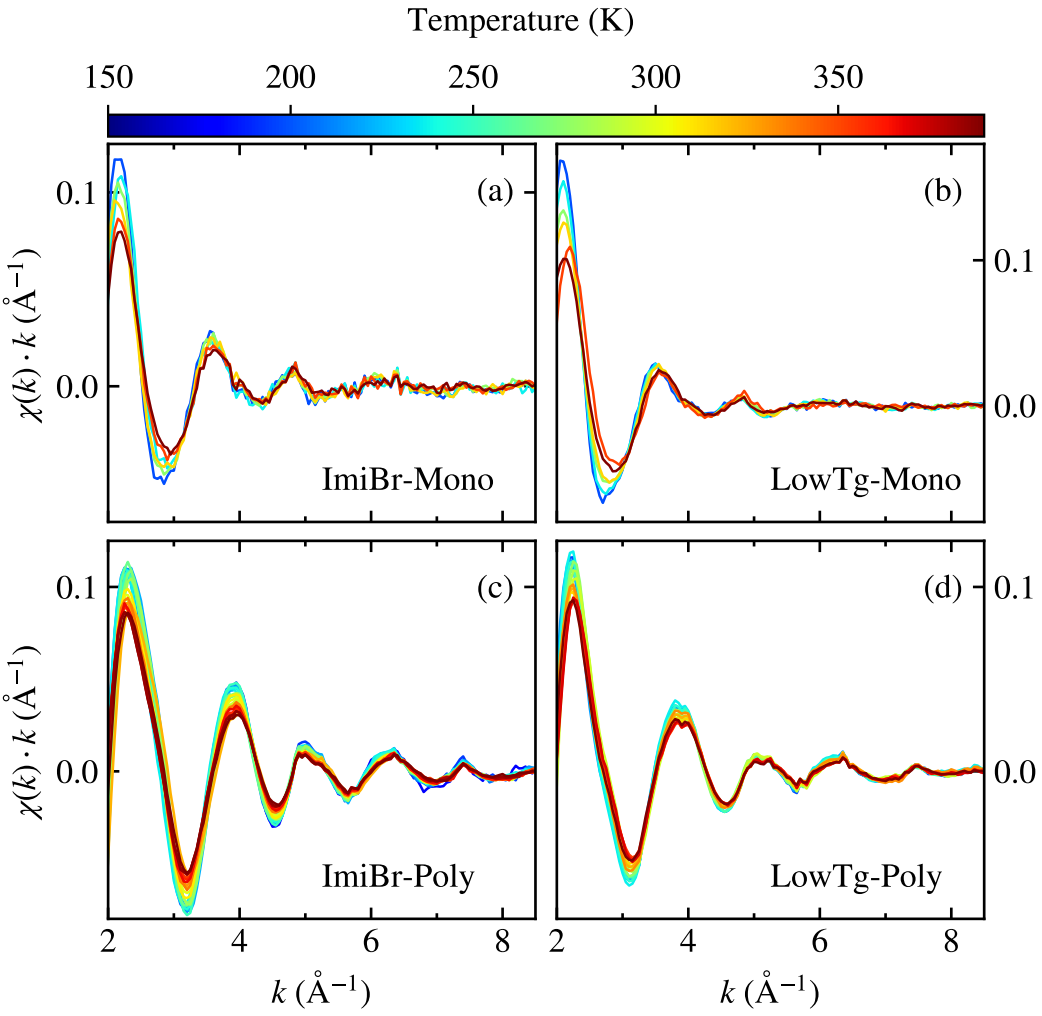

Figure 7.5: The extracted k-weighted EXAFS oscillation of the two monomers (top) and the two polymers (bottom) at various temperature steps.

inducing a shift of the oscillation, indicating that the distance of the bromine anion to the surrounding atoms remains rather unchanged. A Fourier transformation of the EXAFS oscillation yields the pRDF that provides information on the coordination and distance of the local structure surrounding the absorber atom. In particular, the pRDF can be used to study relative changes in the local structural environment of the absorber atom as a function of an external parameter, i.e. temperature in the case of this work. Compared to the RDF, which is calculated in numerous molecular dynamics simulation studies to investigate the structure of a system, the pRDF is shifted to lower distance values caused by the interaction of the photoelectron wave with the excited, positive charged nuclei and the surrounding atoms. According to the literature, the shift is usually in the order of −0.5 Å [296]. The pRDF was calculated by applying the Fourier transform to the *k*-weighted EXAFS oscillations

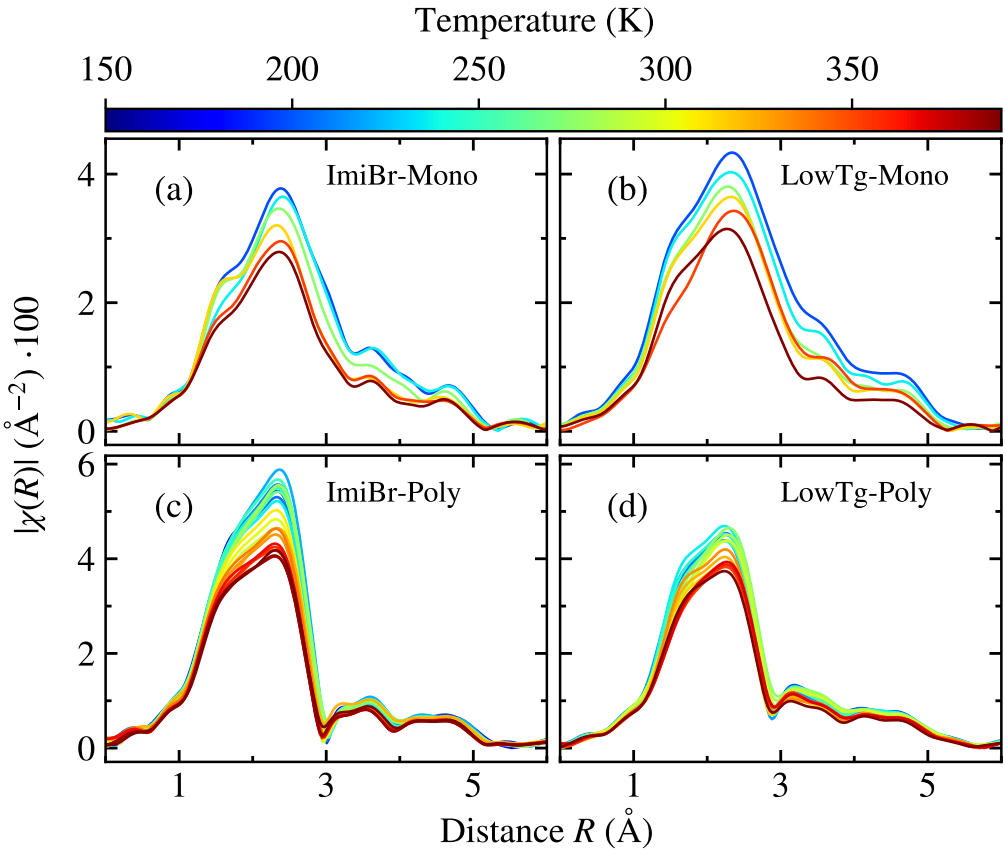

Figure 7.6: The magnitude of the Fourier-transformed of the *k*-weighted EXAFS oscillations in Figure 7.5, i.e. the pRDFs, in a temperature range from 160 K to 400 K for the two monomers ImiBr-Mono (a) and LowTg-Mono (b), and the two polymers ImiBr-Poly (c) and LowTg-Poly (d).

in Figure 7.5 in a k-range from 2 $Å^{-1}$ to 8.5 $Å^{-1}$, after multiplying the data with a Hanning-window function with a width of the cut-off tails of 2 $Å^{-1}$ to smooth the resulting Fourier transformed as it removes ripple and ringing caused by a sudden truncation of the data at the end of the utilized k-range. The resulting magnitudes of the Fourier transformed k-weighted EXAFS oscillations, i.e. the pRDFs, are shown in Figure 7.6 at various temperatures for the two monomers in the top two plots and the two polymers in the lower two plots. In terms of distances, the pRDFs reveal a similar local structural environment of the bromine atoms for all ionic liquids regardless of polymerization or side-chain lengths with a pronounced peak at approximately 2.3 Å. However, with respect to the height of the different maxima, the distance distributions of the two polymer samples are narrower than those of the two monomer samples. In addition, the peaks above 3 Å of the two polymers are more defined than the monomer peaks indicating that the molecular motion of the local structure in the system is suppressed due to the polymerization. The temperature induced changes in the local structure of the bromine atoms are limited to a decease of the overall intensity of the maxima with rising temperature probably induced by the increased thermal motion i.e. disorder in the system. Noteworthy, the distances of the bromine atom to its nearest neighbours hardly change at higher temperature for all investigated ionic liquids, indicating a stable first coordination shell.

7.4.1 Effect of polymerization on structural stability

The influence of the polymerization on the overall structure at room temperature is most pronounced in the analysis of the apolar-polar peak in the XRD patterns, which is significantly increased and altered compared to the molecular ionic liquids, indicating major changes in the cation landscape accompanied by an increase in correlation length of the apolar-polar component. In contrast to these large structural changes, the analysis of the pRDFs reveals that the polymerization hardly changes the distances between the anion and its surrounding atoms, as only a slightly more pronounced long-range order is observed, probably due to an overall more confined structural network in the polymerized ionic liquids. This indicates an overall similar structural environment of the bromine anion, which is presumably located close to the positively charged imidazole ring, regardless of an increased temperature or the polymerization of the cationic group. The structural findings of the qualitative analysis of the determined pRDFs are in line with a previous study on 1-alkyl-3-methylimidazolium bromide, which focused on investigating the structural changes due to an increase of side-chain lengths of up to ten carbon atoms and likewise

found a maximum between 2.2 Å and 2.3 Å in the pRDF for side-chains with more than two carbon atoms [295]. Furthermore, the study found that the shape and position of the pRDF barely changed when the side-chain was extended beyond a length of four, confirming the similarities between the pRDFs of ImiBr and LowTg, which differ in side-chain length by a factor of two but exhibit almost the same peak in terms of form and position.
In order to further investigate the changes of the peak positions due to the polymerization and also to quantify the aforementioned temperature-induced peak shifts, a Gaussian function was fitted to the adjacent peaks and apolar-polar peaks to determine their position. Before performing the Gaussian fit, the apolar-polar peak was extracted by fitting and subtracting a linear function to the underlying signal, which further improves the determination of the peak position. The fitted positions of the adjacent and apolar-polar peaks are shown in the upper and lower two plots of Figure 7.7, respectively. The resulting positions reveal an increase of the apolar-polar distance caused by the polymerization of the sample since the corresponding peak shifts for LowTG and ImiBr from approximately $(0.43 \pm 0.02)\,\text{Å}^{-1}$ to $(0.315 \pm 0.001)\,\text{Å}^{-1}$ and from $(0.484 \pm 0.015)\,\text{Å}^{-1}$ to $(0.282 \pm 0.001)\,\text{Å}^{-1}$, respectively, which corresponds to a change in the correlation length from (14.5 ± 0.4) Å to (19.91 ± 0.09) Å and from (12.97 ± 0.25) Å to (22.30 ± 0.09) Å. The error bars shown are calculated based on the fit of the Gaussian function and reflect the relative errors between the different values, however, the error on the absolute value might be larger due to, e.g. the previous subtraction of the fitted lines. With respect to temperature, the Gaussian fits show that the apolar-polar peak is in general rather stable. A comparison of the determined temperature-dependent peak position of the polymers with the monomers shows that the polymers are more temperature stable, as their peak position hardly changes, while the position for the monomers shifts slightly towards lower q values with rising temperature. In the case of the two monomers, the adjacent peak positions show significant temperature-dependent changes as they shift to lower q values. This trend is also observable for the two polymers, but to a much lesser extent, indicating greater thermal expansion in the two monomers even between neighbouring atoms compared to the polymers.
The temperature-dependent analysis of the adjacent peak in the XRD patterns suggests a stabilizing effect due to the polymerization of the ionic liquid, which partially counteracts the perturbation of the structure caused by an increasing temperature. This becomes evident by comparing the temperature induced changes between 210 K and 390 K of the determined peak positions shown in Figure 7.7 as rather large shifts can be detected of approximately $0.074\,\text{Å}^{-1}$ and $0.056\,\text{Å}^{-1}$ for the monomer LowTg and ImiBr ionic liquids, respectively, which are significantly reduced to $0.025\,\text{Å}^{-1}$ and $0.013\,\text{Å}^{-1}$ after polymerization. The temperature depen-

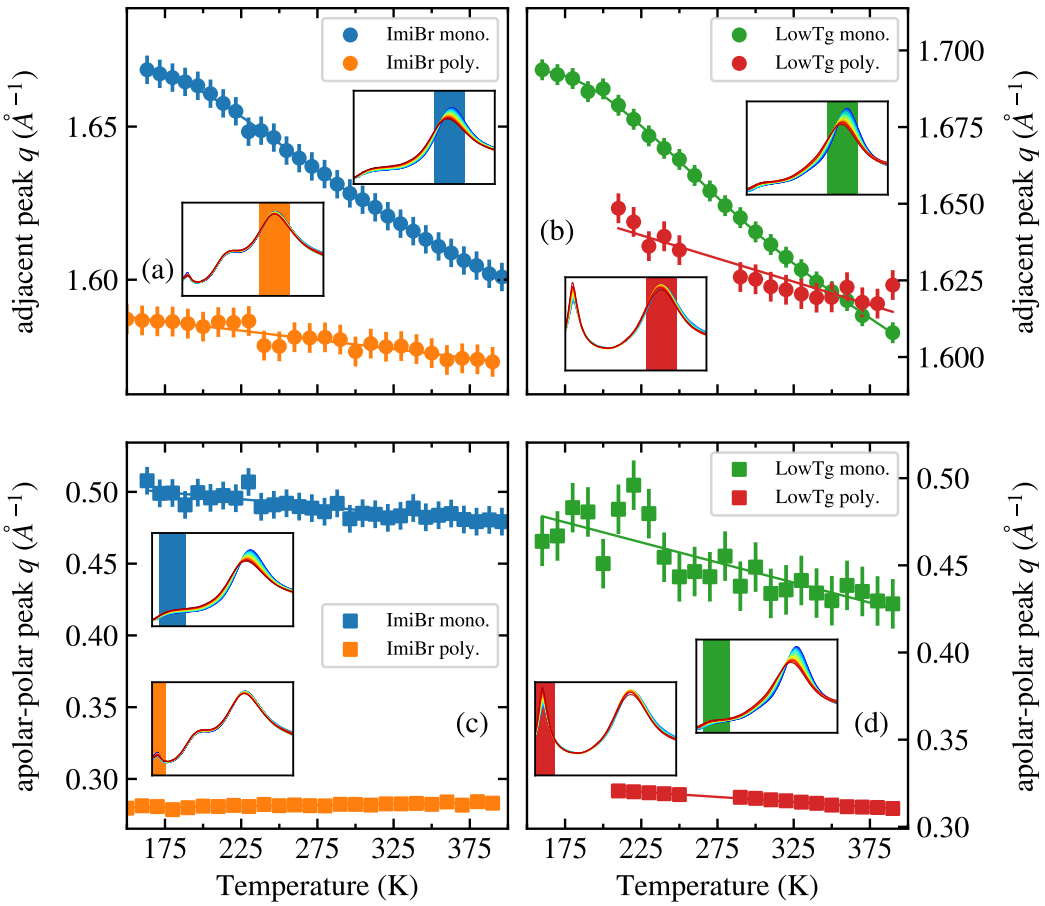

Figure 7.7: The positions of the adjacent peak (a,b) and the apolar-polar peak (c,d) for the ImiBr (a,c) and LowTg (b,d) monomer and polymer ionic liquid as a function of temperature determined with a fit of a Gaussian function. For clarity, the fitted feature of the XRD pattern is indicated in the inset plot with the corresponding colour and lines are plotted as a guide to the eye.

dencies of the monomer and polymer ionic liquids not only differ by a different slope, but the two monomers also show a deviation from the linear curve at temperatures below approximately 200 K. This might be induced by the glass transition of the two monomers, which is between 210 K and 220 K in the case of the ImiBr and is probably at a slightly lower temperature for the LowTg due to the longer side-chain [306–308]. However, this conclusion is ambiguous as an insufficient heat transfer between the Cryostream and the sample at such low temperatures cannot be ruled out as explanation. Investigating the differences in temperature response between monomer and polymer ionic liquids on the anion side by exploiting the determined pRDF in Figure 7.6, reveals considerably smaller differences between

the two systems, as a similar continuous decrease in intensity is observed for all four ionic liquids. This might indicate that the thermal motion of the bromine atoms is not significantly restricted by the polymerization of the cation network.

7.4.2 Influence of the apolar side-chain

Some of the observed features and differences in the XRD patterns between ImiBr and LowTg for both, the molecular and polymerized samples, are connect to the properties of the side-chain of the molecular unit. An example is the peculiar temperature behaviour of the adjacent peak of the polymerized LowTg in Figure 7.4 (d) which gains intensity when the temperature is increased. This dependence is counter-intuitive at first, since an increasing temperature is usually associated with a disturbance of the structural order in the apolar-polar region and thus to a decrease in the intensity of the apolar-polar peak. Indeed, according to Araque *et al.* the temperature increase leads to a reduction of the structural order of the apolar-polar component, however, this reduction allows for a slight increase in the order of the polar-polar component [298, 309]. The polar-polar component refers to correlations between charged components of the ionic liquid, which, however, are not located next to each other but are separated by the apolar tails. However, the change in contributions due to the simultaneous increase and decrease of structural order in the polar-polar and apolar-apolar components, respectively, do not cancel each other out, since the origin of the signal of the polar component can be attributed to the anions which have a larger scattering factor and thus more weight in the detected signal in an XRD experiment [298, 309]. Therefore, with rising temperature, an increase in the intensity of the apolar-polar peak is observed due to the increasing structural order of the polar-polar component, even though the associated structure of the purely apolar component is more disturbed. It is noticeable that this effect only occurs for the polymer LowTg and not for the polymer ImiBr. Although, a conclusive answer cannot be derived unambiguously from the measured data, the reason might be related to one major difference between LowTg and ImiBr namely the position at which the cation is connected to the polymer backbone, which is the apolar tail and the polar head group in the case of ImiBr and LowTg, respectively. The type of polymerization in ImiBr possibly prevents or influences the simultaneous disordering of the apolar component with concomitant ordering of the polar component. However, a simple dependence of the effect with the side-chain length of the ionic liquids cannot be excluded either.
Previous XRD studies on polymerized ionic liquids with varying side-chains observed a linear shift of the apolar-polar peak as a function of side-chain length. In these studies an interdigitation of opposite molecules was observed for longer

side-chains than two. Furthermore, they performed a linear fit of the corresponding distance of the apolar-polar component as a function of the number of carbon atoms in the alkyl side-chain, which revealed slopes and y-axis offsets ranging from 10.2 Å and 1.3 Å $\cdot$ CH_2^{-1} to 7.5 Å and 2 Å $\cdot$ CH_2^{-1} [286, 302, 305]. The determined length of the apolar component for the polymerized ImiBr is significantly larger with a value of (22.3 ± 0.1) Å compared to the previous studies with respect to its side-chain length of five. This increased distance between the apolar domains is probably caused by the position at which the cation is connected to the backbone-chain. In contrast to the previous studies and as mentioned above, in the case of ImiBr, the cation group is attached to the backbone-chain via the end of the apolar side-chain. A similar effect is observed for ionic liquids with very short side-chains, which likewise leads to a close contact between the charged imidazole rings and thus to a strong repulsive interaction that prevents interdigitation of the short aclyl chains [305].
With respect to the monomer ionic liquids, a shift of the apolar-polar peak to larger q values, accompanied by a decrease in peak intensity due to a shortening of side-chain lengths, has also been observed in previous studies [310, 311]. However, comparing the two monomers investigated in this work, the differences in the apolar-polar peak position are minor, although the side-chain length for LowTg is twice as long as for ImiBr. This effect can probably be attributed to the composition of the LowTg side-chain, which consists not only of carbon and hydrogen atoms (alkyl chains) as for ImiBr, but also contains oxygen atoms (polar ether tails). Unlike alkyl chains, these polar diether chains tend to curl toward the cationic head, allowing the anion to solvate not only the charged head group of the cation but also the curled tail group [298, 312]. This mechanism not only shortens the apolar component, resulting in a significantly higher q value of the apolar-polar peak than would be the case for an alkyl side-chain, but it also weakens the separation of polar and apolar groups, leading to an additional decrease in the corresponding peak. This finding confirms the results of a previous study on ionic liquids with polar diether chains [312].

7.5 Summary and conclusion

In this chapter, the structure of four different ionic liquids was investigated by means of XRD and EXAFS as a function of temperature in a range from 160 K to 400 K. The four samples were two monomer ionic liquids and their polymerized counterpart. All observed features of the recorded XRD patterns could be assigned

to various structural properties of the different samples, in accordance with the literature. On this basis, the diffractograms were evaluated and temperature-dependent changes quantified by fitting a Gaussian function to two distinct peaks namely, the apolar-polar and the adjacent peak, whose origin is the alternation of apolar and polar components and the correlation of neighbouring atoms, respectively. The polymerization of the molecular ionic liquids resulted in an enhancement of the apolar-polar peak, accompanied by a shift to smaller q values, indicating an expansion of the apolar component. Furthermore, an overall stabilizing effect of the structure was observed due to the polymerization as both peaks shift to a smaller extend to lower q values with increasing temperature for the two polymer ionic liquids, which is even more pronounced for the adjacent peak and indicates less thermal expansion. The obtained EXAFS oscillations were Fourier transformed to calculate the pRDFs, which revealed a rather similar local structure surrounding the anion for all samples, with a possibly more defined structure at distance around 3 Å in case of the polymer ionic liquids. The overall shape of the obtained pRDFs were in line with the results of a previous study on similar ionic liquid systems. Furthermore, the pRDFs showed no shifts due to an increased temperature as only the peak intensity decreased at higher temperatures due to the thermal motion of the neighbouring atoms of the anion.
Furthermore, a significant importance of the properties and composition of the side-chain for the apolar component in the ionic liquid and consequently the position and shape of the apolar-polar peak was found. Thus, the side-chain of LowTg exhibited an extensive curling i.e. shortening of the apolar component as revealed by the apolar-polar peak position which was determined at significant higher q value than would have been expected from an alkyl side-chain of the same length. In addition, the position of the apolar-polar peak in the XRD patterns of the polymer ImiBr revealed that the polymerization of the cationic groups by connecting its side-chain to the polymer backbone prevents the interdigitation of opposing cations due to the strong Coulomb repulsion of the head group. Such an interdigitation was observed in previous studies in which the cationic head group was attached to the polymer backbone. In summary, it can be concluded from the obtained results that the polymerization of the ionic liquid has a major influence on the apolar-polar component and that both the choice of the cationic side-chain and the connection of the cationic group to the polymer backbone play an important role in the overall structure of the polymerized ionic liquid. This is reflected, among other things, in a significantly increased stability against thermal influences, as was revealed with reference to the investigated temperature range.
Due to the large variety of different structural features investigated, despite the rather small sample set, this work provides a valuable comparative basis for further XRD investigations of molecular and polymerized ionic liquids. Moreover, a

comparison of the results obtained in this work on the structure of ionic liquids with the results of experimental techniques probing the dynamics of the system such as dielectric spectroscopy could be further exploited to link the dynamical with the structural properties of the ionic liquids which would further deepen the understanding of this fascinating liquids in general and in particular of e.g. the conductivity in amorphous conductors by means of a generalized microscopic description of this dynamic process.

8 Conclusion and outlook

In this thesis, the microscopic structure of liquid water and aqueous sodium chloride solution was investigated by means of IXS for a large variety of thermodynamic conditions. The analysis revealed distinct structural changes water undergoes when exposed to high temperatures and/or pressures. It is notable that the water structure's response is complex and vastly different depending on whether the system is pressurised or heated. In addition, the effects of dissolved sodium chloride ions on the water structure are manifold and strongly dependent on the temperature and thus on the ion-ion and ion-water interaction. In the following, a summary of the results of the different studies performed in this thesis is given.
The influence of dissolved sodium chloride on the water structure in a wide temperature range from 25 °C to 600 °C was investigated by a combined experimental and theoretical approach using measured XRS spectra complemented by calculated spectra on the basis of provided AiMD structures, which were further exploited to extract detailed structural information. Within this work, the temperature-dependent experiments were performed on a (2.6 ± 0.2) molal aqueous sodium chloride solution while the experimental data of pure water was taken from a previous study [10] together with generated AiMD trajectories of pure water to recalculate spectra with the same theoretical approach as for the salt solution. The computed spectra revealed an overall good agreement with the experimental spectra, in particular, in terms of the relative changes, which justified to determine structural parameters from the theoretical models. This was further approved by a χ^2 test showing that the models are not interchangeable. This extensive analysis revealed an overall destabilizing influence of the dissolved sodium chloride on the water structure at ambient conditions, which is rather limited to the first hydration shell of the ions. However, with decreasing density, both the experimental spectra and the calculated structural parameters of the two systems exhibited an increasing similarity. A quantitative comparison of the spectral differences between water and the salt solutions in terms of integrated intensities with the amount of associated ions in the system as evaluated from the MD structures implied a strong correlation between these two quantities. This pointed to ion association as the driving force for the decreasing structural differences between the two systems. In addition, analysing the spectral intensities and the computed structural parameters as a function of temperature, a

stabilizing effect on the water structure due to the addition of ions was observable. This slight stabilization was attributed to the increase of bulk density in the salt solutions caused by the excluded volume of the dissolved ions. The determination of the ion clusters in the system revealed a large variety of sizes, occasionally reaching a size of 8 ions at the highest temperature, while most ion pairs are present at 300 °C. These findings challenge the role of dissolved salts as structure breaker and structure maker at higher temperatures. Furthermore, the measured XRS spectra can be used to quantify the accordance of various theoretical models and thereby help to identify the role of hydrogen bonding at supercritical conditions as a mechanism for the formation of structural arrangements, which is still a highly debated subject [15]. Moreover, additional experiments at pressures corresponding to the pressure conditions during the process of metal transportation and ore formation would provide further insights into these highly relevant geochemical processes.
In order to address the ongoing discussion on the pressure response of the water network around 2 kbar to 4 kbar, the influence of high pressure on the water structure at ambient temperature conditions was studied with the same approach, combining the analysis of experimentally recorded XRS spectra with calculated spectra based on structures generated with AiMD simulations and the subsequent extraction of structural parameters from the theoretical model. The AiMD structures were exploited from a previous study on pressurised liquid water and aqueous TMAO solutions [62]. The experimental spectra indicated hardly any structural changes with respect to the closest hydrogen bonded molecules, even at the highest applied pressure of 8.5 kbar. This was confirmed by the calculated numbers of hydrogen bonded molecules, which only increased by 3 %. In particular, the analysis revealed that there is no major breaking of hydrogen bonds between the first and second coordination shell of water, as previously suggested [69]. However, the experimental spectra indicate a continuous approach of water molecules, which are not hydrogen bonded to the water molecule of the scattered oxygen. This is likewise in agreement with the evaluated ratio of hydrogen bonded to non-hydrogen bonded molecules in the close vicinity of a central water molecule as determined from the MD structures, which is gradually decreasing over the entire pressure range. Both the quantitative analysis of the spectral features and the calculated ratio exhibited a change in the slope in its pressure-dependent evolution around 3 kbar, consistent with the pressure at which various previous studies found an anomaly in their measured quantity. This might point towards a transition in the preferred water structure from a low-density to a high-density structure. It should be emphasized that the main conclusions about the pressure-induced changes of the water structure could solely be derived from the experimentally obtained XRS spectra, which underlines the advanced capabilities of this experimental technique to probe the microscopic structure in aqueous fluids. However, the theoretical data nicely confirmed these

findings and provided an additional profound insight into the system. In addition, the spectra of pressurised water were further compared to spectra of ice Ih, ice III and ice VI showing that the spectral changes between ice III and ice VI are similar to the differences between the spectra of liquid water at ambient conditions and 8.5 kbar. This is consistent with the different arrangement of water molecules in the two ice phases, as more non-hydrogen bonded molecules are located in the close vicinity of a central molecule in ice VI than in ice III. Moreover, preliminary XRS experiments were performed on 1 M aqueous trimethylamine-N-oxide solutions. The measured spectra might indicate a different pressure-dependence of some spectral features due to the solute, but the analysis is inconclusive due to the lack of XRS spectra at different pressure points and rather large statistical uncertainties. Similar to the experimental spectra of the aqueous sodium chloride solution recorded under hydrothermal conditions, the experimental data of pressurised water can be further used to benchmark future water models. In addition, spectra of many different ice phases, recorded with the same experimental set-up, could be used to verify to what extend various crystalline ice phases correlate to the structure of water at the corresponding phase boundary. Moreover, completing the preliminary data set of the aqueous TMAO solution could shed light on how the exact process of protein stabilization works at higher pressures and whether it is mediated by the water structure.

So far, the water structure has been analysed by means of XRS on a time-average basis. In order to study the dynamical and structural changes in the water structure due to temperature and the addition of ions, IXS spectra were recorded over a large energy loss and momentum transfer range up to 3 keV and 18.77 $Å^{-1}$, respectively, to map the density response function $\chi(r,t)$ in time and space on sub-angstrom and attosecond scales. The technique was first introduced by Abbamonte *et al.* but on a significant smaller energy loss and momentum transfer range [53]. Thus, on the basis of this pioneering work, a new data treatment procedure was successfully developed to deal with the rising challenges of consistently analysing IXS spectra over such a large scan range. This way, a spatial resolution of 0.34 Å was achieved and a time increment of 0.69 as which corresponds to an improvement by a factor of 3.7 and 59, respectively, compared to the initial study. It was found that the resolved electron density disturbance caused by the incident X-ray photon only affects a relatively small region whose radius barely exceeds 1.5 Å. Hence, the qualitative analysis of $\chi(r,t)$ revealed hardly any changes induced by an increase of temperature or the addition of salts, which is in line with the dynamics of the microscopic water structure, which is almost static on such small time scales. A comparison of $\chi(r,t)$ at different time steps with the previous study exhibited a good agreement despite the vastly different sample environment pointing out the reproducibility of

this experimental technique and the consistency of the developed data treatment procedure. In addition, several parameters were determined to characterise the propagation of the electron density disturbance, namely the velocity, the lifetime and the spatial damping constant, which were indistinguishable within the margin of error for all measured systems despite the elevated temperatures or the addition of salts. For instance, the propagation speed of the disturbance was evaluated with a value of approximately 0.04 Å/as which corresponds to 0.013 % of the speed of light. Moreover, $\chi(q, \omega)$ was used to determine the static electron density around a positive point charge, which revealed an accumulation of electrons within a radius of 1 Å around it and a weak long-range oscillation for larger distances. The long-range oscillation was found to be in good agreement with a previous study on liquid water [240]. There were no unambiguous temperature-dependent differences observable in the static electron density for liquid water. However, the dissolved salts appeared to weaken the long-range oscillation which was attributed to their vastly different charge distribution compared to pure water. The good overall agreement with previous work and the huge improvements of the time and spatial resolution opens exciting opportunities to study valence electron excitations of other sample systems such as inhomogeneous electron gasses by applying the developed data treatment procedure.

To bridge the gap to the study of water ionic liquid mixtures, which are of high relevance for various technical applications, the structure of pure molecular and polymerized ionic liquids without water were studied by means of XRD and EXAFS in a wide range of temperatures from 160 K to 400 K and on a sample set with a huge variety of unique structural features. The analysis of the XRD patterns revealed that the polymerization process has a significant impact on the extent of the apolar component in the systems and stabilizes the ionic liquid against the applied temperatures as considerably less thermal expansion was observed. As probed by the EXAFS experiments, the surrounding structure of the bromine anion was rather unaffected by the polymerization of the ionic liquid or the increased temperatures. It was revealed that the composition of the cationic side-chain and the way in which the cation is connected to the polymer backbone, either via its head or its tail, has a substantial influence on the overall structure. The first one determines if the side-chain is able to curl, as is the case for polar diether side-chains and therefore shorten the apolar component. The latter defines whether opposite side-chains can interdigitate, which is prevented when the side-chains are directly connected to the polymer backbone and the two cationic heads-groups face each other, resulting in strong repulsive Coulomb interactions. The structure and its temperature response could be studied extensively, paving the way for a thorough investigation of ionic liquid-water mixtures, especially the influence of the presence of water on the structure of the ionic liquid and thus its unique properties.

Bibliography

[1] M. F. Chaplin. "Water: Its importance to life." *Biochemistry and Molecular Biology Education* 29.2 (2001), pp. 54–59.

[2] C. A. Dieter, M. A. Maupin, R. R. Caldwell, M. A. Harris, T. I. Ivahnenko, J. K. Lovelace, N. L. Barber, and K. S. Linsey. *Estimated Use of Water in the United States in 2015: U.S. Geological Survey Circular 1441*. 2017, pp. 1–76.

[3] K. Frost and I. Hua. "A spatially explicit assessment of water use by the global semiconductor industry." *2017 IEEE Conference on Technologies for Sustainability, SusTech 2017*. Vol. 2018-Janua. 2018, pp. 1–5.

[4] Z. U. Mian and D. C. Tozer. "No water, no plate tectonics: convective heat transfer and the planetary surfaces of Venus and Earth." *Terra Nova* 2.5 (1990), pp. 455–459.

[5] K. Regenauer-Lieb, D. A. Yuen, and J. Branlund. "The initiation of subduction: Criticality by addition of water?" *Science* 294.5542 (2001), pp. 578–580.

[6] S. S. Russell, C. J. Ballentine, and M. M. Grady. "The origin, history and role of water in the evolution of the inner solar system." *Philosophical Transactions of the Royal Society A: Mathematical, Physical and Engineering Sciences* 375.2094 (2017), pp. 4–6.

[7] S. Avola, M. Guillot, D. da Silva-Perez, S. Pellet-Rostaing, W. Kunz, and F. Goettmann. "Organic chemistry under hydrothermal conditions." *Pure and Applied Chemistry* 85.1 (2013), pp. 89–103.

[8] J. K. Fogo, S. W. Benson, and C. S. Copeland. "The Electrical Conductivity of Supercritical Solutions of Sodium Chloride and Water." *The Journal of Chemical Physics* 22.2 (1954), pp. 212–216.

[9] P. Postorino, R. H. Tromp, M. A. Ricci, A. K. Soper, and G. W. Neilson. "The interatomic structure of water at supercritical temperatures." *Nature* 366.6456 (1993), pp. 668–670.

[10] C. J. Sahle, C. Sternemann, C. Schmidt, S. Lehtola, S. Jahn, L. Simonelli, S. Huotari, M. Hakala, T. Pylkkänen, A. Nyrow, K. Mende, M. Tolan, K. Hämäläinen, and M. Wilke. "Microscopic structure of water at elevated pressures and temperatures." *Proceedings of the National Academy of Sciences of the United States of America* 110.16 (2013), pp. 6301–6.

[11] P. B. Balbuena, K. P. Johnston, and P. J. Rossky. "Molecular Simulation of a Chemical Reaction in Supercritical Water." *Journal of the American Chemical Society* 116.6 (1994), pp. 2689–2690.

[12] N. Yoshii, H. Yoshie, S. Miura, and S. Okazaki. "A molecular dynamics study of sub- and supercritical water using a polarizable potential model." *Journal of Chemical Physics* 109.12 (1998), pp. 4873–4884.

[13] A. G. Kalinichev and S. V. Churakov. "Size and topology of molecular clusters in supercritical water: A molecular dynamics simulation." *Chemical Physics Letters* 302.5-6 (1999), pp. 411–417.

[14] R. D. Mountain. "Voids and clusters in expanded water." *Journal of Chemical Physics* 110.4 (1999), pp. 2109–2115.

[15] P. Schienbein and D. Marx. "Supercritical Water is not Hydrogen Bonded." *Angewandte Chemie* 59.42 (2020), pp. 18578–18585.

[16] D. R. Canchi and A. E. García. "Cosolvent effects on protein stability." *Annual Review of Physical Chemistry* 64 (2013), pp. 273–293.

[17] K. Julius, J. Weine, M. Berghaus, N. König, M. Gao, J. Latarius, M. Paulus, M. A. Schroer, M. Tolan, and R. Winter. "Water-Mediated Protein-Protein Interactions at High Pressures are Controlled by a Deep-Sea Osmolyte." *Physical Review Letters* 121.3 (2018), p. 38101.

[18] R. P. Lowell and M. DuBose. "Hydrothermal systems on Europa." *Geophysical Research Letters* 32.5 (2005), pp. 1–4.

[19] H. W. Hsu, F. Postberg, Y. Sekine, T. Shibuya, S. Kempf, M. Horányi, A. Juhász, N. Altobelli, K. Suzuki, Y. Masaki, T. Kuwatani, S. Tachibana, S. I. Sirono, G. Moragas-Klostermeyer, and R. Srama. "Ongoing hydrothermal activities within Enceladus." *Nature* 519.7542 (2015), pp. 207–210.

[20] D. Deamer and B. Damer. "Can Life Begin on Enceladus? A Perspective from Hydrothermal Chemistry." *Astrobiology* 17.9 (2017), pp. 834–839.

[21] F. Li, Q. Cui, Z. He, T. Cui, J. Zhang, Q. Zhou, G. Zou, and S. Sasaki. "High pressure-temperature Brillouin study of liquid water: Evidence of the structural transition from low-density water to high-density water." *Journal of Chemical Physics* 123.17 (2005), p. 174511.

[22] S. Fanetti, A. Lapini, M. Pagliai, M. Citroni, M. Di Donato, S. Scandolo, R. Righini, and R. Bini. "Structure and dynamics of low-density and high-density liquid water at high pressure." *Journal of Physical Chemistry Letters* 5.1 (2014), pp. 235–240.

[23] D. Bermúdez-Aguirre and G. V. Barbosa-Cánovas. "An Update on High Hydrostatic Pressure, from the Laboratory to Industrial Applications." *Food Engineering Reviews* 3.1 (2011), pp. 44–61.

[24] L. D. Talley. "Salinity Patterns in the Ocean." *Encyclopedia of Global Environmental Change* 1.1 (2002), pp. 1–11.

[25] G. Lagerloef, R. Schmitt, J. Schanze, and H. Y. Kao. "The ocean and the global water cycle." *Oceanography* 23.4 (2010), pp. 82–93.

[26] D. L. Leach, R. D. Taylor, D. L. Fey, S. F. Diehl, and R. W. Saltus. *A deposit model for Mississippi Valley-type lead-zinc ores: Chapter A in mineral deposit models for resource assessment*. Tech. rep. U.S. Geological Survey, 2010.

[27] S. J. Fowler and D. M. Sherman. "The nature of NaCl–H2O deep fluids from ab initio molecular dynamics at 0.5–4.5 GPa, 20–800 °C, and 1–14 m NaCl." *Geochimica et Cosmochimica Acta* 277 (2020), pp. 243–264.

[28] A. Nilsson and L. G. M. Pettersson. "The structural origin of anomalous properties of liquid water." *Nature communications* 6 (2015), p. 8998.

[29] R. J. Speedy. "Stability-limit conjecture. An interpretation of the properties of water." *Journal of Physical Chemistry* 86.6 (1982), pp. 982–991.

[30] P. H. Poole, F. Sciortino, U. Essmann, and H. E. Stanley. "Phase behaviour of metastable water." *Nature* 360.6402 (1992), pp. 324–328.

[31] P. H. Poole, F. Sciortino, T. Grande, H. E. Stanley, and C. A. Angell. "Effect of hydrogen bonds on the thermodynamic behavior of liquid water." *Physical Review Letters* 73.12 (1994), pp. 1632–1635.

[32] S. Sastry, P. G. Debenedetti, F. Sciortino, and H. E. Stanley. "Singularity-free interpretation of the thermodynamics of supercooled water." *Physical Review E* 53.6 (1996), pp. 6144–6154.

[33] P. Gallo, K. Amann-Winkel, C. A. Angell, M. A. Anisimov, F. Caupin, C. Chakravarty, E. Lascaris, T. Loerting, A. Z. Panagiotopoulos, J. Russo, J. A. Sellberg, H. E. Stanley, H. Tanaka, C. Vega, L. Xu, and L. G. M. Pettersson. "Water: A Tale of Two Liquids." *Chemical Reviews* 116.13 (2016), pp. 7463–7500.

[34] C. E. Manning. "The chemistry of subduction-zone fluids." *Earth and Planetary Science Letters* 223.1-2 (2004), pp. 1–16.

[35] P. A. Marrone, M. Hodes, K. A. Smith, and J. W. Tester. "Salt precipitation and scale control in supercritical water oxidation - Part B: Commercial/full-scale applications." *Journal of Supercritical Fluids* 29.3 (2004), pp. 289–312.

[36] D. V. Antsyshkin, A. N. Dunaeva, and O. L. Kuskov. "Thermodynamics of phase transitions in the system ice VI-ice VII-water." *Geochemistry International* 48.7 (2010), pp. 633–642.

[37] A. V. Okhulkov, Y. N. Demianets, and Y. E. Gorbaty. "X-ray scattering in liquid water at pressures of up to 7.7 kbar: Test of a fluctuation model." *The Journal of Chemical Physics* 100.2 (1994), pp. 1578–1588.

[38] M. Krisch, P. Loubeyre, G. Ruocco, F. Sette, A. Cunsolo, M. D'Astuto, R. LeToullec, M. Lorenzen, A. Mermet, G. Monaco, and R. Verbeni. "Pressure Evolution of the High-Frequency Sound Velocity in Liquid Water." *Physical Review Letters* 89.12 (2002), pp. 2–5.

[39] M. A. Schroer, J. Markgraf, D. C. Wieland, C. J. Sahle, J. Möller, M. Paulus, M. Tolan, and R. Winter. "Nonlinear pressure dependence of the interaction potential of dense protein solutions." *Physical Review Letters* 106.17 (2011), pp. 2–5.

[40] A. V. Romanenko, S. V. Rashchenko, S. V. Goryainov, A. Y. Likhacheva, and A. V. Korsakov. "In Situ Raman Study of Liquid Water at High Pressure." *Applied Spectroscopy* 72.6 (2018), pp. 847–852.

[41] P. Wernet, D. Nordlund, U. Bergmann, M. Cavalleri, N. Odelius, H. Ogasawara, L. Å. Näslund, T. K. Hirsch, L. Ojamäe, P. Glatzel, L. G. Pettersson, and A. Nilsson. "The Structure of the First Coordination Shell in Liquid Water." *Science* 304.5673 (2004), pp. 995–999.

[42] T. Head-Gordon and G. Hura. "Water structure from scattering experiments and simulation." *Chemical Reviews* 102.8 (2002), pp. 2651–2670.

[43] W. Schülke. *Electron Dynamics by Inelastic X-Ray Scattering*. Oxford Univ Press, 2007.

[44] T. Suzuki. *X-Ray Raman Scattering. Experiment. I*. 1967.

[45] Y. Mizuno and Y. Ohmura. "Theory of X-Ray Raman Scattering." *Journal of the Physical Society of Japan* 22.2 (1967), pp. 445–449.

[46] K. Tohji and Y. Udagawa. "Novel approach for structure analysis by x-ray Raman scattering." *Physical Review B* 36.17 (1987), pp. 9410–9412.

[47] H. Nagasawa, S. Mourikis, and S. Winfried. "X-Ray Raman Spectrum Of Li, Be and Graphite in a High-Resolution Inelastic Synchrotron X-Ray Scattering Experiment." *Journal of the Physical Society of Japan* 58.2 (1989), pp. 710–717.

[48] M. Krisch and F. Sette. "X-ray Raman scattering from low Z materials." *Surface Review and Letters* 9.2 (2002), pp. 969–976.

[49] U. Bergmann, P. Glatzel, and S. P. Cramer. "Bulk-sensitive XAS characterization of light elements: From X-ray Raman scattering to X-ray Raman spectroscopy." *Microchemical Journal* 71.2-3 (2002), pp. 221–230.

[50] C. Sternemann and M. Wilke. "Spectroscopy of low and intermediate Z elements at extreme conditions: in situ studies of Earth materials at pressure and temperature via X-ray Raman scattering." *High Pressure Research* 36.3 (2016), pp. 275–292.

[51] Y. Q. Cai, H. K. Mao, P. C. Chow, J. S. Tse, Y. Ma, S. Patchkovskii, J. F. Shu, V. Struzhkin, R. J. Hemley, H. Ishii, C. C. Chen, I. Jarrige, C. T. Chen, S. R. Shieh, E. P. Huang, and C. C. Kao. "Ordering of Hydrogen Bonds in High-Pressure Low-Temperature H2O." *Physical Review Letters* 94.2 (2005), pp. 1–4.

[52] T. Pylkkänen, V. M. Giordano, J. C. Chervin, A. Sakko, M. Hakala, J. A. Soininen, K. Hämäläinen, G. Monaco, and S. Huotari. "Role of non-hydrogen-bonded molecules in the oxygen K-edge spectrum of ice." *Journal of Physical Chemistry B* 114.11 (2010), pp. 3804–3808.

[53] P. Abbamonte, K. D. Finkelstein, M. D. Collins, and S. M. Gruner. "Imaging density disturbances in water with a 41.3-attosecond time resolution." *Physical Review Letters* 92.23 (2004), p. 237401.

[54] P. Abbamonte, G. C. L. Wong, D. G. Cahill, J. P. Reed, R. H. Coridan, N. W. Schmidt, G. H. Lai, Y. I. Joe, and D. Casa. "Ultrafast imaging and the phase problem for inelastic X-ray scattering." *Advanced Materials* 22.10 (2010), pp. 1141–1147.

[55] J. L. Anthony, E. J. Maginn, and J. F. Brennecke. "Solution thermodynamics of imidazolium-based ionic liquids and water." *Journal of Physical Chemistry B* 105.44 (2001), pp. 10942–10949.

[56] L. E. Ficke and J. F. Brennecke. "Interactions of ionic liquids and water." *Journal of Physical Chemistry B* 114.32 (2010), pp. 10496–10501.

[57] L. Cammarata, S. G. Kazarian, P. A. Salter, and T. Welton. "Molecular states of water in room temperature ionic liquids." *Physical Chemistry Chemical Physics* 3.23 (2001), pp. 5192–5200.

[58] G. W. Robinson, S. Singh, S.-B. Zhu, and M. W. Evans. *Water in Biology, Chemistry and Physics*. World Scientific, 1996.

[59] F. Franks. *Water. A Matrix of Life*. RSC Paperbacks. The Royal Society of Chemistry, 2000, pp. X001–X004.

[60] M. Tarek and D. J. Tobias. "Role of Protein-Water Hydrogen Bond Dynamics in the Protein Dynamical Transition." *Physical Review Letters* 88.13 (2002), p. 4.

[61] A. Jha. *The water book*. Headline, 2015.

[62] S. Imoto, H. Forbert, and D. Marx. "Water structure and solvation of osmolytes at high hydrostatic pressure: Pure water and TMAO solutions at 10 kbar versus 1 bar." *Physical Chemistry Chemical Physics* 17.37 (2015), pp. 24224–24237.

[63] C. Schmidt and C. E. Manning. "Pressure-induced ion pairing in MgSO4 solutions: Implications for the oceans of icy worlds." *Geochemical Perspectives Letters* 3.1 (2017), pp. 66–74.

[64] T. Yamaguchi, N. Fukuyama, K. Yoshida, and Y. Katayama. "Ion Solvation and Water Structure in an Aqueous Sodium Chloride Solution in the Gigapascal Pressure Range." *Journal of Physical Chemistry Letters* 12.0 (2021), pp. 250–256.

[65] P. Kumar, S. Han, and H. E. Stanley. "Anomalies of water and hydrogen bond dynamics in hydrophobic nanoconfinement." *Journal of Physics Condensed Matter* 21.50 (2009), p. 504108.

[66] A. Nilsson and L. Pettersson. "Perspective on the structure of liquid water." *Chemical Physics* 389.1-3 (2011), pp. 1–34.

[67] G. Pallares, M. A. Gonzalez, J. L. F. Abascal, C. Valeriani, and F. Caupin. "Equation of state for water and its line of density maxima down to -120 MPa." *Physical Chemistry Chemical Physics* 18.8 (2016), pp. 5896–5900.

[68] V. Holten, C. Qiu, E. Guillerm, M. Wilke, J. Rička, M. Frenz, and F. Caupin. "Compressibility Anomalies in Stretched Water and Their Interplay with Density Anomalies." *Journal of Physical Chemistry Letters* 8.22 (2017), pp. 5519–5522.

[69] A. K. Soper and M. A. Ricci. "Structures of high-density and low-density water." *Physical Review Letters* 84.13 (2000), pp. 2881–2884.

[70] K. Ichikawa, Y. Kameda, T. Yamaguchi, H. Wakita, and M. Misawa. "Neutron-diffraction investigation of the intramolecular structure of a water molecule in the liquid phase at high temperatures." *Molecular Physics* 73.1 (1991), pp. 79–86.

[71] G. S. Tschumper, M. L. Leininger, B. C. Hoffman, E. F. Valeev, H. F. Schaefer, and M. Quack. "Anchoring the water dimer potential energy surface with explicitly correlated computations and focal point analyses." *Journal of Chemical Physics* 116.2 (2002), pp. 690–701.

[72] D. Eisenberg and W. Kauzmann. *The Structure and Properties of Water*. Vol. 15. Oxford University Press, 2005.

[73] W. L. Jorgensen and J. D. Madura. "Temperature and size dependence for monte carlo simulations of TIP4P water." *Molecular Physics* 56.6 (1985), pp. 1381–1392.

[74] S. W. Benson. "Bond energies." *Journal of Chemical Education* 42.9 (1965), p. 502.

[75] H. Lu, Y. Wang, Y. Wu, P. Yang, L. Li, and S. Li. "Hydrogen-bond network and local structure of liquid water: An atoms-in-molecules perspective." *Journal of Chemical Physics* 129.12 (2008).

[76] U. Bergmann, A. Di Cicco, P. Wernet, E. Principi, P. Glatzel, and A. Nilsson. "Nearest-neighbor oxygen distances in liquid water and ice observed by x-ray Raman based extended x-ray absorption fine structure." *Journal of Chemical Physics* 127.17 (2007).

[77] V. Migliorati, G. Chillemi, G. Mancini, A. Zitolo, S. Tatoli, A. Filipponi, and P. D'Angelo. "Ion hydration in high-density water." *Journal of Physics: Conference Series* 190 (2009).

[78] M. Chen, H. Y. Ko, R. C. Remsing, M. F. Calegari Andrade, B. Santra, Z. Sun, A. Selloni, R. Car, M. L. Klein, J. P. Perdew, and X. Wu. "Ab initio theory and modeling of water." *Proceedings of the National Academy of Sciences of the United States of America* 114.41 (2017), pp. 10846–10851.

[79] D. C. Rapaport. "Hydrogen bonds in water network organization and lifetimes." *Molecular Physics* 50.5 (1983), pp. 1151–1162.

[80] J. Martí. "Dynamic properties of hydrogen-bonded networks in supercritical water." *Physical Review E - Statistical Physics, Plasmas, Fluids, and Related Interdisciplinary Topics* 61.1 (2000), pp. 449–456.

[81] A. M. Saitta and F. Datchi. "Structure and phase diagram of high-density water: The role of interstitial molecules." *Physical Review E* 67.2 (2003), p. 4.

[82] D. P. Fernández, A. R. Goodwin, E. W. Lemmon, J. M. Levelt Sengers, and R. C. Williams. "A formulation for the static permittivity of water and steam at temperatures from 238 K to 873 K at pressures up to 1200 MPa, including derivatives and Debye-Hückel coefficients." *Journal of Physical and Chemical Reference Data* 26.4 (1997), pp. 1125–1166.

[83] W. M. Haynes, D. R. Lide, and T. J. Bruno. *CRC handbook of chemistry and physics : a ready-reference book of chemical and physical data*. English. Ninety-seven edition. CRC Press, 2017.

[84] S. Varma and S. B. Rempe. "Coordination numbers of alkali metal ions in aqueous solutions." *Biophysical Chemistry* 124.3 (2006), pp. 192–199.

[85] N. Akiya and P. E. Savage. "Roles of Water for Chemical Reactions in High-Temperature Water." *Chemical Reviews* 102.8 (2002), pp. 2725–2750.

[86] J. Niskanen, C. J. Sahle, K. Gilmore, F. Uhlig, J. Smiatek, and A. Föhlisch. "Disentangling structural information from core-level excitation spectra." *Physical Review E* 96.1 (2017), pp. 1–8.

[87] A. Luzar and D. Chandler. "Effect of environment on hydrogen bond dynamics in liquid water." *Physical Review Letters* 76.6 (1996), pp. 928–931.

[88] J. S. Tse, D. M. Shaw, D. D. Klug, S. Patchkovskii, G. Vankó, G. Monaco, and M. Krisch. "X-ray Raman spectroscopic study of water in the condensed phases." *Physical Review Letters* 100.9 (2008), pp. 1–4.

[89] J. Niskanen, M. Fondell, C. J. Sahle, S. Eckert, R. M. Jay, K. Gilmore, A. Pietzsch, M. Dantz, X. Lu, D. E. McNally, T. Schmitt, V. Vaz da Cruz, V. Kimberg, F. Gel'mukhanov, and A. Föhlisch. "Compatibility of quantitative X-ray spectroscopy with continuous distribution models of water at ambient conditions." *Proceedings of the National Academy of Sciences of the United States of America* 116.10 (2019), pp. 4058–4063.

[90] P. Schienbein and D. Marx. "Assessing the properties of supercritical water in terms of structural dynamics and electronic polarization effects." *Physical Chemistry Chemical Physics* 22.19 (2020), pp. 10462–10479.

[91] M. Blume. "Magnetic scattering of x rays (invited)." *Journal of Applied Physics* 57.8 (1985), pp. 3615–3618.

[92] H. A. Kramers and W. Heisenberg. "Über die Streuung von Strahlung durch Atome." *Zeitschrift für Physik* 31.1 (1925), pp. 681–708.

[93] S. X. Wang and L. F. Zhu. "Non-resonant inelastic X-ray scattering spectroscopy: A momentum probe to detect the electronic structures of atoms and molecules." *Matter and Radiation at Extremes* 5.5 (2020), p. 054201.

[94] K. Sturm. "Dynamic Structure Factor: An Introduction." *Zeitschrift fur Naturforschung - Section A Journal of Physical Sciences* 48.1-2 (1993), pp. 233–242.

[95] L. Van Hove. "Correlations in space and time and born approximation scattering in systems of interacting particles." *Physical Review* 95.1 (1954), pp. 249–262.

[96] U. Bergmann, O. C. Mullins, and S. P. Cramer. "X-ray Raman spectroscopy of carbon in asphaltene: Light element characterization with bulk sensitivity." *Analytical Chemistry* 72.11 (2000), pp. 2609–2612.

[97] A. Nyrow, C. Sternemann, M. Wilke, R. A. Gordon, K. Mende, H. Yavaş, L. Simonelli, N. Hiraoka, C. J. Sahle, S. Huotari, G. B. Andreozzi, A. B. Woodland, M. Tolan, and J. S. Tse. "Iron speciation in minerals and glasses probed by M2/3-edge X-ray Raman scattering spectroscopy." *Contributions to Mineralogy and Petrology* 167.5 (2014), p. 1012.

[98] C. Sternemann, M. Volmer, M. Paulus, H. Enkisch, M. Tolan, W. Schülke, A. Soininen, H. Nagasawa, and G. Schmidt. "Momentum-transfer dependence of x-ray Raman scattering at the Be K-edge." *Physical Review B* 68.11 (2003), p. 035111.

[99] J. A. Soininen, A. L. Ankudinov, and J. J. Rehr. "Inelastic scattering from core electrons: A multiple scattering approach." *Physical Review B* 72.4 (2005), p. 045136.

[100] J. A. Soininen, A. Mattila, J. J. Rehr, S. Galambosi, and K. Hämäläinen. "Experimental determination of the core-excited electron density of states." *Journal of Physics Condensed Matter* 18.31 (2006), pp. 7327–7336.

[101] H. Yavaş, M. Sundermann, K. Chen, A. Amorese, A. Severing, H. Gretarsson, M. W. Haverkort, and L. H. Tjeng. "Direct imaging of orbitals in quantum materials." *Nature Physics* 15.6 (2019), pp. 559–562.

[102] R. Kubo. "The fluctuation-dissipation theorem." *Reports on Progress in Physics* 29 (1966), p. 255.

[103] P. Abbamonte, J. P. Reed, Y. I. Joe, Y. Gan, and D. Casa. "Implicit spatial averaging in inversion of inelastic x-ray scattering data." *Physical Review B* 80.5 (2009), p. 054302.

[104] D. Koningsberger and R. Prins. *X-Ray Absorption: Principles, Applications, Techniques of EXAFS, SEXAFS and XANES*. Wiley, 1987.

[105] C. Bessada, D. Zanghi, M. Salanne, A. Gil-Martin, M. Gibilaro, P. Chamelot, L. Massot, A. Nezu, and H. Matsuura. "Investigation of ionic local structure in molten salt fast reactor LiF-ThF4-UF4 fuel by EXAFS experiments and molecular dynamics simulations." *Journal of Molecular Liquids* 307 (2020), p. 112927.

[106] J. Prietzel, W. Klysubun, and L. C. C. Hurtarte. "The fate of calcium in temperate forest soils: a Ca K-edge XANES study." *Biogeochemistry* 6 (2020), pp. 195–222.

[107] S. Diaz-Moreno, A. Munoz-Paez, J. M. Martinez, R. R. Pappalardo, and E. Sanchez Marcos. "EXAFS investigation of inner- and outer-sphere chloroaquo complexes of Cr3+ in aqueous solutions." *Journal of the American Chemical Society* 118.50 (1996), pp. 12654–12664.

[108] M. Krstulović, A. D. Rosa, N. Biedermann, G. Spiekermann, T. Irifune, M. Muñoz, and M. Wilke. "Ge coordination in NaAlGe3O8 glass upon compression to 131 GPa." *Physical Review B* 101.21 (2020), pp. 1–12.

[109] E. A. Stern. "Structure determination by X-ray absorption." *Contemporary Physics* 19.4 (1978), pp. 289–310.

[110] J. J. Rehr and R. C. Albers. "Theoretical approaches to x-ray absorption fine structure." *Reviews of Modern Physics* 72.3 (2000), p. 621.

[111] J. Als-Nielsen and D. McMorrow. *Elements of Modern X-ray Physics*. 2011.

[112] D. E. Sayers, E. A. Stern, and F. W. Lytle. "New technique for investigating noncrystalline structures: Fourier analysis of the extended x-ray-absorption fine structure." *Physical Review Letters* 27.18 (1971), pp. 1204–1207.

[113] P. D'Angelo, A. Zitolo, V. Migliorati, E. Bodo, G. Aquilanti, J. L. Hazemann, D. Testemale, G. Mancini, and R. Caminiti. "X-Ray absorption spectroscopy investigation of 1-alkyl-3-methylimidazolium bromide salts." *Journal of Chemical Physics* 135.7 (2011).

[114] M. Elbers, C. Sternemann, K. Julius, M. Paulus, G. Surmeier, N. König, J. Nase, J. Bolle, R. Wagner, T. Irifune, and M. Tolan. "Pressure stability of the first hydration shell of yttrium in aqueous YCl3 solution." *High Pressure Research* 40.1 (2020), pp. 194–204.

[115] J. M. Cowley. *Diffraction physics*. 2nd. North-Holland, 1981.

[116] M. A. Schroer, M. Paulus, C. Jeworrek, C. Krywka, S. Schmacke, Y. Zhai, D. C. Wieland, C. J. Sahle, M. Chimenti, C. A. Royer, B. Garcia-Moreno, M. Tolan, and R. Winter. "High-pressure SAXS study of folded and unfolded ensembles of proteins." *Biophysical Journal* 99.10 (2010), pp. 3430–3437.

[117] C. Branci, M. Womes, P. E. Lippens, J. Olivier-Fourcade, and J. C. Jumas. "Use of X-ray absorption spectra as a 'fingerprint' of the local environment in complex chalcogenides." *Journal of Solid State Chemistry* 150.2 (2000), pp. 363–370.

[118] C. Weis, C. Sternemann, V. Cerantola, C. J. Sahle, G. Spiekermann, M. Harder, Y. Forov, A. Kononov, R. Sakrowski, H. Yavaş, M. Tolan, and M. Wilke. "Pressure driven spin transition in siderite and magnesiosiderite single crystals." *Scientific Reports* 7.1 (2017), pp. 1–10.

[119] J. J. Rehr, J. J. Kas, F. D. Vila, M. P. Prange, and K. Jorissen. "Parameter-free calculations of X-ray spectra with FEFF9." *Physical Chemistry Chemical Physics* 12.21 (2010), pp. 5503–5513.

[120] K. Gilmore, J. Vinson, E. L. Shirley, D. Prendergast, C. D. Pemmaraju, J. J. Kas, F. D. Vila, and J. J. Rehr. "Efficient implementation of core-excitation Bethe-Salpeter equation calculations." *Computer Physics Communications* 197 (2015), pp. 109–117.

[121] J. Lehtola, M. Hakala, A. Sakko, and K. Hämäläinen. "ERKALE-A flexible program package for X-ray properties of atoms and molecules." *Journal of Computational Chemistry* 33.18 (2012), pp. 1572–1585.

[122] C. Fiolhais, F. Nogueira, and M. A. L. Marques. *A Primer in Density Functional Theory*. 1. 2003.

[123] P. Hohenberg and W. Kohn. "Inhomogeneous Electron Gas." *Physical Review* 136.3B (1964), B864–B871.

[124] W. Kohn and L. J. Sham. "Self-Consistent Equations Including Exchange and Correlation Effects." *American Physical Society* 140.4a (1965), A1133–A1138.

[125] J. P. Perdew, K. Burke, and M. Ernzerhof. "Generalized gradient approximation made simple." *Physical Review Letters* 77.18 (1996), pp. 3865–3868.

[126] T. J. Giese and D. M. York. "Density-functional expansion methods: Evaluation of LDA, GGA, and meta-GGA functionals and different integral approximations." *Journal of Chemical Physics* 133.24 (2010).

[127] L. Fritsche. "Generalized Kohn-Sham theory for electronic excitations in realistic systems." *Physical Review B* 33.6 (1986), pp. 3976–3989.

[128] A. Sakko, M. Hakala, J. A. Soininen, and K. Hämäläinen. "Density functional study of x-ray Raman scattering from aromatic hydrocarbons and polyfluorene." *Physical Review B* 76.20 (2007), pp. 1–7.

[129] J. C. Slater and K. H. Johnson. "Self-consistent-field Xα cluster method for polyatomic molecules and solids." *Physical Review B* 5.3 (1972), pp. 844–853.

[130] L. Triguero, L. Pettersson, and H. Ågren. "Calculations of near-edge x-ray-absorption spectra of gas-phase and chemisorbed molecules by means of density-functional and transition-potential theory." *Physical Review B - Condensed Matter and Materials Physics* 58.12 (1998), pp. 8097–8110.

[131] M. Leetmaa, M. P. Ljungberg, A. Lyubartsev, A. Nilsson, and L. G. Pettersson. "Theoretical approximations to X-ray absorption spectroscopy of liquid water and ice." *Journal of Electron Spectroscopy and Related Phenomena* 177.2-3 (2010), pp. 135–157.

[132] J. Sánchez-Oneto, J. R. Portela, E. Nebot, and E. Martínez de la Ossa. "Hydrothermal oxidation: Application to the treatment of different cutting fluid wastes." *Journal of Hazardous Materials* 144.3 (2007), pp. 639–644.

[133] J. A. Onwudili, E. Yildirir, and P. T. Williams. "Catalytic hydrothermal degradation of carbon reinforced plastic wastes for carbon fibre and chemical feedstock recovery." *Waste and Biomass Valorization* 4.1 (2013), pp. 87–93.

[134] R. Morales Ibarra, M. Sasaki, M. Goto, A. T. Quitain, S. M. García Montes, and J. A. Aguilar-Garib. "Carbon fiber recovery using water and benzyl alcohol in subcritical and supercritical conditions for chemical recycling of thermoset composite materials." *Journal of Material Cycles and Waste Management* 17.2 (2015), pp. 369–379.

[135] A. Kruse. "Hydrothermal biomass gasification." *Journal of Supercritical Fluids* 47.3 (2009), pp. 391–399.

[136] P. W. Dunne, A. S. Munn, C. L. Starkey, T. A. Huddle, and E. H. Lester. "Continuous-flow hydrothermal synthesis for the production of inorganic nanomaterials." *Philosophical Transactions of the Royal Society A: Mathematical, Physical and Engineering Sciences* 373.2057 (2015), p. 20150015.

[137] P. E. van Keken. "The structure and dynamics of the mantle wedge." *Earth and Planetary Science Letters* 215.3-4 (2003), pp. 323–338.

[138] J. W. Hedenquist and J. B. Lowenstern. "The role of magmas in the formation of hydrothermal ore deposits." *Nature* 370.August (1994), pp. 519–527.

[139] B. W. D. Yardley and R. J. Bodnar. "Fluids in the continental crust." *Geochemical Perspectives* 3.1 (2014), pp. I–127.

[140] P. H. De Jong and G. W. Neilson. "Hydrogen-bond structure in an aqueous solution of sodium chloride at sub- and supercritical conditions." *Journal of Chemical Physics* 107.20 (1997), pp. 8577–8585.

[141] O. A. Karim and J. A. McCammon. “Dynamics of a Sodium Chloride Ion Pair in Water.” *Journal of the American Chemical Society* 108.8 (1986), pp. 1762–1766.

[142] Y. Marcus and G. Hefter. “Ion pairing.” *Chemical Reviews* 106.11 (2006), pp. 4585–4621.

[143] E. H. Oelkers and H. C. Helgeson. “Calculation of dissociation constants and the relative stabilities of polynuclear clusters of 1:1 electrolytes in hydrothermal solutions at supercritical pressures and temperatures.” *Geochimica et Cosmochimica Acta* 57.12 (1993), pp. 2673–2697.

[144] D. M. Sherman. “Metal complexation and ion association in hydrothermal fluids: Insights from quantum chemistry and molecular dynamics.” *Geofluids* 10.1-2 (2010), pp. 41–57.

[145] E. Roedder. *Fluid inclusions*. De Gruyter, 1984.

[146] O. Klein-BenDavid, E. S. Izraeli, E. Hauri, and O. Navon. “Fluid inclusions in diamonds from the Diavik mine, Canada and the evolution of diamond-forming fluids.” *Geochimica et Cosmochimica Acta* 71.3 (2007), pp. 723–744.

[147] P. T. Cummings and A. A. Chialvo. “Molecular simulation of supercritical water and aqueous solutions.” *Journal of Physics Condensed Matter* 8.47 (1996), pp. 9281–9287.

[148] A. A. Chialvo, P. T. Cummings, and H. D. Cochran. “Solvation structure, hydrogen bonding, and ion pairing in dilute supercritical aqueous NaCl mixtures.” *International Journal of Thermophysics* 17.1 (1996), pp. 147–156.

[149] M. T. Reagan, J. G. Harris, and J. W. Tester. “Molecular simulations of dense hydrothermal NaCl-H2O solutions from subcritical to supercritical conditions.” *Journal of Physical Chemistry B* 103.37 (1999), pp. 7935–7941.

[150] H. Shen, T. Hao, J. Wen, R. R. Tan, and F. S. Zhang. “Properties of pure water and sodium chloride solutions at high temperatures and pressures: A simulation study.” *Molecular Simulation* 41.18 (2015), pp. 1488–1494.

[151] S. L. Wallen, B. J. Palmer, and J. L. Fulton. “The ion pairing and hydration structure of Ni2+ in supercritical water at 425 °C determined by x-ray absorption fine structure and molecular dynamics studies.” *Journal of Chemical Physics* 108.10 (1998), pp. 4039–4046.

[152] T. M. Seward, C. M. Henderson, and J. M. Charnock. “Indium(III) chloride complexing and solvation in hydrothermal solutions to 350°C: An EXAFS study.” *Chemical Geology* 167.1-2 (2000), pp. 117–127.

[153] A. Filipponi, S. De Panfilis, C. Oliva, M. A. Ricci, P. D'Angelo, and D. T. Bowron. "Ion hydration under pressure." *Physical Review Letters* 91.16 (2003), pp. 19–22.

[154] G. S. Pokrovski, B. R. Tagirov, J. Schott, E. F. Bazarkina, J. L. Hazemann, and O. Proux. "An in situ X-ray absorption spectroscopy study of gold-chloride complexing in hydrothermal fluids." *Chemical Geology* 259.1-2 (2009), pp. 17–29.

[155] C. J. Sahle, J. Niskanen, C. Schmidt, J. Stefanski, K. Gilmore, Y. Forov, S. Jahn, M. Wilke, and C. Sternemann. "Cation Hydration in Supercritical NaOH and HCl Aqueous Solutions." *The Journal of Physical Chemistry B* 121.50 (2017), pp. 11383–11389.

[156] L. Å. Näslund, D. C. Edwards, P. Wernet, U. Bergmann, H. Ogasawara, L. G. Pettersson, S. Myneni, and A. Nilsson. "X-ray absorption spectroscopy study of the hydrogen bond network in the bulk water of aqueous solutions." *Journal of Physical Chemistry A* 109.27 (2005), pp. 5995–6002.

[157] I. Waluyo, D. Nordlund, U. Bergmann, D. Schlesinger, L. G. Pettersson, and A. Nilsson. "A different view of structure-making and structure-breaking in alkali halide aqueous solutions through x-ray absorption spectroscopy." *Journal of Chemical Physics* 140.24 (2014), p. 244506.

[158] M. Elbers, C. Schmidt, C. Sternemann, C. J. Sahle, S. Jahn, C. Albers, R. Sakrowski, H. Gretarsson, M. Sundermann, M. Tolan, and M. Wilke. "Ion association in hydrothermal aqueous NaCl solutions: Implications for the microscopic structure of supercritical water." *Physical Chemistry Chemical Physics* 23.27 (2021), pp. 14845–14856.

[159] S. Huotari, C. J. Sahle, C. Henriquet, A. Al-Zein, K. Martel, L. Simonelli, R. Verbeni, H. Gonzalez, M. C. Lagier, C. Ponchut, M. Moretti Sala, M. Krisch, and G. Monaco. "A large-solid-angle X-ray Raman scattering spectrometer at ID20 of the European Synchrotron Radiation Facility." *Journal of Synchrotron Radiation* 24.2 (2017), pp. 521–530.

[160] D. Ketenoglu, G. Spiekermann, M. Harder, E. Oz, C. Koz, M. C. Yagci, E. Yilmaz, Z. Yin, C. J. Sahle, B. Detlefs, and H. Yavaş. "X-ray Raman spectroscopy of lithium-ion battery electrolyte solutions in a flow cell." *Journal of Synchrotron Radiation* 25.2 (2018), pp. 537–542.

[161] C. J. Sahle, A. Mirone, J. Niskanen, J. Inkinen, M. Krisch, and S. Huotari. "Planning, performing and analyzing X-ray Raman scattering experiments." *Journal of Synchrotron Radiation* 22.2 (2015), pp. 400–409.

[162] S. Huotari, T. Pylkkänen, R. Verbeni, G. Monaco, and K. Hämäläinen. "Direct tomography with chemical-bond contrast." *Nature Materials* 10.7 (2011), pp. 489–493.

[163] C. J. Sahle, A. D. Rosa, M. Rossi, V. Cerantola, G. Spiekermann, S. Petitgirard, J. Jacobs, S. Huotari, M. M. Sala, and A. Mirone. "Direct tomography imaging for inelastic X-ray scattering experiments at high pressure." *Journal of Synchrotron Radiation* 24.1 (2017), pp. 269–275.

[164] C. Schmidt and K. Rickers. "In-situ determination of mineral solubilities in fluids using a hydrothermal diamond-anvil cell and SR-XRF: Solubility of AgCl in water." *American Mineralogist* 88.2-3 (2003), pp. 288–292.

[165] C. Schmidt and T. M. Seward. "Raman spectroscopic quantification of sulfur species in aqueous fluids: Ratios of relative molar scattering factors of Raman bands of H2S, HS−, SO2, HSO4−, SO42−, S2O32−, S3− and H2O at ambient conditions and information on changes with pressure and temperature." *Chemical Geology* 467 (2017), pp. 64–75.

[166] C. Schmidt. "Raman spectroscopic study of a H2O + Na2SO4 solution at 21-600 °C and 0.1 MPa to 1.1 GPa: Relative differential $\nu 1$ - SO42 - Raman scattering cross sections and evidence of the liquid-liquid transition." *Geochimica et Cosmochimica Acta* 73.2 (2009), pp. 425–437.

[167] M. Steele-MacInnis, P. Lecumberri-Sanchez, and R. J. Bodnar. "HokieFlincs H2O-NaCl: A Microsoft Excel spreadsheet for interpreting microthermometric data from fluid inclusions based on the PVTX properties of H2O-NaCl." *Computers and Geosciences* 49 (2012), pp. 334–337.

[168] R. J. Bodnar. "Revised equation and table for determining the freezing point depression of H2O-Nacl solutions." *Geochimica et Cosmochimica Acta* 57.3 (1993), pp. 683–684.

[169] T. D. Kühne et al. "CP2K: An electronic structure and molecular dynamics software package -Quickstep: Efficient and accurate electronic structure calculations." *Journal of Chemical Physics* 152.19 (2020), p. 194103.

[170] J. VandeVondele, M. Krack, F. Mohamed, M. Parrinello, T. Chassaing, and J. Hutter. "Quickstep: Fast and accurate density functional calculations using a mixed Gaussian and plane waves approach." *Computer Physics Communications* 167.2 (2005), pp. 103–128.

[171] A. D. Becke. "Density-functional exchange-energy approximation with correct asymptotic behavior." *Physical Review A* 38.6 (1988), pp. 3098–3100.

[172] C. Lee, W. Yang, and R. G. Parr. "Development of the Colle-Salvetti correlation-energy formula into a functional of the electron density." *Phys. Rev. B* 37.2 (1988), pp. 785–789.

[173] S. Goedecker and M. Teter. "Separable dual-space Gaussian pseudopotentials." *Physical Review B - Condensed Matter and Materials Physics* 54.3 (1996), pp. 1703–1710.

[174] J. VandeVondele and J. Hutter. "Gaussian basis sets for accurate calculations on molecular systems in gas and condensed phases." *Journal of Chemical Physics* 127.11 (2007), p. 114105.

[175] G. Bussi, D. Donadio, and M. Parrinello. "Canonical sampling through velocity rescaling." *Journal of Chemical Physics* 126.1 (2007), p. 014101.

[176] B. Hammer, L. B. Hansen, and J. K. Nørskov. "Improved adsorption energetics within density-functional theory using revised Perdew-Burke-Ernzerhof functionals." *Physical Review B - Condensed Matter and Materials Physics* 59.11 (1999), pp. 7413–7421.

[177] T. H. Dunning. "Gaussian basis sets for use in correlated molecular calculations. I. The atoms boron through neon and hydrogen." *The Journal of Chemical Physics* 90.2 (1989), pp. 1007–1023.

[178] W. Kutzelnigg, U. Fleischer, and M. Schindler. *The IGLO-Method: Ab-initio Calculation and Interpretation of NMR Chemical Shifts and Magnetic Susceptibilities*. Vol. 23. Springer, Berlin/Heidelberg, 1990, pp. 165–262.

[179] J. D. Smith, C. D. Cappa, B. M. Messer, W. S. Drisdell, R. C. Cohen, and R. J. Saykally. "Probing the local structure of liquid water by X-ray absorption spectroscopy." *Journal of Physical Chemistry B* 110.40 (2006), pp. 20038–20045.

[180] H. Fukui, S. Huotari, D. Andrault, and T. Kawamoto. "Oxygen K-edge fine structures of water by x-ray Raman scattering spectroscopy under pressure conditions." *The Journal of chemical physics* 127.13 (2007), p. 134502.

[181] I. Juurinen, T. Pylkkänen, K. O. Ruotsalainen, C. J. Sahle, G. Monaco, K. Hämälainen, S. Huotari, and M. Hakala. "Saturation behavior in X-ray Raman scattering spectra of aqueous LiCl." *Journal of Physical Chemistry B* 117.51 (2013), pp. 16506–16511.

[182] G. Lelong, L. Cormier, L. Hennet, F. Michel, J. P. Rueff, J. M. Ablett, and G. Monaco. "Lithium Borates from the Glass to the Melt: A Temperature-Induced Structural Transformation Viewed from the Boron and Oxygen Atoms." *Inorganic Chemistry* 60.2 (2021), pp. 798–806.

[183] Q. Sun. "Raman spectroscopic study of the effects of dissolved NaCl on water structure." *Vibrational Spectroscopy* 62 (2012), pp. 110–114.

[184] Y. Marcus. "Effect of ions on the structure of water: Structure making and breaking." *Chemical Reviews* 109.3 (2009), pp. 1346–1370.

[185] I. Waluyo, C. Huang, D. Nordlund, U. Bergmann, T. M. Weiss, L. G. Pettersson, and A. Nilsson. "The structure of water in the hydration shell of cations from x-ray Raman and small angle x-ray scattering measurements." *Journal of Chemical Physics* 134.6 (2011), p. 064513.

[186] Y. L. Jeyachandran, F. Meyer, A. Benkert, M. Bär, M. Blum, W. Yang, F. Reinert, C. Heske, L. Weinhardt, and M. Zharnikov. "Investigation of the Ionic Hydration in Aqueous Salt Solutions by Soft X-ray Emission Spectroscopy." *Journal of Physical Chemistry B* 120.31 (2016), pp. 7687–7695.

[187] T. M. Seward, C. M. Henderson, J. M. Charnock, and T. Driesner. "An EXAFS study of solvation and ion pairing in aqueous strontium solutions to 300°C." *Geochimica et Cosmochimica Acta* 63.16 (1999), pp. 2409–2418.

[188] D. M. Sherman and M. D. Collings. "Ion association in concentrated NaCl brines from ambient to supercritical conditions: Results from classical molecular dynamics simulations." *Geochemical Transactions* 3 (2002), pp. 102–107.

[189] G. V. Bondarenko, Y. E. Gorbaty, A. V. Okhulkov, and A. G. Kalinichev. "Structure and hydrogen bonding in liquid and supercritical aqueous NaCl solutions at a pressure of 1000 bar and temperatures up to 500 °C: A comprehensive experimental and computational study." *Journal of Physical Chemistry A* 110.11 (2006), pp. 4042–4052.

[190] C. Schmidt. "Raman spectroscopic determination of carbon speciation and quartz solubility in H2O+Na2CO3 and H2O+NaHCO3 fluids to 600°C and 1.53GPa." *Geochimica et Cosmochimica Acta* 145 (2014), pp. 281–296.

[191] J. P. Brodholt. "Molecular dynamics simulations of aqueous NaCl solutions at high pressures and temperatures." *Chemical Geology* 151.1-4 (1998), pp. 11–19.

[192] I. Howell and G. W. Neilson. "The coordination of Ni2+ in aqueous solution at elevated temperature and pressure." *Journal of Chemical Physics* 104.5 (1996), pp. 2036–2042.

[193] A. S. Quist and W. L. Marshall. "Electrical conductances of aqueous sodium chloride solutions from 0 to 800° and at pressures to 4000 bars." *Journal of Physical Chemistry* 72.2 (1968), pp. 684–703.

[194] C. E. Manning. "Thermodynamic Modeling of Fluid-Rock Interaction at Mid-Crustal to Uper-Mantle Conditions." *Reviews in Mineralogy & Geochemistry* 76 (2013), pp. 135–164.

[195] A. P. Gaiduk and G. Galli. "Local and Global Effects of Dissolved Sodium Chloride on the Structure of Water." *Journal of Physical Chemistry Letters* 8.7 (2017), pp. 1496–1502.

[196] A. Botti, F. Bruni, S. Imberti, M. A. Ricci, and A. K. Soper. "Ions in water: The microscopic structure of concentrated NaOH solutions." *Journal of Chemical Physics* 120.21 (2004), pp. 10154–10162.

[197] C. Huang, K. T. Wikfeldt, T. Tokushima, D. Nordlund, Y. Harada, U. Bergmann, M. Niebuhr, and T. M. Weiss. "The inhomogeneous structure of water." *Proceedings of the National Academy of Sciences of the United States of America* 106.36 (2009), pp. 15214–15218.

[198] A. K. Soper. "Is water one liquid or two?" *Journal of Chemical Physics* 150.23 (2019), p. 234503.

[199] T. Kawamoto, S. Ochiai, and H. Kagi. "Changes in the structure of water deduced from the pressure dependence of the Raman OH frequency." *Journal of Chemical Physics* 120.13 (2004), pp. 5867–5870.

[200] R. M. Khusnutdinoff and A. V. Mokshin. "Short-range structural transformations in water at high pressures." *Journal of Non-Crystalline Solids* 357.7 (2011), pp. 1677–1684.

[201] P. H. Yancey. "Organic osmolytes as compatible, metabolic and counteracting cytoprotectants in high osmolarity and other stresses." *Journal of Experimental Biology* 208.15 (2005), pp. 2819–2830.

[202] T. Ohto, J. Hunger, E. H. Backus, W. Mizukami, M. Bonn, and Y. Nagata. "Trimethylamine-N-oxide: Its hydration structure, surface activity, and biological function, viewed by vibrational spectroscopy and molecular dynamics simulations." *Physical Chemistry Chemical Physics* 19.10 (2017), pp. 6909–6920.

[203] C. Krywka, C. Sternemann, M. Paulus, M. Tolan, C. Royer, and R. Winter. "Effect of osmolytes on pressure-induced unfolding of proteins: A high-pressure SAXS study." *ChemPhysChem* 9.18 (2008), pp. 2809–2815.

[204] J. Möller, S. Grobelny, J. Schulze, A. Steffen, S. Bieder, M. Paulus, M. Tolan, and R. Winter. "Specific anion effects on the pressure dependence of the protein-protein interaction potential." *Physical Chemistry Chemical Physics* 16.16 (2014), pp. 7423–7429.

[205] T. Irifune, A. Kurio, S. Sakamoto, T. Inoue, and H. Sumiya. "Ultrahard polycrystalline diamond from graphite." *Nature* 421 (2003), pp. 599–600.

[206] S. Petitgirard, J. Jacobs, V. Cerantola, I. E. Collings, R. Tucoulou, L. Dubrovinsky, and C. J. Sahle. "A versatile diamond anvil cell for X-ray inelastic, diffraction and imaging studies at synchrotron facilities." *Review of Scientific Instruments* 90.9 (2019).

[207] C. Schmidt and M. A. Ziemann. "In-situ Raman spectroscopy of quartz: A pressure sensor for hydrothermal diamond-anvil cell experiments at elevated temperatures." *American Mineralogist* 85.11-12 (2000), pp. 1725–1734.

[208] B. Hetényi, F. De Angelis, P. Giannozzi, and R. Car. "Calculation of near-edge x-ray-absorption fine structure at finite temperatures: Spectral signatures of hydrogen bond breaking in liquid water." *Journal of Chemical Physics* 120.18 (2004), pp. 8632–8637.

[209] D. Prendergast and G. Galli. "X-ray absorption spectra of water from first principles calculations." *Physical Review Letters* 96.21 (2006), pp. 1–4.

[210] W. Chen, X. Wu, and R. Car. "X-Ray absorption signatures of the molecular environment in water and ice." *Physical Review Letters* 105.1 (2010), pp. 1–4.

[211] W. Wagner and A. Pruß. "The IAPWS formulation 1995 for the thermodynamic properties of ordinary water substance for general and scientific use." *Journal of Physical and Chemical Reference Data* 31.2 (2002), pp. 387–535.

[212] J. Urquidi, S. Singh, C. H. Cho, and G. W. Robinson. "Origin of temperature and pressure effects on the radial distribution function of water." *Physical Review Letters* 82.12 (1999), pp. 2348–2350.

[213] T. Strässle, A. M. Saitta, Y. L. Godec, G. Hamel, S. Klotz, J. S. Loveday, and R. J. Nelmes. "Structure of dense liquid water by neutron scattering to 6.5 GPa and 670 K." *Physical Review Letters* 96.6 (2006), pp. 1–4.

[214] Y. Katayama, T. Hattori, H. Saitoh, T. Ikeda, K. Aoki, and K. Funakoshi. "Structure of liquid water under high pressure up to 17 GPa." *Physical Review B* 81.1 (2010), pp. 1–6.

[215] L. B. Skinner, M. Galib, J. L. Fulton, C. J. Mundy, J. B. Parise, V. T. Pham, G. K. Schenter, and C. J. Benmore. "The structure of liquid water up to 360 MPa from x-ray diffraction measurements using a high Q-range and from molecular simulation." *Journal of Chemical Physics* 144.13 (2016).

[216] Q. Sun, H. Zheng, J. A. Xu, and E. Hines. "Raman spectroscopic studies of the stretching band from water up to 6 kbar at 290 K." *Chemical Physics Letters* 379.5-6 (2003), pp. 427–431.

[217] T. Okada, K. Komatsu, T. Kawamoto, T. Yamanaka, and H. Kagi. "Pressure response of Raman spectra of water and its implication to the change in hydrogen bond interaction." *Spectrochimica Acta - Part A: Molecular and Biomolecular Spectroscopy* 61.10 (2005), pp. 2423–2427.

[218] F. Mallamace, C. Corsaro, E. Fazio, S. H. Chen, and D. Mallamace. "A study of the hydrogen bonds effect on the water density and the liquid-liquid transition." *Science China: Physics, Mechanics and Astronomy* 62.10 (2019).

[219] A. Polian and M. Grimsditch. "New high-pressure phase of H2O: Ice X." *Physical Review Letters* 52.15 (1984), pp. 1312–1314.

[220] J. S. Tse, K. H. Tan, and J. M. Chen. "Oxygen K-edge XANES of crystalline and amorphous ice." *Chemical Physics Letters* 174.6 (1990), pp. 603–608.

[221] U. Bergmann, P. Wernet, P. Glatzel, M. Cavalleri, L. G. Pettersson, A. Nilsson, and S. P. Cramer. "X-ray Raman spectroscopy at the oxygen K edge of water and ice: Implications on local structure models." *Physical Review B - Condensed Matter and Materials Physics* 66.9 (2002), pp. 1–4.

[222] B. Kamb. "Structure of Ice VI." *Science* 150.5 (1965), pp. 205–209.

[223] B. Kamb and A. Prakash. "Structure of ice III." *Acta Crystallographica Section B* 24.10 (1968), pp. 1317–1327.

[224] W. F. Kuhs, J. L. Finney, C. Vettier, and D. V. Bliss. "Structure and hydrogen ordering in ices VI, VII, and VIII by neutron powder diffraction." *The Journal of Chemical Physics* 81.8 (1984), pp. 3612–3623.

[225] V. Petrenko and R. Whitworth. *Physics of Ice*. 2002.

[226] C. G. Salzmann. "Advances in the experimental exploration of water's phase diagram." *Journal of Chemical Physics* 150.6 (2019).

[227] M. F. Chaplin. "Structure and Properties of Water in its Various States." *Encyclopedia of Water* (2019), pp. 1–19.

[228] W. F. Kuhs and M. S. Lehmann. "The structure of ice Ih by neutron diffraction." *Journal of Physical Chemistry* 87.21 (1983), pp. 4312–4313.

[229] M. Canpolat, F. W. Starr, M. R. Sadr-lahijany, A. Scala, O. Mishima, S. Havlin, and H. E. Stanley. "Local structural heterogeneities in liquid water under pressure." *Chemical Physics Letters* 294 (1998), pp. 9–12.

[230] M. Matsumoto, T. Yagasaki, and H. Tanaka. "GenIce: Hydrogen-Disordered Ice Generator." *Journal of Computational Chemistry* 39.1 (2018), pp. 61–64.

[231] M. B. Gillett, J. R. Suko, F. O. Santoso, and P. H. Yancey. "Elevated levels of trimethylamine oxide in muscles of deep-sea gadiform teleosts: A high-pressure adaptation?" *Journal of Experimental Zoology* 279.4 (1997), pp. 386–391.

[232] R. H. Kelly and P. H. Yancey. "High contents of trimethylamine oxide correlating with depth in deep-sea teleost fishes, skates, and decapod crustaceans." *Biological Bulletin* 196.1 (1999), pp. 18–25.

[233] Q. Zou, B. J. Bennion, V. Daggett, and K. P. Murphy. "The molecular mechanism of stabilization of proteins by TMAO and its ability to counteract the effects of urea." *Journal of the American Chemical Society* 124.7 (2002), pp. 1192–1202.

[234] C. J. Sahle, M. a. Schroer, I. Juurinen, and J. Niskanen. "Influence of TMAO and urea on the structure of water studied by inelastic X-ray scattering." *Physical Chemistry Chemical Physics* 18 (2016), pp. 16518–16526.

[235] C. J. Sahle, M. A. Schroer, J. Niskanen, M. Elbers, C. M. Jeffries, and C. Sternemann. "Hydration in aqueous osmolyte solutions: The case of TMAO and urea." *Physical Chemistry Chemical Physics* 22.20 (2020), pp. 11614–11624.

[236] K. A. Dill. "Dominant Forces in Protein Folding." *Biochemistry* 29.31 (1990), pp. 7133–7155.

[237] A. Luzar and D. Chandler. "Hydrogen-bond kinetics in liquid water." *Nature* 379 (1996), pp. 55–57.

[238] J. B. Asbury, T. Steinel, K. Kwak, S. A. Corcelli, C. P. Lawrence, J. L. Skinner, and M. D. Fayer. "Dynamics of water probed with vibrational echo correlation spectroscopy." *Journal of Chemical Physics* 121.24 (2004), pp. 12431–12446.

[239] U. Heugen, G. Schwaab, E. Bründermann, M. Heyden, X. Yu, D. M. Leitner, and M. Havenith. "Solute-induced retardation of water dynamics probed directly by terahertz spectroscopy." *Proceedings of the National Academy of Sciences of the United States of America* 103.33 (2006), pp. 12301–12306.

[240] R. H. Coridan, N. W. Schmidt, G. H. Lai, and G. C. Wong. "Hydration structures near finite-sized nanoscopic objects reconstructed using inelastic x-ray scattering measurements." *Journal of Physics Condensed Matter* 21.42 (2009).

[241] R. H. Coridan, N. W. Schmidt, G. H. Lai, R. Godawat, M. Krisch, S. Garde, P. Abbamonte, and G. C. Wong. "Hydration dynamics at femtosecond time scales and angstrom length scales from inelastic x-ray scattering." *Physical Review Letters* 103.23 (2009), pp. 1–4.

[242] R. H. Coridan and G. C. L. Wong. "Molecular Solvation Dynamics from Inelastic X-Ray Scattering Measurements." *Advances in Chemical Physics*. Vol. 149. John Wiley & Sons, Ltd, 2012, pp. 83–127.

[243] T. Iwashita, B. Wu, W.-R. Chen, S. Tsutsui, A. Q. R. Baron, and T. Egami. "Seeing real-space dynamics of liquid water through inelastic x-ray scattering." *Science Advances* 3.12 (2017), e1603079.

[244] P. Abbamonte, T. Graber, J. P. Reed, S. Smadici, C. L. Yeh, A. Shukla, J. P. Rueff, and W. Ku. "Dynamical reconstruction of the exciton in LiF with inelastic x-ray scattering." *Proceedings of the National Academy of Sciences of the United States of America* 105.34 (2008), pp. 12159–12163.

[245] Y. Q. Cai, P. Chow, C. C. Chen, H. Ishii, K. L. Tsang, C. C. Kao, K. S. Liang, and C. T. Chen. "Optical design and performance of the Taiwan inelastic X-Ray scattering beamline (BL12XU) at SPring-8." *AIP Conference Proceedings* 705 (2004), pp. 340–343.

[246] C. Y. Huang, Y. Q. Cai, S. C. Chung, Y. F. Song, and K. L. Tsang. "Microfocusing system of the Taiwan contract beamline BL12XU at SPring-8 for IXS experiments under high pressure." *AIP Conference Proceedings* 879 (2007), pp. 971–974.

[247] N. Hiraoka, H. Fukui, H. Tanida, H. Toyokawa, Y. Q. Cai, and K. D. Tsuei. "An X-ray Raman spectrometer for EXAFS studies on minerals: Bent Laue spectrometer with 20 keV X-rays." *Journal of Synchrotron Radiation* 20.2 (2013), pp. 266–271.

[248] H. Rowland. " LXI. Preliminary notice of the results accomplished in the manufacture and theory of gratings for optical purposes ." *The London, Edinburgh, and Dublin Philosophical Magazine and Journal of Science* 13.84 (1882), pp. 469–474.

[249] T. Hagiya, K. Matsuda, N. Hiraoka, Y. Kajihara, K. Kimura, and M. Inui. "Static density response function studied by inelastic x-ray scattering: Friedel oscillations in solid and liquid Li." *Physical Review B* 102.5 (2020), p. 54208.

[250] M. J. Cooper. "Compton scattering and electron momentum determination." *Reports on Progress in Physics* 48.4 (1985), pp. 415–481.

[251] R. Ribberfors. "Relationship of the relativistic Compton cross section to the momentum distribution of bound electron states." *Physical Review B* 12.6 (1975), pp. 2067–2074.

[252] R. Ribberfors. "Relationship of the relativistic Compton cross section to the momentum distribution of bound electron states. II. Effects of anisotropy and polarization." *Physical Review B* 12.8 (1975), pp. 3136–3141.

[253] P. M. Bergstrom, T. Surić, K. Pisk, and R. H. Pratt. "Compton scattering of photons from bound electrons: Full relativistic independent-particle-approximation calculations." *Physical Review A* 48.2 (1993), pp. 1134–1162.

[254] P. Holm. "Relativistic Compton cross section for general central-field Hartree-Fock wave functions." *Physical Review A* 37.10 (1988), pp. 3706–3719.

[255] K. Binder and D. W. Heermann. *Monte Carlo Simulation in Statistical Physics: An Introduction*. Springer, 2019.

[256] J. Felsteiner, P. Pattison, and M. Cooper. "Effect of multiple scattering on experimental Compton profiles: A Monte Carlo calculation." *Philosophical Magazine* 30.3 (1974), pp. 537–548.

[257] J. Chomilier, L. Geneviève, and Felsteiner Joshua. "Correction for multiple scattering in Compton profile experiments: Application for synchrotron source photons." *Nuclear Instruments and Methods in Physics Research* 235.3 (1985), pp. 603–606.

[258] F. Bell. "On the multiple scattering of linearly polarized gamma rays." *Nuclear Instruments and Methods in Physics Research B* 86.3-4 (1994), pp. 251–256.

[259] P. Fajardo, V. Honkimäki, T. Buslaps, and P. Suortti. "Experimental validation of multiple scattering calculations with high energy X-ray photons." *Nuclear Instruments and Methods in Physics Research B* 134 (1998), pp. 337–345.

[260] F. Biggs, L. Mendelsohn, and M. J. B. "Hartree-Fock Compton profiles for the elements." 16.3 (1975), pp. 201–309.

[261] S. Huotari, K. Hämäläinen, S. Manninen, A. Issolah, and M. Marangolo. "Asymmetry of Compton profiles." *Journal of Physics and Chemistry of Solids* 62.12 (2001), pp. 2205–2213.

[262] S. Wang. "Generalization of the Thomas-Reiche-Kuhn and the Bethe sum rules." *Physical Review A* 60.1 (1999), pp. 262–266.

[263] F. Lehmkühler, Y. Forov, M. Elbers, I. Steinke, C. J. Sahle, C. Weis, N. Tsuji, M. Itou, Y. Sakurai, A. Poulain, and C. Sternemann. "Temperature dependence of the hydrogen bond network in trimethylamine: N -oxide and guanidine hydrochloride-water solutions." *Physical Chemistry Chemical Physics* 19.41 (2017), pp. 28470–28475.

[264] Y. S. Badyal, M. L. Saboungi, D. L. Price, S. D. Shastri, D. R. Haeffner, and A. K. Soper. "Electron distribution in water." *Journal of Chemical Physics* 112.21 (2000), pp. 9206–9208.

[265] M. R. Milovanović, J. M. Živković, D. B. Ninković, I. M. Stanković, and S. D. Zarić. "How flexible is the water molecule structure? Analysis of crystal structures and the potential energy surface." *Physical Chemistry Chemical Physics* 22.7 (2020), pp. 4138–4143.

[266] A. K. Soper and M. G. Phillips. "A new determination of the structure of water at 25°C." *Chemical Physics* 107.1 (1986), pp. 47–60.

[267] R. Jimenez, G. R. Fleming, P. V. Kumar, and M. Maroncelli. "Femtosecond solvation dynamics of water." *Nature* 369.6480 (1994), pp. 471–473.

[268] S. Yeremenko, M. S. Pshenichnikov, and D. A. Wiersma. "Hydrogen-bond dynamics in water explored by heterodyne-detected photon echo." *Chemical Physics Letters* 369.1-2 (2003), pp. 107–113.

[269] P. Salucci et al. "Ultrafast Hydrogen-Bond Dynamics in the Infrared." *Science* 301 (2003), pp. 1698–1702.

[270] D. Laage and J. T. Hynes. "A molecular jump mechanism of water reorientation." *Science* 311.5762 (2006), pp. 832–835.

[271] D. Laage and J. T. Hynes. "On the molecular mechanism of water reorientation." *Journal of Physical Chemistry B* 112.45 (2008), pp. 14230–14242.

[272] S. A. Hassan. "Computer simulation of ion cluster speciation in concentrated aqueous solutions at ambient conditions." *Journal of Physical Chemistry B* 112.34 (2008), pp. 10573–10584.

[273] K. J. Goodman and J. T. Brenna. "Curve Fitting for Restoration of Accuracy for Overlapping Peaks in Gas Chromatography/Combustion Isotope Ratio Mass Spectrometry." *Analytical Chemistry* 66.8 (1994), pp. 1294–1301.

[274] G. Giuliani and G. Vignale. *Quantum Theory of the Electron Liquid*. Cambridge University Press, 2005.

[275] J. P. Reed, B. Uchoa, Y. I. Joe, Y. Gan, D. Casa, E. Fradkin, and P. Abbamonte. "The effective fine-structure constant of freestanding graphene measured in graphite." *Science* 330.6005 (2010), pp. 805–808.

[276] G. E. Simion and G. F. Giuliani. "Friedel oscillations in a Fermi liquid." *Physical Review B - Condensed Matter and Materials Physics* 72.4 (2005), pp. 1–8.

[277] Y. Pavlyukh, A. Rubio, and J. Berakdar. "Time evolution of excitations in normal Fermi liquids." *Physical Review B - Condensed Matter and Materials Physics* 87.20 (2013), pp. 1–9.

[278] F. Lépine, M. Y. Ivanov, and M. J. Vrakking. "Attosecond molecular dynamics: Fact or fiction?" *Nature Photonics* 8.3 (2014), pp. 195–204.

[279] C. Chen, Z. Tao, A. Carr, P. Matyba, T. Szilvási, S. Emmerich, M. Piecuch, M. Keller, D. Zusin, S. Eich, M. Rollinger, W. You, S. Mathias, U. Thumm, M. Mavrikakis, M. Aeschlimann, P. M. Oppeneer, H. Kapteyn, and M. Murnane. "Distinguishing attosecond electron-electron scattering and screening in transition metals." *Proceedings of the National Academy of Sciences of the United States of America* 114.27 (2017), E5300–E5307.

[280] M. A. Ratner, P. Johansson, and D. F. Shriver. "Polymer electrolytes: Ionic transport mechanisms and relaxation coupling." *MRS Bulletin* 25.3 (2000), pp. 31–37.

[281] M. Frey, H. Didzoleit, C. Gainaru, and R. Böhmer. "Dynamics in glass forming sulfuric and nitric acid hydrates." *Journal of Physical Chemistry B* 117.40 (2013), pp. 12164–12174.

[282] D. Mecerreyes. "Polymeric ionic liquids: Broadening the properties and applications of polyelectrolytes." *Progress in Polymer Science (Oxford)* 36.12 (2011), pp. 1629–1648.

[283] Z. Wojnarowska, H. Feng, Y. Fu, S. Cheng, B. Carroll, R. Kumar, V. N. Novikov, A. M. Kisliuk, T. Saito, N. G. Kang, J. W. Mays, A. P. Sokolov, and V. Bocharova. "Effect of Chain Rigidity on the Decoupling of Ion Motion from Segmental Relaxation in Polymerized Ionic Liquids: Ambient and Elevated Pressure Studies." *Macromolecules* 50.17 (2017), pp. 6710–6721.

[284] C. Gainaru, E. W. Stacy, V. Bocharova, M. Gobet, A. P. Holt, T. Saito, S. Greenbaum, and A. P. Sokolov. "Mechanism of Conductivity Relaxation in Liquid and Polymeric Electrolytes: Direct Link between Conductivity and Diffusivity." *Journal of Physical Chemistry B* 120.42 (2016), pp. 11074–11083.

[285] V. Strehmel, D. Strunk, H. Wetzel, and N. Strehmel. "Investigation of lignin obtained by processing of Betula pendula with ionic liquids." *Sustainable Chemistry and Pharmacy* 6 (2017), pp. 107–113.

[286] D. Salas-De La Cruz, M. D. Green, Y. Ye, Y. A. Elabd, T. E. Long, and K. I. Winey. "Correlating backbone-to-backbone distance to ionic conductivity in amorphous polymerized ionic liquids." *Journal of Polymer Science, Part B: Polymer Physics* 50.5 (2012), pp. 338–346.

[287] K. N. Marsh, J. A. Boxall, and R. Lichtenthaler. "Room temperature ionic liquids and their mixtures - A review." *Fluid Phase Equilibria* 219.1 (2004), pp. 93–98.

[288] M. Freemantle. "Designer Solvents: Ionic liquids may boost clean technology development." *Chemical & Engineering News* 76.13 (1998), pp. 32–37.

[289] A. Eftekhari and T. Saito. "Synthesis and properties of polymerized ionic liquids." *European Polymer Journal* 90 (2017), pp. 245–272.

[290] V. Bocharova, Z. Wojnarowska, P. F. Cao, Y. Fu, R. Kumar, B. Li, V. N. Novikov, S. Zhao, A. Kisliuk, T. Saito, J. W. Mays, B. G. Sumpter, and A. P. Sokolov. "Influence of Chain Rigidity and Dielectric Constant on the Glass Transition Temperature in Polymerized Ionic Liquids." *Journal of Physical Chemistry B* 121.51 (2017), pp. 11511–11519.

[291] C. Prescher and V. B. Prakapenka. "DIOPTAS: a program for reduction of two-dimensional X-ray diffraction data and data exploration." *High Pressure Research* 35.3 (2015), pp. 223–230.

[292] W. A. Caliebe, V. Murzin, A. Kalinko, and M. Görlitz. "High-flux XAFS-beamline P64 at PETRA III." *AIP Conference Proceedings* 2054 (2019).

[293] E. Burattini, P. D'Angelo, A. Di Cicco, A. Filipponi, and N. V. Pavel. "Multiple scattering X-ray absorption analysis of simple brominated hydrocarbon molecules." *Journal of Physical Chemistry* 97.21 (1993), pp. 5486–5494.

[294] M. Newville, P. Līviņš, Y. Yacoby, J. J. Rehr, and E. A. Stern. "Near-edge x-ray-absorption fine structure of Pb: A comparison of theory and experiment." *Physical Review B* 47.21 (1993), pp. 14126–14131.

[295] P. D'Angelo, A. Zitolo, G. Aquilanti, and V. Migliorati. "Using a combined theoretical and experimental approach to understand the structure and dynamics of imidazolium-based ionic liquids/water mixtures. 2. EXAFS spectroscopy." *Journal of Physical Chemistry B* 117.41 (2013), pp. 12516–12524.

[296] S. D. Kelly, D. Hesterberg, and B. Ravel. "Analysis of Soils and Minerals Using X-ray Absorption Spectroscopy." *Methods of Soil Analysis Part 5—Mineralogical Methods*. John Wiley & Sons, Ltd, 2015. Chap. 14, pp. 387–463.

[297] M. Newville. "Larch: An analysis package for XAFS and related spectroscopies." *Journal of Physics: Conference Series* 430.1 (2013).

[298] J. C. Araque, J. J. Hettige, and C. J. Margulis. "Modern Room Temperature Ionic Liquids, a Simple Guide to Understanding Their Structure and How It May Relate to Dynamics." *Journal of Physical Chemistry B* 119.40 (2015), pp. 12727–12740.

[299] A. Perera and R. Mazighi. "Simple and complex forms of disorder in ionic liquids." *Journal of Molecular Liquids* 210 (2015), pp. 243–251.

[300] A. Perera. "Charge ordering and scattering pre-peaks in ionic liquids and alcohols." *Physical Chemistry Chemical Physics* 19.2 (2017), pp. 1062–1073.

[301] H. V. Annapureddy, H. K. Kashyap, P. M. De Biase, and C. J. Margulis. "What is the origin of the prepeak in the x-ray scattering of imidazolium-based room-temperature ionic liquids?" *Journal of Physical Chemistry B* 114.50 (2010), pp. 16838–16846.

[302] M. H. Allen, S. Wang, S. T. Hemp, Y. Chen, L. A. Madsen, K. I. Winey, and T. E. Long. "Hydroxyalkyl-containing imidazolium homopolymers: Correlation of structure with conductivity." *Macromolecules* 46.8 (2013), pp. 3037–3045.

[303] H. Liu and S. J. Paddison. "Direct Comparison of Atomistic Molecular Dynamics Simulations and X-ray Scattering of Polymerized Ionic Liquids." *ACS Macro Letters* 5.4 (2016), pp. 537–543.

[304] H. Liu and S. J. Paddison. "Alkyl Chain Length Dependence of Backbone-to-Backbone Distance in Polymerized Ionic Liquids: An Atomistic Simulation Perspective on Scattering." *Macromolecules* 50.7 (2017), pp. 2889–2895.

[305] V. Delhorbe, D. Bresser, H. Mendil-Jakani, P. Rannou, L. Bernard, T. Gutel, S. Lyonnard, and L. Picard. "Unveiling the Ion Conduction Mechanism in Imidazolium-Based Poly(ionic liquids): A Comprehensive Investigation of the Structure-to-Transport Interplay." *Macromolecules* 50.11 (2017), pp. 4309–4321.

[306] C. Krause, J. R. Sangoro, C. Iacob, and F. Kremer. "Charge transport and dipolar relaxations in imidazolium-based ionic liquids." *Journal of Physical Chemistry B* 114.1 (2010), pp. 382–386.

[307] J. Leys, R. N. Rajesh, P. C. Menon, C. Glorieux, S. Longuemart, P. Nockemann, M. Pellens, and K. Binnemans. "Influence of the anion on the electrical conductivity and glass formation of 1-butyl-3-methylimidazolium ionic liquids." *Journal of Chemical Physics* 133.3 (2010).

[308] U. H. Choi, Y. Ye, D. Salas De La Cruz, W. Liu, K. I. Winey, Y. A. Elabd, J. Runt, and R. H. Colby. "Dielectric and viscoelastic responses of imidazolium-based ionomers with different counterions and side chain lengths." *Macromolecules* 47.2 (2014), pp. 777–790.

[309] J. J. Hettige, H. K. Kashyap, and C. J. Margulis. "Communication: Anomalous temperature dependence of the intermediate range order in phosphonium ionic liquids." *Journal of Chemical Physics* 140.11 (2014), pp. 1–5.

[310] A. Triolo, O. Russina, H. J. Bleif, and E. Di Cola. "Nanoscale segregation in room temperature ionic liquids." *Journal of Physical Chemistry B* 111.18 (2007), pp. 4641–4644.

[311] O. Russina, A. Triolo, L. Gontrani, R. Caminiti, D. Xiao, L. G. Hines, R. A. Bartsch, E. L. Quitevis, N. Plechkova, and K. R. Seddon. "Morphology and intermolecular dynamics of 1-Alkyl-3-methylimidazolium bis{(trifluoromethane)sulfonyl}amide ionic liquids: Structural and dynamic evidence of nanoscale segregation." *Journal of Physics Condensed Matter* 21.42 (2009), p. 424121.

[312] H. K. Kashyap, C. S. Santos, R. P. Daly, J. J. Hettige, N. S. Murthy, H. Shirota, E. W. Castner, and C. J. Margulis. "How does the ionic liquid organizational landscape change when nonpolar cationic alkyl groups are replaced by polar isoelectronic diethers?" *Journal of Physical Chemistry B* 117.4 (2013), pp. 1130–1135.

Publications

- **M. Elbers**, C. Sternemann, K. Julius, M. Paulus, G. Surmeier, N. König, J. Nase, J. Bolle, R. Wagner, T. Irifune, and M. Tolan. "Pressure stability of the first hydration shell of yttrium in aqueous YCl_3 solution." *High Pressure Research* 40.1 (2020) pp. 194-204
- **M. Elbers**, C. Schmidt, C. Sternemann, C. J. Sahle, S. Jahn, C. Albers, R. Sakrowski, H. Gretarsson, M. Sundermann, M. Tolan, and M. Wilke. "Ion association in hydrothermal aqueous NaCl solutions: Implications for the microscopic structure of supercritical water." *Physical Chemistry Chemical Physics* 23.27 (2021) pp. 14845-14856
- C.J. Sahle, M.A. Schroer, J. Niskanen, **M. Elbers**, C.M. Jeffries, and C. Sternemann. "Hydration in aqueous osmolyte solutions: the case of TMAO and urea." *Physical Chemistry Chemical Physics* 22.20 (2020) pp. 11614-11624
- K. Julius, J. Weine, M. Gao, J. Latarius, **M. Elbers**, M. Paulus, M. Tolan, and R. Winter. "Impact of macromolecular crowding and compression on protein- protein interactions and liquid−liquid phase separation phenomena." *Macromolecules* 52.4 (2019) pp. 1772–1784
- W. Tillmann, L. Hagen, D. Stangier, M. Krabiell, P. Schröder, J. Tiller, C. Krumm, C. Sternemann, M. Paulus, **M. Elbers**. "Influence of etching pretreatment on nano-grained WC-Co surfaces and properties of PVD/HVOF duplex coatings." *Surface Coatings Technology* 374 (2019) pp. 32-43
- Y. Forov, M. Paulus, S. Dogan, P. Salmen, C. Weis, T. Gahlmann, A. Behrendt, C. Albers, **M. Elbers**, W. Schnettger, S. Egger, E. Zwar, H. Rehage, I. Kiesel, T. Riedl, and M. Tolan. "The adsorption behavior of lysozyme at titanium oxide-water interfaces." *Langmuir* 34.19 (2018) pp. 5403–5408
- F. Lehmkühler, Y. Forov, **M. Elbers**, I. Steinke, Ch.J. Sahle, C. Weis, M. Itou, Y. Sakurai, A. Poulain, C. Sternemann. "Temperature dependence of the hydrogen bond network in Trimethylamine N-oxide and guanidine hydrochloride-water solutions." *Physical Chemistry Chemical Physics* 19.41 (2017) pp. 28470-28475

Acknowledgments

Without the manifold support of various people over the last few years, this thesis would not have been possible. I would like to express my sincere thanks to all of them.
First of all, I would like to thank Prof. Dr. Metin Tolan for his support and the opportunity to write a thesis about such exciting topics in his workgroup.
Also many thanks to Prof. Dr. Max Wilke for the good cooperation in the investigation of hydrothermal sodium chloride solutions and especially for his role as second referee of this thesis.
For the financial support I thank the Bundesministerium für Bildung und Forschung (05KP16PE1) as well as the Deutsche Forschungsgesellschaft (1079/6-1).
I am very grateful to Dr. Christian Sternemann for his outstanding support over the past years including all the valuable discussions and the constructive feedback. I couldn't have asked for a better supervision. In addition, I would like to thank him for his fast and reliable proofreading of this work.
I consider myself very lucky to have experienced such a fantastic working atmosphere in the E1a workgroup and therefore sincerely thank each member for it.
In particular, I would like to thank my two office colleagues during this time, Dr. Karin Julius and Robin Sakrowski, for the great atmosphere in our office and the productive as well as very funny conversations. Besides thanks to Karin for the productivity-boosting coffee breaks.
My thanks also go to the "Chaosbüro" and his inhabitants Dr. Göran Surmeier, Dr. Susanne Dogan and Christian Albers for always putting a smile on my face whenever I came to visit.
I would also like to thank Manuela Linke for her help with all kinds of administrative matters and Thorsten Witt for his support with all computer-related issues.
The experiments as the basis of my work could only be carried out with the great help of many people. Many thanks to: Christian Albers, Jennifer Bolle, Dr. Susanne Dogan, Dr. Yury Forov, Dr. Nozomu Hiraoka, Prof. Dr. Simo Huotari, Prof. Dr. Sandro Jahn, Jan Latarius, Dr. Felix Lehmkühler, Philipp Münzner, Mike Moron, Dr. Michael Paulus, Dr. Christoph Sahle, Robin Sakrowski, Dr. Christian Schmidt, Dr. Christian Sternemann, Dr. Göran Surmeier, Dr. Christopher Weis, Prof. Dr. Max Wilke.

In the same way, I would also like to thank the local contacts at the Beamlines for their excellent support: Dr. Wolfgang Caliebe, Dr. Hlynur Gretarsson, Dr. Nozumo Hiraoka, Dr. Michael Paulus, Dr. Christoph Sahle, Dr. Christian Sternemann, Dr. Martin Sundermann, Ralph Wagner, Dr. Hasan Yavas and also the entire Beamlines staff.
I acknowledge the computing time provided on the Linux HPC cluster at TU Dortmund (LiDO3, partially funded by the DFG project 271512359) as well as the whole LiDo team for their maintenance and good support.
I am very thankful to Dr. Christoph Sahle for his great help with the DFT calculations and his open ear for all kind of questions. Moreover, a huge thanks to him for the opportunity to perform the XRS measurements on high pressure water with him and all his preparation with the high pressure cells.
I also thank Dr. Christian Schmidt for inviting me to the on-site introduction of hydrothermal diamond anvil cells at the GFZ in Potsdam, as well as the whole preparation of the DAC for a successful beamtime and for answering all my questions regarding hydrothermal fluids.
Many thanks to Prof. Dr. Jahn for performing and providing the AiMD simulations of aqueous NaCl solutions at high temperatures as part of the collaboration on this project.
I would like to thank Catalin Gainaru for the opportunity to study ionic liquids with him and also Philipp Münzner for his great help in preparing the samples for the experiments together.
I am thankful to Prof. Dr. Nozumo Hiraoka for his invitation to join him in the fascinating study of water with IXS.
I thank Prof. Dr. John Tse for the fruitful discussions on water at high pressures.
I would also like to thank Dr. Sho Imoto for providing the AiMD trajectories of water and aqueous TMAO solutions at high pressures.
Many thanks to Dr. Christoph Hasse, who accompanied me throughout my studies up to the master's thesis and with whom the joint work was a lot of fun.
I also thank my family, which of course includes my girlfriend's family, and all my friends for their great support in so many ways over the last years.
Last but not least I would also like to thank my girlfriend Johanna Förster from the bottom of my heart. Her support over the past few years is probably as immeasurable as liquid water in the no-man's land and I am incredibly grateful to have her by my side.